Functional characterization of two major membrane transport proteins in excitatory signaling: vesicular glutamate transporters and voltage-gated calcium channels

Inaugural dissertation

for the attainment of the title of doctor
in the Faculty of Mathematics and Natural Sciences
at the Heinrich Heine University Düsseldorf

presented by

Victor Manuel Lugo Garcia
from Caracas, Venezuela

Jülich, November 2025

from the Institute of Biological Information Processing,
Molecular and Cellular Physiology,
at the Forschungszentrum Jülich

Published by permission of the
Faculty of Mathematics and Natural Sciences at
Heinrich Heine University Düsseldorf

Supervisor: Prof. Dr. Christoph Fahlke
Co-supervisor: Prof. Dr. Christine Rose

Date of oral examination: 22/01/2026

Abstract

Excitatory signaling is a fundamental mechanism underlying neuronal communication, shaping processes that range from brain development to sensory perception. In the mammalian brain, glutamate serves as the primary excitatory neurotransmitter. Two key steps underlying glutamatergic transmission are the packaging of glutamate into synaptic vesicles by vesicular glutamate transporters (VGLUTs) and the entry of calcium through voltage-gated calcium (Ca_V) channels, which triggers vesicular glutamate release. This thesis characterizes the functional properties of VGLUT variants and analyzes the effects of protein–protein interactions on Ca_V channel surface expression and function.

VGLUTs harness the transmembrane proton potential ($\Delta\tilde{\mu}_{H^+}$) generated by the vacuolar-type H^+-ATPase (V-ATPase) to accumulate glutamate within synaptic vesicles. The functional properties of VGLUTs thus constitute a major determinant of synaptic strength. In addition to transporting glutamate, VGLUTs function as chloride channels. The first aim of this investigation was to characterize the molecular mechanisms that underlie this anion conductance. Structure-guided mutagenesis of rat VGLUT1 (rVGLUT1) identified residues that shape pore properties, gating kinetics, and the pH dependence of the anion channel. The *Drosophila* ortholog DVGLUT was subsequently analyzed for functional comparison with its mammalian counterparts. Similar to rVGLUT1, DVGLUT functions as a glutamate/proton exchanger. However, the DVGLUT channel showed distinct differences in luminal chloride–dependent modulation and anion conduction. Finally, a VGLUT3 mutation associated with human deafness was evaluated in the mouse ortholog. This study revealed notable biophysical differences in channel properties compared with wild-type transporters. Together, these investigations advance the understanding of structure–function relationships underlying VGLUT activity and, in turn, synaptic vesicle filling and excitatory neurotransmission.

Ca_V channels are expressed both pre- and postsynaptically, where they couple membrane depolarization to calcium influx. At presynaptic terminals, Ca^{2+} entry through Ca_V channels triggers neurotransmitter release, whereas in postsynaptic dendrites it modulates excitability and synaptic plasticity. The expression levels and functional states of Ca_V channels at the plasma membrane constitute major determinants of synaptic strength and neuronal function. The core components of Ca_V channels are the pore-forming α_1-subunit and the auxiliary β-subunit. The β-subunit promotes intracellular trafficking of the Ca_V α_1 subunit to the plasma membrane and engages in multiple protein–protein interactions that modulate channel activity. Actin, responsible for maintaining cell shape and facilitating intracellular trafficking, associates with the neuronal Ca_V β-subunit to regulate vesicle pool availability. This study investigated the effects of actin-association–deficient Ca_V β mutants on Ca_V channel surface expression and function. The results revealed a role for actin–Ca_V β interactions in removing functionally impaired Ca_V channels. Actin–Ca_V β coupling thus represents a mechanism that ensures reliable calcium signaling at the plasma membrane.

Zusammenfassung

Erregende Signalübertragung ist ein grundlegender Mechanismus der neuronalen Kommunikation und prägt Prozesse, die von der Gehirnentwicklung bis zur sensorischen Wahrnehmung reichen. Im Säugetiergehirn dient Glutamat als primärer erregender Neurotransmitter. Zwei entscheidende Schritte der glutamatergen Transmission sind das Verpacken von Glutamat in synaptische Vesikel durch vesikuläre Glutamattransporter (VGLUTs) sowie der Einstrom von Calcium über spannungsabhängige Calciumkanäle (Ca_V), der die vesikuläre Glutamatfreisetzung auslöst. Diese Arbeit charakterisiert die funktionellen Eigenschaften verschiedener VGLUT-Varianten und untersucht die Auswirkungen von Protein–Protein-Wechselwirkungen auf die Oberflächenexpression und Funktion von Ca_V-Kanälen.

VGLUTs nutzen das transmembrane Protonenpotential ($\Delta\tilde{\mu}_{H^+}$), das durch die vakuoläre H^+-ATPase (V-ATPase) erzeugt wird, um Glutamat in synaptischen Vesikeln anzureichern. Die funktionellen Eigenschaften der VGLUTs stellen somit einen wesentlichen Faktor für die synaptische Stärke dar. Neben dem Transport von Glutamat fungieren VGLUTs als Chloridkanäle. Das erste Ziel dieser Arbeit bestand darin, die molekularen Mechanismen zu charakterisieren, die dieser Anionenleitfähigkeit zugrunde liegen. Durch strukturgeleitete Mutagenese von Ratten-VGLUT1 (rVGLUT1) konnten Aminosäurereste identifiziert werden, die die Poreneigenschaften, die Gating-Kinetik und die pH-Abhängigkeit des Anionenkanals bestimmen. Anschließend wurde das *Drosophila*-Ortholog DVGLUT funktionell mit seinen Säugetierhomologen verglichen. Ähnlich wie rVGLUT1 fungiert DVGLUT als Glutamat/Proton-Austauscher, zeigte jedoch deutliche Unterschiede in der luminalen, chloridabhängigen Modulation und der Anionenleitung. Schließlich wurde eine VGLUT3-Mutation, die mit menschlicher Taubheit assoziiert ist, im Maus-Ortholog untersucht. Diese Studie offenbarte bemerkenswerte biophysikalische Unterschiede in den Kanaleigenschaften im Vergleich zu Wildtyp-Transportern. Insgesamt erweitern diese Untersuchungen das Verständnis der Struktur–Funktions-Beziehungen, die der VGLUT-Aktivität und damit der Vesikelfüllung und erregenden Neurotransmission zugrunde liegen.

Ca_V-Kanäle werden sowohl prä- als auch postsynaptisch exprimiert, wo sie die Membrandepolarisation mit dem Calciumeinstrom koppeln. In präsynaptischen Endigungen löst der Ca^{2+}-Einstrom über Ca_V-Kanäle die Neurotransmitterfreisetzung aus, während er in postsynaptischen Dendriten die Erregbarkeit und synaptische Plastizität moduliert. Die Expressionsniveaus und funktionellen Zustände von Ca_V-Kanälen an der Plasmamembran stellen zentrale Determinanten der synaptischen Stärke und neuronalen Funktion dar. Die Kernkomponenten der Ca_V-Kanäle sind die porenbildende α_1-Untereinheit und die Hilfsuntereinheit β. Die β-Untereinheit fördert den intrazellulären Transport der Ca_V α_1-Untereinheit zur Plasmamembran und geht vielfältige Protein–Protein-Wechselwirkungen ein, die die Kanalaktivität modulieren.

Aktin, das für die Aufrechterhaltung der Zellform und die Vermittlung des intrazellulären Transports verantwortlich ist, bindet an die neuronale $Ca_V\beta$-Untereinheit und reguliert so die Verfügbarkeit von Vesikelpools. Diese Arbeit untersuchte die Auswirkungen von Aktinassoziations-defizienten $Ca_V\beta$-Mutanten auf die Oberflächenexpression und Funktion der Ca_V-Kanäle. Die Ergebnisse zeigen, dass die Aktin–$Ca_V\beta$-Wechselwirkung eine Rolle bei der Entfernung funktionell beeinträchtigter Ca_V-Kanäle spielt. Die Kopplung zwischen Aktin und $Ca_V\beta$ stellt somit einen Mechanismus dar, der eine verlässliche Calciumsignalübertragung an der Plasmamembran gewährleistet.

En nombre de la familia Lugo Garcia

Table of Contents

List of Figures

List of Acronyms

A_{fast}	amplitude coefficient of fast component
AMPA	α-amino-3-hydroxy-5-methyl-4-isoxazolepropionic acid
B	number of bootstrap samples
C_m	membrane capacitance
C_p	pipette capacitance
Ca_V	voltage-gated calcium
$Ca_V\alpha_1$	alpha1 subunit of Ca_V channels
$Ca_V\alpha_2$	alpha2 subunit of Ca_V channels
$Ca_V\beta$	beta subunit of Ca_V channels
$Ca_V\gamma$	gamma subunit of Ca_V channels
$Ca_V\delta$	delta subunit of Ca_V channels
CNS	central nervous system
DMEM	Dulbecco's Modified Eagle Medium
EAAT	excitatory amino acid transporter
E	measured response
E_{Glu^-}	Nernst potential for glutamate
E_{H^+}	Nernst potential for protons
E_{rev}	reversal potential
E_{A^-}	Nernst potential for anion A^-
E_{P^+}	Nernst potential for cation P^+
EC_{50}	half-maximal effective concentration
EPSC	excitatory postsynaptic current
F	Faraday constant
F-actin	filamentous actin
FBS	fetal bovine serum
GABA	γ-aminobutyric acid
g	unitary conductance
GluR	glutamate receptor
HEK293T	human embryonic kidney 293T cell line

$I(t)$	macroscopic current as a function of time
I_c	capacitive current
I_i	initial current
I_{inj}	injected current
I_{leak}	leak current
I_m	membrane current
I_{mean}	mean macroscopic current
$I_{mean,max}$	maximal mean current
I_{ss}	steady-state current
i	unitary current
$K(V)$	voltage-dependent equilibrium constant
K_d	equilibrium dissociation constant
KA	kainate
k_{on}	association rate constant
k_{off}	dissociation rate constant
KO	knockout
L	ligand concentration
mGluR	metabotropic glutamate receptor
N	total number of channels
N_C	number of closed channels
N_O	number of open channels
n	Hill coefficient
NMDA	N-methyl-D-aspartate
PAC	proton-activated chloride channel
P_o	open probability
$P_{o,max}$	maximal open probability
PMF	proton motive force
PNS	peripheral nervous system
Q	capacitive charge
R	universal gas constant
R_a	access resistance
R_f	feedback resistor

R_{leak}	leak resistance
R_p	pipette resistance
R_s	series resistance
T	absolute temperature
TM	transmembrane helix
V	transmembrane voltage
V-ATPase	vacuolar-type H^+-ATPase
$V_{1/2}$	half-activation potential
V_{cmd}	command voltage
V_{eq}	reversal potential of conducting ion
V_m	membrane potential
VGLUT	vesicular glutamate transporter
WT	wild-type
z	effective charge displacement
α	rate constant for closed-to-open transition
β	rate constant for open-to-closed transition
$\Delta G(V)$	voltage-dependent free-energy difference
ΔG_0	intrinsic free-energy difference
$\Delta\psi$	membrane potential difference ($\psi_{in} - \psi_{out}$)
τ	relaxation time constant
τ_{fast}	fast time constant
τ_{slow}	slow time constant

Part I

Vesicular glutamate transporters

Chapter 1:
Introduction

1.1. Organization of the glutamatergic synapse

Neural information is conveyed through synapses. A synapse is a specialized intercellular junction that mediates transmission between neurons or between a neuron and an effector cell [1]. Synapses are classified as either electrical or chemical according to their molecular architecture and mode of transmission. Electrical synapses are formed by intercellular channels known as gap junctions, which directly connect the cytoplasm of adjacent cells and permit the diffusion of ions and small molecules. In contrast, chemical synapses consist of a presynaptic terminal—typically the axon terminal of a neuron—aligned with the membrane of a postsynaptic cell and separated by an extracellular space of 15–20 nm, termed the synaptic cleft [1, 2].

Neurotransmitters are chemical messengers released from presynaptic terminals that elicit postsynaptic responses. In chemical synapses, neurotransmitter exocytosis is triggered by an action potential–evoked influx of calcium ions through Ca_V channels. The released neurotransmitter binds to postsynaptic receptors, thereby initiating receptor-specific signal transduction. This mode of neurotransmission permits millisecond-scale information transfer between neurons in the central nervous system (CNS) and neurons or effector cells in the peripheral nervous system (PNS) [3].

A glutamatergic synapse is a chemical synapse where glutamate serves as the principal neurotransmitter. In the mammalian CNS, glutamate release represents the primary mode of excitatory neurotransmission [4]. Glutamate receptors (GluRs) are classified as ionotropic or metabotropic based on how they transduce glutamate binding events into postsynaptic signaling. Ionotropic glutamate receptors (iGluRs) are tetrameric, glutamate-gated ion channels that mediate rapid, localized postsynaptic depolarizations via cation influx [5]. iGluRs are further subclassified on the basis of pharmacological agonist selectivity into AMPA (α-amino-3-hydroxy-5-methyl-4-isoxazolepropionic acid), kainate (KA), and NMDA (N-methyl-D-aspartate) receptors [4–6]. If they are sufficient to reach threshold, iGluR-mediated depolarizations initiate an action potential. In contrast, metabotropic

glutamate receptors (mGluRs) are constitutively dimeric membrane proteins expressed at pre-, post-, and extrasynaptic sites, where glutamate binding activates G protein-coupled signaling pathways. mGluRs are grouped into three classes (I–III) according to sequence homology, ligand affinity, and G protein-coupling specificity [21]. These receptors modulate diverse aspects of neurotransmission, including neurotransmitter release, neuronal excitability, intracellular signaling, synaptic integration, and synaptic plasticity [4–6, 21].

Efficient clearance of glutamate from the synaptic cleft is essential to prevent excessive postsynaptic stimulation. Prolonged glutamate exposure can trigger excitotoxicity—a pathological process that leads to cell damage and death [7]. Excitatory amino acid transporters (EAATs) translocate glutamate into cells via secondary active transport, thereby terminating the synaptic signal. Specifically, they couple the uphill import of glutamate to Na^+ influx and K^+ efflux. The EAAT family comprises five isoforms (EAAT1–5) with high substrate affinity, expressed in glial and neuronal cells, each exhibiting a distinct distribution pattern [7]. In addition to their role as glutamate carriers, EAATs function as anion channels, thereby contributing to cellular chloride homeostasis [8].

Neurons cannot synthesize glutamate from glucose because they lack pyruvate carboxylase, an enzyme that replenishes tricarboxylic acid (TCA) cycle intermediates [9]. Instead, neurons rely on astrocytes to maintain their glutamate pool. Astrocytes take up glutamate through the EAATs located in perisynaptic processes. In astrocytes, glutamate enters multiple metabolic pathways, most notably its ATP-dependent amidation to glutamine, catalyzed by glutamine synthetase [10]. A system of Na^+-coupled neutral amino acid transporters (SNATs) mediates glutamine export from astrocytes and import into neurons [9]. In neuronal mitochondria, phosphate-activated glutaminase catalyzes the deamination of glutamine, producing glutamate and ammonia. This glutamate–glutamine cycle supports synaptic loading by replenishing presynaptic glutamate stores [9, 10].

GluRs transduce the synaptic glutamate signal, EAATs shape and terminate it, and the glutamate–glutamine cycle replenishes the neurotransmitter pool. Nonetheless, glutamatergic neurotransmission ultimately depends on efficient loading of glutamate into synaptic vesicles and its subsequent release from presynaptic terminals. While vesicle fusion is triggered by calcium influx through Ca_V channels, loading of glutamate into vesicles is mediated by VGLUTs. These transporters couple channel-like anion conductance

with carrier-mediated substrate transport, providing a valuable model for studying electrogenic membrane processes. Notably, VGLUT dysfunction has been implicated in multiple pathophysiological conditions, highlighting their potential as therapeutic targets. VGLUTs thus constitute a compelling system for elucidating how dual channel and carrier mechanisms support the selective loading of neurotransmitters into synaptic vesicles.

1.2. Structure and function of vesicular glutamate transporters

VGLUTs are vesicular transporters that belong to the SLC17 family of solute carrier proteins. Three mammalian isoforms have been identified: VGLUT1 (*SLC17A7*), VGLUT2 (*SLC17A6*), and VGLUT3 (*SLC17A8*). They share about 75% sequence identity and exhibit isoform-specific expression patterns [11, 12]. VGLUT1 and VGLUT2 were initially classified as Na^+-dependent inorganic phosphate cotransporters based on sequence similarity and transport activity in heterologous systems [28, 29]. Subsequent studies redefined them as glutamate transporters driven by the proton electrochemical gradient ($\Delta\tilde{\mu}_{H^+}$) established across the vesicular membrane [30, 32]. This conceptual shift led to the identification of a third isoform, VGLUT3, with similar transport properties but a distinct expression profile relative to VGLUT1 and VGLUT2 [33, 40]. VGLUTs consist of 560–582 amino acids arranged into 12 transmembrane helices (TM1–TM12), with both termini oriented toward the cytoplasm [11]. A cryo–EM structure of rat VGLUT2, resolved at neutral pH in the apo (glutamate-free), outward-facing (lumen-facing) conformation, revealed an architecture in which the transmembrane helices surround an electropositive, water-filled central cavity (Figure 1.1). This structural arrangement, characteristic of a Major Facilitator Superfamily (MFS) fold, is consistent with glutamate transport via an alternating-access mechanism [12].

VGLUT1 is the most abundant isoform in the CNS, with predominant expression in the cortex, hippocampus, cerebellum, and basolateral amygdala [11, 24, 26, 40]. In contrast, VGLUT2 is primarily expressed in subcortical regions including the thalamus, midbrain, brainstem, and amygdala [11, 24, 26, 40]. VGLUT1 and VGLUT2 are largely segregated but can be co-expressed in specific populations, such as pinealocytes, and are also present in spinal cord neurons and afferent terminals [11, 24]. Outside the CNS, VGLUT2 is expressed in the stomach, intestine, and testis, and both VGLUT1 and VGLUT2 occur in the pancreas [46]. Although VGLUT1 and VGLUT2 are mainly confined to classical glutamatergic synapses, all three isoforms are also present in noncanonical neurotransmitter systems [24].

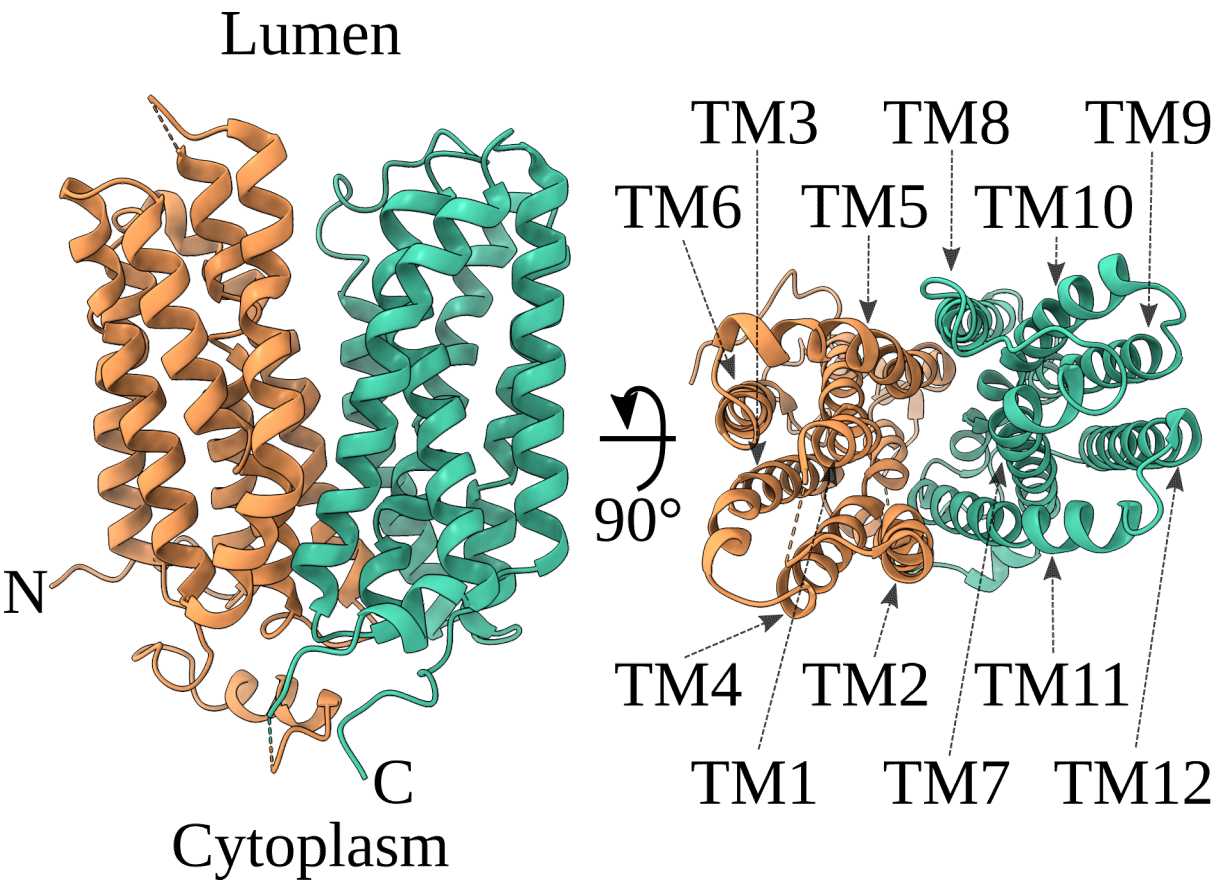

Figure 1.1. Molecular architecture of VGLUT2 revealed by cryo–EM. The cryo–EM structure of rat VGLUT2 in the apo (substrate-free), outward-facing (lumen-facing) conformation reveals twelve transmembrane helices (TM1–TM12) surrounding a central cavity (PDB ID 8SBE) [12]. The left panel shows a side (membrane-parallel) view, and the right panel shows the corresponding luminal (membrane-perpendicular) view.

VGLUT3, the least abundant isoform, is concentrated in cholinergic, γ-aminobutyric acid (GABA)ergic interneurons, and serotonergic neuronal populations [11, 24, 26, 27, 40]. This noncanonical VGLUT expression enables the co-packaging and co-release of glutamate with other neurotransmitters. This process is thought to enhance neurotransmitter release and postsynaptic responsiveness via vesicular synergy [24]. VGLUT3 is also detected in subsets of glutamatergic neurons in the brain and in cochlear inner hair cells (IHC) [24, 27]. Additional expression sites also include limbic circuits, striatal regions, and retinal amacrine cells [24, 26]. These diverse expression patterns highlight the roles of VGLUTs as essential modulators of neurotransmission throughout the nervous system.

The biological importance of VGLUTs is underscored by their involvement in movement, psychiatric, metabolic, and sensory disorders. Region-specific alterations in VGLUT1 and VGLUT2 expression levels have been reported in postmortem human brain

tissue. In Parkinson's disease, both isoforms are increased in the striatum, whereas cortical VGLUT1 is reduced [36]. In Alzheimer's disease, VGLUT2 is decreased in specific cortical regions, whereas VGLUT1 is modestly reduced in the hippocampus [39]. Aberrant VGLUT1 expression is also observed in patients with temporal lobe epilepsy and schizophrenia, paralleling findings in mouse models of schizophrenia [37, 38, 41].

Homozygous VGLUT1 knockout (KO) mice fail to thrive and die within the third postnatal week [52]. Their neurons exhibit markedly reduced spontaneous release and significantly smaller amplitudes of miniature and evoked excitatory postsynaptic currents (mEPSCs and EPSCs). In heterozygous animals, VGLUT1 insufficiency is linked to anxiety-like and depression-like behaviors as well as long-term memory impairments [43]. In pancreatic β-cells of mice, inhibition of VGLUT1 prevents incretin-induced insulin secretion and reduces insulin granule exocytosis [47]. Homozygous VGLUT2-deficient mice die neonatally from respiratory failure associated with disrupted glutamatergic transmission in brainstem respiratory circuits [25, 35]. Both homozygous and heterozygous VGLUT2 mutants show graded reductions in postsynaptic response amplitude; heterozygotes otherwise appear behaviorally normal but display altered neuropathic pain processing and impaired responses to aversive stimuli [25]. Conditional KO of VGLUT2 in sensory neurons impairs perception of acute pain and heat hyperalgesia while sparing mechanical hypersensitivity induced by peripheral injury [42]. Selective deletion of VGLUT2 in midbrain dopaminergic neurons blunts psychostimulant-evoked locomotor responses, while ablation in hypothalamic appetite-regulating neurons disrupts energy balance, causing obesity even under a standard diet [44, 45].

In contrast, VGLUT3 dysfunction yields distinct phenotypes. The p.A224V mutation in *SLC17A8*, which encodes VGLUT3, causes autosomal dominant nonsyndromic hearing loss type 25 (DFNA25) [51]. Knock-in mice carrying the equivalent deafness-causing mutation develop progressive hearing loss, with a 70% decrease in VGLUT3 expression at CNS terminals and fewer transporter-positive vesicles [55]. VGLUT3 KO mice are profoundly deaf, show early degeneration of cochlear ganglion neurons, and develop primary generalized epilepsy while maintaining normal locomotor behavior [50]. Homozygous deletion of VGLUT3 in striatal cholinergic interneurons reduces acetylcholine release owing to impaired vesicular synergy with the vesicular acetylcholine transporter (VAChT) [53]. This produces a hypocholinergic phenotype with enhanced cocaine-induced locomotor activity

and reduced sensitivity to drug-induced motor rigidity. Loss of VGLUT3 impairs glutamate and serotonin co-release from serotonergic neurons, an effect associated with heightened anxiety-like behaviors [49]. Rare variants of *SLC17A8* are enriched in individuals with substance abuse, and mouse studies show that deletion of VGLUT3 in nucleus accumbens cholinergic interneurons increases dopamine release and cocaine self-administration, highlighting VGLUT3 as a key regulator of reward circuitry and addiction susceptibility [54].

VGLUTs mediate uptake of cytosolic glutamate into synaptic vesicles by harnessing the $\Delta\tilde{\mu}_{H^+}$ established by the V-ATPase across the vesicle membrane. This electrochemical potential is defined as the molar free energy change per proton and expressed as [11, 12]:

$$\Delta\tilde{\mu}_{H^+} = -RT\ln(10)\,\Delta\mathrm{pH} + F\,\Delta\Psi \qquad (\mathrm{J\,mol^{-1}})$$

Here, $\Delta\mathrm{pH} = \mathrm{pH}_{\mathrm{cytosol}} - \mathrm{pH}_{\mathrm{lumen}}$ quantifies the chemical component of the proton gradient, where $\mathrm{pH} = -\log_{10}[H^+]$. $\Delta\Psi = \Psi_{\mathrm{cytosol}} - \Psi_{\mathrm{lumen}}$ denotes the electrical potential difference across the vesicle membrane (V). R is the universal gas constant (8.314 J/(mol K)), T is the absolute temperature (typically 310 K under physiological conditions), and F is the Faraday constant (96 485 C/mol). This proton-motive force (PMF) provides a thermodynamic framework for studying the structure–function relationships that govern VGLUT substrate transport and channel function.

Glutamate loading into synaptic vesicles and proteoliposomes containing VGLUT is mainly driven by $\Delta\Psi$ [13, 14, 17, 18, 64]. Uptake increases at cytosolic chloride concentrations below 10 mM, whereas higher concentrations inhibit transport by dissipating $\Delta\Psi$, interfering with glutamate binding, or both [13–18, 64]. Moreover, luminal chloride enhances vesicular glutamate filling while limiting further activation by cytosolic chloride. These effects suggest that there are chloride-binding sites accessible from both sides of the membrane during the VGLUT transport cycle [17]. VGLUTs also exhibit a K^+/H^+ exchange mode, which would alkalinize the vesicle lumen, depleting $\Delta\mathrm{pH}$ while maintaining $\Delta\Psi$, thus promoting glutamate uptake [17]. Transport assays demonstrated a VGLUT-mediated chloride translocation loosely coupled to glutamate transport [17, 18]. This may reflect a mechanism whereby electrogenic chloride efflux from newly endocytosed, chloride-loaded

vesicles sustains vesicle depolarization and supports ΔΨ-driven glutamate accumulation [18].

VGLUT-mediated chloride currents were recorded in oocytes expressing internalization-deficient VGLUTs [19]. All three mammalian isoforms exhibit an inwardly rectifying chloride conductance activated by extracellular (luminal-side) chloride and protons. Notably, this chloride conductance is uncoupled from glutamate transport and partially inhibited by cytosolic glutamate. Luminal chloride and protons also enhance glutamate transport. Together, these modulatory mechanisms support glutamate accumulation in synaptic vesicles while preventing efflux through VGLUTs transiently localized at the plasma membrane during vesicle recycling.

The function of VGLUT1 was further investigated in synaptic vesicles from cultured hippocampal neurons using fluorescence imaging together with pharmacological and ionic manipulations [20]. Analysis of V-ATPase–dependent re-acidification kinetics revealed that VGLUT1 mediates a stoichiometric exchange of cytosolic glutamate for luminal protons. In addition, VGLUT1-mediated luminal chloride efflux—thermodynamically uncoupled from glutamate transport—contributes to the generation of ΔΨ, which drives glutamate uptake before V-ATPase–dependent acidification. Together, VGLUT-mediated chloride efflux and glutamate uptake ensure electroneutral and isosmotic filling of synaptic vesicles.

Whole-endosome recordings from mammalian cells expressing different VGLUT isoforms revealed that both luminal and cytosolic chloride activate glutamate and chloride currents, whereas luminal glutamate lacks allosteric effects on either current [22]. Analysis of these currents suggests that VGLUTs mediate glutamate and chloride fluxes via distinct processes: chloride permeates through a channel-like pathway, whereas glutamate is translocated by a carrier-like mechanism. These findings support a model in which chloride efflux sustains the ΔΨ that drives glutamate accumulation in synaptic vesicles [18, 20].

Heterologous expression of plasma-membrane–targeted VGLUT1, combined with whole-cell patch-clamp recordings and quantitative modeling of vesicle filling dynamics, provided further mechanistic insights into VGLUT function [23]. Notably, this approach revealed the thermodynamic basis of glutamate selectivity over aspartate in the vesicle lumen and the biophysical properties of the VGLUT1 ion channel. Dynamic changes in the ionic composition of the luminal-side solution, together with noise analysis of macroscopic

currents, revealed that VGLUT1 functions as an inwardly rectifying anion channel with short open times and an estimated unitary chloride transport rate of $1.5 \times 10^5\,s^{-1}$ at -160 mV. Analysis of reversal potential shifts across ΔpH gradients showed that VGLUT1 exchanges glutamate for protons at a 1:1 stoichiometry [20]. In contrast, aspartate transport by VGLUT1 is only partially coupled to proton exchange. The glutamate/proton exchange has a unitary turnover rate of approximately $600\,s^{-1}$ at -160 mV. Kinetic modeling based on these data predicts a preferential glutamate accumulation in the vesicle lumen over aspartate, driven by the higher rate of the coupled glutamate/proton exchange relative to aspartate uniport. Furthermore, limiting VGLUT1-mediated chloride conductance reduces $\Delta\Psi$, thereby diminishing neurotransmitter accumulation. These results show that the dual functions of VGLUT1—glutamate/proton exchange and chloride conductance—support selective and energetically favorable accumulation of glutamate in the vesicle lumen [18, 20, 22].

Structure–function relationships in VGLUTs have been explored through both computational modeling and experimental mutagenesis. Structural analysis of VGLUT2 indicates that R88 (TM1) and R322 (TM7) within the binding pocket each coordinate one of the carboxyl groups of glutamate [12]. Alanine substitution of R88 or R322 substantially alters mEPSC properties in KO-rescue mice [12]. Neutralization of R134 in VGLUT1, R322 in VGLUT2, or R326 in VGLUT3 abolishes both chloride and glutamate currents [19, 22]. In contrast, R80A in VGLUT1, R88A in VGLUT2, and R93A in VGLUT3 suppress anion influx but spare efflux in whole-endosome recordings [22]. Mutation of a third conserved arginine in TM4—R176A in VGLUT1, R184A in VGLUT2, and R189A in VGLUT3—preserves chloride and glutamate currents in the absence of luminal chloride [22]. Neither R322A nor R88A affects glutamate transport in functional assays, whereas R184A, H128A (TM2), and E191A (TM4) in VGLUT2 markedly reduce uptake [34]. The equivalent mutation H120A in VGLUT1 partially uncouples glutamate/proton exchange and alters channel gating [23]. Computational analyses identify H128, E191, and R184 as key residues mediating the allosteric activation of VGLUT2 by chloride or protons [12, 56]. Solvent-accessible surface analysis of VGLUT2 suggests a cytosolic gate for chloride conduction that is formed by opposing histidines, H199 (TM4) and H434 (TM10) [12]. The functionally relevant amino acids are mapped in Figure 3.1. These studies highlight residues that integrate allosteric sensing of chloride and protons with substrate transport and channel activity. Nevertheless,

the molecular mechanisms underlying these dual functions of VGLUTs remain unresolved.

1.3. Experimental approach and scope

Building on the mechanistic insights outlined above, this investigation characterizes VGLUT function through site-directed mutagenesis and electrophysiological recordings. Structure-guided mutations of key residues were introduced into a rat VGLUT1 construct engineered for expression at the plasma membrane of mammalian cells. Whole-cell recordings under well-defined ionic conditions were used to analyze mutational effects on pore properties, voltage-dependent gating, and the pH dependence of the VGLUT channels. Subsequently, the substrate transport and ion channel properties of the *Drosophila* ortholog DVGLUT were analyzed for comparison with its mammalian counterparts. This comparative study revealed a conserved glutamate transport activity but divergent mechanisms of luminal chloride modulation, channel gating, and anion conduction. Finally, functional assessment of a mouse VGLUT3 variant corresponding to a human deafness mutation revealed distinct alterations in voltage- and pH-dependent gating of the associated anion channel function. Collectively, these experiments establish a framework for analyzing how VGLUTs integrate glutamate transport with chloride conductance.

Chapter 2:
Materials and Methods

Plasma membrane–targeted VGLUTs were introduced into mammalian cell lines via transient transfection or stable, inducible systems. Functional properties were assessed by electrophysiological recordings. All experiments were conducted under ambient conditions. Data analysis was performed using custom Python 3 scripts.

2.1. Design and cloning of expression constructs

Recombinant cDNAs encoding internalization-deficient forms of rat VGLUT1 (*Slc17a7*), mouse VGLUT3 (*Slc17a8*), and *Drosophila* DVGLUT (*VGlut*) were subcloned into pcDNA3.1 or pcDNA5/FRT/TO vectors and introduced into mammalian cells. Surface enrichment was achieved by replacing known endosomal retention motifs. A fluorescent protein was fused to the C-terminus of each construct to enable microscopic detection. Throughout this study, "wild-type (WT)" denotes plasma membrane–targeted constructs bearing a C-terminal fluorescent tag and an otherwise unmodified transporter sequence:

Rat VGLUT1 (rVGLUT1): Alanine substitutions were introduced at E6, E7, L11, E505, E506, F510, and V511 [23], and constructs were C-terminally tagged with enhanced green fluorescent protein (EGFP).

***Drosophila* DVGLUT:** Alanine substitutions were introduced at Y38, E39, E40, M41, E42, G43, and G44, and constructs were C-terminally tagged with EGFP.

Mouse VGLUT3 (mVGLUT3): The substitutions I13G, L14G, I31A, L33A, I535G, and I536G were introduced, and constructs were C-terminally tagged with monomeric yellow fluorescent protein (mVenus).

Site-directed mutagenesis of WT templates was performed using overlap extension PCR [59]. For all constructs, at least two clones were generated and functionally evaluated.

2.2. Transient and inducible expression in mammalian cells

HEK293T cells were maintained in DH10 medium, an in-house formulation of DMEM with GlutaMAX®-I and 4.5 g/L D-glucose (Gibco, Thermo Fisher Scientific, USA),

supplemented with 10% fetal bovine serum (FBS) and 1× penicillin–streptomycin. Cultures were incubated at 37 °C in a humidified 5% CO_2 atmosphere.

Mammalian cells were transiently transfected with pcDNA3.1 constructs using Lipofectamine® 2000 (1 mg/mL; Invitrogen, Thermo Fisher Scientific, USA). Plasmid DNA and Lipofectamine were mixed at a 3:1 ratio (μg:μL) in Opti-MEM™ Reduced Serum Medium (1×; Gibco, Thermo Fisher Scientific, USA), incubated at room temperature for at least 35 min, and then added to cultured cells. After at least 6 h of exposure to the transfection mixture, cells were either maintained in fresh DH10 medium for later replating or replated directly into culture dishes for subsequent experimental use. Electrophysiological recordings were performed approximately 16 h after replating.

The Flp-In™ T-REx™ system was used to generate stable, inducible cell lines expressing recombinant VGLUTs. A HEK293-derived Flp-In™ T-REx™ host cell line, preselected for zeocin resistance, was co-transfected with the pcDNA5/FRT/TO expression vector harboring the recombinant VGLUT construct and the pOG44 plasmid encoding Flp recombinase. Host cells were cultured in DH10 medium supplemented with 1 μL/mL zeocin and 2 μL/mL blasticidin. Lipofectamine-mediated co-transfection was performed in antibiotic-free medium for 16 h. Recombination at the genomic FRT site inserted the VGLUT expression cassette, inactivated the *lacZ*–zeocin resistance fusion gene, and integrated a hygromycin resistance marker. Forty-eight hours after transfection, the medium was replaced with DH10 medium supplemented with blasticidin and hygromycin (each at 2 μL/mL). Monoclonal colonies were selected based on hygromycin resistance. Expression of the stably integrated VGLUT genes was induced by adding at least 1 μL/mL tetracycline to the culture medium. Experiments were performed about 16 h after replating.

HEK293T cells endogenously express TMEM206 (PACC1), which encodes the proton-activated chloride channel (PAC) localized to the plasma membrane. This channel is activated by acidic pH and positive membrane potentials [105, 106]. This endogenous conductance confounds isolation of VGLUT-mediated currents at positive voltage steps and at luminal-side pH values below 5.5. To resolve this, the PAC current component was eliminated by CRISPR-Cas9–mediated ablation [107]. HEK293T cells were transiently transfected with Cas9n plasmids, selected by puromycin resistance, and sorted as GFP-positive single cells to establish monoclonal clones. PAC KO was confirmed by

sequencing of the targeted exons and further validated by electrophysiological recordings.

2.3. Principles and implementation of whole-cell patch-clamp electrophysiology

Whole-cell patch-clamp recordings were used to measure plasma membrane currents in mammalian cells. In the whole-cell configuration, an electronic feedback system implements the voltage-clamp principle by continuously monitoring the membrane potential and injecting current to maintain the membrane potential at the command voltage, thereby enabling precise measurement of transmembrane current [65]. Figure 2.1 shows a minimal equivalent circuit representation of the whole-cell configuration [66]. Ideally, the injected current (I_{inj}) is equal in magnitude and opposite in sign to the transmembrane current (I_m) [65, 66]. The recorded voltage (V_{rec}) is generated across the feedback resistor (R_f), which sets the measurement gain and sensitivity to current fluctuations [67]. The corresponding output signal is given by:

$$V_{\text{rec}} = -I_m R_f$$

The membrane potential (V_m) is given by the command voltage (V_{cmd}) minus the voltage drop across the series resistance and any additional voltage offsets [66]. The series resistance is defined as $R_s = R_p + R_a$, where R_p is the pipette resistance and R_a is the access resistance. Voltage offsets (V_{off}) may arise from artifacts such as liquid junction potentials or electrode-related effects. This relationship is expressed as:

$$V_m = V_{\text{cmd}} - R_s I_m - V_{\text{off}}$$

Low-resistance pipettes reduce R_s, enhancing voltage control and signal resolution; chlorided silver wire (Ag/AgCl) electrodes minimize offset potentials. A high-resistance seal and low endogenous conductance reduce leak current (I_{leak}), thereby increasing the membrane leak resistance (R_{leak}) and improving recording fidelity.

2.3.1. Instrumentation and recording setup

Patch-clamp recordings were conducted on an anti-vibration table enclosed within a Faraday cage (TMC, USA). Transmembrane currents were recorded using an EPC

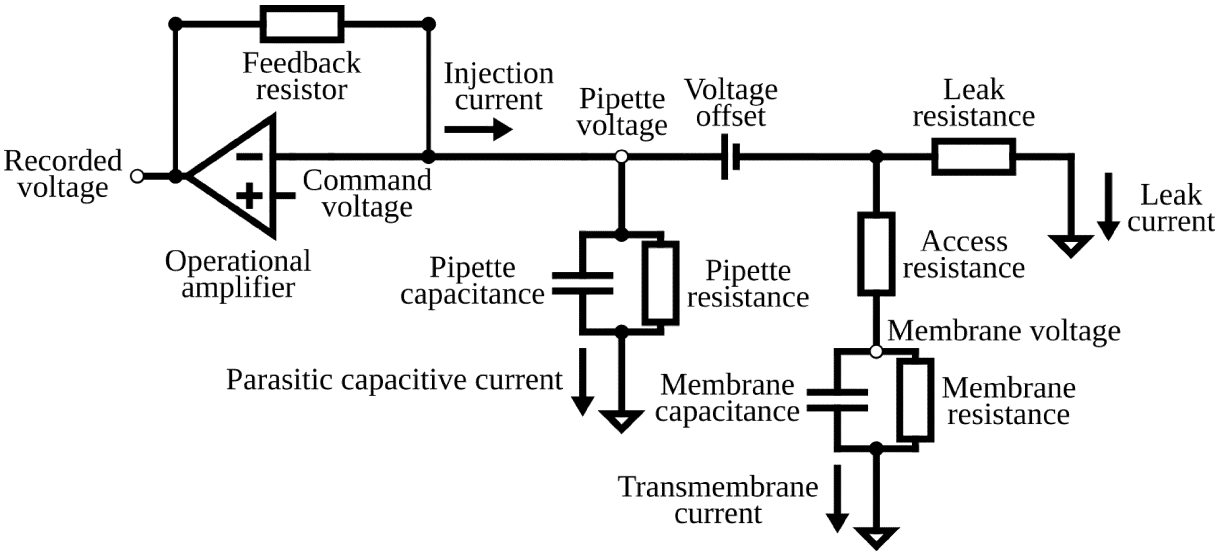

Figure 2.1. Whole-cell patch-clamp principle and equivalent circuit: feedback control of membrane potential and measurement of transmembrane current. The diagram illustrates a simplified equivalent circuit representation of the whole-cell patch-clamp configuration [66]. Whole-cell mode is achieved by forming a gigaohm seal and rupturing the membrane patch under the pipette tip, thereby establishing electrical continuity between the cytoplasm and the amplifier circuit [65]. The operational amplifier compares the membrane voltage (V_m) to the command voltage (V_{cmd}) and injects current (I_{inj}) through the pipette electrode to null the voltage difference. The recorded voltage (V_{rec}) is generated at the amplifier output as the transmembrane current (I_m) flows through the feedback resistor (R_f), which defines the current-to-voltage gain and scales the output signal. Voltage offsets (V_{off}) may arise from electrode junction potentials, ionic gradients, or amplifier electronics. Pipette resistance (R_p) and access resistance (R_a) together form the series resistance (R_s). Pipette capacitance (C_p), membrane capacitance (C_m), and R_s are electronically compensated to minimize voltage drops across the access pathway and reduce capacitive transients. High-resistance seals and low endogenous membrane conductance maximize the total leak resistance (R_{leak}) and minimize leak current (I_{leak}).

10 USB amplifier controlled by PatchMaster software (HEKA Elektronik, Germany). Cultured cells were visualized using an inverted phase-contrast Axiovert 135 microscope (Zeiss, Germany), equipped with a fluorescence lamp and a blue-excitation/green-emission filter set. The headstage and recording electrode were positioned using an SM-6 micromanipulator (Luigs & Neumann, Germany). Manual perfusion control was achieved using a custom-built, gravity-driven system that delivered solutions through fused-silica capillary tips (inner diameter 100 µm; Chromatographie Service GmbH, Germany).

Borosilicate glass capillaries with an outer diameter of 1.2 mm and an internal filament (Harvard Apparatus, USA) were pulled into recording pipettes using a P-1000 Flaming/Brown Micropipette Puller (Sutter Instrument, USA) and then polished with an

MF-830 Microforge (Narishige, Japan). The resulting pipettes were filled with intracellular solution and mounted in a pipette holder. Under all experimental conditions, open pipette resistance remained below 3 MΩ. For experiments analyzing macroscopic current fluctuations, pipette tips were coated with Moyco Dental Wax (Moyco Technologies, USA) prior to heat polishing to reduce pipette capacitance and minimize electrical noise.

Both bath and pipette silver wire electrodes were chloridized overnight prior to each experiment. Potassium chloride–agar salt bridges (0.5 mM KCl, 2% agar) were applied to the electrodes when luminal-side chloride concentration was altered or when either the bath or pipette solution was chloride-free. Liquid junction potentials were estimated using the pClamp junction potential calculator (Molecular Devices, USA) and numerically corrected before applying voltage protocols. The pH of all solutions was adjusted at room temperature using an inoLab pH 7110 meter (Xylem Analytics, Germany). Osmolality was measured using an Osmomat 3000 Basic freezing-point osmometer (Gonotec, Germany).

Pipette capacitance and plasma membrane capacitance were electronically neutralized prior to each recording. Series resistance was maintained below 5 MΩ, and compensation was subsequently applied to at least 70%. Electrical signals were digitized at 50 kHz or 100 kHz and low-pass filtered during acquisition using cascaded 2.4 kHz and 10.5 kHz Butterworth filters implemented in the PatchMaster software interface.

2.3.2. Recording solutions and buffer systems

When required, glucose was added to the extracellular solution to establish an outward osmotic gradient and maintain mild hypertonicity during recordings. Sodium salts were omitted to decrease background conductances in mammalian cells, while permeant anions were supplied in bulk with choline as the countercation.

For experiments in which cells were dialyzed with chloride- or nitrate-based intracellular solutions and perfused with extracellular solutions of different pH values, the pipette solution contained either 115 mM choline chloride with 5 mM $MgCl_2$ or an equivalent 125 mM mixture of HNO_3 and choline hydroxide with 5 mM $Mg(OH)_2$. Intracellular calcium was chelated using 10 mM EGTA, and the intracellular pH was buffered with 10 mM HEPES and adjusted to pH 7.4 with choline hydroxide

or trimethylammonium hydroxide. Extracellular solutions contained (in mM): 136 choline chloride, 2 $MgCl_2$, 2 $CaCl_2$, and either 10 MES, 10 HEPES, or 10 CHES, and were adjusted with choline hydroxide to pH values of 5.0–9.5.

For experiments in which cells were dialyzed with glutamate-based intracellular solutions, the pipette solution contained (in mM): 140 glutamic acid neutralized with choline hydroxide, 10 EGTA, 5 $Mg(OH)_2$, and either 30 MES, 30 HEPES, or 30 AMPSO, and the pH was further adjusted to 6.0–8.5 using choline hydroxide. Bath and other extracellular solutions contained 1 $MgCl_2$, 1 $CaCl_2$, variable amounts of choline chloride, and a mixture of glutamic acid and choline hydroxide, adjusted to a combined concentration of 140 mM. These solutions were buffered with 30 HEPES or 50 MES, and the pH was adjusted to 7.5, 5.5, or 5.0 using choline hydroxide. Total chloride concentrations depended on the relative proportions of choline chloride and the glutamic acid/choline hydroxide mixture.

2.4. Quantitative modeling and statistical testing

2.4.1. Nonlinear model fitting with `curve_fit`

Empirical data were fitted using `curve_fit`, a function from the `optimize` submodule of the `SciPy` library. Curve fitting estimates the model parameters that best describe the relationship between measured variables. Let x denote the independent variable and y denote the dependent variable. `curve_fit` applies a nonlinear least squares optimization algorithm to fit a model f to the data. The model is defined as:

$$y = f(x; \theta) + \varepsilon$$

where θ is the vector of estimated parameters, and ε is the residual term representing the difference between observed values and model predictions. The algorithm iteratively updates the parameter estimates to minimize the sum of squared residuals, $S(\theta)$, given by:

$$S(\theta) = \sum_{i=1}^{n} [y_i - f(x_i; \theta)]^2$$

The resulting vector, $\hat{\theta}$, represents the best-fit parameter values inferred from the data.

2.4.2. Nonparametric bootstrap resampling

Nonparametric bootstrap resampling was used to estimate the sampling distribution of fit parameters. Given a dataset of n paired measurements $\{(x_i, y_i)\}_{i=1}^{n}$, B bootstrap samples were generated by resampling, with replacement, n pairs from the original dataset. Each resampled dataset is denoted $\mathcal{D}_b^* = \{(x_i^*, y_i^*)\}_{i=1}^{n}$, where $b = 1, \ldots, B$. Resampling assumes that the observed data serve as an empirical representation of the underlying population distribution [68]. The model $f(x;\theta)$ was fitted to each $\mathcal{D}_b^*$, yielding parameter vectors $\{\theta_b^*\}_{b=1}^{B}$, which define an empirical distribution $F_{\hat{\theta}}^*$. The bootstrap method approximates the unknown sampling distribution $F_{\hat{\theta}}$ by the empirical distribution: $F_{\hat{\theta}}^* \approx F_{\hat{\theta}}$ [68].

Statistical summaries derived from this distribution include:

the bootstrap mean: $\bar{\theta}^* = \frac{1}{B}\sum_{b=1}^{B}\theta_b^*$;

the bootstrap standard error: $\mathrm{SE}(\hat{\theta}) = \sqrt{\frac{1}{B-1}\sum_{b=1}^{B}\left(\theta_b^* - \bar{\theta}^*\right)^2}$;

percentile-based confidence intervals: $\mathrm{CI}_{1-\alpha} = \left(Q_{\alpha/2}^*,\ Q_{1-\alpha/2}^*\right)$, where $1-\alpha$ is the confidence level, and Q_p^* denotes the p-th quantile of the empirical distribution $F_{\hat{\theta}}^*$.

This approach provides statistical characterization of parameter uncertainty and enables direct comparison of estimates across models and datasets, without relying on parametric assumptions [68, 69]. To assess statistical differences, a two-tailed p-value was computed from the bootstrap distribution of parameter differences. The p-value was defined as twice the smaller proportion of bootstrap values below or above zero, representing the probability of observing such a difference under the null hypothesis:

$$p = 2\min\left(\mathbb{P}(\Delta^* \leq 0),\ \mathbb{P}(\Delta^* \geq 0)\right)$$

where Δ^* denotes the bootstrapped differences in parameter estimates.

2.4.3. Nested model comparison using partial F-tests

The extra sum-of-squares F-test was used to assess whether a regression model with p coefficients yielded a statistically significant reduction in $S(\theta)$ compared with a nested

model having fewer predictors. The F-statistic was computed as[114] :

$$F = \frac{(S_{\text{restricted}} - S_{\text{full}})/d}{S_{\text{full}}/(n-p-1)}$$

where $S_{\text{restricted}}$ and S_{full} represent the residual sums of squares for the restricted and full models, respectively; n indicates the number of observations; p denotes the number of predictors in the full model; and d corresponds to the difference in the number of estimated parameters between the two models. The associated p-value was obtained from the F-distribution with d and $n-p-1$ degrees of freedom, quantifying the probability of observing such an improvement in model fit under the null hypothesis that all additional regression coefficients of the full model are equal to zero.

2.4.4. Relaxation kinetics of macroscopic currents

The relaxation of a transmembrane macroscopic current following a perturbation reflects the kinetics of ion channel gating [57]. Consider a population of channels embedded in a membrane that transition reversibly between a non-conducting closed state and a conducting open state. The relationships between the rate constants governing these transitions are derived from the law of mass action [57, 60].

Let N be the total number of channels, and $N_c(t)$ and $N_o(t)$ denote the number of closed and open channels, respectively, at time t. Then:

$$N = N_c(t) + N_o(t)$$

The following kinetic scheme represents the average behavior of channels with homogeneous gating properties:

$$N_c \underset{\beta}{\overset{\alpha}{\rightleftharpoons}} N_o$$

Here, α and β are the rate constants for the closed-to-open and open-to-closed transitions, respectively. The time derivative of N_o is expressed as:

$$\frac{dN_o}{dt} = \alpha(N - N_o) - \beta N_o$$

Solving this differential equation with the initial condition $N_o(0) = N_{o,\text{i}}$ yields the time

evolution of the open-channel population:

$$N_o(t) = N_{o,\mathrm{ss}} + \left(N_{o,\mathrm{i}} - N_{o,\mathrm{ss}}\right) e^{-t/\tau}$$

where $N_{o,\mathrm{ss}} = \frac{\alpha N}{\alpha+\beta}$ is the steady-state number of open channels and $\tau = \frac{1}{\alpha+\beta}$ is the relaxation time constant.

Because the macroscopic current $I(t)$ is proportional to the number of open channels, the current relaxation can be modeled as:

$$I(t) = I_{\mathrm{ss}} + (I_{\mathrm{i}} - I_{\mathrm{ss}})\, e^{-t/\tau}$$

where I_{ss} is the steady-state current and I_{i} is the initial current. Assuming all channels are initially closed $\left(N_{o,\mathrm{i}} = 0 \Rightarrow I_{\mathrm{i}} = 0\right)$, the solution simplifies to:

$$I(t) = I_{\mathrm{ss}} \left(1 - e^{-t/\tau}\right)$$

This expression describes the monoexponential rise of a population of channels that transition from the closed to the open state.

Conversely, if all channels are initially open $\left(N_{o,\mathrm{i}} = N\right)$ and a perturbation shifts the system toward closure such that $|I_{\mathrm{i}}| > |I_{\mathrm{ss}}|$, the macroscopic current decays to the new steady-state level as:

$$I(t) = I_{\mathrm{ss}} + (I_{\mathrm{i}} - I_{\mathrm{ss}})\, e^{-t/\tau}$$

When all channels close at steady state ($I_{\mathrm{ss}} = 0$), the expression reduces to:

$$I(t) = I_{\mathrm{i}}\, e^{-t/\tau}$$

This form characterizes the exponential decay of current during the transition of the channel population from the open to the closed state.

This framework provides a quantitative basis for analyzing gating kinetics within the two-state model approximation, thereby enabling extraction of rate constants from experimental current traces under voltage-clamp conditions. If the channel population occupies more than two discrete states and the transitions occur at constant rates that

are slow enough to be temporally resolved, the average channel kinetics can be modeled as a sum of exponentials. In macroscopic current analysis, the number of exponential components provides a lower bound on the number of kinetically distinguishable states, though it does not specify whether multiple open or closed states are present [70].

For example, the activation of a current with two kinetically distinct components can be described by a biexponential function that approaches steady state:

$$I(t) = I_{\text{ss}} \left(1 - A_{\text{fast}} e^{-t/\tau_{\text{fast}}} - A_{\text{slow}} e^{-t/\tau_{\text{slow}}}\right)$$

Here, τ_{fast} and τ_{slow} are the fast and slow time constants, and A_{fast} and A_{slow} are their corresponding amplitude coefficients. The time constants define the rates at which the individual kinetic components decay, whereas the amplitudes represent the relative contributions of each component to the macroscopic current as it relaxes to steady state.

2.4.5. Noise analysis of macroscopic currents

The discrete, stochastic opening and closing of ion channels can be characterized by analyzing macroscopic currents. In electrophysiology, noise (or fluctuation) analysis estimates average single-channel behavior by relating the variance of the transmembrane current to its mean [57, 58]. In stationary noise analysis, the current must remain constant or change slowly compared with the duration of the analyzed trace [57].

The current is assumed to arise from N identical, independent ion channels embedded in a membrane and exhibiting binomial open–closed transitions. The open probability P_o is defined as the average fraction of time a channel spends in the open state during the measurement interval. When open, each channel conducts a unitary current i that varies linearly with the driving force across the membrane, given by $i = g(V_m - V_{\text{eq}})$. Here, g is the single-channel conductance, V_m is the membrane potential, and V_{eq} is the reversal potential of the ion carrying the current. The average current across such a membrane under steady-state conditions can be expressed as:

$$I_{\text{mean}} = NiP_o$$

The variance of the macroscopic current depends on N, i, and P_o as:

$$\sigma_I^2 = Ni^2 P_o(1 - P_o)$$

Substituting for P_o yields:

$$\sigma_I^2 = iI_{\text{mean}} - \frac{I_{\text{mean}}^2}{N}$$

This equation defines a parabolic relationship between current variance and the mean current, with the unitary current corresponding to the slope at both intercepts ($I_{\text{mean}} = 0$ and $I_{\text{mean}} = iN$).

In practice, the total variance of the recorded electrophysiological signal σ_s^2 includes both the biological current noise σ_I^2 and a voltage-independent background noise component σ_{bg}^2, expressed as [57]:

$$\sigma_s^2 = \sigma_I^2 + \sigma_{\text{bg}}^2 + 2\,\text{Cov}(I, \text{bg})$$

Assuming current fluctuations arising from stochastic channel gating are independent of background noise, the covariance term $\text{Cov}(I, \text{bg})$ is taken to be zero. Accordingly, the unitary properties underlying the macroscopic current can be estimated from the variance after correcting for the background component:

$$\sigma_s^2 - \sigma_{\text{bg}}^2 = iI_{\text{mean}} - \frac{I_{\text{mean}}^2}{N}$$

The maximum open probability $P_{o,\text{max}}$ is estimated from the peak measured current $I_{\text{mean,max}}$ using the relationship:

$$P_{o,\text{max}} = \frac{I_{\text{mean,max}}}{iN}$$

This expression defines an upper bound on the open probability across the channel population under conditions of maximal activation.

When open probability cannot be reliably modulated over a broad range, the curvature of the variance–mean relationship may not be adequately resolved. In such cases, a linear approximation can be used to estimate the unitary current:

$$\sigma_s^2 - \sigma_{\text{bg}}^2 = iI_{\text{mean}}$$

This approach provides a lower-bound estimate of the unitary current but does not permit inference of channel number or maximal open probability.

2.4.6. Hill model of dose–response relationships

In whole-cell patch-clamp experiments, the extracellular environment can be systematically varied to evaluate the concentration-dependent effects of ligands on membrane-embedded targets. The resulting data can be modeled using a dose–response relationship, derived as follows [71]:

Consider a system in which a ligand L reversibly binds to a target T with n identical and independent binding sites. The binding equilibrium can be represented as:

$$T + nL \underset{k_{\text{off}}}{\overset{k_{\text{on}}}{\rightleftharpoons}} TL_n$$

Here, k_{on} and k_{off} denote the microscopic rate constants for association and dissociation, respectively. At equilibrium the forward and reverse reaction rates are equal according to the law of mass action:

$$k_{\text{on}}[T][L]^n = k_{\text{off}}[TL_n]$$

The equilibrium dissociation constant K_d is given by:

$$K_d = \frac{k_{\text{off}}}{k_{\text{on}}} = \frac{[T][L]^n}{[TL_n]}$$

The fractional occupancy θ is defined as:

$$\theta = \frac{[TL_n]}{[T] + [TL_n]}$$

Substituting the expression for K_d yields:

$$\theta = \frac{[L]^n}{K_d + [L]^n}$$

If ligand binding elicits a measurable response E that ranges from E_{min} in the absence of ligand to E_{max} at full occupancy, the response can be modeled as a linear function of occupancy:

$$E = E_{\text{min}} + (E_{\text{max}} - E_{\text{min}})\theta$$

Substituting for θ yields:

$$E = E_{\min} + \frac{(E_{\max} - E_{\min})[L]^n}{K_d + [L]^n}$$

The ligand concentration that elicits a half-maximal response is termed the half-maximal effective concentration, or EC_{50}. Under this model, EC_{50} is related to K_d by:

$$EC_{50}^n = K_d$$

Substituting this into the previous equation yields the Hill equation in standard form:

$$E = E_{\min} + \frac{(E_{\max} - E_{\min})[L]^n}{EC_{50}^n + [L]^n}$$

With the Hill coefficient fixed at 1, the relationship takes a hyperbolic form equivalent to a Michaelis–Menten–type dependence, without implying an underlying enzymatic process. The Hill equation therefore provides a quantitative framework for characterizing the modulatory effects of ligands on transmembrane targets.

2.4.7. Thermodynamic quantification of coupling stoichiometry

Thermodynamic analysis of substrate-translocation reaction cycles in carriers and pumps enables quantitative determination of transport stoichiometry [23, 61–63].

Considering a carrier-mediated antiport that translocates a monovalent anion A^- from the intracellular to the extracellular compartment and a monovalent cation P^+ in the opposite direction, let n and m denote the number of anions and cations, respectively, moved per transport cycle. The reaction is schematically represented as:

$$n\,A^-_{in} + m\,P^+_{out} \rightleftharpoons n\,A^-_{out} + m\,P^+_{in}$$

At thermodynamic equilibrium the net free-energy change over the transport cycle is zero; thus, the electrochemical potential differences of the two species satisfy:

$$n\,\Delta G_{A^-} = m\,\Delta G_{P^+}$$

Assuming formal charges $z_A = -1$ and $z_P = +1$, the electrochemical potential

differences are:

$$n\left(RT\ln\frac{[\mathrm{A}^-]_{\mathrm{out}}}{[\mathrm{A}^-]_{\mathrm{in}}}-F\Delta\psi\right)=m\left(RT\ln\frac{[\mathrm{P}^+]_{\mathrm{out}}}{[\mathrm{P}^+]_{\mathrm{in}}}+F\Delta\psi\right)$$

where $\Delta\psi=\psi_{\mathrm{in}}-\psi_{\mathrm{out}}$ denotes the membrane potential.

This equilibrium condition establishes a *zero-flux constraint* corresponding to the reversal potential of the transport cycle, which represents the state at which no net ionic movement occurs. Solving for $\Delta\psi$ yields:

$$\Delta\psi=\frac{n}{n+m}\frac{RT}{F}\ln\frac{[\mathrm{A}^-]_{\mathrm{out}}}{[\mathrm{A}^-]_{\mathrm{in}}}+\frac{m}{n+m}\frac{RT}{F}\ln\frac{[\mathrm{P}^+]_{\mathrm{in}}}{[\mathrm{P}^+]_{\mathrm{out}}}$$

$$=\frac{n}{n+m}E_{\mathrm{A}^-}+\frac{m}{n+m}E_{\mathrm{P}^+}$$

where E_{A^-} and E_{P^+} denote the corresponding Nernst potentials of A^- and P^+.

This relationship allows the coupling stoichiometry $n:m$ to be determined from electrophysiological measurements under near-equilibrium conditions.

Chapter 3:
Functional probing of rVGLUT1 ion channel properties

3.1. Results

Several conserved amino acids in VGLUTs are implicated in substrate coordination, ion permeation, and allosteric regulation by chloride and protons [12, 19, 22, 23, 34, 56]. Figure 3.1 maps these residues onto the cryo-EM structure of rat VGLUT2, highlighting arginines R88 and R322 that form the glutamate-binding site, R176 that defines the allosteric site for luminal chloride regulation, and histidines H199 and H434 that may contribute to channel gating. Guided by this structural framework, targeted substitutions were introduced into rVGLUT1 to assess the contributions of these residues to the pH-dependent ion channel function. Mammalian cells were transfected with rVGLUT1 constructs optimized for plasma membrane insertion and fused to eGFP at the C terminus. To isolate rVGLUT1 channel currents, cells were dialyzed with choline-based cytosolic solutions containing chloride or nitrate while excluding other permeant anions. Channel activity was modulated by stepwise pH titration of the luminal-side choline chloride solution. Voltage-elicited rVGLUT1 channel currents were recorded using the whole-cell patch-clamp configuration.

3.1.1. Contribution of binding pocket and luminal vestibule residues to rVGLUT1 channel function

VGLUTs can function as inwardly rectifying anion channels allosterically modulated by luminal protons and chloride ions [19, 22, 23, 72]. Figure 3.2A shows whole-cell recordings of WT rVGLUT1 voltage-elicited chloride currents in luminal-side solutions containing 144 mM chloride at pH 5.5 (left) or 7.4 (right). At neutral or basic luminal-side pH, the WT rVGLUT1 channel remains closed, yielding background-level current amplitudes. In contrast, luminal acidification produces robust inward currents upon hyperpolarizing voltage steps and no detectable currents at positive potentials. Point alanine substitutions were introduced at residues in the luminal vestibule or within the substrate-binding pocket. Representative proton-activated currents (pH 5.5, left) and normalized steady-state I–V relationships (right) of mutants Y319A, H348A, and E388A are shown in Figure 3.2B. Recordings were obtained using cytosolic chloride and luminal-side solutions containing

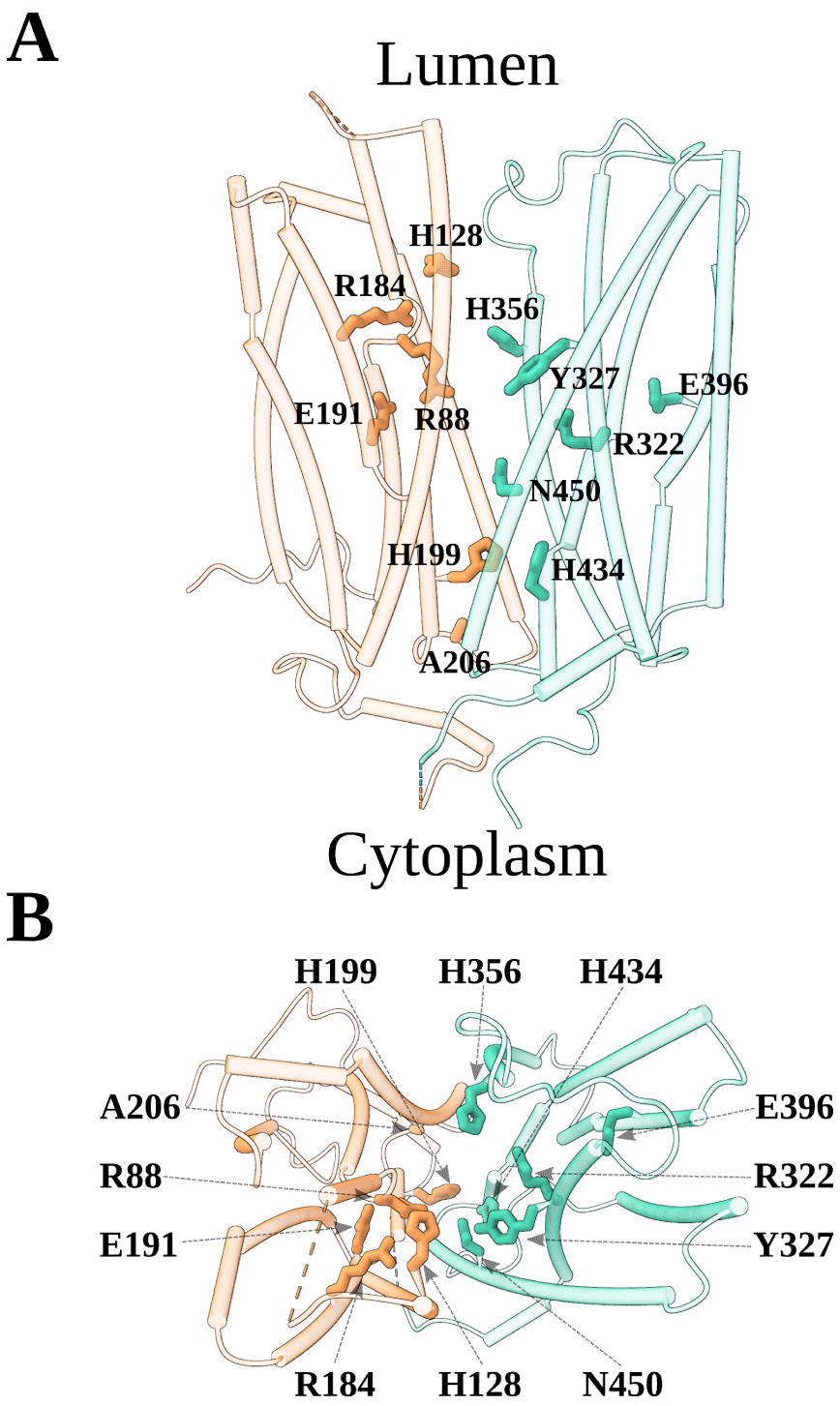

Figure 3.1. Functionally relevant residues mapped onto the VGLUT2 structure. The functionally relevant residues identified by mutagenesis and computational analyses are mapped onto the cryo-EM structure of rat VGLUT2 [12]. **A.** The side view, parallel to the membrane plane, shows the spatial distribution of these residues within the transmembrane architecture. **B.** The luminal view, perpendicular to the membrane plane, shows the arrangement of the same residues around the central cavity.

144 mM chloride at pH 5.5 (open circles) or pH 7.4 (filled circles). Whereas mutations at Y319 and H348 do not alter the shape of the voltage-dependent current response, E388A produces a modest steepening of the I–V curve under activating acidic conditions. E388 is positioned within a cluster of charged residues adjacent to R314 in the substrate-binding pocket and may indirectly regulate glutamate binding [12, 73].

The rVGLUT1 channel follows a lyotropic anion selectivity sequence [23]. Accordingly, cells expressing rVGLUT1 exhibit higher inward current amplitudes with cytosolic nitrate solutions than with chloride solutions. Figure 3.2C shows WT rVGLUT1 voltage-elicited currents recorded under nitrate dialysis and perfused with luminal-side 144 mM chloride solutions at pH 5.5 (left) or 7.4 (right). The enhancement of current amplitudes by cytosolic nitrate facilitates the characterization of alanine substitutions at arginine residues. Proton-activated currents (pH 5.5, left) and normalized steady-state I–V relationships (right) of mutants R80A, R314A, and R176A are shown in Figure 3.2D. Recordings were obtained with cytosolic nitrate and luminal-side 144 mM chloride solutions at pH 5.5 (open squares) or pH 7.4 (filled squares). Unlike a previous report under Cl^- dialysis [19], cells expressing the R314A mutant display robust proton- and voltage-activated nitrate currents. In addition, R314A induces a mild shift in the apparent voltage dependence of steady-state currents, similar to the effect of the alanine substitution at the neighboring E388.

To further examine how mutations at key residues affect voltage-dependent rVGLUT1 channel gating under steady-state acidic conditions, relaxation analysis of macroscopic currents was conducted. Kinetic analysis provides insight into the transition rates and occupancies of conformational states underlying channel gating [57, 70, 72]. Currents elicited by voltage steps from 0 mV to −160 mV were recorded using luminal-side solutions of different pH, with proton-activated currents at pH 5.0 and background currents at neutral to basic pH 7.0–9.5. Background-subtracted traces were fitted with either monoexponential or biexponential activation models. Curve selection relied on partial F-test statistics, and in all cases, the biexponential model ($I(t) = I_{\text{fast}}e^{-t/\tau_{\text{fast}}} + I_{\text{slow}}e^{-t/\tau_{\text{slow}}} + I_{\text{ss}}$) consistently provided a superior fit ($p < 0.001$, see Materials and Methods). The analysis excluded rVGLUT1 nitrate currents, as their fast activation kinetics under the recording conditions fell outside the range of reliable modeling. Figure 3.3 shows the bootstrap distributions of normalized traces and their corresponding fits for Y319A (**A**) and E388A (**B**). Notably, both mutants altered the activation kinetics by increasing the fast (τ_{fast}, Figure 3.3C, left) and

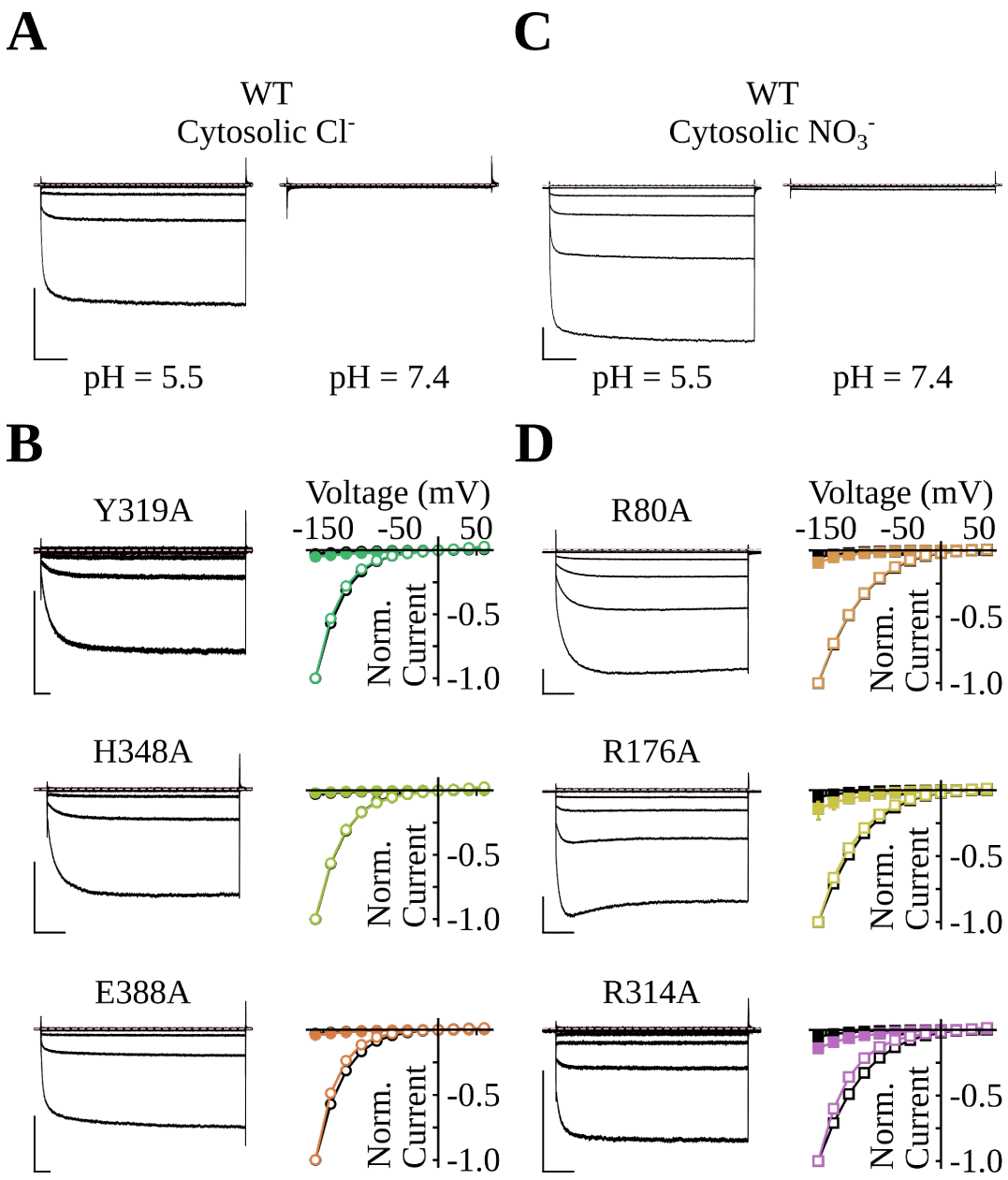

Figure 3.2. Effects of luminal vestibule and binding pocket mutations on the steady-state voltage dependence of rVGLUT1 chloride and nitrate currents. Whole-cell recordings show voltage-elicited WT rVGLUT1 currents with cytosolic Cl^- (**A**) or NO_3^- (**C**), recorded in luminal-side 140 mM Cl^- solutions at pH 5.5 (left) or 7.4 (right). Traces show currents elicited by voltage steps from a holding potential of 0 mV to −160 mV, −120 mV, −80 mV, −40 mV, 0 mV, and 40 mV. Scale bar: 1 nA, 25 ms. Dashed lines indicate the 0 pA current level. Representative currents (left) and corresponding normalized I–V curves (right) are shown for mutated transporters with cytosolic Cl^- (**B**) or NO_3^- (**D**). Currents were elicited using the same voltage protocol as in **A** and **C**, in luminal-side 140 mM Cl^- solutions at pH 5.5. I–V plots show the mean and 95% confidence intervals of bootstrapped distributions (5000 iterations) of late currents, elicited by voltage steps between −160 mV and 60 mV, and measured at luminal-side solutions at pH 5.5 (open markers) or 7.4 (filled markers). Black symbols represent WT measurements with cytosolic Cl^- (circles) or NO_3^- (squares). Number of cells per construct: WT (cytosolic Cl^-) = 23, Y319A = 15, H348A = 6, E388A = 15; WT (cytosolic NO_3^-) = 20, R80A = 13, R176A = 7, R314A = 15.

the slow (τ_{slow}, Figure 3.3C, middle) relaxation time constants. In addition, Y319A reduced the fractional amplitude of the fast component, defined as $I_{fast}/(I_{fast} + I_{slow})$ (Figure 3.3C, right). Tyrosine 319 lies luminal to the substrate-coordinating R322 and projects toward the central cavity of the transporter (Figure 3.1). It is conserved across VGLUT isoforms and has been proposed to stabilize interactions with glutamate via hydrogen bonds [73].

Luminal protons critically modulate VGLUT channel activity [19, 22, 23, 72]. To characterize the role of specific residues in proton sensing, titration curves were generated using luminal-side choline–chloride solutions ranging from pH 5.0 to 9.5. Because rVGLUT1 constructs exhibit non-saturating steady-state current responses across the tested pH range, mechanistic modeling was not feasible. Instead, a phenomenological hyperbolic model with multiple adjustable parameters was fitted to the data. This empirical formulation describes both baseline activity and the curvature of the pH-dependent response. Bootstrap resampling with replacement was used for refitting the model at each iteration, generating a distribution of response profiles. Direct comparison of the resulting curve shapes enables statistical inference of mutant pH dependence, suggesting contributions of specific residues to proton sensing. A similar empirical strategy was applied to assess luminal chloride effects on glutamate/proton exchange stoichiometry in rVGLUT1 [23]. Figure 3.4 shows titration curves of normalized late current amplitudes elicited at −160 mV across luminal pH values under dialysis with either chloride (**A**) or nitrate (**B**). Alanine substitutions at Y319, H348, E388, and R176 do not alter the pH-dependent response, whereas mutations in the glutamate-binding arginines R80A and R314A have mild effects. Arginine side chains are constitutively protonated; thus, neutralization is expected to disrupt electrostatic interactions required for proton-dependent channel function.

Fluctuation analysis of macroscopic current traces is used to characterize the pore properties of ion channels and transporter-associated channel modes [74, 75, 76, 77]. Previous work characterized rVGLUT1 as an anion channel with low unitary current amplitude and short-lived open states [23]. Stationary noise analysis was conducted to evaluate the contribution of specific residues to the rVGLUT1 channel pore. The open probability was modulated by varying the pH of luminal-side solutions between 5.0–9.5. Figure 3.5 shows representative chloride (**A**) and nitrate (**D**) currents elicited at −160 mV from WT rVGLUT1-expressing cells, with the analyzed region highlighted (blue traces). Representative variance–mean current relationships are shown in Figure 3.5 for ensembles

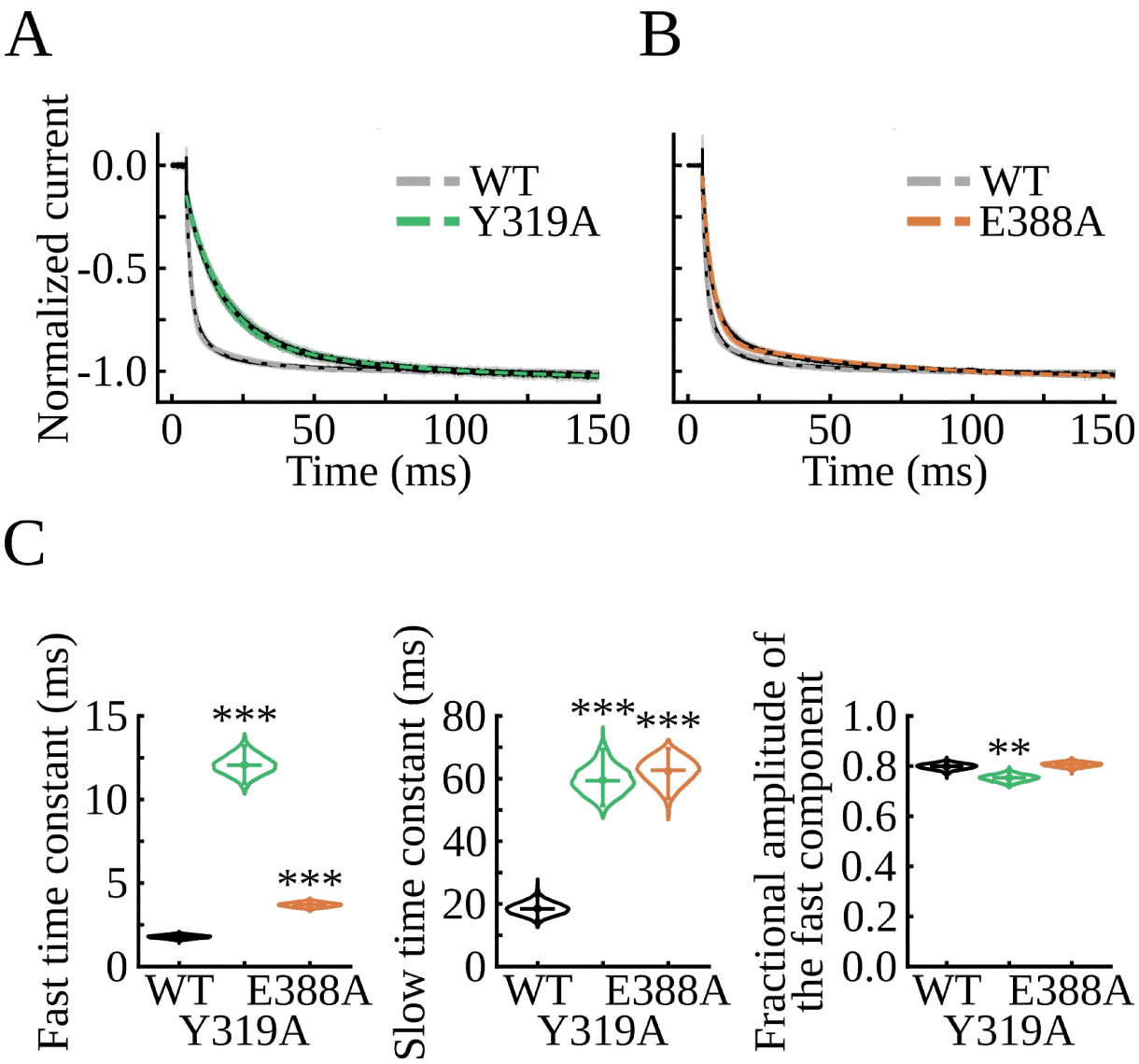

Figure 3.3. Effects of Y319A and E388A on rVGLUT1 channel activation. Normalized background-subtracted recordings (solid lines) with their biexponential fits (dashed lines) of the form $I(t) = I_{\text{fast}}e^{-t/\tau_{\text{fast}}} + I_{\text{slow}}e^{-t/\tau_{\text{slow}}} + I_{\text{ss}}$ are shown for macroscopic Cl^- currents of Y319A (**A**) and E388A (**B**). The traces show the mean and 95% confidence intervals from 5000 bootstrap iterations. Proton-activated currents were elicited at −160 mV from a holding potential of 0 mV at luminal-side pH 5.0, whereas background currents were obtained at pH 7.0–9.5. In each iteration, recordings were resampled with replacement, and the model was fitted to the averaged current. **C, left:** Distribution of fast time constants (τ_{fast}). **C, middle:** Distribution of slow time constants (τ_{slow}). **C, right:** Distribution of fractional amplitude of the fast component ($I_{\text{fast}}/(I_{\text{fast}} + I_{\text{slow}})$). Number of cells per construct: WT = 22, Y319A = 7, E388A = 8. Within each violin plot, the vertical bar spans the 95% confidence interval, the horizontal line indicates the median, and the central point indicates the mean of the distribution. Two-tailed nonparametric bootstrap tests were used for statistical comparisons. Significance levels: $p < 0.05$ (*), $p < 0.01$ (**), $p < 0.001$ (***).

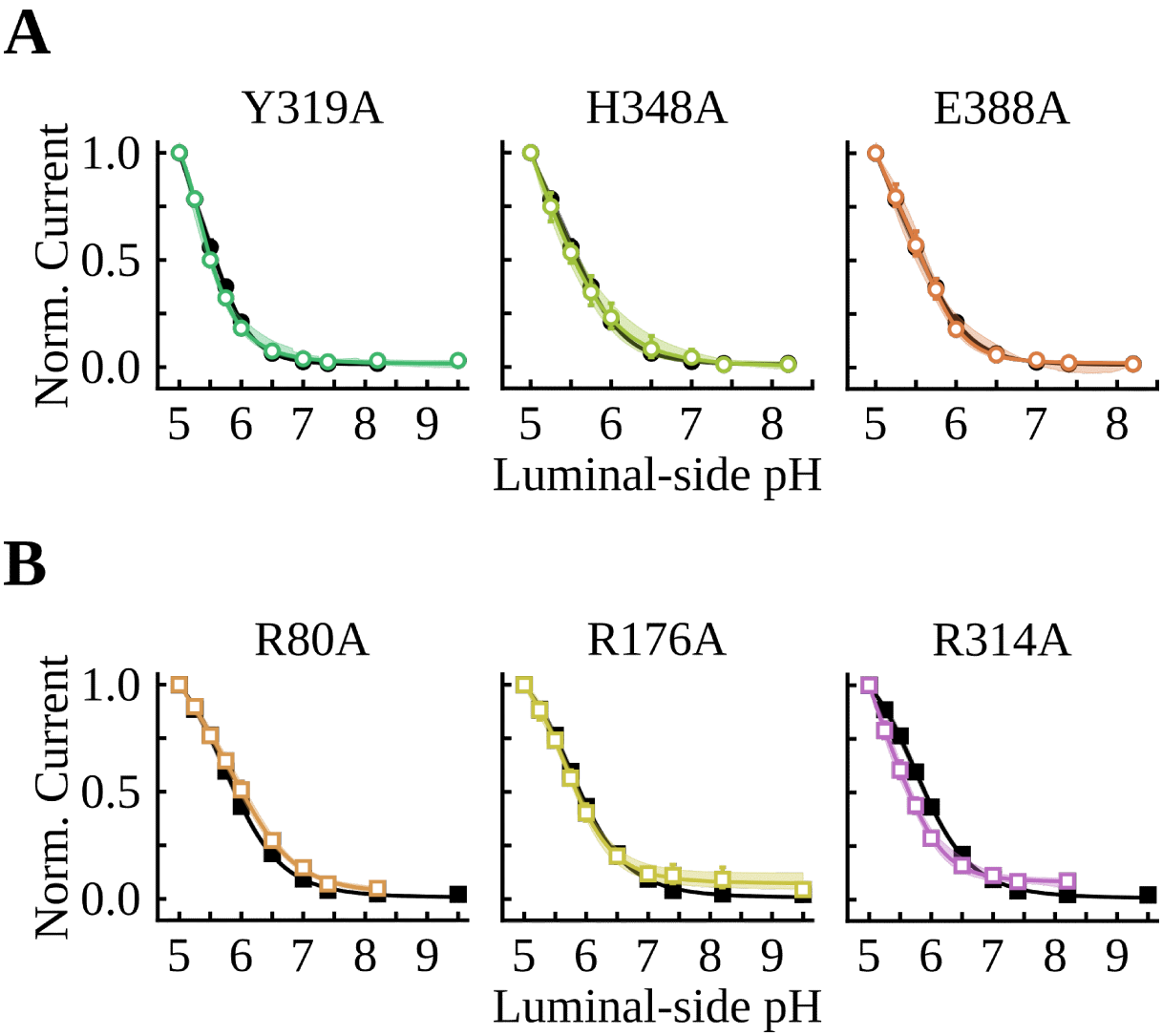

Figure 3.4. Effects of luminal vestibule and binding pocket mutations on the steady-state pH dependence of rVGLUT1 channel function. Normalized pH-dependent response plots of mean late currents (symbols) and their phenomenological hyperbolic fits (lines) are shown for Cl^- (**A**) and NO_3^- (**B**) currents from mutant transporters. The empirical model included adjustable parameters to describe both baseline activity and the curvature of the pH-dependent current responses. Currents elicited by voltage steps to −160 mV were recorded across luminal-side solutions at pH 5.0–9.5. Steady-state values extracted at the end of the current trace, normalized to currents at pH 5.0, were resampled with replacement (10 000 iterations), and the model was fitted to the averaged currents in each bootstrap iteration. Black symbols represent WT measurements with cytosolic Cl^- (circles) or NO_3^- (squares). All plots show the mean and 95% confidence intervals of the distributions. Number of cells per construct: WT (cytosolic Cl^-) = 23, Y319A = 15, H348A = 7, E388A = 15; WT (cytosolic NO_3^-) = 20, R80A = 13, R176A = 8, R314A = 15.

of WT rVGLUT1-expressing cells dialyzed with chloride (**B**) or nitrate (**E**). Variance–mean current relationships were modeled by either a parabolic ($\sigma_I^2 - \sigma_{\text{bg}}^2 = i\,I_{\text{mean}} - \frac{I_{\text{mean}}^2}{N}$) or a linear model ($\sigma_I^2 - \sigma_{\text{bg}}^2 = i\,I_{\text{mean}}$). Model selection was based on partial F-test statistics. If the parabolic model yielded a significantly better fit ($p < 0.01$), unitary currents were derived from it; otherwise, from the linear model. Relationships were pooled after bootstrap resampling (10 000 iterations), and distributions of chloride (Figure 3.5C) and nitrate (Figure 3.5F) unitary currents were obtained. No significant differences were found between the chloride and nitrate unitary currents of WT rVGLUT1, consistent with the interpretation that cytosolic nitrate enhances macroscopic current amplitudes by increasing the proton-dependent open probability of the channel [23].

Stationary noise analysis revealed residue-specific effects on rVGLUT1 unitary currents. Alanine substitution of Y319 decreased unitary current amplitudes, consistent with a role in supporting anion conduction via polar and weak ionic interactions in the local coordination environment. R314A strongly reduced unitary nitrate current amplitudes, likely reflecting the loss of an electrostatic interaction that stabilizes anion conduction along the permeation pathway. In contrast, R80A did not produce significant changes, suggesting an asymmetric contribution between the glutamate-binding arginines in mediating anion permeation. E388A modestly increased unitary current, possibly by disrupting the R314 cluster of the substrate binding pocket and facilitating more favorable interactions between R314 and permeating chloride ions. R176, which acts as a luminal chloride-binding site that allosterically activates both anion channel and transport functions, produced a striking increase in unitary current upon neutralization. This effect could reflect an altered electrostatic environment in which chloride ions that might otherwise dwell near the arginine side chain exit the rVGLUT1 cavity more readily. Together, these results highlight the contributions of conserved amino acids within the binding pocket and luminal vestibule of VGLUTs to their anion channel function, underscoring a structural–functional coupling between channel activity and substrate translocation.

3.1.2. Contribution of cytosolic vestibule residues to rVGLUT1 anion conduction

Structural analysis of the outward-facing conformation suggests that the principal chloride conduction pathway in VGLUT2 converges toward a putative gate on the cytosolic

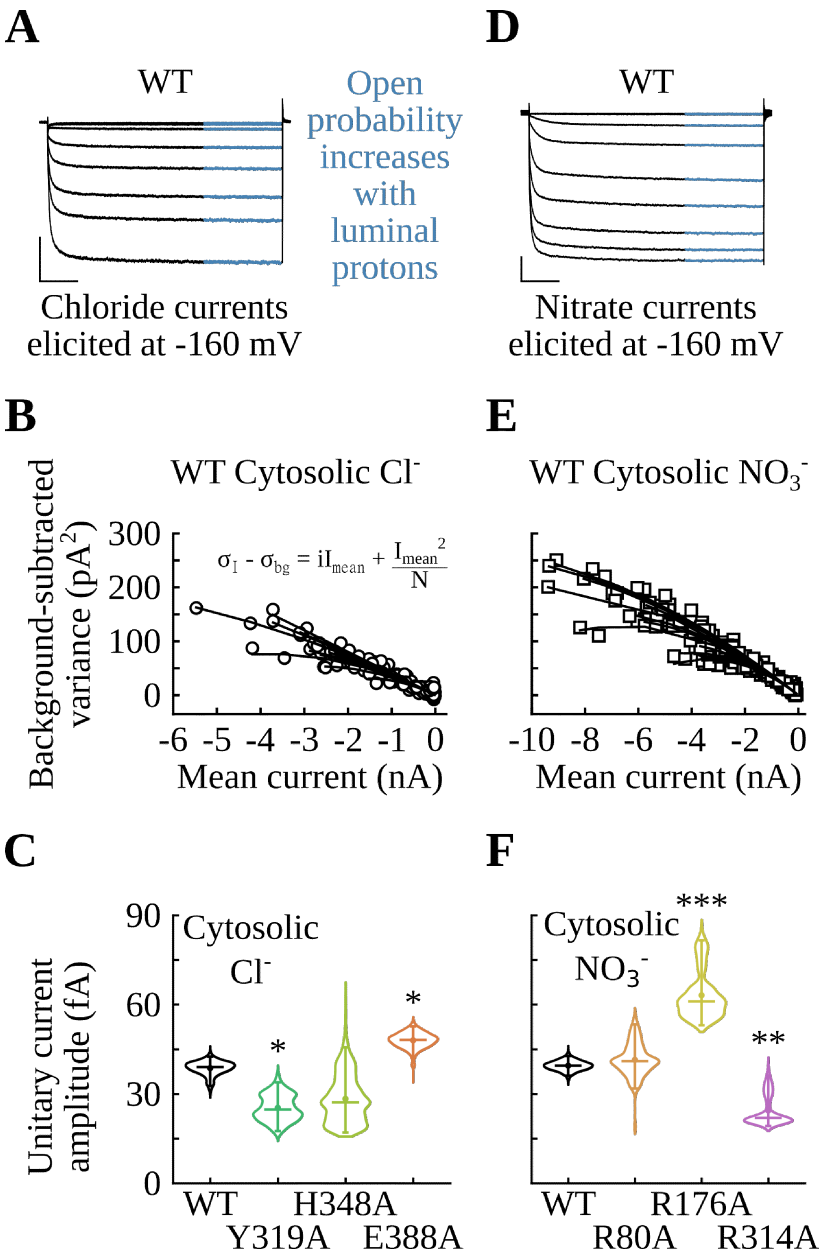

Figure 3.5. Effects of binding site and luminal vestibule mutations on the unitary currents of rVGLUT1. WT rVGLUT1 current traces elicited at −160 mV are shown for cells dialyzed with Cl^- (**A**) or NO_3^- (**D**) and exposed to 144 mM luminal-side Cl^- solutions at pH values of 5.0–8.2. Scale bar = 1 nA, 25 ms. The blue traces represent the regions of analysis. Representative variance–mean relationships and parabolic model fits of WT rVGLUT1 are shown for ensembles of cells dialyzed with Cl^- (**B**) or NO_3^- (**E**). Steady-state currents were obtained from traces elicited at −160 mV and lasting at least 100 ms. Bootstrap distributions (10 000 iterations) of unitary currents are shown for ensembles of cells expressing mutant transporters and dialyzed with Cl^- (**C**) or NO_3^- (**F**). Pooled unitary currents were extracted from parabolic fits of the form $\sigma_I^2 - \sigma_{bg}^2 = iI_{mean} - \frac{I_{mean}^2}{N}$ or linear fits of the form $\sigma_I^2 - \sigma_{bg}^2 = iI_{mean}$ (see Materials and Methods). Number of cells per construct: WT (cytosolic Cl^-) = 22, Y319A = 13, H348A = 6, E388A = 14; WT (cytosolic NO_3^-) = 20, R80A = 13, R176A = 8, R314A = 15. Within each violin plot, the vertical bar denotes the 95% confidence interval, the horizontal line the median, and the central point the mean of the distribution. Two-tailed nonparametric bootstrap tests were used for statistical comparisons. Significance levels: $p < 0.05$ (*), $p < 0.01$ (**), $p < 0.001$ (***).

side formed by H199 and H434 (Figure 3.1)[12]. The histidine pair does not interact directly; rather, each is coordinated by asparagine 431. N431 is part of a layer of polar residues positioned between H434 and R322, which also includes N319 and N450. This polar layer has been suggested to support substrate binding[73]. Similarly, T194, a polar side chain located between R80 and H199, has an untested function. These amino acids thus constitute rational mutagenesis targets for studying VGLUT anion channel function. Electrophysiological analysis, as described for the luminal-facing residues, was similarly applied to probe the cytosolic-facing residues in rVGLUT1: T186, H199, H426, and N442.

Figure 3.6 shows representative whole-cell proton-activated currents from mutant transporters in luminal-side solutions at pH 5.5 (left) and their normalized I–V curves (right). Recordings were obtained with cytosolic chloride (**A**) or nitrate (**B**) and luminal-side solutions containing 144 mM chloride at pH 5.5 (open symbols) or pH 7.4 (filled symbols). Single charge-neutralizing alanine substitutions at H191—and particularly at H426—blunted the steady-state voltage-dependent response. However, neither the double mutant H191A H426A nor the single-point mutations N442A and T186A altered the I–V relationships. In contrast, substitution of one or both histidines with the bulkier, positively charged lysine resulted in the most pronounced reduction in apparent voltage sensitivity across the tested mutations and markedly disrupted inward rectification, with prominent currents elicited at positive potentials. In addition, whereas the WT VGLUT1 channel is closed at neutral luminal-side pH, lysine substitutions increased chloride or nitrate current amplitudes above background levels upon membrane hyperpolarization.

Cytosolic vestibule mutations were further characterized using kinetic analysis of channel activation under steady acidic conditions. Whole-cell chloride current traces elicited at −160 mV in luminal-side solutions at pH 5.0 were background-subtracted from equivalent traces at pH 7.0–9.5 and modeled with exponential functions (see Materials and Methods). As outlined above, the biexponential activation model provided a superior fit for alanine substitutions in all cases (partial F-test: $p < 0.001$). Lysine substitutions at histidine residues produced complex activation kinetics that fell outside the range of reliable model fitting (Figure 3.6). Figure 3.7 shows distributions of background-subtracted currents and their corresponding biexponential fits for the double mutant H191A H426A (**A**) and N442A (**B**). Both mutants profoundly slowed the activation kinetics. N442A increased the fast (Figure 3.7C, left) and slow (Figure 3.7C, middle) time constants and decreased the

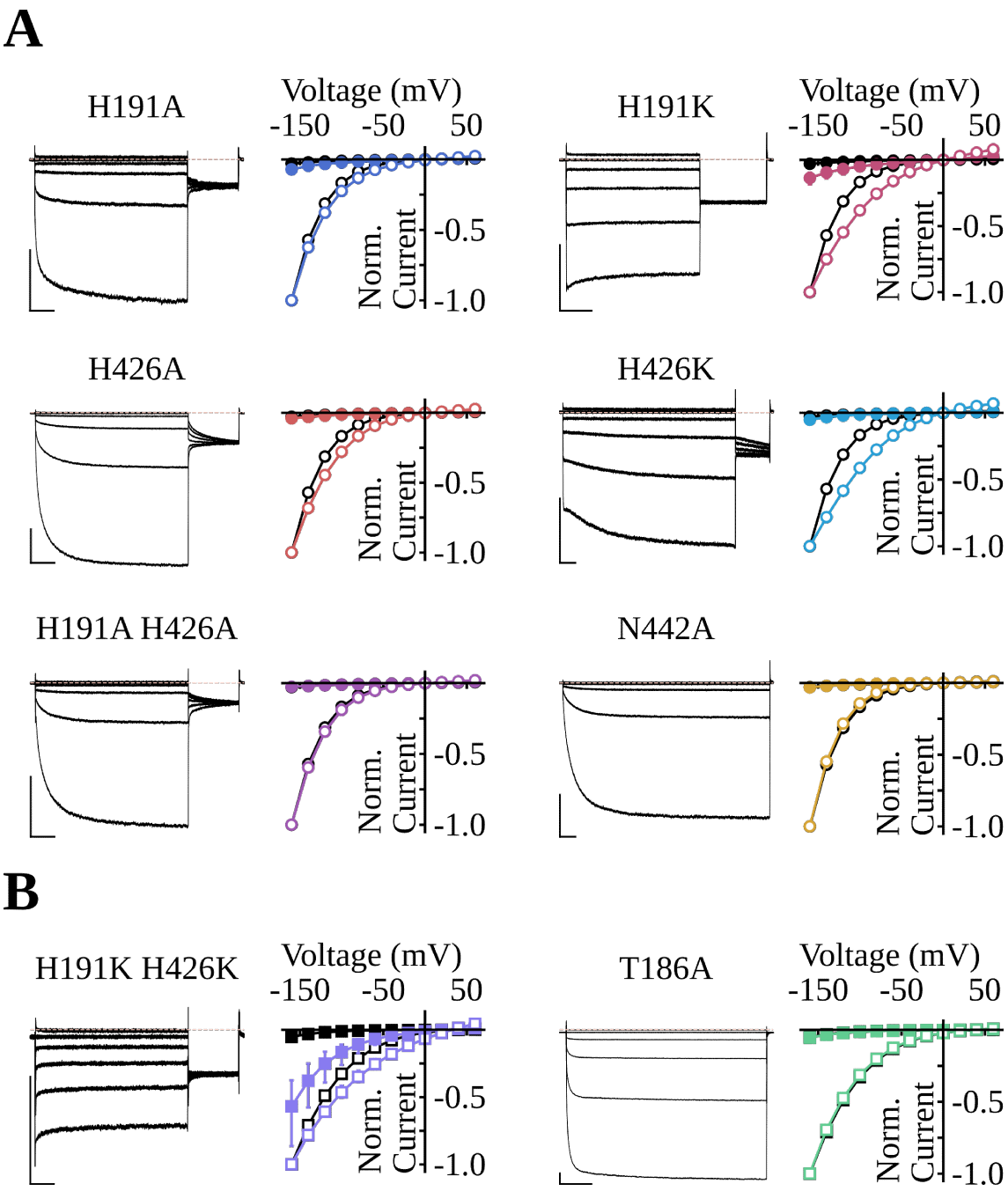

Figure 3.6. Effects of alanine and lysine substitutions at cytosolic vestibule residues on the steady-state voltage dependence of rVGLUT1 chloride and nitrate currents. Macroscopic currents (left) and corresponding I–V curves (right) are shown for mutant transporters with cytosolic Cl^- (**A**) or NO_3^- (**B**). Traces show currents recorded in luminal-side solutions containing 144 mM Cl^- at pH 5.5 and elicited by voltage steps from a holding potential of 0 mV to −160 mV, −120 mV, −80 mV, −40 mV, 0 mV, and 40 mV. Scale bar: 1 nA, 25 ms. I–V plots show the mean and 95% confidence intervals of bootstrapped distributions (5000 iterations) of late currents, measured at luminal-side pH 5.5 (open markers) or pH 7.4 (filled markers), and elicited by voltage steps between −160 mV and 60 mV from a holding potential of 0 mV. Black symbols represent WT measurements with cytosolic Cl^- (circles) or NO_3^- (squares). Number of cells per construct: WT (cytosolic Cl^-) = 23, H191A = 15, H191K = 11, H426A = 16, H426K = 19, H191A H426A = 13, N442A = 13; WT (cytosolic NO_3^-) = 20, H191K H426K = 5, T186A = 16.

fractional amplitude of the fast component (Figure 3.7C, right). Both single and double alanine substitutions at the potential gating histidines caused pronounced alterations in the kinetics of channel opening. Single histidine-to-alanine mutations mildly reduced the fast time constant while producing contrasting effects on the slow time constants. Moreover, mutation of H426 in single and double alanine mutants greatly reduced the fractional amplitude of the fast component. These results support the interpretation that the cytosolic-facing histidines contribute to a gating mechanism for chloride conduction.

Under symmetrical transmembrane chloride concentrations, rVGLUT1 channels close monoexponentially at positive membrane potentials [23, 72]. To further investigate molecular determinants of VGLUT channel gating, the time course of voltage-dependent channel closing was assessed. H426K rVGLUT1 displays above-background current amplitudes at depolarizing voltages (Figure 3.6), a feature further analyzed by regression modeling. To eliminate endogenous proton-activated outward currents during membrane depolarization, an in-house–generated HEK293T cell line lacking TMEM206 was employed (see Materials and Methods). Whole-cell currents were elicited at 160 mV after a hyperpolarizing step at −160 mV (Figure 3.8A). This prepulse protocol enables the characterization of the time course of channel closure from a uniform conducting state. Proton-activated rVGLUT1 currents were recorded in luminal-side solutions at pH 5.0, while background currents were obtained at neutral (WT) or basic (H426K) pH. Background-subtracted currents were resampled, pooled, and fitted with a monoexponential current-decay model (Figure 3.8B). Whereas WT VGLUT1 closes rapidly to zero current levels, H426K incompletely closes and sustains elevated residual current amplitudes (Figure 3.8C). Substitution of histidines with lysines may hinder closure of the putative cytosolic gate, preventing the typical transition to the nonconductive state reached at positive membrane potentials.

Luminal acidification is necessary for VGLUT substrate translocation and channel function. Polar and protonatable residues in the cytosolic vestibule—such as the putative gating histidines H199 and H426—are well positioned to contribute to the mechanism that couples protonation with channel gating. Figure 3.9 shows normalized titration curves for late chloride (**A**) or nitrate (**B**) currents from mutant transporters elicited at −160 mV in luminal-side solutions containing 144 mM chloride across pH 5.0–9.5. As described previously, the shape of the pH-dependent current response was assessed using a combination of bootstrap resampling and empirical fitting with a hyperbolic model

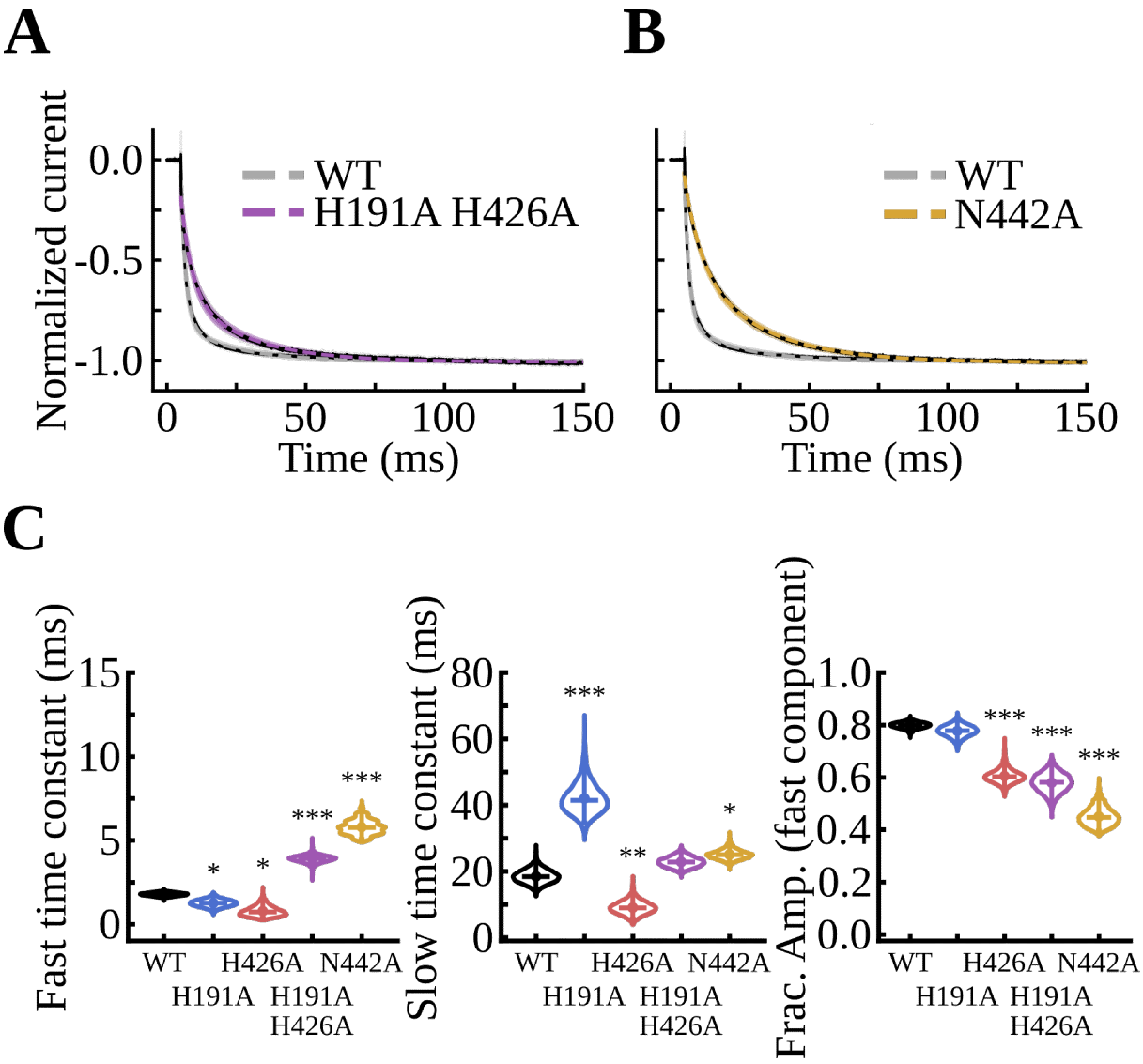

Figure 3.7. Effects of cytosolic vestibule mutations on rVGLUT1 channel activation. Normalized current traces (solid lines) with their biexponential fits (dashed lines) of the form $I(t) = I_{\text{fast}}e^{-t/\tau_{\text{fast}}} + I_{\text{slow}}e^{-t/\tau_{\text{slow}}} + I_{\text{ss}}$ are shown for macroscopic chloride currents of H191A H426A (**A**) and N442A (**B**). The traces show the mean and 95% confidence intervals from 5000 bootstrap iterations. Proton-activated currents were elicited at −160 mV from a holding potential of 0 mV under luminal-side solutions at pH 5.0, whereas background currents were recorded at pH 7.0–9.5. In each iteration, background-subtracted currents were resampled with replacement and fitted to the averaged current. **C, left:** Distribution of fast time constants (τ_{fast}). **C, middle:** Distribution of slow time constants (τ_{slow}). **C, right:** Distribution of fractional amplitude of the fast component ($I_{\text{fast}}/(I_{\text{fast}} + I_{\text{slow}})$). Number of cells per construct: WT = 22; H191A = 8; H426A = 12; H191A H426A = 12; N442A = 6. Within each violin plot, the vertical bar spans the 95% confidence interval, the horizontal line indicates the median, and the central point indicates the mean of the distribution. Two-tailed nonparametric bootstrap tests were used for statistical comparisons. Significance levels: $p < 0.05$ (*), $p < 0.01$ (**), $p < 0.001$ (***).

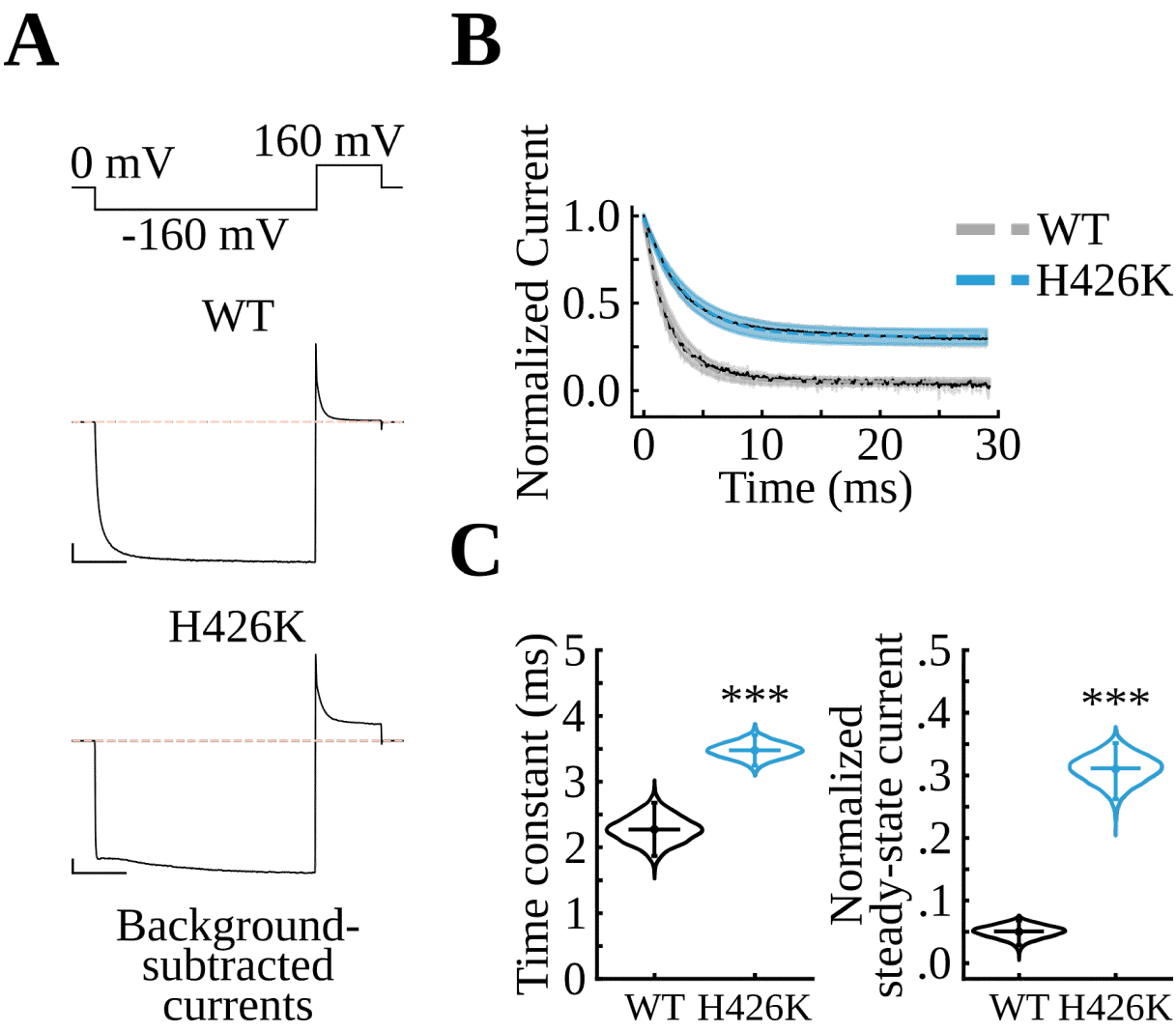

Figure 3.8. H426K prevents rVGLUT1 channel closure at positive membrane potentials. **A:** Representative background-subtracted traces for WT and H426K rVGLUT1, elicited at 160 mV following a prepulse at −160 mV (holding potential 0 mV). **B:** Mean and 95% confidence intervals of bootstrap distributions (10 000 iterations) obtained from normalized currents, together with their monoexponential fits of the form $I(t) = I_0 e^{-t/\tau} + I_{ss}$, for WT and H426K. The model was fitted to Cl^- currents recorded in luminal-side solutions at pH 5.0 after subtraction of currents obtained at pH 7.5 (WT) or 8.1 (H426K). **C:** Distributions of time constants and normalized steady-state current values. Number of cells per construct: WT = 9; H426K = 9. Within each violin plot, the vertical bar spans the 95% confidence interval, the horizontal line indicates the median, and the central point indicates the mean of the distribution. Two-tailed nonparametric bootstrap tests were used for statistical comparisons. Significance levels: $p < 0.05$ (*), $p < 0.01$ (**), $p < 0.001$ (***).

containing adjustable parameters. Single alanine substitutions at H191, N442, and T186 did not alter the shape of steady-state current responses. In contrast, H426A—but not H199A or the double alanine mutant—shifted the titration curve to the right. Notably, all lysine substitutions at the putative gating histidines produced striking right-shifted curves. H191K H426K, in particular, exhibited the shallowest pH-dependent response. The introduction of lysine at these positions thus uncouples channel closure from luminal proton concentration, likely through a combination of steric and electrostatic effects.

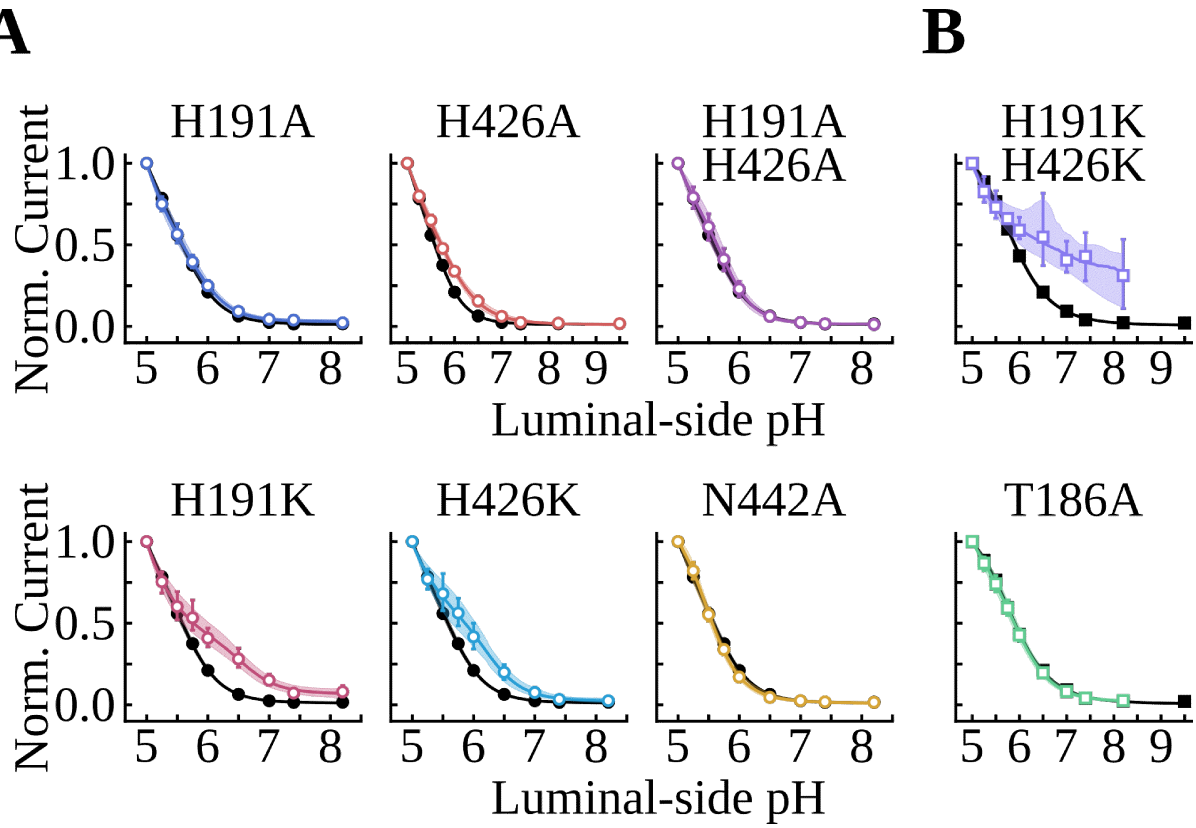

Figure 3.9. Effects of cytosolic vestibule mutations on the steady-state pH dependence of rVGLUT1 channel function. Normalized pH-dependent response plots of late currents (symbols) and their phenomenological hyperbolic fits (lines) are shown for Cl^- (**A**) and NO_3^- (**B**) currents from mutant transporters. The empirical model included adjustable parameters to describe both baseline activity and the curvature of the pH-dependent current responses. Currents elicited by voltage steps to −160 mV were recorded across luminal-side solutions at pH 5.0–9.5. Steady-state values extracted at the end of the current trace, normalized to currents at pH 5.0, were resampled with replacement (10 000 iterations), and the model was fitted to the averaged currents in each bootstrap iteration. Black symbols represent WT measurements with cytosolic Cl^- (circles) or NO_3^- (squares). All plots show the mean and 95% confidence intervals of the distributions. Number of cells per construct: WT (cytosolic Cl^-) = 23, H191A = 16, H426A = 16, H191A H426A = 13, H191K = 12, H426K = 22, N442A = 13; WT (cytosolic NO_3^-) = 20, H191K H426K = 5, T186A = 16.

The effects of cytosolic vestibule mutations on the rVGLUT1 channel pore were next probed by stationary noise analysis. As detailed above, whole-cell currents were elicited at −160 mV, and channel open probability was modulated by varying the luminal-side proton concentration. Figure 3.10A shows chloride currents from the H426K rVGLUT1 mutant, with the analyzed region highlighted (blue traces). These traces were resampled to generate variance–mean current relationships, from which unitary currents were extracted using linear or parabolic models. H426K exhibited linear variance–mean relationships (Figure 3.10B, $p > 0.01$), consistent with a reduced modulation of open probability by protonation. Distributions of chloride (left) and nitrate (right) unitary current amplitudes are shown in Figure 3.10C. Among alanine substitutions, only the single-point mutation H199A significantly reduced the amplitude. Notably, H426K caused the strongest reduction in unitary current amplitude, consistent with altered pore architecture at the cytosolic gate, where the bulkier lysine side chain may restrict the permeation pathway.

3.2. Discussion and conclusions

The loading of synaptic vesicles with glutamate by VGLUTs underlies mammalian excitatory neurotransmission. The vesicular V-type ATPase generates a $\Delta\tilde{\mu}_{H^+}$ that energetically drives vesicular glutamate uptake. However, the molecular determinants by which VGLUTs couple to the PMF to support substrate transport and channel function are still incompletely understood. The results presented here underscore the contribution of key residues to the proton- and voltage-dependent ion channel activity of VGLUTs.

Protonatable and polar residues lining the luminal and cytosolic vestibules, together with those forming the substrate-binding pocket (Figure 3.1), represent rational targets for assessing molecular determinants that shape VGLUT channel activity [12, 19, 22, 23, 34, 56]. Alanine neutralization of charged residues R134 and E388 within the binding pocket (Figure 3.2B,D), as well as mutations of the cytosolic-facing histidines H191 and H426 (Figure 3.6A,B), altered the I–V relationships. At steady state, changes in the I–V profiles likely reflect shifts in voltage-dependent conformational equilibria or structural changes altering anion permeation. Notably, insertion of lysines at positions H199 and H426 prevented full channel closure at positive potentials (Figure 3.6A,B and Figure 3.8). As with the electrogenic carriers EAATs [78, 79], which also display anion conductance [76, 77], the influence of voltage on the VGLUT conformational cycle extends across multiple

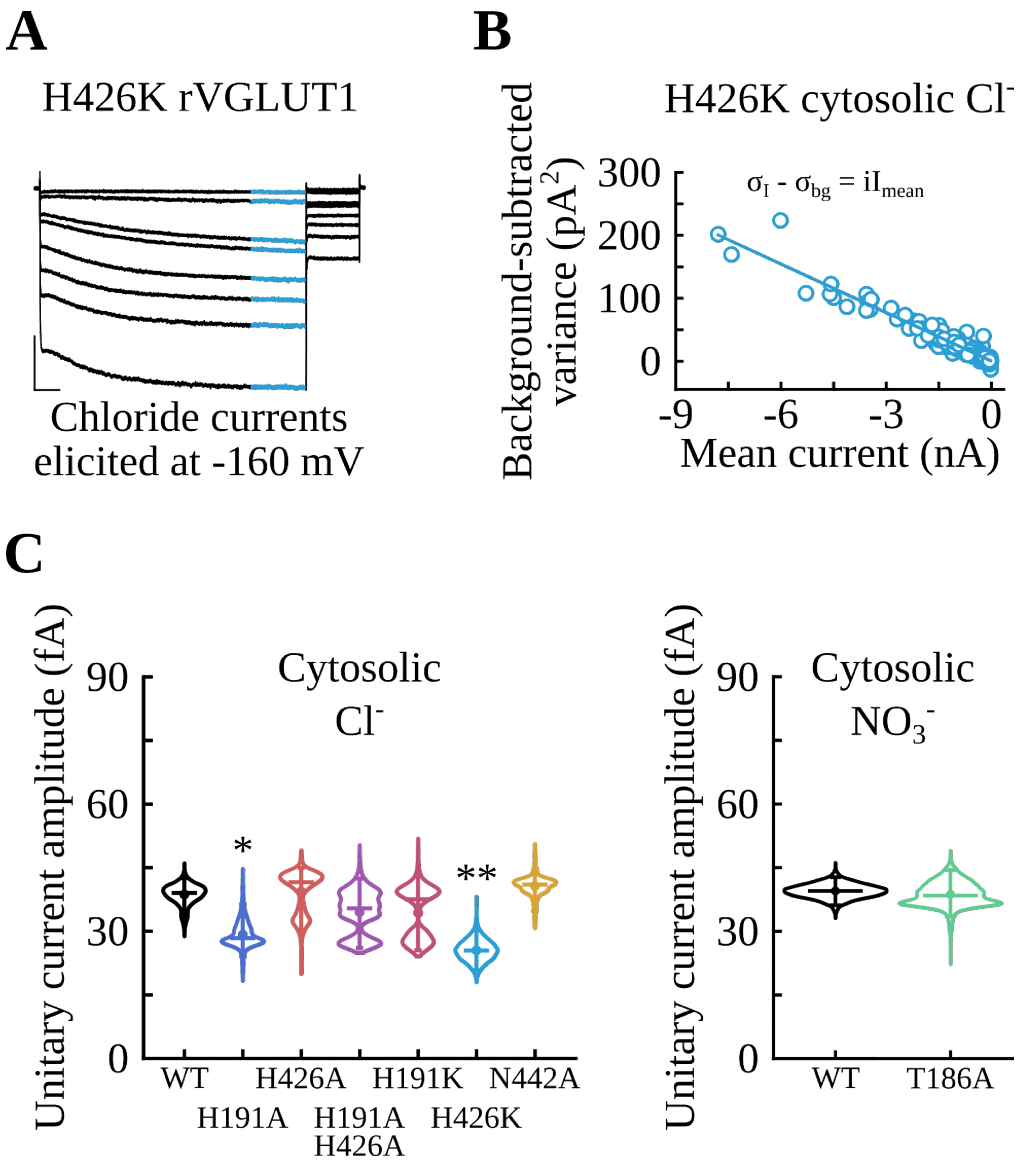

Figure 3.10. Effects of cytosolic vestibule mutations on the unitary currents of rVGLUT1. **A:** Representative H426K rVGLUT1 chloride recordings elicited at −160 mV in 144 mM luminal-side Cl^- solutions at pH 5.0–8.2. The blue traces represent the regions of analysis. Scale bars: 1 nA, 25 ms. **B:** Representative variance–mean relationships and linear model fits for H426K rVGLUT1 are shown for ensembles of cells dialyzed with Cl^-. Steady-state currents were extracted from current traces elicited at −160 mV and lasting at least 100 ms. **C:** Bootstrap distributions (10 000 iterations) of unitary currents are shown for ensembles of cells expressing mutant transporters dialyzed with Cl^- (left) or NO_3^- (right). Pooled unitary currents were extracted from parabolic fits of the form $\sigma_I^2 - \sigma_{bg}^2 = iI_{mean} - \frac{I_{mean}^2}{N}$ or linear fits of the form $\sigma_I^2 - \sigma_{bg}^2 = iI_{mean}$ (see Materials and Methods). Number of cells per construct: WT (cytosolic Cl^-) = 22, H191A = 13, H426A = 17, H191A H426A = 11, H191K = 8, H426K = 16; WT (cytosolic NO_3^-) = 20, T186A = 13. Within each violin plot, the vertical bar denotes the 95% confidence interval, the horizontal line the median, and the central point the mean of the distribution. Two-tailed nonparametric bootstrap tests were used for statistical comparisons. Significance levels: $p < 0.05$ (*), $p < 0.01$ (**), $p < 0.001$ (***).

transitions [72]. These results highlight the voltage dependence of VGLUT channel behavior through the collective contribution of charged residues lining its inner cavity.

The effects of mutations on voltage-dependent channel opening and closing were further assessed by analysis of relaxation kinetics. Voltage-elicited channel activation reflects the underlying rate constants and state occupancies during the closed-to-open transition [57, 70]. In addition to steady-state alterations in I–V relationships, several residues affected time-dependent VGLUT channel gating. Alanine substitutions at Y319 and E388, residues surrounding the glutamate-coordinating R314, profoundly slowed activation kinetics (Figure 3.3). In addition, alanine substitution at N442, located between R314 and H426, altered all modeled parameters of channel opening (Figure 3.7). In particular, the slowing of channel opening kinetics and changes in fractional occupancies in N442A and Y319A mutants suggest disruption of interactions that mediate conformational transitions, ion conduction, or both. These kinetic changes were paralleled by a marked reduction in unitary current amplitude for Y319A (Figure 3.5). Both N442 and Y319 are proposed to stabilize glutamate binding [73], and these findings support roles of these residues in both substrate translocation and ion channel activity.

Alanine substitutions at H191 and H426 altered the time course of activation during membrane depolarization (Figure 3.7). These histidines form a cytosolic-side gate for the inner cavity of VGLUTs in the outward-facing conformation [12]. Whereas single alanine substitutions accelerated the fast time constant, the H191A H426A double mutant markedly slowed it. Notably, H426A, alone or in the double mutant, modified fractional occupancies during channel activation, suggesting a redistribution of states along the closed-to-open transition. Lysine substitutions at these histidines accelerated activation kinetics to rates exceeding the temporal resolution of biexponential fitting of whole-cell currents (Figure 3.6). In addition, the H426K mutant partially prevented channel closure at positive membrane potentials, significantly altering channel kinetics and thereby allowing prominent outward current amplitudes at acidic luminal-side pH (Figure 3.8). A lysine substitution at this position may destabilize nonconducting states, thereby accounting for the accelerated activation and incomplete closure. Together, these results highlight the contributions of the cytosolic-side histidines H191 and H426 in shaping VGLUT channel

gating by fine-tuning conformational transitions and supporting channel closure.

VGLUTs have been characterized as glutamate/proton exchangers [23]. Their architecture features a dense network of polar and protonatable residues that are thought to sense luminal pH and contribute to proton translocation. Within this framework, these amino acids are expected to determine the pH-dependent gating of VGLUT channels. Analysis of the steady-state current responses to luminal-side pH changes in mutant rVGLUT1 transporters showed non-saturating behavior that was insensitive to most of the alanine substitutions (Figures 3.4, 3.9). This non-saturating behavior may enable the transporter to remain responsive even under highly acidic luminal conditions, thereby ensuring that activity scales with proton concentration at pH values typical of mature synaptic vesicles [83–85]. Among the tested alanine substitutions, those at the conserved R314 and H426, located in the C-terminal half of VGLUTs, produced clear shifts in the pH dependence of the current responses. Notably, all lysine substitutions caused a rightward shift of the titration curves (Figure 3.9). This is consistent with the expected effects of replacing histidines, which may function as protonation switches, with constitutively protonated lysines at positions implicated in coupling protonation to channel opening.

Solvent accessibility calculations from the outward-facing conformation predict a chloride conduction pathway through R80 and R314, with exit via a putative opening between H191 and H426 [12]. Although the inner cavity of VGLUTs is highly electropositive, the rVGLUT1 channel instead exhibits a lyotropic permeability sequence [23], which is not readily reconciled with electrostatics alone. Recordings of WT rVGLUT1 showed indistinguishable unitary current amplitudes for chloride and nitrate (Figure 3.5). The enhanced macroscopic current amplitudes recorded under nitrate dialysis are thus attributable to increased open probability of the VGLUT channel. This suggests that the properties of the cytosolic charge carrier, together with the allosteric effects of luminal chloride, modulate the electrostatic landscape of the channel pore, partially neutralizing the pore environment. This energetic reshaping would then render channel activation more favorable for larger, polarizable, and weakly hydrated anions. Consistent with this interpretation, faster opening kinetics were observed for nitrate currents relative to chloride recordings at negative membrane potentials (Figure 3.2A,C).

Mutagenesis of residues lining the inner cavity of rVGLUT1 revealed distinct effects on

channel conductance. Because single-residue mutations may exert long-range effects on channel properties, the assignment of candidate pore-forming residues must be carefully contextualized [80]. A strong candidate for direct interaction with permeating anions is R314, which positions a permanent positive charge near the midpoint of the conduction pathway. Consistent with this, neutralization of R314 reduced the unitary current amplitude by roughly half. In contrast, the R80A substitution did not alter unitary current amplitudes. These results suggest that the glutamate-binding arginines contribute unequally to the electrostatic environment that shapes anion permeation. Similarly, the reduced unitary current amplitude observed in H426K likely reflects an increased steric constraint within the permeation pathway. In contrast, the E388A mutant exhibited increased unitary current amplitudes. This could reflect the absence of side-chain interactions within the R314 cluster, enabling R314 to engage more consistently with permeant anions under steady-state gating equilibrium, as assessed by stationary noise analysis. Finally, the increased unitary current amplitude observed upon neutralization of the chloride-binding residue R176 may reflect reduced chloride occupancy near the luminal vestibule exit, thereby increasing the exit rate of permeant anions from the VGLUT cavity.

Chapter 4:
Functional properties of an insect VGLUT ortholog

4.1. Results

The *Drosophila* VGLUT ortholog, designated DVGLUT, shares approximately 40 % sequence identity with mammalian VGLUTs [81]. It is expressed in motoneurons and interneurons and localizes to all glutamatergic neuromuscular junctions. DVGLUT function was characterized using an approach equivalent to that used for rVGLUT1, combining site-directed mutagenesis with whole-cell patch-clamp recordings.

4.1.1. DVGLUT channel conducts chloride at positive potentials

DVGLUT function was first evaluated by measuring currents under near-symmetric transmembrane chloride concentrations. Figure 4.1A shows recordings obtained from a DVGLUT-expressing cell under chloride dialysis at neutral pH and perfused with luminal-side solutions containing 144 mM chloride at different pH values. Proton-activated currents were elicited by square voltage pulses from −160 mV to 160 mV and corrected by subtracting background currents recorded at luminal-side pH 7.4. Similar to mammalian VGLUTs, the I–V relationships of the fly transporter exhibited inwardly rectifying chloride currents (Figure 4.1B). However, unlike VGLUTs, the DVGLUT channel fails to close at positive membrane potentials. Figure 4.1C plots background-subtracted current amplitudes recorded at 160 mV and −160 mV at luminal-side pH 5.0 in cells expressing either DVGLUT (open symbols) or rVGLUT1 (filled symbols). The resulting current ratio normalizes transporter expression levels across cells and was fitted with linear functions. Whereas rVGLUT1 closes at positive membrane potentials with a slope statistically indistinguishable from zero (partial F-test, $p = 0.015$), DVGLUT current relationships are best fit with a positive slope ($r^2 = 0.9$). Titration curves were generated from mean amplitudes extracted from current traces elicited at −160 mV or 100 mV and recorded in luminal-side solutions at pH values ranging from 5.0 to 8.2 (Figure 4.1D). The normalized current response profiles were fitted using a hyperbolic model with adjustable parameters, as described previously for rVGLUT1. Mammalian and insect VGLUTs display identical pH-dependent current response curves at depolarizing potentials. Moreover, the DVGLUT channel shows similar pH dependence at negative and positive membrane potentials.

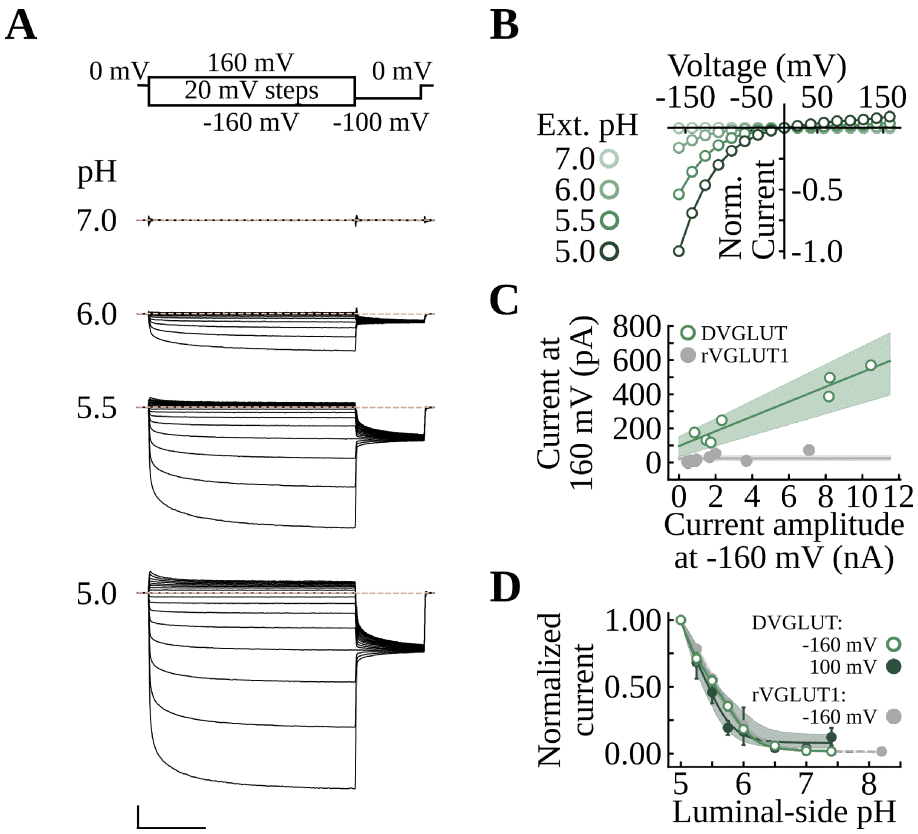

Figure 4.1. DVGLUT remains conductive at positive membrane potentials, unlike mammalian counterparts. **A**: Whole-cell recordings show DVGLUT currents obtained with cytosolic Cl^- in luminal-side solutions containing 144 mM Cl^- at pH 7.0, 6.0, 5.5, and 5.0. Currents were elicited by voltage steps ranging from −160 mV to 160 mV, applied from a holding potential of 0 mV. Background correction was performed using currents obtained in luminal-side solutions at pH 7.4. Scale bars: 1 nA, 10 ms. Dashed lines indicate the 0 nA current level. **B**: Normalized I–V relationships for DVGLUT Cl^- currents recorded using the same voltage protocols and solutions as in panel A. Data points show the mean and 95% confidence intervals of bootstrap distributions (10 000 iterations). Number of cells per construct: DVGLUT = 32. **C**: Relationship between Cl^- current amplitudes recorded at 160 mV and those elicited at −160 mV for DVGLUT (open symbols) and rVGLUT1 (filled symbols). Straight lines and shaded areas represent the mean and 95% confidence intervals of linear fits from bootstrap resampling (10 000 iterations). Number of cells per construct: DVGLUT = 7, rVGLUT1 = 11. **D**: Titration curves show normalized pH-dependent responses of mean late currents (symbols) and their phenomenological hyperbolic fits (lines). DVGLUT currents were elicited at −160 mV (open symbols) and 100 mV (filled green symbols), whereas rVGLUT1 currents were elicited at −160 mV. The empirical model included adjustable parameters to describe both baseline activity and the curvature of the pH-dependent current responses. Currents were recorded across luminal-side pH 5.0–8.2. Steady-state values extracted at the end of the current trace, normalized to currents at pH 5.0, were resampled with replacement (10 000 iterations), and the model was fitted to the averaged currents in each iteration. Number of cells per construct: DVGLUT (−160 mV) = 34, DVGLUT (100 mV) = 24, rVGLUT1 = 23.

To further investigate differences in anion channel gating between DVGLUT and mammalian VGLUTs, relaxation kinetics were analyzed. Figure 4.2A depicts the mean and 95% confidence intervals of normalized, background-subtracted chloride channel activation time courses for DVGLUT (black) and rVGLUT1 (gray). Proton-activated currents were elicited at −160 mV from a holding potential of 0 mV in luminal-side solutions containing 144 mM chloride at pH 5.0, whereas background currents were recorded at pH 7.4. The DVGLUT channel activates faster than its mammalian counterpart, to a degree that makes biexponential fitting unreliable. To study the kinetics at positive membrane potentials, a prepulse protocol was employed. As previously described, a positive 160 mV step was applied after a conditioning −160 mV pulse (Figure 4.2B). Whereas rVGLUT1 chloride currents decay to zero amplitude, the DVGLUT channel remains partially open (Figure 4.2C), with steady current amplitudes dependent on luminal-side pH (Figure 4.2D).

4.1.2. DVGLUT channels exhibit high luminal chloride sensitivity

Luminal chloride activates both substrate transport and channel activity of VGLUTs. This modulation was examined in DVGLUT channel function. Figure 4.3A illustrates representative DVGLUT chloride currents recorded in luminal-side solutions at pH 5.0 containing 0 mM, 2.2 mM, and 140 mM chloride. The DVGLUT channel conducts currents above background amplitudes at 0 mM chloride under negative membrane potentials and exhibits similar voltage dependence across the range of chloride concentrations (Figure 4.3B). A Hill dose–response model—with the Hill coefficient fixed at 1 (Michaelis–Menten-like; see Materials and Methods)—was fitted to normalized current responses obtained at −160 mV by stepwise variation of luminal-side chloride (Figure 4.3C). DVGLUT displayed a significantly lower IC_{50} than rVGLUT1 (2.5 ± 0.4 mM vs 34.2 ± 17.9 mM; $p < 0.001$). VGLUTs possess a well-characterized luminal chloride binding site, where neutralization of a conserved arginine side chain renders transporter and channel functions chloride independent [22]. The homologous R199A substitution in DVGLUT produced a similar effect. The R199A DVGLUT mutant exhibited more than twofold higher currents recorded at 0 mM luminal-side chloride (I_{min}: DVGLUT = 0.33 ± 0.02; R199A = 0.76 ± 0.04; $p < 0.001$). The differences in chloride dependence between fly and mammalian transporters thus arise from structural determinants not solely defined by the canonical luminal chloride binding site.

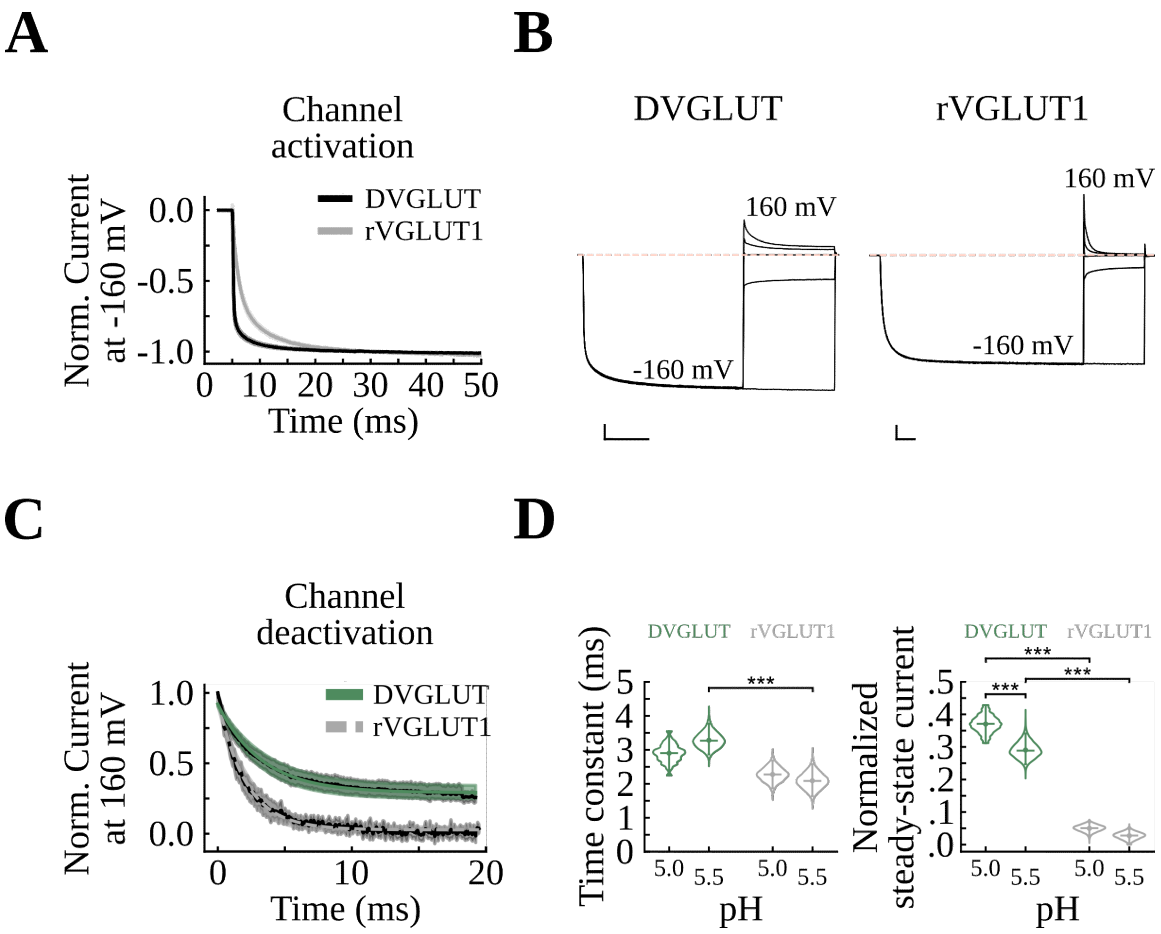

Figure 4.2. DVGLUT channel gating diverges from mammalian VGLUTs at positive membrane potentials. **A**: Background-subtracted Cl^- current activation traces measured in 144 mM luminal-side Cl^- solution at pH 5.0 are shown for DVGLUT (black line) and rVGLUT1 (gray line), elicited at −160 mV from a holding potential of 0 mV. Mean and 95% confidence intervals were obtained from bootstrap distributions (10 000 iterations). Number of cells per construct: DVGLUT = 7, rVGLUT1 = 22. **B**: Representative current traces elicited using a prepulse voltage protocol are shown for DVGLUT (left) and rVGLUT1 (right). The protocol consisted of a −160 mV step followed by variable test potentials ranging from 160 mV to −160 mV. Dashed lines indicate the 0 nA current level. Scale bars: 1 nA, 10 ms. **C**: Normalized background-subtracted currents elicited at 160 mV in 144 mM luminal-side Cl^- solution at pH 5.0 are displayed together with their monoexponential decay fits (lines) for DVGLUT (green) and rVGLUT1 (gray). Background currents were measured at pH 7.4. Traces represent the mean and 95% confidence intervals of bootstrap distributions (10 000 iterations). Data were resampled with replacement, and model fitting was applied to the mean traces of each iteration. **D**: Distributions of time constants and normalized steady-state current amplitudes. Number of cells per construct: DVGLUT (pH 5.0) = 4, DVGLUT (pH 5.5) = 15, rVGLUT1 (pH 5.0) = 9, rVGLUT1 (pH 5.5) = 11. Within each violin plot, the vertical bar spans the 95% confidence interval, the horizontal line indicates the median, and the central point denotes the mean of the distribution. Two-tailed nonparametric bootstrap tests were used for statistical comparisons. Significance levels: $p < 0.05$ (*), $p < 0.01$ (**), $p < 0.001$ (***).

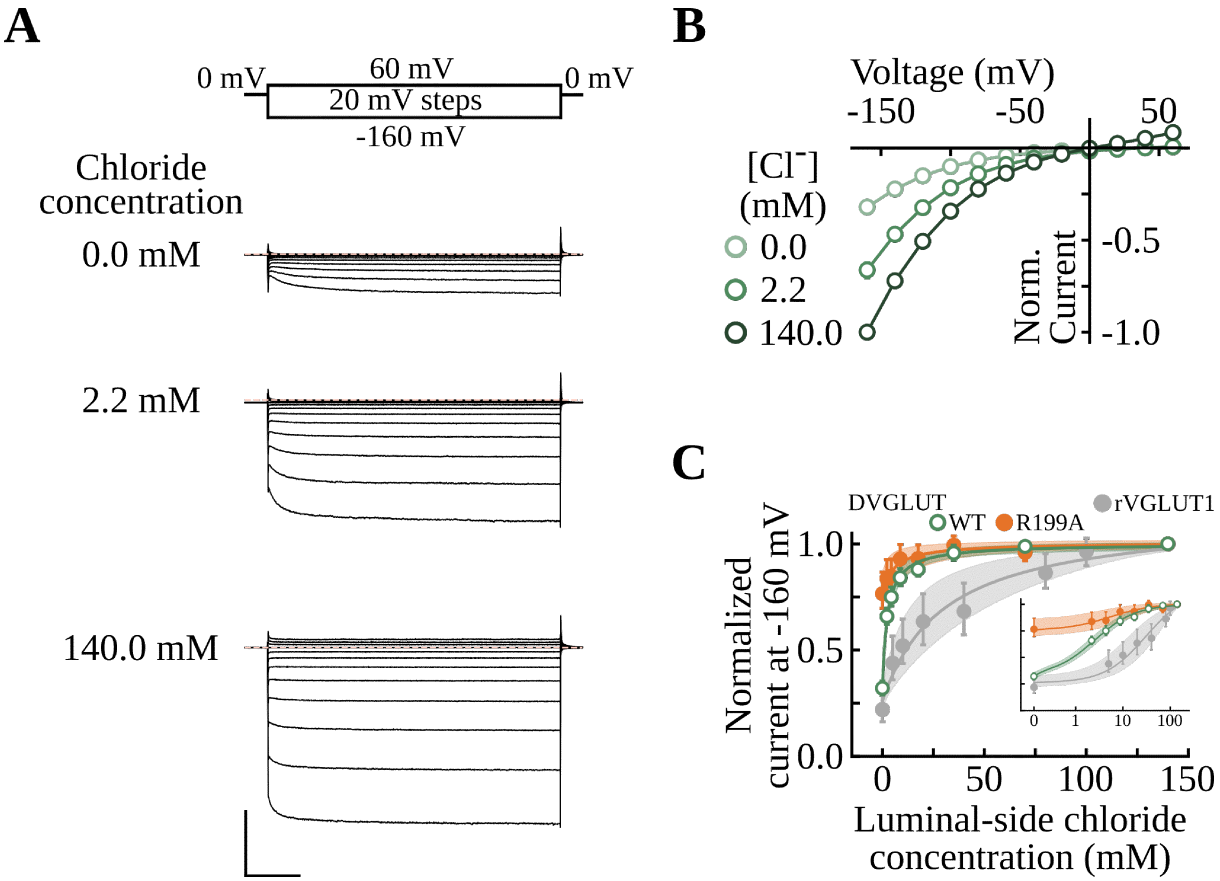

Figure 4.3. DVGLUT channels exhibit reduced dependence on luminal chloride compared with mammalian VGLUTs. A: Representative Cl^- current recordings from a DVGLUT-expressing cell perfused with luminal-side solutions at pH 5.0 containing 0 mM, 2.2 mM, or 140 mM Cl^-. Currents were elicited by voltage steps ranging from −160 mV to 60 mV, applied from a holding potential of 0 mV. Scale bars: 1 nA, 25 ms. Dashed lines indicate the 0 nA current level. **B**: Normalized DVGLUT I–V relationships were recorded at luminal-side Cl^- concentrations of 0 mM, 2.2 mM, and 140 mM under the same voltage protocol as in panel A. The plot shows the mean and 95% confidence intervals obtained from bootstrap distributions (10 000 iterations). **C**: Dose–response curves obtained by titrating Cl^- in luminal-side solutions at pH 5.0 are shown for WT DVGLUT (open symbols), R199A DVGLUT (filled orange symbols), and rVGLUT1 (filled gray symbols; data reproduced from [72]). The plot displays the mean and 95% confidence intervals obtained from 25 000 bootstrap iterations of normalized current amplitudes elicited at −160 mV and scaled to the responses measured at the highest Cl^- concentration, together with their fitted dose–response curves (see Materials and Methods). Currents were resampled with replacement, and the model was fitted to the average current values after each iteration. *Inset*: same data displayed on a semilogarithmic scale. Number of cells per construct: WT DVGLUT = 17, R199A DVGLUT = 17.

4.1.3. DVGLUT channel conducts anions with low unitary conductance

The DVGLUT channel function was further characterized by recording currents using different cytosolic anions. DVGLUT-expressing cells were dialyzed with choline-based solutions containing chloride, nitrate, or iodide at neutral pH. Cells were then perfused with luminal-side solutions containing 144 mM Cl^- at variable pH 5.0–7.4. Figure 4.4A depicts representative macroscopic currents elicited by voltage steps from −160 mV to 60 mV either under background or proton-activated pH conditions. Each intracellular anion elicited a distinct macroscopic response at hyperpolarizing potentials and in acidic luminal-side solutions. Figure 4.4B shows the pH dependence for all three anions, fitted using a phenomenological model with flexible parameters as described previously. Nitrate and iodide currents exhibited right-shifted pH dependence relative to chloride currents, similar to mammalian transporters [23]. To analyze DVGLUT pore properties, stationary noise analysis of macroscopic currents was used. Variance–mean relationships were generated for each cytosolic anion, and bootstrap distributions were obtained for the extracted unitary current amplitudes (Figure 4.4C). No statistical differences were found in the amplitude of the unitary current between chloride, nitrate, and iodide. In addition, the unitary current amplitude of DVGLUT was approximately one quarter that of rVGLUT1, indicating distinct unitary properties between fly and mammalian transporters.

4.1.4. DVGLUT functions as an apparent glutamate/proton exchanger

The canonical function of VGLUTs is to transport glutamate from the neuronal cytosol into the lumen of synaptic vesicles. This process is driven by luminal acidification and activated by luminal chloride. To study the glutamate transport function of DVGLUT, whole-cell recordings were performed using cytosolic glutamate solutions devoid of other permeable anions. Figure 4.5A depicts macroscopic currents from DVGLUT-expressing cells dialyzed with glutamate at pH 8.0 and perfused with luminal-side solutions at pH 5.5 (top) or pH 5.0 (bottom), containing either 4 mM (left) or 40 mM (right) chloride. The shown current traces were elicited by voltage steps ranging from −160 mV to 80 mV, applied from a holding potential of −50 mV. Recordings were background-subtracted using currents measured in luminal-side solutions at pH 7.5 with the same chloride concentration in each case. Thus, each chloride concentration tested represents a distinct dataset of DVGLUT-expressing cells. Negative membrane potentials elicited robust glutamate

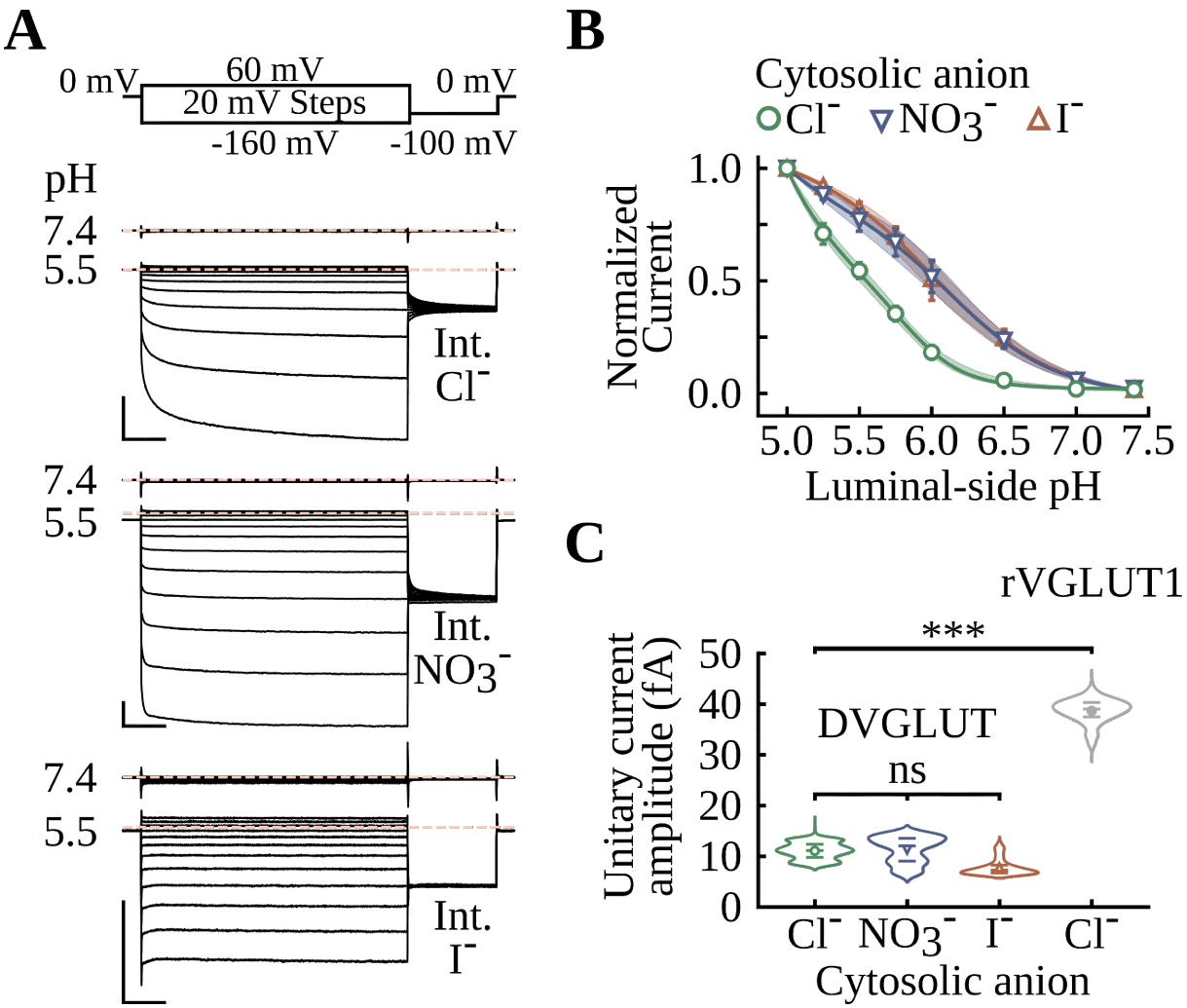

Figure 4.4. DVGLUT conducts smaller unitary currents than rVGLUT1, independent of cytosolic anion. **A**: Representative currents from cells dialyzed with Cl^-, NO_3^-, or I^-, recorded in luminal-side solutions at pH 5.5 and 7.4. Currents were elicited by voltage steps from −160 mV to 60 mV, applied from a holding potential of 0 mV. Scale bars: 1 nA, 25 ms. Dashed lines indicate the 0 nA current level. **B**: Titration curves of steady-state currents and their phenomenological fits at luminal-side pH 5.0–7.4 for cytosolic Cl^- (open circles), NO_3^- (open downward triangles), and I^- (open upward triangles). The plots show the mean and 95% confidence intervals obtained from bootstrap distributions (20 000 iterations). Currents were resampled with replacement, and the model was fitted to the average current values after each iteration. Number of cells per internal anion: Cl^- = 24, NO_3^- = 20, I^- = 13. **C**: Bootstrap distributions (10 000 iterations) of unitary current amplitudes. Unitary currents were estimated from variance–mean current relationships (see Materials and Methods) after resampling with replacement in each iteration. Number of cells per internal anion: Cl^- = 20, NO_3^- = 16, I^- = 9. Within each violin plot, horizontal lines denote the median and span the 95% confidence interval, while the central square marks the mean of the distribution. Two-tailed nonparametric bootstrap tests were used for statistical comparisons. Significance levels: $p < 0.05$ (*), $p < 0.01$ (**), $p < 0.001$ (***), not significant (n.s.).

currents that scaled with luminal-side acidification, whereas outward current amplitudes scaled with both luminal acidification and chloride concentration (Figure 4.5B).

A transporter mediating the translocation of chemical species reaches thermodynamic equilibrium when the electrochemical potentials of all transported substrates sum to zero (see Materials and Methods)[23, 61–63]. For an electrogenic carrier, this equilibrium is reflected by the voltage at which the transmembrane current reaches zero and thus depends on the concentrations and transport stoichiometry of the charged species. The effects of luminal-side acidification at different chloride concentrations on DVGLUT substrate translocation were characterized by estimating reversal potentials, as shown in Figure 4.5C. At constant cytosolic pH, luminal-side acidification from pH 5.5 to pH 5.0 had no significant effect on the reversal potential at 4 mM luminal-side chloride ($p > 0.05$), whereas it produced a mild negative shift at 40 mM chloride ($p < 0.05$). In contrast, a tenfold increase in luminal-side chloride produced a strong negative shift in reversal potential of roughly 90 mV at both luminal-side pH 5.5 and 5.0 ($p < 0.001$). Notably, at luminal-side pH 5.5 and 40 mM chloride, the reversal potential measured in DVGLUT-expressing cells dialyzed with 140 mM glutamate at pH 8.0 was more negative than the predicted value for rVGLUT1 under the same ionic conditions[23]. This observation is consistent with the higher outward chloride conductance of the insect transporter, thereby shifting the reversal potential to more negative values compared with mammalian transporters.

VGLUTs function as electrogenic glutamate/proton exchangers whose reversal potential (E_{rev}) is defined by the weighted sum of the Nernst potentials of glutamate (E_{Glu^-}) and protons (E_{H^+})[23]:

$$E_{rev} = \frac{n}{n+m} E_{Glu^-} + \frac{m}{n+m} E_{H^+}$$

where n and m denote the number of glutamate and proton species translocated per transport cycle, respectively. For VGLUTs, $n = m$, corresponding to a strict 1:1 coupling ratio. To identify whether DVGLUT also transports glutamate by stoichiometric coupling with protons, reversal potentials were measured as a function of cytosolic pH under a constant luminal-side pH, using square voltage pulses[23]. Given the prominent outward chloride conductance and apparent high luminal chloride affinity of DVGLUT, luminal-side chloride was maintained at 4 mM in all solutions to minimize the influence of chloride influx on the reversal potential analysis using cytosolic glutamate (Figure 4.5C).

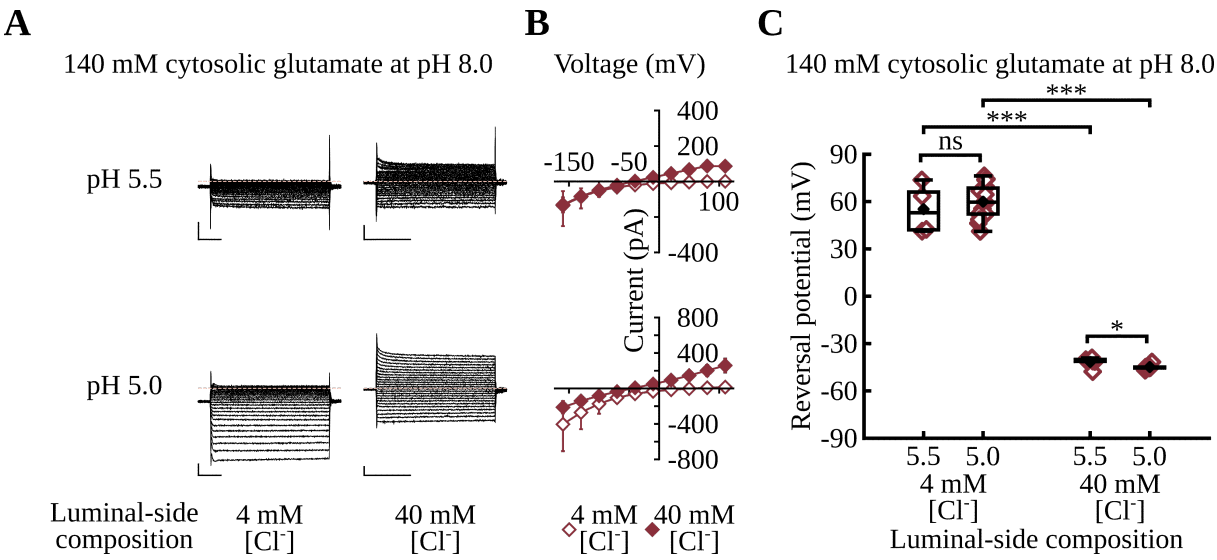

Figure 4.5. Higher outward chloride conductance in DVGLUT shifts glutamate transport reversal potential to more negative values than rVGLUT1. A: Representative currents from cells expressing DVGLUT dialyzed with 140 mM glutamate at pH 8.0, recorded in luminal-side solutions at pH 5.5 (top) and pH 5.0 (bottom) containing 4 mM (left) or 40 mM (right) chloride. Recordings were background-subtracted using currents obtained at pH 7.5. Current traces were elicited by voltage steps from −160 mV to 80 mV from a holding potential of −50 mV. Scale bars: 100 pA, 10 ms. Dashed lines indicate the 0 pA current level. **B**: I–V relationships from ensembles of cells measured under the same ionic conditions as in panel A (top: luminal-side pH 5.5; bottom: luminal-side pH 5.0). Data points represent the mean and 95% confidence intervals obtained from bootstrap distributions (10 000 iterations). Number of cells per condition: 4 mM chloride, pH 5.0 = 15 and pH 5.5 = 15; 40 mM chloride, pH 5.5 = 9 and pH 5.0 = 6. **C**: Reversal potential values estimated from cells in panel B. Number of cells per condition: 4 mM chloride, pH 5.5 = 4 and pH 5.0 = 14; 40 mM chloride, pH 5.5 = 6 and pH 5.0 = 6. Within each box plot, horizontal lines denote the median and span the 95% confidence interval, and the filled symbol marks the mean of the distribution. Two-tailed nonparametric bootstrap tests were used for statistical comparisons. Significance levels: $p < 0.05$ (*), $p < 0.01$ (**), $p < 0.001$ (***), not significant (n.s.).

Figure 4.6A depicts representative recordings from DVGLUT-expressing cells dialyzed with 140 mM glutamate at pH 6.0 or pH 8.5 and exposed to luminal-side 4 mM chloride solutions at pH 5.0. Currents were background-subtracted using recordings obtained at luminal-side pH 7.5. Background-subtracted I–V relationships depict robust luminal-side pH-dependent shifts in glutamate current amplitudes at negative membrane potentials, regardless of the cytosolic pH (Figure 4.6B). Reversal potentials were monitored as a function of E_{H^+} while maintaining a fixed transmembrane glutamate gradient at luminal-side pH 5.0 (Figure 4.6C). These data were fitted with a linear model, yielding a slope of 0.49 ± 0.05, reflecting a coupling ratio consistent with a 1:1 stoichiometric glutamate/H^+ exchange. This suggests that glutamate accumulation within synaptic

vesicles relies on an evolutionarily conserved proton-coupled antiport mechanism, shared by insect and mammalian VGLUTs that exhibit divergent luminal chloride dependencies.

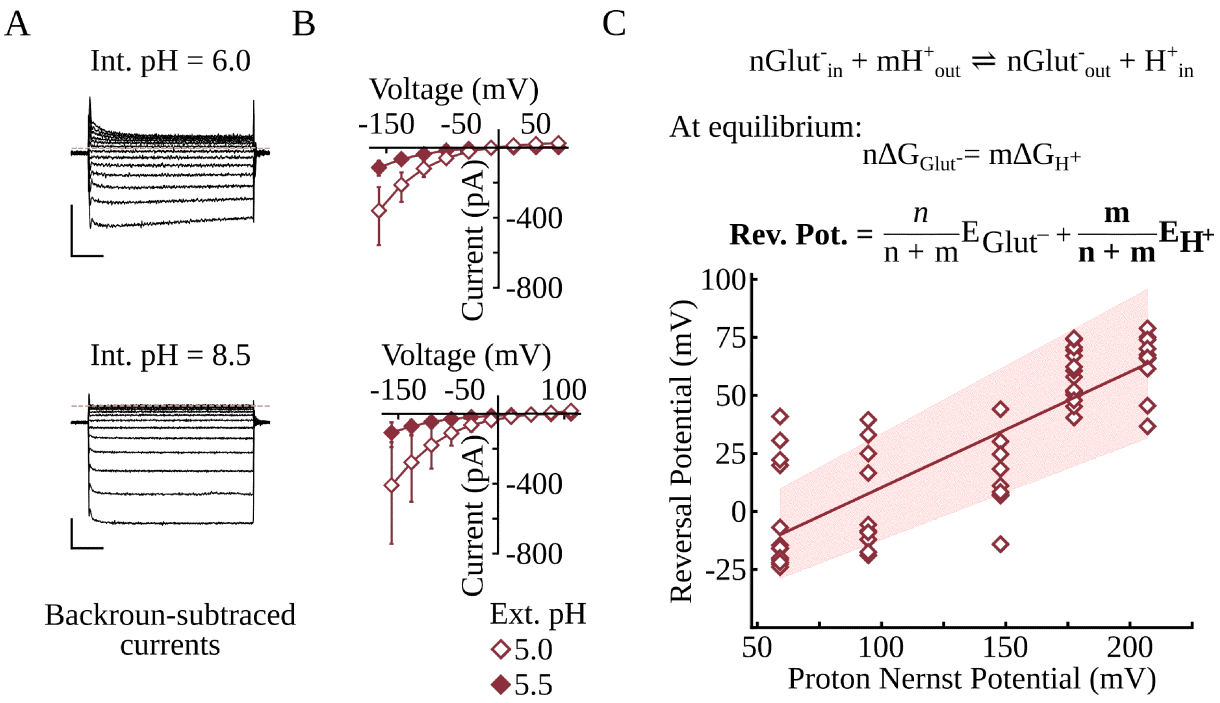

Figure 4.6. DVGLUT couples glutamate transport to proton exchange on a 1:1 stoichiometry. **A**: Representative currents from cells dialyzed with 140 mM glutamate at pH 6.0 or 8.5, recorded in luminal-side solutions at pH 5.0 containing 4 mM Cl^-, and background-subtracted using traces acquired at luminal-side pH 7.5. Currents were elicited by voltage steps ranging from −160 mV to 100 mV, from a holding potential of −50 mV. Scale bars: 250 pA, 10 ms. Dashed lines indicate the 0 pA current level. **B**: Mean and 95% confidence intervals of bootstrap distributions (10 000 iterations) of steady-state I–V currents, recorded under conditions of 4 mM luminal-side Cl^- at pH 5.0 or 5.5, and 140 mM cytosolic glutamate at pH 6.0 (14 cells) or pH 8.0 (11 cells). **C**: Reversal potentials were measured at fixed luminal-side pH 5.0 and plotted against E_{H^+}. Data represent the mean and 95% confidence intervals of bootstrap distributions (10 000 iterations) of fitted slopes. Number of cells per cytosolic pH: 6.0 = 13, 6.6 = 11, 7.5 = 9, 8.0 = 14, 8.5 = 10.

4.2. Discussion and conclusions

The present results characterize the dual transport and channel activities of DVGLUT. Negative membrane potential steps elicit chloride currents through the DVGLUT channel (Figure 4.1), with faster activation kinetics than those of mammalian equivalents (Figure 4.2A). Although both insect and mammalian transporters exhibit inwardly rectifying I–V relationships, the DVGLUT channel sustains detectable proton-dependent

current amplitudes even at positive membrane potentials (Figures 4.1 and 4.2).

The pH dependence of steady-state chloride currents through the DVGLUT channel exhibits non-saturating responses, with right-shifted activation profiles for nitrate and iodide (Figure 4.4B), consistent with previous observations in rVGLUT1 [23]. Unitary current amplitudes remain invariant across cytosolic anions and are approximately one quarter of those measured for rVGLUT1 (Figure 4.4C). Notably, DVGLUT displays a higher apparent affinity for luminal chloride than mammalian equivalents, while remaining susceptible to neutralization of the canonical luminal chloride-binding site (Figure 4.3C). Together, these results reveal conserved features of channel activation between insect and mammalian VGLUTs, yet highlight marked differences in gating kinetics and pore conduction that likely reflect divergent electrostatic landscapes between the channel architectures.

DVGLUT substrate transport experiments performed near equilibrium reveal glutamate translocation coupled to apparent proton exchange at a 1:1 stoichiometry (Figure 4.6). As with all measurements involving reversal potential estimation, the derived voltage reflects the weighted contributions of permeating or translocated ionic species. In the absence of parallel conductances, a 1:1 glutamate/proton exchange process would be expected to yield a reversal potential more positive than that observed for DVGLUT under the tested experimental conditions. However, DVGLUT exhibits a pronounced outward chloride conductance, stoichiometrically uncoupled from the putative glutamate/proton transport cycle and dependent on luminal-side proton and chloride concentrations (Figure 4.5). Chloride efflux through VGLUTs is proposed to further depolarize the vesicular $\Delta\Psi$, thereby enhancing the driving force and enabling electroneutral and isosmotic glutamate accumulation in synaptic vesicles [18, 20, 22, 23]. The increased outward conductance of DVGLUTs compared with mammalian transporters may represent a physiological consequence of higher resting cytosolic chloride concentration [86].

In summary, this work establishes the dual function of DVGLUT as an anion channel and a coupled glutamate/proton transporter. These findings underscore both conserved and divergent mechanisms involved in synaptic vesicle filling across species. Comparative analysis of its molecular determinants may refine models of vesicular loading by revealing how anion conductance and stoichiometric coupling shape excitatory neurotransmission.

Chapter 5:
Functional analysis of a deafness-related mutation in mVGLUT3

5.1. Results

VGLUT3 is expressed in the IHC of the auditory system. The p.A211V mutation in the human *SLC17A8* gene, which encodes VGLUT3, causes dominant progressive deafness (DFNA25) [50, 51]. Knock-in of the equivalent mutation, p.A224V, results in progressive hearing loss in mice [88]. The functional consequences of the A224V substitution in mVGLUT3 were evaluated using heterologous expression and patch-clamp recordings.

5.1.1. A224V mutation alters mVGLUT3 ion channel gating

To assess the effect of the A224V mutation on mVGLUT3 channel currents, recordings were performed in cells dialyzed with chloride at neutral pH and exposed to luminal-side solutions containing 144 mM chloride at pH values ranging from 5.0 to 8.2. Figure 5.1A shows representative currents recorded in response to voltage steps from −160 mV to 80 mV at different luminal-side pH values. Negative membrane potentials elicit mVGLUT3 proton-activated chloride currents with kinetics similar to those of other VGLUTs. In contrast, A224V inward currents display an activation time course characterized by an instantaneous peak that relaxes to a steady state at pH 5.0. A224V also exhibits prominent outward current amplitudes at positive membrane potentials. These gating alterations result in linearized I–V relationships for the mutant transporter (Figure 5.1B, top).

Figure 5.1B (bottom) illustrates late channel current responses obtained during stepwise pH titration of the luminal-side solutions. As previously described in the rVGLUT1 and DVGLUT studies, the curvature and baseline activity of the proton-dependent, steady-state current profiles were analyzed using phenomenological modeling with adjustable parameters and bootstrap resampling. The A224V mVGLUT3 mutant exhibits current amplitudes above background levels at neutral pH values, whereas currents measured at acidic pH values show saturating behavior. This results in a rightward shift of the proton-dependent titration curve constructed from steady-state current responses elicited at −160 mV relative to WT mVGLUT3 (open symbols). In contrast, current

responses from the mutant transporter measured at 80 mV (filled symbols) closely resemble those of WT mVGLUT3 at hyperpolarizing potentials. The A224V mutation markedly alters the voltage and proton dependence of mVGLUT3 anion channel function.

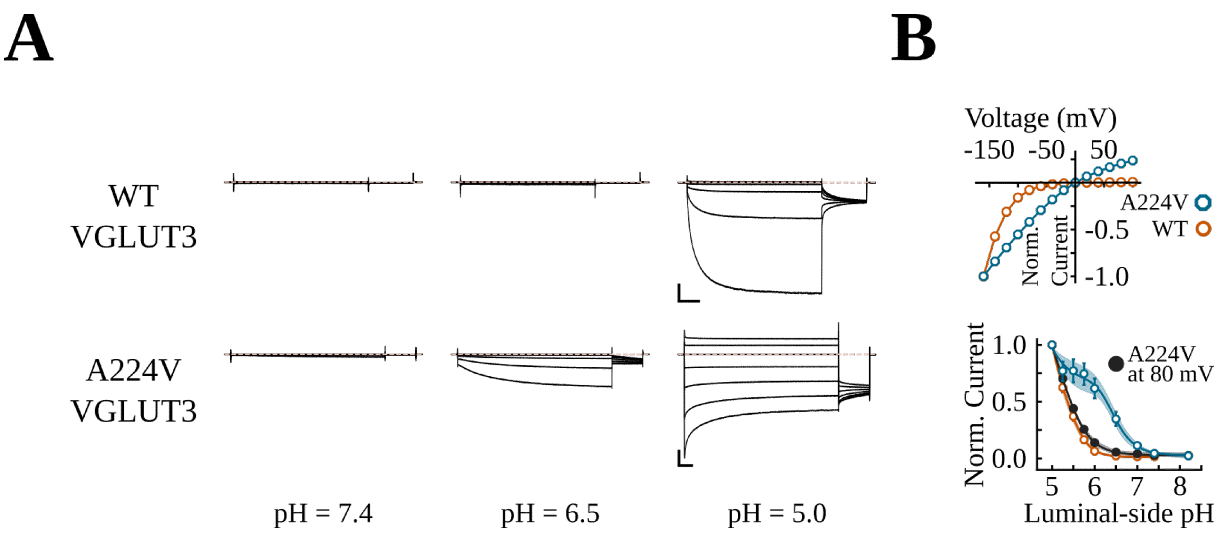

Figure 5.1. A224V alters the voltage and pH dependence of mVGLUT3 chloride currents. A: Representative recordings of whole-cell Cl^- currents from cells expressing WT or A224V mVGLUT3, elicited at −160 mV, −120 mV, −80 mV, −40 mV, 0, 40 mV, and 80 mV in luminal-side solutions containing 144 mM chloride at pH 7.4, 6.5, or 5.0. Scale bars represent 1 nA and 25 ms. The dashed line indicates the zero-current level. **B (top):** Normalized I–V relationships showing the mean and 95% confidence intervals of late currents derived from bootstrap distributions (5 000 iterations) for WT and A224V mVGLUT3 at luminal-side pH 5.0. **B (bottom):** Late currents elicited at −160 mV (open symbols) or 80 mV (filled symbols) across luminal-side solutions with pH values from 5.0 to 8.2, with their phenomenological fits. The plots show the mean and 95% confidence intervals obtained from bootstrap distributions (10 000 iterations). Currents were resampled with replacement, and the model was fitted to the average current values after each iteration. Number of cells analyzed per construct: WT mVGLUT3 = 17; A224V mVGLUT3 = 18.

Stationary noise analysis of whole-cell currents did not reveal a significant difference in unitary current amplitude (WT: 27 ± 3 fA; A224V: 23 ± 8 fA; $p = 0.51$; 13 and 14 cells, respectively). Thus, A224V alters channel gating but not pore conduction properties.

To further characterize the effects of luminal-side acidification on channel activity, currents were elicited by sequential voltage pulses during solution exchanges. Figure 5.2A shows representative currents from a cell expressing A224V mVGLUT3. A voltage sweep consisting of an activating −160 mV step followed by a 100 mV step was applied at two-second intervals. Open symbols indicate the steady-state current at the end of the

hyperpolarizing pulse; filled symbols denote the current elicited during the depolarizing step. At negative membrane potentials, a shift from luminal-side pH 8.2 to pH 5.5 activates chloride conductance, marked by an instantaneous current peak that relaxes to a steady state (inset). With continued voltage sweeps at acidic pH, the amplitude of the inward steady-state current declines (arrow in inset), whereas the persistent outward current of the mutant transporter remains largely unchanged within experimental resolution. Returning to an alkaline luminal-side pH closes the channels, and both inward and outward currents revert to baseline. Approximately 25 s later, a second exchange to pH 5.5 partially restores the inward current, which again decays with a similar time course. Figure 5.2B shows a quantification of this process for both A224V and WT mVGLUT3. Open octagons show normalized inward current decay at -160 mV for the first acidification step in the mutant transporter (same cell shown in Figure 5.2A). This decay was modeled as a single-exponential process with a τ of 20 ms. This corresponds to the fastest current decay observed across all tested luminal-side pH conditions. For comparison, small blue-edged open markers represent a step to pH 5.0, which exhibited an approximately linear decay over the recorded period, with a τ exceeding 400 s. This slow decay closely matches the response of WT mVGLUT3 to a step to pH 5.5 (open orange-edged symbols). These dynamics suggest that the channel current decay upon luminal-side acidification in the A224V mutant transporter occurs on a timescale similar to glutamate vesicular filling [87].

5.2. Discussion and conclusions

The single-point mutation A211V in human mVGLUT3 segregates with a progressive, high-frequency, nonsyndromic deafness phenotype identified in two families [50, 51]. In rodent models, this variant causes a marked reduction in VGLUT3 expression across brain regions, BON cells, and hippocampal neurons [55]. However, the mutation does not alter evoked synaptic transmission, including glutamate release, vesicle pool size, or release probability. Functional effects are limited to spontaneous release activity, manifesting as a mild reduction in mEPSC amplitude and a more pronounced reduction in mEPSC frequency. These effects have been attributed to an uneven distribution of mVGLUT3 within synaptic vesicle membranes [55]. The model proposes that synaptic vesicles exhibit heterogeneous VGLUT3 content, with individual vesicles containing normal, reduced, or undetectable transporter levels. This uneven distribution reduces the fraction of release-competent vesicles (lower mEPSC frequency), whereas vesicles with reduced

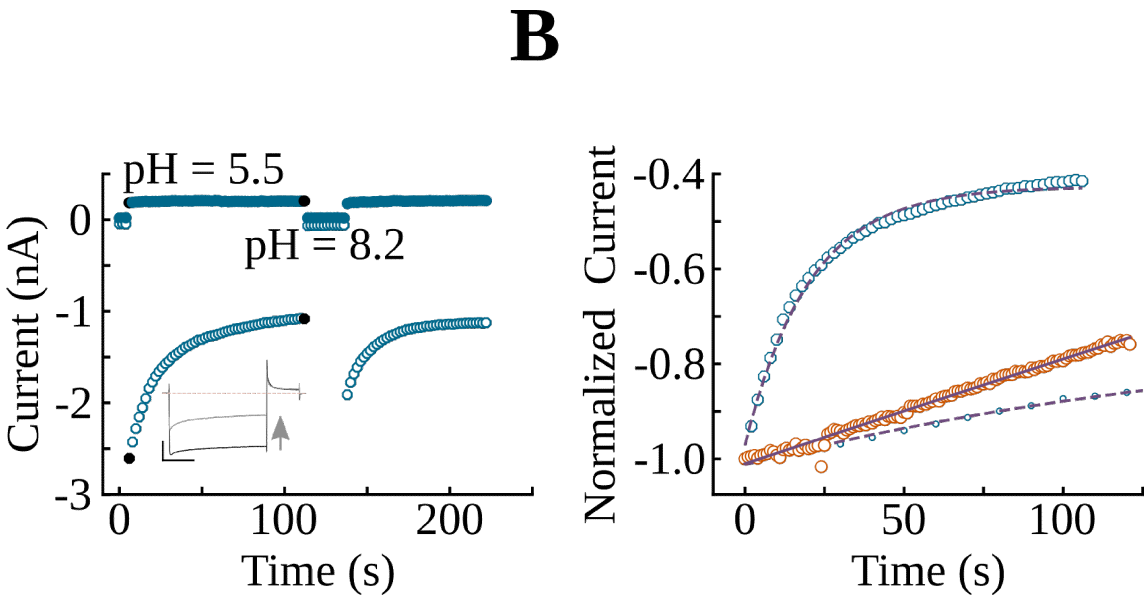

Figure 5.2. Exponential decay of A224V chloride currents upon luminal-side acidification. **A:** Representative recording from a cell expressing A224V mVGLUT3. The plot shows Cl^- current decay at luminal-side pH 5.5 during consecutive voltage sweeps. Open markers represent the late inward current recorded at −160 mV, and filled markers represent the outward current recorded at 100 mV. Current traces in the inset correspond to the black symbols indicating the onset and offset of the first acidification step. Scale bars represent 1 nA and 25 ms. The dashed line indicates the zero-current level. **B:** Normalized inward currents elicited by consecutive sweeps to −160 mV upon luminal-side acidification. Open octagons and small open circles represent currents recorded from A224V mVGLUT3 at pH 5.5 and pH 5, respectively. Open orange-edged circles represent currents from WT mVGLUT3 at pH 5.5. Purple dashed lines represent the monoexponential fits.

VGLUT3 content release proportionally less glutamate (smaller mEPSC amplitude). Thus, evoked release remains unaffected, whereas spontaneous release is selectively diminished.

The homozygous p.A224V mutation in mice selectively alters the structure and function of IHCs, which transduce sound-evoked mechanical stimuli into glutamate release. These changes include disruption of the stereocilia ultrastructure and an increase in the sustained releasable pool (SRP) of synaptic vesicles, despite unchanged calcium influx[88]. The deafness-associated mutation may exert its deleterious effects by impairing intracellular trafficking and synaptic signaling dynamics within IHCs.

Although the reported effects suggest alterations to trafficking or synaptic signaling, they do not establish whether the p.A211V mutation directly modifies VGLUT3 function. This study presents an analysis of the effects of the A211V mutation on VGLUT3 channel function, based on the orthologous A224V mVGLUT3 protein. Acidification of luminal-side

solutions induces voltage-dependent alterations in the steady-state response and the kinetics of chloride channel activation. Hyperpolarization-evoked currents exhibited time-dependent deactivation, whereas prominent outward current amplitudes persisted at positive membrane potentials. Concomitant with these gating changes, proton-dependent titration curves shifted to the right for the mutant transporter relative to WT mVGLUT3.

In the outward-facing cryo-EM structure of rat VGLUT2, A206—equivalent to A224 in mVGLUT3—is located within a cytosolic loop between TM4 and TM5, oriented toward the N-terminal H199 residue that, alongside H434, defines the putative gate of VGLUT channels (Figure 3.1). This alanine is part of a KWAPPLER sequence conserved among VGLUT variants. Whatever mechanism underlies the effects of A224V on mVGLUT3 turnover at synaptic terminals [51, 88], replacement of alanine with the bulkier valine causes prominent functional changes, as demonstrated here. These biophysical alterations warrant further investigation to elucidate their contribution to the pathophysiological phenotype.

Part II

Voltage-gated calcium channels

Chapter 6:
Background and experimental focus

6.1. Cellular mechanisms of calcium homeostasis

Precise spatiotemporal control of cytosolic Ca^{2+} signals is essential for cell viability and function. Increases in cytosolic Ca^{2+} concentration trigger several cellular events, including fertilization, proliferation, development, neurotransmission, contraction, and secretion [89–91]. The ubiquitous role of Ca^{2+} in cellular function is attributed to its physicochemical properties. A flexible coordination stereochemistry—typically eightfold—along with variable bond lengths and angles enables it to accommodate binding sites of irregular geometry found in complex cellular molecules. The binding affinity, specificity, and interaction versatility of Ca^{2+}, together with the adoption of phosphate-based compounds as the cellular energy currency, have established the evolutionary requirement to maintain low cytosolic Ca^{2+} concentrations [89, 90].

The resting cytosolic Ca^{2+} concentration is approximately 100 nM, whereas the extracellular concentration is about 2 mM. This difference generates a driving force that strongly favors Ca^{2+} influx [91]. The shape of the cytosolic calcium signal reflects the dynamic interplay between systems that deliver or extrude Ca^{2+} and intracellular components that transiently bind, sequester, or relay it to downstream molecular targets. The extrusion machinery comprises plasma membrane and organellar pumps and transporters, while buffering is mediated primarily by cytosolic proteins [89–91]. Calcium entry occurs by facilitated diffusion through specific and tightly regulated channels. Calcium channels are broadly categorized as receptor-operated, store-operated, and voltage-gated (Ca_V) channels [89]. Ca_V channels constitute the principal focus of this study.

6.2. Core subunits of Ca_V channels

Ca_V channels are transmembrane proteins that convert changes in membrane potential into calcium influx. They belong to a superfamily of voltage-gated ion channels that includes Na^+ and K^+ channels [92]. Ca_V channels form complexes made up of several distinct subunits encoded by separate genes: α_1, α_2, β, γ, and δ [89, 92–95]. The α_1 and β subunits

constitute the core components of the macromolecular Ca_V channel complex [108].

6.2.1. Pore-forming $Ca_V\alpha_1$ subunit

The ion-conducting subunit, α_1, is a single-chain polypeptide of roughly 190 kDa. It contains four internally homologous domains (I–IV), each with six transmembrane segments (S1–S6), which together form a pseudo-tetrameric structure resembling K^+ channels. Within each repeat, the first four transmembrane segments (S1–S4) form the voltage-sensing domain (VSD), with the S4 segment acting as the principal voltage sensor. The S5–S6 segments, along with the extracellular loop between them, form the pore-lining region, including the ion selectivity filter. The well-established binding site for the auxiliary β subunit is located in the intracellular loop between domain repeats I and II, and is termed the α_1 interacting domain (AID) (Figure 6.1) [95, 96]. The AID consists of a conserved consensus motif of 18 amino acids (QQxExxLxGYxxWIxxxE) [92–95].

The main criteria used to classify Ca_V channels are defined by properties of the α_1 subunit, encompassing sequence similarity, biophysical characteristics, pharmacological sensitivity, and expression profile [92–95]. The modern molecular classification, derived from α_1 subunit sequence homology, distinguishes three major subfamilies: $Ca_V1.x$ ($Ca_V1.1$–$Ca_V1.4$), $Ca_V2.x$ ($Ca_V2.1$–$Ca_V2.3$), and $Ca_V3.x$ ($Ca_V3.1$–$Ca_V3.3$) [109]. According to their voltage-dependent gating, $Ca_V1.x$ and $Ca_V2.x$ are high-voltage-activated (HVA) channels, whereas $Ca_V3.x$ are low-voltage-activated (LVA) channels and open near the resting membrane potential. Further classification—based on biophysical and pharmacological characteristics and expression profiles—identifies L-, N-, P/Q-, and R-type channels within the HVA group, and T-type channels within the LVA group. These subtypes differ markedly in gating behavior, drug sensitivity, and cellular localization. L-type ($Ca_V1.x$) channels activate and inactivate slowly, conduct a long-lasting current, and are widely expressed in excitable tissues, mediating processes such as excitation–contraction coupling in muscle, excitation–secretion coupling in endocrine cells, and postsynaptic plasticity and excitability in neurons. They are selectively blocked by dihydropyridines. N-type ($Ca_V2.2$) channels carry fast-inactivating currents and are predominantly expressed at presynaptic terminals in both the CNS and PNS, where they mediate neurotransmitter release. They are selectively blocked by ω-Conotoxin GVIA. P/Q-type ($Ca_V2.1$) channels are mainly presynaptic, mediating fast neurotransmitter release in the CNS, particularly in

Purkinje neurons. They are selectively blocked by ω-Agatoxin IVA. R-type ($Ca_V2.3$) channel currents persist after pharmacological blockade of other HVA channels. These channels are broadly expressed in presynaptic and somatodendritic compartments throughout the CNS. Finally, T-type (LVA; $Ca_V3.x$) channels are fast-inactivating and mediate transient calcium influx, shaping postsynaptic excitability and rhythmic firing in neurons.

6.2.2. Modulatory $Ca_V\beta$ subunit

$Ca_V\beta$ is a soluble protein of 55–72 kDa that binds tightly to the intracellular AID sequence of the pore-forming subunit [95, 96, 100]. Four genes encode four isoforms (β_1–β_4), each with multiple splice variants. The protein contains two highly conserved domains: the Src homology 3 (SH3) domain and the guanylate kinase (GK) domain, each structurally related to members of the membrane-associated guanylate kinase (MAGUK) protein family. This family serves as a molecular scaffold linking signaling complexes to the cytoskeleton at the plasma membrane [97]. In particular, the SH3 domain features a conserved hydrophobic surface that binds PxxP sequences in target proteins. $Ca_V\beta$ interacts with the AID region of the α_1 subunit through a hydrophobic groove in the GK domain known as the AID-binding pocket (Figure 6.1). $Ca_V\beta$ enhances current density by promoting the trafficking of the α_1 subunit to the plasma membrane, prolonging its surface lifetime, and increasing the probability of channel opening. As a result, $Ca_V\beta$ accelerates the kinetics of channel opening and shifts the voltage dependence of activation toward more negative potentials. $Ca_V\beta$ also interacts with additional molecular partners, some of which may further regulate calcium channel function [96, 100]. The β subunit is therefore essential in establishing physiological current density through HVA calcium channels at the plasma membrane.

6.2.3. Actin interactions with Ca_V channels

$Ca_V\beta$ interacts with several intracellular proteins, including filamentous actin (F-actin) [101]. In co-sedimentation assays, both the SH3 and GK domains of $Ca_V\beta_2$ bind actin independently. Super-resolution microscopy further shows that $Ca_V\beta_2$ spatially overlaps with actin filaments throughout HeLa cells and HL-1 cardiomyocytes. Moreover, treatment with cytochalasin D—an inhibitor of actin polymerization—attenuates the increase in

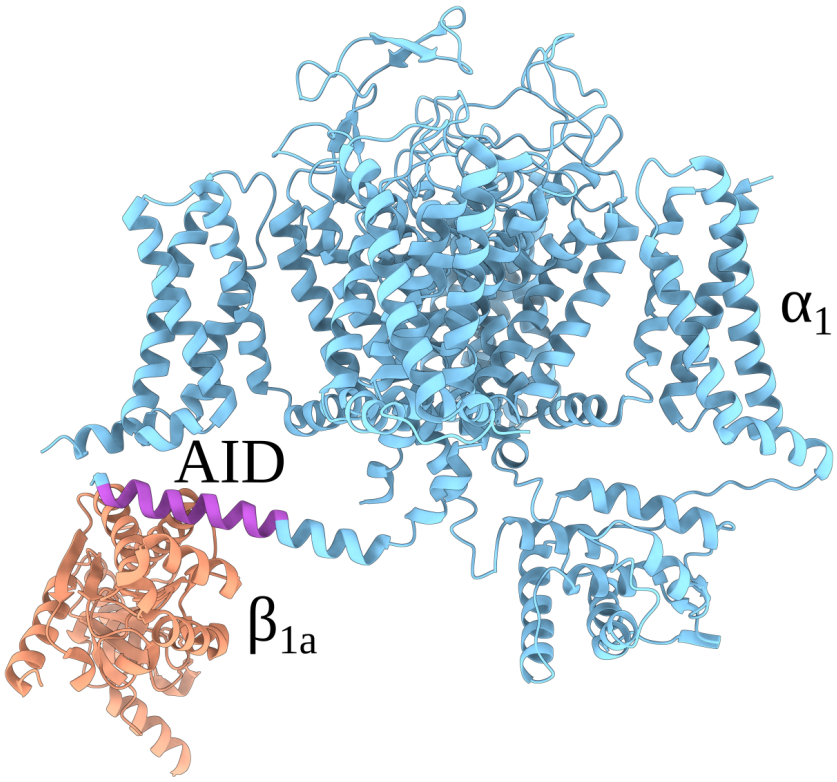

Figure 6.1. Core complex of Ca_V channels. The cryo-EM structure of rabbit $Ca_V1.1$ is shown in complex with its auxiliary β_{1a} subunit (PDB ID: 5GJV) [98]. The overall architecture is displayed in a membrane-parallel view. Highlighted are the pore-forming α_1 subunit (blue), the modulatory β_{1a} subunit (red), and the α_1–β interaction interface, including the alpha-interacting domain (AID; purple), located within the intracellular loop between domains I and II.

calcium current density induced by $Ca_V\beta_2$ overexpression in HL-1 cardiomyocytes.

Analysis of $Ca_V1.2$ channel trafficking kinetics in HL-1 cells revealed a role for actin in channel recycling [102]. Live-cell imaging of calcium channels tagged with an HA epitope and labeled with fluorescent anti-HA antibodies indicated a cell surface lifetime of approximately 7.5 minutes. Internalization of these channels occurs via clathrin-mediated endocytosis and is primarily directed to recycling endosomes. Notably, this trafficking route requires functional actin; disruption of the actin cytoskeleton reroutes the channels from recycling endosomes to lysosomes. These findings highlight an essential role for actin-mediated endocytic recycling in maintaining calcium channel surface expression.

The role of $Ca_V\beta_2$ in regulating the trafficking of $Ca_V1.2$ channels was investigated using dual-color microscopy and single-particle tracking in HEK293T cells [104]. Enhanced $Ca_V\beta$–$Ca_V\alpha_{1.2}$ association increases the residence time of calcium channels at the plasma

membrane. Trajectory analysis shows that both channel subunits move with identical mean speeds for the fastest anterograde transport component, whereas retrograde transport of $Ca_V\alpha_{1.2}$ is slower and independent of $Ca_V\beta$ dynamics. Thus, $Ca_V\beta$ promotes fast anterograde transport and regulates endocytic turnover of $Ca_V1.2$ channels.

$Ca_V\beta_4$ is the most abundant isoform in the cerebellum, and variants of the *CACNB4* gene encoding it are linked to certain forms of epilepsy [110, 111]. Biochemical and electrophysiological work further characterized the interactions of α_1 and β_4 with actin [103]. The $Ca_V\beta_4$ SH3–GK core sediments with actin, as observed for $Ca_V\beta_2$ [101]. Moreover, $Ca_V\beta$ can simultaneously interact with $Ca_V\alpha_1$ and F-actin *in vitro*. Differential analysis of mEPSCs in hippocampal neurons transfected with $Ca_V\beta_4$ and treated with cytochalasin D, together with estimates of the readily releasable pool (RRP), indicates that F-actin upregulates spontaneous and depolarization-evoked neurotransmitter release in a $Ca_V\beta_4$-dependent manner. These observations suggest that actin interactions with $Ca_V\beta_4$ help maintain vesicle availability and contribute to the fine-tuning of synaptic activity.

6.2.4. Rationale and experimental framework

As outlined above, mounting evidence indicates that $Ca_V\beta$–F-actin interactions play a major role in regulating calcium channel expression and turnover and in synaptic vesicle mobilization. However, the molecular determinants governing this association and its mechanistic contribution to Ca_V channel trafficking remain poorly understood. In particular, no structural model exists to explain how $Ca_V\beta$ subunits engage actin to control calcium channel stability and clearance.

An integrative study was conducted to address this gap. The investigation identified the protein–protein interaction interface between $Ca_V\beta$ and actin and examined its functional relevance to channel turnover. This multidisciplinary approach combined cross-linking mass spectrometry, computational modeling, mutagenesis, and electrophysiology, which together established a mechanistic framework linking the $Ca_V\beta$–actin interaction to endocytic recycling and the maintenance of a functional pool of Ca_V channels. The present thesis forms part of this collaborative work and investigates the effects of actin-association–deficient $Ca_V\beta$ mutants on Ca_V channel surface expression and function.

The findings were published in the peer-reviewed study:

Castilla, F.[†], **Lugo, V.[†]**, Miranda-Laferte, E., Jordan, N., Huesgen, P. F., Santiago-Schübel, B., Alfonso-Prieto, M., and Hidalgo, P. 2025. **Mapping the interaction surface between $Ca_V\beta$ and actin and its role in calcium channel clearance.** *Nat. Commun.* 16, 4352: 1–21. *doi:10.1038/s41467-025-59548-x*

The specific contribution is detailed as:

—Shared first authorship[†]: Designed and conducted all whole-cell patch-clamp experiments to investigate the effects of two actin-association-deficient $Ca_V\beta$ subunits on Ca_V channel expression and function. Analyzed all resulting electrophysiological data and generated the corresponding figures.

The instrumentation employed is as described in Materials and Methods, and details regarding expression constructs, mutagenesis, cell culture handling, transfection procedures, electrophysiology protocols, and solution compositions are provided in the published manuscript. Two quantitative frameworks essential for assessing Ca_V channel voltage-dependent gating and surface expression are introduced below.

6.2.5. Voltage dependence of ion channel gating

Voltage-gated channels convert transmembrane voltage changes into ionic fluxes through conformational rearrangements that open or close the conduction pore [115, 116].

In a minimal two-state model of channel activation, a population of channels N undergoes a voltage-dependent transition between a non-conducting closed state and a conducting open state. Let $N = N_O + N_C$, where N_C and N_O denote the numbers of closed and open channels, respectively. The transitions between these states occur with voltage-dependent rate constants $k_{\text{open}}(V)$ and $k_{\text{close}}(V)$, as depicted schematically below:

$$N_C \underset{k_{\text{close}}(V)}{\overset{k_{\text{open}}(V)}{\rightleftharpoons}} N_O$$

At equilibrium, the ratio of open to closed channels defines the voltage-dependent equilibrium constant K, which is thermodynamically related to the free-energy difference

between the open and closed states by:

$$K(V) = \frac{N_O}{N_C} = e^{-\frac{\Delta G(V)}{RT}}$$

Here, $\Delta G(V)$ represents the voltage-dependent free-energy difference between the closed and open states, R is the universal gas constant, and T is the absolute temperature. The dependence of ΔG on the membrane potential V arises from the movement of charged elements within the channel and can be expressed as:

$$\Delta G(V) = \Delta G_0 - zFV$$

In this expression, ΔG_0 denotes the intrinsic free-energy difference between the closed and open states in the absence of an applied potential, z represents the effective charge displacement accompanying channel activation, and F is the Faraday constant.

Substituting $\Delta G(V)$ into the equilibrium expression yields:

$$K(V) = e^{-\frac{\Delta G_0 - zFV}{RT}}$$

At the potential $V_{1/2}$, the populations of open and closed channels are equal ($N_O = N_C$), and the equilibrium constant equals unity ($K(V_{1/2}) = 1$). Applying this condition to the previous expression gives:

$$1 = e^{-\frac{\Delta G_0 - zFV_{1/2}}{RT}}$$

Taking the natural logarithm of both sides leads to:

$$0 = -\frac{\Delta G_0 - zFV_{1/2}}{RT}$$

which simplifies to:

$$\Delta G_0 = zFV_{1/2}$$

Thus, the intrinsic free-energy difference at zero potential corresponds to the electrical work associated with charge displacement through the potential difference $V_{1/2}$. Substituting this result back into the general expression for $\Delta G(V)$ yields:

$$\Delta G(V) = zF(V_{1/2} - V)$$

The explicit voltage dependence of the equilibrium constant is given by:

$$K(V) = e^{\frac{zF(V-V_{1/2})}{RT}}$$

This expression indicates that the equilibrium between the open and closed states varies exponentially with the membrane potential, with a slope set by the effective charge z.

At steady state, the probability of channel opening, P_o, is given by the fraction of channels in the open state:

$$P_o(V) = \frac{N_O}{N_O + N_C}$$

Correspondingly, the probability of the channel being closed is $1 - P_o(V) = \frac{N_C}{N_O+N_C}$. The equilibrium constant reflects the balance between open and closed channels at steady state and can therefore be expressed as:

$$K(V) = \frac{N_O}{N_C} = \frac{P_o(V)}{1 - P_o(V)}$$

Substituting the explicit voltage dependence of $K(V)$ obtained above yields:

$$\frac{P_o(V)}{1 - P_o(V)} = e^{\frac{zF(V-V_{1/2})}{RT}}$$

Solving for $P_o(V)$ gives:

$$P_o(V) = \frac{1}{1 + e^{-\frac{zF(V-V_{1/2})}{RT}}}$$

which expresses the steady-state voltage dependence of channel opening in the two-state approximation. An analysis of the macroscopic current elicited by a voltage perturbation enables the estimation of the fraction of activated channels upon reaching a new equilibrium. Consequently, studying the voltage dependence of activation provides a means of assessing the relative stability of the open and closed states of channels. This framework provides a quantitative basis for assessing ion-channel function under different experimental conditions, ranging from pharmacological treatments to mutational effects.

6.2.6. Voltage sensing and gating currents

Voltage-gated channels sense changes in membrane potential through charged or dipolar elements located within their VSDs, whose displacements are driven by the membrane electric field [112, 113]. Because the movement of these charged particles is coupled to conformational transitions of the channel gate, they are termed gating charges. Gating charge displacements give rise to capacitive currents known as gating currents. For an idealized capacitor—such as a proteolipid membrane in solution—the capacitive charge Q is defined as $Q = CV$, where C is the membrane capacitance and V is the transmembrane voltage. The capacitive current I_c is the time derivative of the charge:

$$I_c = \frac{dQ}{dt} = C\frac{dV}{dt} + V\frac{dC}{dt}$$

The term $C\frac{dV}{dt}$ reflects the redistribution of mobile charge across the membrane as determined by the membrane capacitance. This separation depends linearly on voltage, as the surrounding solution acts as an effectively infinite reservoir of charge, with the magnitude constrained by C. In contrast, the term $V\frac{dC}{dt}$ captures an apparent change in capacitance resulting from the confined movement of gating charges within the membrane field. As gating charges approach their maximal displacement under strong depolarizing or hyperpolarizing conditions, their movement plateaus.

Experimentally, differences in the voltage dependence of mobile charge redistribution in solution and confined charge displacement within the membrane enable the isolation of gating currents. Capacitive currents recorded at voltages where gating charges are immobilized are subtracted from currents at voltages that elicit gating charge movement. This subtraction removes the linear components and isolates the net gating current. Integration of the gating current yields the total gating charge, representing the cumulative displacement of all gating charges. The total gating charge scales with the number of voltage-gated channels at the plasma membrane, including non-conducting channels that still contain functional voltage sensors. Thus, gating current measurements serve as a quantitative proxy for channel surface density and can be combined with ionic current measurements to assess the fraction of functionally active channels.

nature communications

Article

https://doi.org/10.1038/s41467-025-59548-x

Mapping the interaction surface between $Ca_V\beta$ and actin and its role in calcium channel clearance

Received: 30 January 2024

Accepted: 25 April 2025

Published online: 10 May 2025

Check for updates

Francisco Castilla[1,2,8,10], Victor Lugo[1,2,10], Erick Miranda-Laferte[1], Nadine Jordan[1], Pitter F. Huesgen[3,9], Beatrix Santiago-Schübel[3,4] ✉, Mercedes Alfonso-Prieto[5,6] ✉ & Patricia Hidalgo[1,7] ✉

Defective ion channel turnover and clearance of damaged proteins are associated with aging and neurodegeneration. The L-type $Ca_V1.2$ voltage-gated calcium channel mediates depolarization-induced calcium signals in heart and brain. Here, we determined the interaction surface between actin and two calcium channel subunits, $Ca_V\beta_2$ and $Ca_V\beta_4$, using cross-linking mass spectrometry and protein-protein docking, and uncovered a role in replenishing conduction-defective $Ca_V1.2$ channels. Computational and in vitro mutagenesis identified hotspots in $Ca_V\beta$ that decreased the affinity for actin but not for $Ca_V1.2$. When coexpressed with $Ca_V1.2$, none of the tested actin-association-deficient $Ca_V\beta$ mutants altered the single-channel properties or the total number of channels at the cell surface. However, coexpression with the $Ca_V\beta_2$ hotspot mutant downregulated current amplitudes, and with a concomitant reduction in the number of functionally available channels, indicating that current inhibition resulted from a build-up of conduction silent channels. Our findings established $Ca_V\beta_2$–actin interaction as a key player for clearing the plasma membrane of corrupted $Ca_V1.2$ proteins to ensure the maintenance of a functional pool of channels and proper calcium signal transduction. The $Ca_V\beta$–actin molecular model introduces a potentially druggable protein-protein interface to intervene Ca_V-mediated signaling processes.

Voltage-gated calcium (Ca_V) channels convert electrical signals into increased intracellular calcium concentrations in neuronal, heart muscle, and endocrine cells, thereby triggering a variety of physiological responses[1]. The functional core of the Ca_V complex is formed by the pore-forming subunit ($Ca_V\alpha_1$) and the β-subunit ($Ca_V\beta$). The latter regulates multiple calcium signaling pathways by directly controlling calcium permeation and intracellular $Ca_V\alpha_1$ trafficking[2–6]. Dysfunction of Ca_V subunits is associated with several cardiovascular, neurological, and psychiatric pathological conditions that are collectively known as calcium channelopathies[1,7–16].

[1]Institute of Biological Information Processing (IBI-1)—Molecular and Cellular Physiology, Forschungszentrum Jülich, Jülich, Germany. [2]Graduate Program, Faculty of Mathematics and Natural Sciences, Heinrich-Heine University, Düsseldorf, Germany. [3]Central Institute of Engineering, Electronics and Analytics (ZEA-3), Forschungszentrum Jülich, Jülich, Germany. [4]Institute of Biological Information Processing (IBI-7)—Structural Biochemistry, Forschungszentrum Jülich, Jülich, Germany. [5]Institute of Neuroscience and Medicine (INM-9)—Computational Biomedicine, Forschungszentrum Jülich, Jülich, Germany. [6]Cécile and Vogt Institute for Brain Research, Medical Faculty, Heinrich-Heine University, Düsseldorf, Germany. [7]Institute of Biochemistry, Heinrich-Heine University, Düsseldorf, Germany. [8]Present address: Biologics Analytical Research and Development, AbbVie Deutschland GmbH & Co. KG, Ludwigshafen, Germany. [9]Present address: Institute of Biology II, University of Freiburg, Freiburg, Germany. [10]These authors contributed equally: Francisco Castilla, Victor Lugo. ✉e-mail: b.santiago-schuebel@fz-juelich.de; m.alfonso-prieto@fz-juelich.de; pa.hidalgo@fz-juelich.de

The $Ca_V\beta$ family comprises four subclasses ($Ca_V\beta_1$–$Ca_V\beta_4$), each with several alternative splice variants[2,4,6,17–19]. $Ca_V\beta$ is one of the smallest members of the membrane-associated guanylate kinase (MAGUK) family. It has a modular architecture, with two highly conserved protein-protein interaction (PPI) domains (a Src homology 3 (SH3) domain and a guanylate kinase (GK) domain) that form the structural and functional core of the protein that recapitulates most of the channel modulatory functions[20–22]. In contrast, the N- and C-terminal regions and the HOOK linker joining the two conserved domains are variable in sequence and length[17].

High-resolution crystal structures are available for the $Ca_V\beta_2$, $Ca_V\beta_3$, and $Ca_V\beta_4$ subunits, both alone and in complex with a highly conserved consensus sequence among $Ca_V\alpha_1$ subunits: a segment of 18 amino acids located in the intracellular I–II loop and known as the α_1 interaction domain (AID)[23–26]. $Ca_V\beta$ has an elongated shape, with the SH3 and GK domains located on opposite sides of the protein's core. No crystallographic data are available for the flexible regions. The AID forms an α-helix that fits into a conserved hydrophobic groove (α-binding pocket) formed exclusively by GK domain residues.

Beyond its canonical role in potentiating Ca_V-mediated calcium currents as part of the Ca_V complex, $Ca_V\beta$ also interacts with diverse protein partners to fulfill a variety of cellular functions, including with filamentous actin[2,4,18,27–33]. The association between $Ca_V\beta$-actin has been demonstrated by in vitro binding assays and in vivo via fluorescence lifetime imaging microscopy and single-molecule localization microscopy[32]. However, in the absence of a molecular model for the $Ca_V\beta$–actin interaction, its function has been explored by disrupting the interaction using inhibitors of actin polymerization[32,33]. Based on this strategy, actin association with two $Ca_V\beta$ isoforms, $Ca_V\beta_2$ and $Ca_V\beta_4$ (which are highly expressed in the heart and brain, respectively) was proposed to upregulate L-type calcium currents in HL-1 cardiomyocytes and to increase the readily releasable pool of synaptic vesicles independent of channel function in primary hippocampal neurons, respectively[32,33].

In this work, we identified the actin interaction surface of $Ca_V\beta_2$ and $Ca_V\beta_4$ by implementing a strategy that combined chemical cross-linking mass spectrometry (XL-MS) with computational biology, followed by experimental validation of the resulting $Ca_V\beta$–actin models (Fig. 1). We identified several hotspot residues and generated mutants with significantly reduced in vitro affinity for actin, but not for the AID, in the background of $Ca_V\beta_2$ and the $Ca_V\beta_4$ truncated variant ($Ca_V\beta_4$ R482X). This $Ca_V\beta_4$ variant lacking the 39 C-terminal amino acids has been linked to juvenile myoclonic epilepsy but its etiology is unclear[13,34].

Electrophysiological recordings in HEK293 cells showed that, as compared with the wild-type $Ca_V\beta4$, neither $Ca_V\beta4$ R482X nor the actin-association-deficient $Ca_V\beta4$ R482X hotspot mutant affect macroscopic ionic currents mediated by $Ca_V1.2$ or $Ca_V2.2$.

However, cells coexpressing $Ca_V1.2$ and an actin-association-deficient $Ca_V\beta_2$ mutant have diminished ionic currents compared with those coexpressing $Ca_V1.2$ and the wild-type $Ca_V\beta_2$. Through gating current measurements combined with stationary noise analysis, we show the $Ca_V\beta_2$ mutant mediates current downregulation by reducing the number of functionally available channels.

Here, we propose a model in which the $Ca_V\beta_2$–actin interaction is required for the normal endocytic turnover of conduction-defective L-type Ca_V proteins at the cell surface and, thus, for proper calcium signaling and protein homeostasis.

Results

Identification of cross-linked peptides by mass spectrometry

We mapped the contact surface between recombinant $Ca_V\beta_2$ and in vitro polymerized actin using XL-MS. Given that recombinant full-length $Ca_V\beta$ proteins are less stable under the lower salt conditions used for actin polymerization than their corresponding core regions counterparts, we employed the core region of $Ca_V\beta_2$ ($Ca_V\beta_2$-core, Fig. 2A)[22,32]. The $Ca_V\beta_2$-core eluted as a monodisperse peak following size exclusion chromatography, with no indication of protein aggregation (Fig. 2B).

For chemical cross-linking, we employed two MS-cleavable cross-linkers, disuccinimidyl sulfoxide (DSSO) and disuccinimidyl dibutyric urea (DSBU), with spacer arms of 10.3 Å and 12.5 Å, respectively, that mainly react with lysine[35,36]. The cross-linking reaction was optimized for cross-linker concentration and incubation time, and compared to control reactions, in which either no cross-linker was added to the reaction or to the individual proteins and each protein alone was incubated with the cross-linkers (Fig. 2C and Supplementary Fig. 1). These experiments established 2.5 and 5.0 molar excess of DSSO and DSBU, respectively, and an incubation time of 60 minute as the optimal conditions for detecting cross-linking specific products between $Ca_V\beta_2$ and actin (Fig. 2C). The stability of the $Ca_V\beta_2$–actin complex was assessed using a F-actin cosedimentation assay, which is widely used to analyze the association of proteins with actin filaments[37,38]. The fraction of $Ca_V\beta_2$-core bound to actin show statistically non-significant difference after a 30- or 90- minute incubation time with actin, indicating that the complex formation is stable at least for 90 minutes under our experimental conditions (Supplementary Fig. 2).

To identify the sites of cross-linking, the reaction was performed in independent replicates and cross-linked proteins were resolved by SDS-PAGE (Supplementary Fig. 1). Although the efficiency of the cross-linking reaction for $Ca_V\beta_2$-core (48.2 kDa) and actin (43 kDa) was low, sufficient intermolecular cross-linked products were obtained with both cross-linkers. Products had an apparent molecular mass of about 110 kDa, which is fully absent in control reactions, suggesting that intermolecular chemical cross-links had formed between the $Ca_V\beta_2$-core and actin (Fig. 2C). The bands containing those cross-linked products were excised from the gel followed by in-gel trypsinization. The resulting peptides were analyzed by nano LC-MS/MS and identified from acquired mass spectrometry data using three software packages, MaxLynx, Merox and MetaMorpheus, as described in the Methods[39–41].

Within the five DSSO replicates, MetaMorpheus, MaxLynx and Merox detected a total of 893, 249 and 67 cross-linked-peptide-to-spectrum matches (CSMs), which included 179, 52 and 14 inter-linked CSMs, respectively (Supplementary Table 1). The inter-linked CSMs resulted in 56 intermolecular crosslinks (inter-XLs), of which eight inter-XLs were identified by all three software packages, 15 by MaxLynx and MetaMorpheus, one by MetaMorpheus and Merox, and 32 by MetaMorpheus only (Supplementary Fig. 3A).

Using the four DSBU replicates, MetaMorpheus, MaxLynx and Merox detected a total of 370 CSMs (including 19 inter-link CSMs), 331 CSMs (14 inter-link CSMs) and 103 CSMs (seven inter-link CSMs), respectively (Supplementary Table 1). 15 inter-XLs were identified, with four inter-XLs found by all three software packages, six by MaxLynx and MetaMorpheus, two by MetaMorpheus and Merox, one by MaxLynx and Merox, and two by MetaMorpheus only (Supplementary Fig. 3B).

Taking together the inter-XLs found with the two cross-linkers and removing redundancy, a total of 22 unique inter-XLs were identified (Fig. 2D and Supplementary Table 2). Comparing interlinks obtained with DSBU and DSSO resulted in seven common inter cross-links, 14 inter-XLs identified only with DSSO and one inter-XL only with DSBU (Supplementary Fig. 3C). Of the 22 unique inter-XLs, 16 were identified by at least two distinct software packages (Supplementary Table 2).

In the primary sequence the residues involved in inter-XLs are distributed within two distinct regions in actin (K52 and K63 in one; K293, K317, K328, and K330 in the other), and are mostly located within the GK domain in $Ca_V\beta_2$ (K274, K347, K354, K358 and K362) (Fig. 2D). When the aforementioned residues are mapped on the three-dimensional structure, they are distributed within two discrete

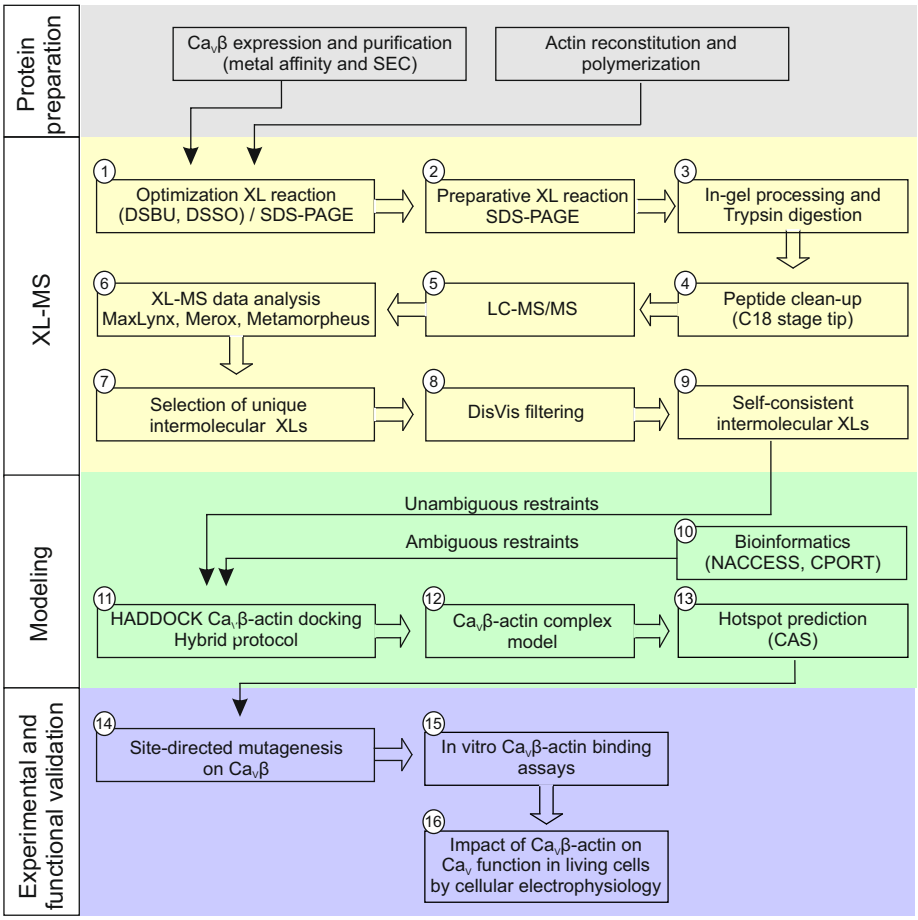

Fig. 1 | Workflow diagram illustrating the strategy used to identify the interaction surface between $Ca_V\beta$ and actin by combining cross-linking mass spectrometry (XL-MS) with protein-protein docking and experimental validation. The overall strategy can be divided in four phases; a pre-phase, named protein preparation, aimed to generate the proteins under study, and XL-MS, modeling and experimental and functional validation phases. The optimization of the XL-reaction conditions was done by testing different amounts of the XL (DSBU and DSSO) at different reaction times, as shown in Supplementary Fig. 1, and visualized by SDS-PAGE (1). Replicas of the optimal XL-reaction conditions were carried out for further analysis (2). The band containing the specific cross-linked product between $Ca_V\beta$ and actin was excised and in gel trypsinized (3). The mix of peptides were subjected to C18 stage tip cleaning (4) and LC-MS/MS (5). XL-MS data analysis was performed using three different search engines (6). Unique intermolecular cross-links that were identified by at least two search engines (7) were considered for filtering using DisVis (8) to obtain a set of self-consistent XL-MS derived distance restraints (9). XL-MS restraints together with bioinformatics-predicted restraints from NACCESS and CPORT programs, considered as unambiguous and ambiguous restraints, respectively (10), served as input files for the HADDOCK hybrid docking protocol (11) to generate $Ca_V\beta$–actin models (12). The top four HADDOCK models of the selected docking cluster were used to predict hotspots via Computational Alanine Scanning (CAS) with six predictors (Anchor, BeAtMuSiC, Bude Alanine Scan, Mutabind2, Robetta and SAAMBE-3D) (13). Hotspot mutations selected based on the average ΔΔG over the six predictors were introduced by site-directed mutagenesis into $Ca_V\beta$ (14). The impact of the $Ca_V\beta$ hotspot mutants on its binding affinity for actin were assessed by in vitro assays (15), and the mutants with decreased affinity were tested for its effect on calcium channel function in living cells by electrophysiology (16).

patches of an actin monomer, but form a contiguous surface on two adjacent monomers within the actin protofilament (Fig. 2E). The latter agrees with $Ca_V\beta$ binding to actin filaments[32].

We employed DisVis analysis[42,43] to evaluate the information content of the distance restraints between $Ca_V\beta$ and actin and considered a total of 16 unique inter-XLs with monomeric actin or of 32 XLs with dimeric actin (since the 16 unique inter-XLs can be a priori assigned to either monomer of the two adjacent actin subunits). After several iterations of DisVis filtering, a set of 11 self-consistent inter-XLs were identified, with a lower average violated fraction for dimeric actin (Fig. 2F and Supplementary Table 3).

Structural model of the interaction between $Ca_V\beta_2$ and actin

Although DisVis analysis hints at association of $Ca_V\beta$ with dimeric actin, it does not fully discard binding to monomeric actin. Therefore, docking-based modeling of the $Ca_V\beta_2$–actin interaction was performed for both dimeric and monomeric actin. Calculations were carried out on the HADDOCK 2.4 webserver using the XL-MS distance restraints resulting from DisVis analysis and interface information predicted with bioinformatics[44,45].

For the $Ca_V\beta_2$–actin dimer complex, all generated models were clustered using an interface ligand (i-l)-RMSD cutoff of 7.5 Å, resulting in one cluster containing 198 models (Supplementary Fig. 4A and Supplementary Tables 4A and 5A). The similarity across those models was assessed with two RMSD-based metrics, the ligand (l)-RMSD and the interface (i)-RMSD, taking $Ca_V\beta_2$ as ligand and actin as receptor, as described[46,47]. The l-RMSD reports the RMSD of the backbone atoms of the $Ca_V\beta_2$ ligand after optimally aligning the actin receptor and the i-RMSD provides the backbone RMSD of the interface residues (using a 10 Å distance cutoff) of both actin and $Ca_V\beta_2$. We obtained values of 4.3 ± 4.1 and 1.0 ± 0.4 Å for l-RMSD and i-RMSD, respectively (Supplementary Fig. 4B, C and Supplementary Table 5A), indicating a high

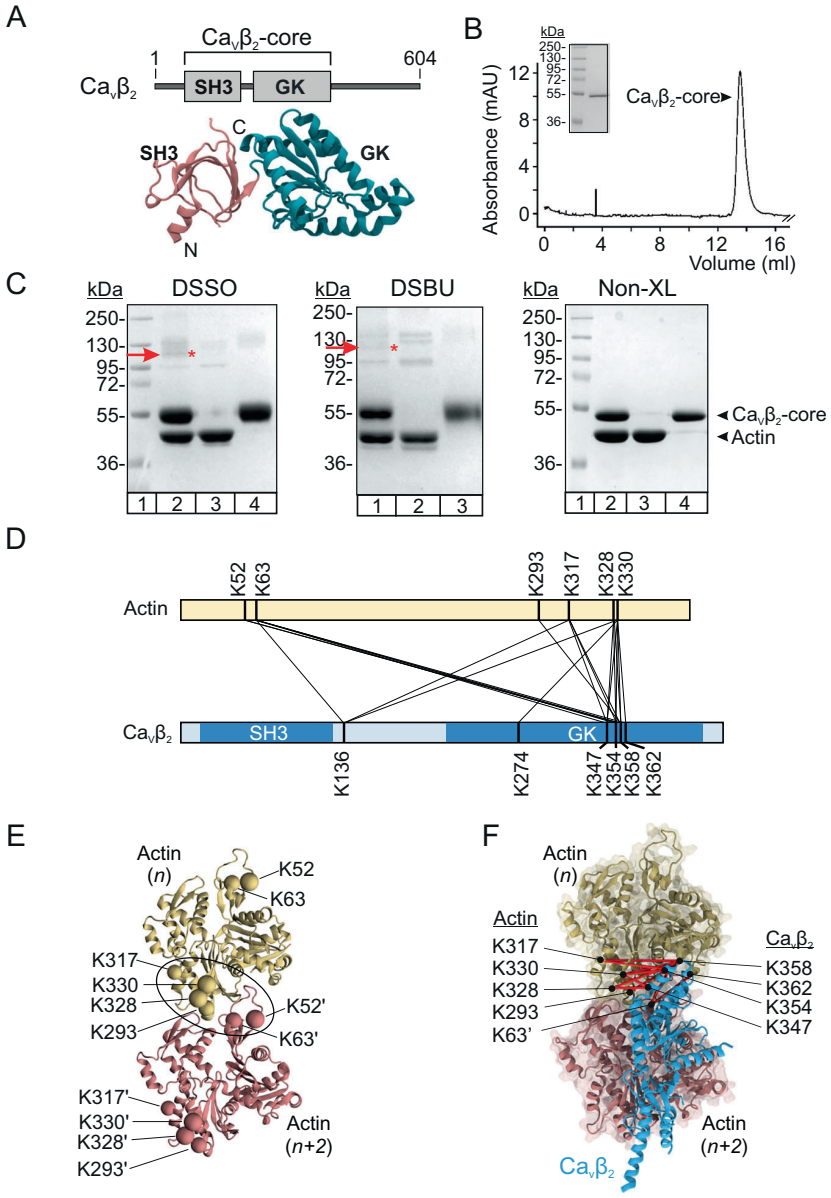

Fig. 2 | Chemical XL-MS and computational analysis define a set of distance constraints for modeling the Ca$_V$β–actin complex. A Domain architecture (top) and crystal structure (bottom) of rat Ca$_V$β$_2$ (UniProtKB Q8VGC3-2; PDB 5V2P). Src homology 3 (SH3) and guanylate kinase (GK) domains forming the protein core are labeled. Numbers represent the first and last residues. **B** Size exclusion chromatography profile of the Ca$_V$β$_2$-core; inset, purified protein resolved by SDS-PAGE. Numbers denote the size of molecular weight (MW) standards. The experiments were repeated at least 3 times. **C** Representative SDS-PAGE images of optimal cross-linking reactions for the Ca$_V$β$_2$-core and actin using DSSO, DSBU, and control reaction with only vehicle, no cross-linker (Non-XL) from 5, 4 and 3 independent replicas, respectively. DSSO: lane 1, MW standards; lane 2, Ca$_V$β$_2$-core–actin cross-linking; lane 3, actin alone incubated with DSSO; and lane 4, Ca$_V$β$_2$-core alone incubated with DSSO. DSBU: lane 1, Ca$_V$β$_2$-core–actin cross-linking; lane 2, actin alone incubated with DSBU; and lane 3, Ca$_V$β$_2$-core alone incubated with DSBU. MW standards lane was omitted and the full image is shown in Supplementary Fig. 1. The red arrow and asterisk denote the band that was excised from the gel for tryptic digestion and LC-MS/MS analysis. Non-XL control: lane 1, MW standards; lane 2, Ca$_V$β$_2$-core and actin together incubated with DMSO; lane 3, actin alone incubated with DMSO; and lane 4, Ca$_V$β$_2$-core alone incubated with DMSO. **D** Linear representation depicting the location and residue number of unique intermolecular cross-links between Ca$_V$β$_2$-core and actin (UniProtKB P68135, PDB 5OOE). **E** Three-dimensional ribbon representation of two adjacent actin monomers in one protofilament, named *n* and *n + 2*, shown in yellow and pink, respectively. Actin amino acids participating in the unique intermolecular cross-links (shown as spheres, with those in monomer *n + 2* labeled with a prime (′) symbol) form a contiguous patch across two adjacent actin subunits (black contour). **F** Structural mapping of inter-cross-links (red lines) that satisfied data consistency upon DisVis filtering for one Ca$_V$β$_2$ molecule and two adjacent actin monomers. Actin is shown in space-filling and ribbon mode, but for clarity Ca$_V$β$_2$ is displayed in ribbon mode only.

similarity of the PPI interface across docking models, despite a shift in the position and orientation of Ca$_V$β$_2$ relative to actin, according to the CAPRI classification[46,47].

Next, we tested the cluster models for their consistency with the inter-XLs between Ca$_V$β$_2$ and actin (Supplementary Fig. 4D). No violations of the maximum-bound distance of 30 Å between the Cα-Cα of two cross-linked residues were observed in all 198 models, except for one Ca$_V$β–actin cross-link pair (K358–K317), where for a fraction of complexes the distance was up to 35 Å (Supplementary Fig. 4D). Previous studies have considered a maximum Cα-Cα distance of 35 Å to

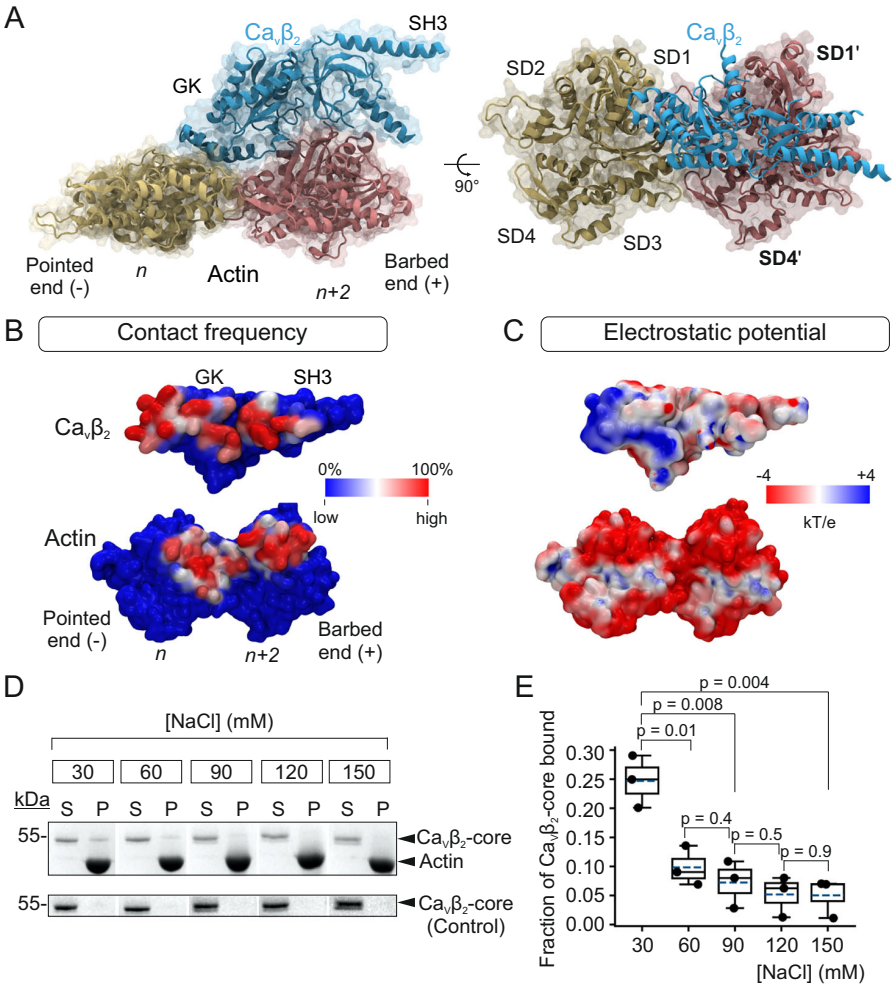

Fig. 3 | Model of $Ca_V\beta_2$ bound to actin shows an extended contact surface and electrostatic complementarity. A Space-filling and ribbon diagram showing two views related by a 90° rotation of the best-scoring docking model of $Ca_V\beta_2$ complexed with actin. One molecule of $Ca_V\beta_2$ (blue) interacts with two adjacent monomers in one actin protofilament, named *n* (yellow) and *n* + *2* (pink). Actin subunits are labeled based on their position along the filament from the pointed end (−) to the barbed end (+). For clarity, $Ca_V\beta_2$ is shown in ribbon mode only in the right panel. The four actin subdomains, SD1–SD4, are labeled in the *n* monomer. Subdomains in monomer *n* + *2* are indicated with a prime (′); SD2′ and SD3′ were omitted. **B** Surface models showing the contact frequency of $Ca_V\beta_2$ and actin residues. **C** Same as in *B* but showing the electrostatic potential map of both proteins. **D** SDS-PAGE analysis of a representative F-actin cosedimentation assay using the indicated NaCl concentrations. Briefly, the $Ca_V\beta_2$-core was incubated with phalloidin-stabilized actin filaments, the mixture was centrifuged, and the supernatant (S) and pellet (P) fractions separated. The pellet was resuspended in the same volume of SDS-loading buffer as the volume of supernatant, and the supernatant and pellet fractions were resolved by denaturing SDS-PAGE. Control assays included the $Ca_V\beta_2$-core only (lower panel). For clarity, irrelevant lanes were cropped from the source images (as indicated by the white space); full gel images are shown in Supplementary Fig. 8. **E** Fraction of $Ca_V\beta_2$-core bound to actin (calculated by densitometry) against NaCl concentration. Box plot shows the mean (dashed line), median (continuous line), interquartile range (25th–75th percentiles, box edges) and whiskers (1.5× interquartile range). Each dot represents an independent experiment; *p*-values, two-tailed *t*-test. Each experiment was repeated three times. Also see Supplementary Fig. 8.

account for conformational flexibility and ambiguity in the cross-link assignment, in particular for DSSO and DSBU[48–56]. In contrast, control docking simulations without XL-MS restraints resulted in 99% models with Cα-Cα inter-XL distances larger than the upper bound distance of 35 Å (Supplementary Table 6 and Supplementary Fig. 5). This corroborates the importance of using XL-MS restraints in protein-protein docking to identify the $Ca_V\beta_2$–actin interface in line with previous studies[57–62].

The top scoring model for the XL-MS guided protein-protein complex illustrates that $Ca_V\beta_2$ fits onto a hollow formed by two adjacent actin monomers within a single protofilament (Fig. 3A). The GK domain establishes contacts with both monomers, specifically with subdomains SD1 and SD3 and SD1′ and SD2′ of actin subunits *n* and *n* + *2*, respectively. The SH3 domain interacts only with SD1′ of the *n* + *2* monomer.

The PPI interface between $Ca_V\beta_2$ and the actin dimer was defined by mapping the contact frequency for each residue of the protein complex onto the corresponding three-dimensional structures (Fig. 3B). The residues with the largest contact frequency form continuous patches in $Ca_V\beta_2$, extending along both the SH3 and GK domains, and in actin, extending along both monomers. This binding mode is in agreement with in vitro assays showing that both SH3 and GK domains separately binding to actin filaments[32] and with the protein-protein interface reported for other actin binding proteins[38,63–66].

In contrast, docking simulations with $Ca_V\beta_2$ and a single actin monomer resulted in a protein-protein complex model in which the SH3 domain does not establish any intermolecular contact with actin (Supplementary Figs. 6 and 7 and Supplementary Tables 4C).

Moreover, binding of $Ca_V\beta_2$ to the *n* + *2* subunit would result in the SH3 domain clashing with the adjacent (*n*) subunit (Supplementary Fig. 7B). Therefore, our docking results with monomeric actin are incompatible with the two-domain binding mode of $Ca_V\beta_2$ with actin filaments, whereas the $Ca_V\beta_2$–actin dimer model is in agreement with this experimental evidence[32].

Calculation of the electrostatic potential surface of $Ca_V\beta_2$ and actin showed a positively charged patch on the $Ca_V\beta_2$-binding surface, mainly located in the GK domain, that matches a predominant negative charge distribution on the actin interaction surface, suggesting electrostatic binding complementarity (Fig. 3C). To examine the contribution of electrostatic interactions to $Ca_V\beta_2$–actin dimer complex formation, we measured the dependence on ionic strength. Binding of $Ca_V\beta_2$-core to actin was assessed using the F-actin cosedimentation assay at NaCl concentrations of 30–150 mM. To avoid the effects of the different salt concentrations on actin polymerization, we used phalloidin to stabilize the actin filaments[37]. In this assay, the $Ca_V\beta_2$-core was incubated with in vitro polymerized actin, and the pellet and supernatant fractions obtained by high-speed centrifugation were resolved by SDS-PAGE. In control reactions, the $Ca_V\beta_2$-core alone was centrifuged and both fractions were resolved by SDS-PAGE (Fig. 3D): the $Ca_V\beta_2$-core was virtually excluded from the pellet at all NaCl concentrations tested, whereas the fraction of the $Ca_V\beta_2$-core that cosedimented with actin decreased with increasing NaCl concentrations (Fig. 3E and Supplementary Fig. 8). Therefore, $Ca_V\beta_2$ binding to actin depends on the salt concentration, confirming that electrostatic interactions contribute to the stability of the complex.

Identification of hotspot residues at the $Ca_V\beta_2$/actin interaction interface

Computational alanine scanning was used to predict which $Ca_V\beta_2$ residues contribute most to the protein-protein binding energy (so-called hotspots) using six different webservers (Anchor, BeAtMuSiC, BUDE Alanine Scan, Mutabind2, Robetta, and SAAMBE-3D)[67–73]. For each of the six predictors, the change in free energy due to alanine substitution (ΔΔG) of each $Ca_V\beta_2$ residue at the PPI interface was calculated as an average over the top four structures of the best cluster, which displayed an i-RMSD of 0.9 ± 0.6 Å (Supplementary Figs. 9A and Supplementary Table 5A). Average ΔΔG values for all six predictors were used to rank the $Ca_V\beta_2$ residues as hotspots (Supplementary Fig. 9B), and the top seven predicted hotspot residues at the $Ca_V\beta_2$ interaction surface were selected for experimental mutagenesis and in vitro binding assays. Two of these are located on the SH3 domain (K90 and R128) and five on the GK domain (K347, Q350, K354, K358, and N365) (Fig. 4A). The highly ranked hydrophobic residue, L364, that lies within the hotspot region in the GK domain was also included in the experimental validation. The hotspots establish interactions with actin residues located in the *n* subunit and *n* + *2* subunit (Supplementary Fig. 10 and Supplementary Table 7A).

Alanine substitution of the eight selected hotspot residues in the $Ca_V\beta_2$-core was used to generate two different mutant proteins, $Ca_V\beta_2$-core 8Ala and $Ca_V\beta_2$-core 6Ala, bearing alanine substitutions either at all eight hotspots (GK + SH3) or at the six located within the GK domain (Fig. 4B). These amino acid substitutions did not destabilize the $Ca_V\beta_2$-core in mutant proteins, as indicated by the lack of aggregates and the nearly symmetric single elution peak after size exclusion chromatography (Fig. 4B).

F-actin cosedimentation assays were used to compare the ability of wild-type (WT) and mutant proteins to interact with F-actin. In control reactions, a negligible amount of WT or mutant $Ca_V\beta_2$-core was sedimented by high-speed centrifugation (Fig. 4C, lanes 3, 7, and 11). In the presence of actin, the fraction of cosedimenting $Ca_V\beta_2$-core was significantly reduced for the mutant proteins (bound fraction: 0.24 ± 0.03 for $Ca_V\beta_2$-core WT, 0.11 ± 0.03 for $Ca_V\beta_2$-core 6Ala, and 0.09 ± 0.02 for $Ca_V\beta_2$-core 8Ala) (Fig. 4D and Supplementary Fig. 11 A). To discount the possibility that the reduced actin-binding activity of $Ca_V\beta_2$-core hotspot mutants was due to their reduced stability in F-actin cosedimentation assay buffer, we compared the intrinsic fluorescence of these proteins. Tiny differences in the thermal unfolding curves and unfolding transition temperature (T_m) were observed among WT and mutant $Ca_V\beta_2$-core proteins, indicating that they have comparable structural stability in the assay buffer (Supplementary Fig. 11B).

Inspection of the molecular model for $Ca_V\beta$–actin complex showed no overlap between the actin-binding hotspots identified in this study and those reported to be critical for $Ca_V\beta$ association with the $Ca_V\alpha_1$ high-affinity AID site[25,74] (Fig. 4E). Pull down assays using the AID peptide as bait showed that the actin-association-deficient $Ca_V\beta_2$ mutants retain the ability to associate with the AID (Fig. 4F and Supplementary Fig. 11C).

Together, these results indicate the key residues that contribute to the molecular interaction surface between $Ca_V\beta_2$ and actin.

Integrating $Ca_V\beta_2$-derived XL-MS data for $Ca_V\beta_4$ and actin computational docking

$Ca_V\beta_4$, the central component of the Ca_V complex in the human brain, also associates with actin[33]. The high degree of conservation in the primary sequence and domain structure among the members of the $Ca_V\beta$ family of proteins, including $Ca_V\beta_2$ and $Ca_V\beta_4$, anticipates a shared interaction interface with actin. Moreover, the amino acid sequence alignment between $Ca_V\beta_2$ and $Ca_V\beta_4$ shows that all four lysine residues involved in the XL-MS-derived distance restraints used for modeling of $Ca_V\beta_2$/actin interaction are conserved in $Ca_V\beta_4$ (Supplementary Fig. 12). We exploited this fact to guide molecular docking for $Ca_V\beta_4$ and actin using the analogous unambiguous restraints, together with bioinformatics-based predictions of interfacial residues to define ambiguous restraints.

Clustering of the $Ca_V\beta_4$–actin docking models, as done for $Ca_V\beta_2$, resulted in five clusters, out of which cluster #3 and #4 were discarded according to the average HADDOCK score of the top four structures (Supplementary Tables 4B and 5B–D). Clusters #1, #2 and #5 showed overlapping HADDOCK scores and selection among them was done based on their similarity with the experimentally-validated $Ca_V\beta_2$–actin model (Supplementary Table 4B). We calculated the average structure of the top four models for each cluster and compared with the average structure of the $Ca_V\beta_2$–actin complex, using the latter as reference for the alignment (Fig. 5A). The average structure of cluster #1 displayed the lowest l-RMSD (4.8 Å, compared to 12.7 Å and 12.2 Å for clusters #2 and #5, respectively). We also evaluated the i-RMSD to assess the similarity of the PPI surfaces by extracting the set of interface residues in common between the two $Ca_V\beta$/actin complex models, that displayed 86% sequence identity for the $Ca_V\beta$ interface residues. The average structure of cluster #1 also showed the lowest i-RMSD (2.7 Å versus 3.3 Å and 6.5 Å for clusters #2 and #5, respectively); thus, cluster #1 was chosen for further analysis.

This cluster was populated with 135 models, with l-RMSD and i-RMSD values of 3.8 ± 3.4 Å and 1.9 ± 1.2 Å, respectively, with respect to the best HADDOCK scored structure within this cluster. No violations of the upper cutoff distance of 35 Å between the Cα-Cα of two cross-linked residues was observed across the 135 models (Supplementary Fig. 13).

As for $Ca_V\beta_2$/actin, computational alanine scanning of the $Ca_V\beta_4$–actin interaction was carried out using the six predictors and the top four structures of the selected cluster #1, which showed i-RMSD 2.7 ± 1.8 Å. Several potential hotspots in $Ca_V\beta_4$ that are implicated in actin binding were identified (Supplementary Fig. 14), including residues analogous to the set of eight residues in $Ca_V\beta_2$ experimentally proven to affect actin binding and forming intermolecular contacts with a common subset of actin residues (Supplementary Table 7).

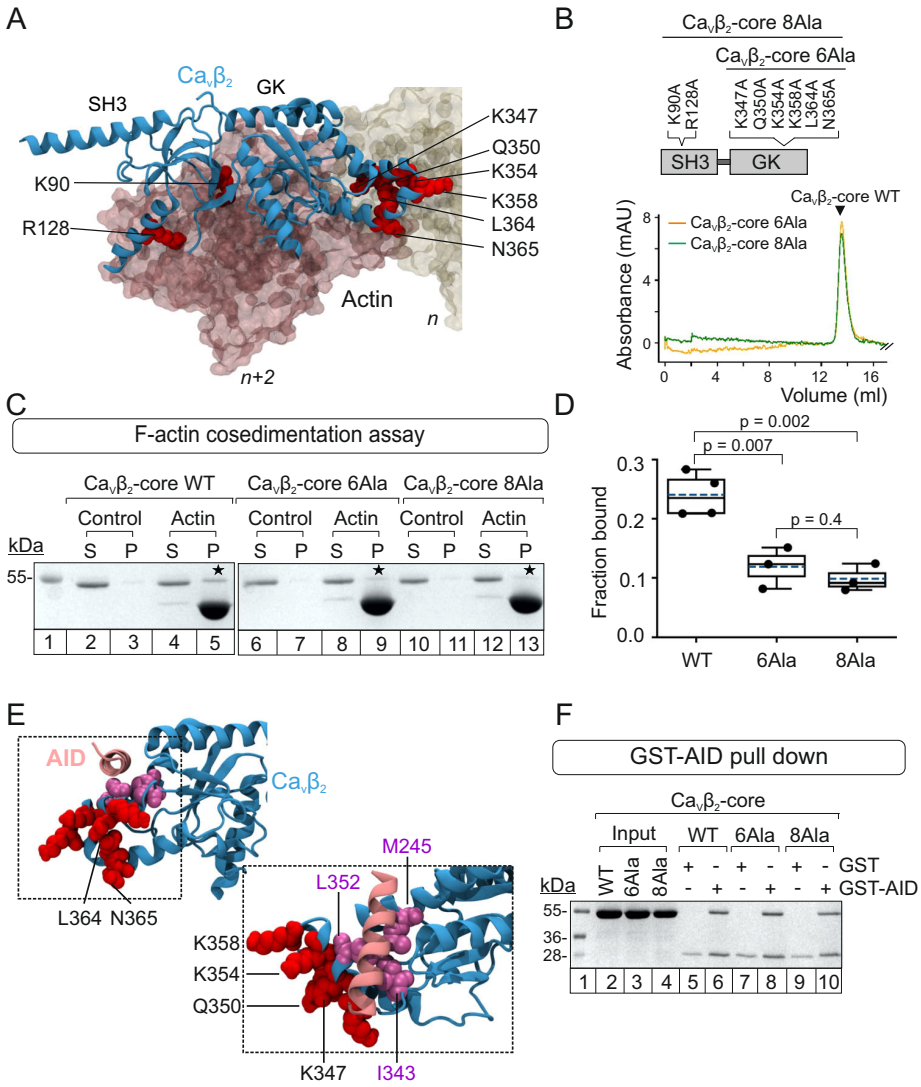

Fig. 4 | Alanine substitution of predicted PPI hotspots decreases the in vitro affinity of $Ca_V\beta_2$ for actin but not for the AID peptide. A Structure of $Ca_V\beta_2$ (blue ribbon), indicating the eight predicted hotspot residues (red spheres) mutated to alanine in the $Ca_V\beta_2$-core. Two actin subunits interacting with $Ca_V\beta_2$ are shown in space-filling mode, oriented from the barbed end (*n* + *2*, pink) to the pointed end (*n*, yellow). **B** Linear diagram of the $Ca_V\beta_2$-core domain, indicating the positions of hotspot mutations and size exclusion chromatography profiles of the hotspot mutants, $Ca_V\beta_2$-core 6Ala (orange) and $Ca_V\beta_2$-core 8Ala (green). The arrow denotes the elution volume for $Ca_V\beta_2$-core WT. **C** SDS-PAGE of representative F-actin cosedimentation assays for the $Ca_V\beta_2$-core WT (lanes 2–5), $Ca_V\beta_2$-core 6Ala (lanes 6–9), and $Ca_V\beta_2$-core 8Ala (lanes 10–13). MW standard (lane 1). $Ca_V\beta_2$-core-derived proteins were centrifuged either alone (control) or after incubation with polymerized actin (actin). S, supernatant; P, pellet. Asterisks denote bands of $Ca_V\beta_2$-core-derived proteins that pelleted with actin. Each experiment was repeated three times; full images are shown in Supplementary Fig. 11A. **D** Fraction of the indicated $Ca_V\beta_2$-core proteins bound to actin. Box plot shows the mean (dashed line), median (continuous line), interquartile range (25th–75th percentiles, box edges) and whiskers (1.5× interquartile range). Each dot represents an independent experiment; *p*-values, unpaired two-tailed *t*-test. **E** $Ca_V\beta_2$ complexed with the AID peptide (PDB 5V2P). $Ca_V\beta_2$ is depicted as a blue ribbon with hotspots for actin binding as red van der Waals spheres and the critical residues for $Ca_V\beta$ association (L352, I343, and M245)[25,74] in purple. The AID is shown as a pink ribbon. **F** SDS-PAGE of a representative pull down assay using as bait GST, either alone or fused to AID (GST-AID) and as prey $Ca_V\beta_2$-core WT (WT), $Ca_V\beta_2$-core 6Ala (6Ala), or $Ca_V\beta_2$-core 8Ala (8Ala). MW standards (lane 1), $Ca_V\beta_2$-core proteins used as input (lanes 2–4), elution fractions from the GST (control, lanes 5, 7, and 9) and GST-AID pull down assays (lanes 6, 8, and 10). Each experiment was repeated three times; full images are shown in Supplementary Fig. 11C.

Since recombinant full-length $Ca_V\beta_4$ is not stable enough under the F-actin cosedimentation assay buffer[33], we resorted to the truncated $Ca_V\beta_4$ R482X naturally occurring variant associated with juvenile myoclonic epilepsy[13] for the experimental validation. $Ca_V\beta_4$ R482X appeared the best candidate to investigate differences in actin affinity produced by the hotspot mutations due to its amenability for recombinant expression and purification, and its higher apparent affinity for actin found in F-cosedimentation assays (Figs. 5B and Supplementary Fig. 15A).

Based on $Ca_V\beta_2$, we generated two analogous $Ca_V\beta_4$ R482X mutants containing alanine substitutions in all eight hotspot residues ($Ca_V\beta_4$ R482X 8Ala) or in the six located within the GK domain ($Ca_V\beta_4$ R482X 6Ala) (Fig. 5B). Size exclusion chromatography profiles confirmed the structural integrity of recombinant $Ca_V\beta_4$ R482X bearing no Ala substitution and the derived hotspot mutants (Fig. 5C). Moreover, intrinsic fluorescence measurements in actin cosedimentation assay buffer showed that the unfolding transition temperatures were comparable for all three proteins (Supplementary

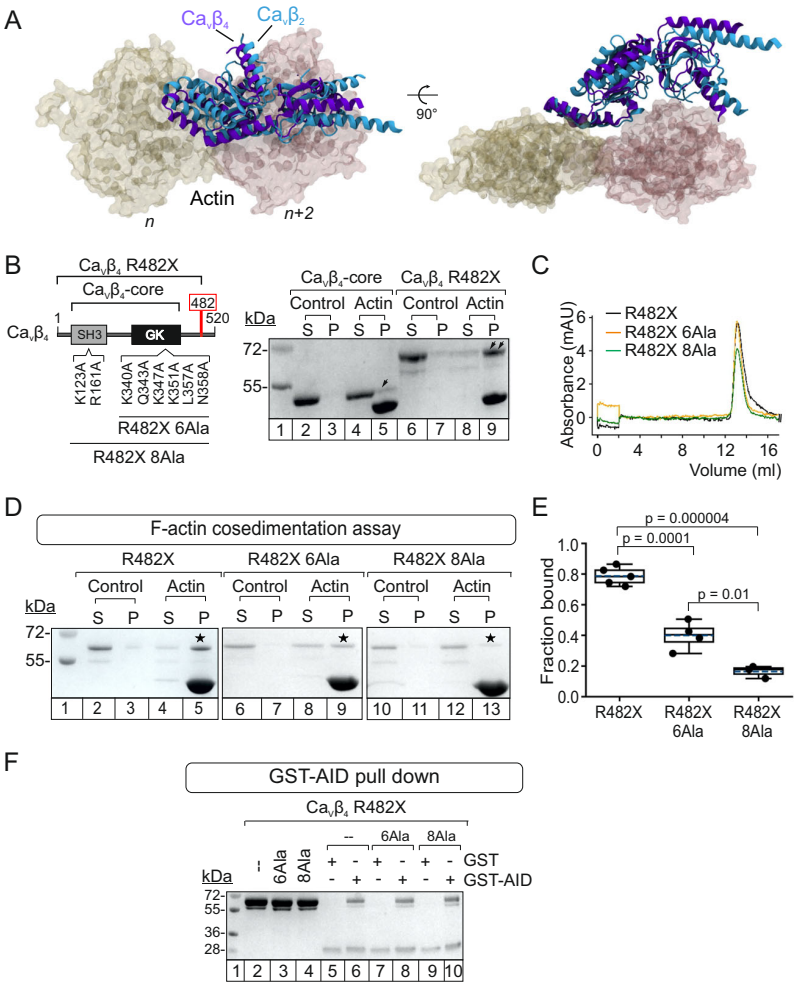

Fig. 5 | $Ca_V\beta_4$ R482X hotspot mutations blunt association with actin. **A** Superimposition of the actin-bound structures of $Ca_V\beta_2$ (cyan ribbon) and $Ca_V\beta_4$ (purple ribbon). Each $Ca_V\beta$ structure represents the average of the four best-scoring models of the selected docking cluster. For clarity, two actin subunits used as a reference for the alignment are shown in space-filling mode (yellow and pink). **B** Linear diagram and comparison of the in vitro actin-binding affinities by F-actin cosedimentation assay for $Ca_V\beta_4$-core (lanes 2–5) and $Ca_V\beta_4$ R482X (lanes 6–9). Numbers denote the positions of predicted hotspots substituted by alanine in the $Ca_V\beta_4$ R482X background according to human $Ca_V\beta_4$ (UniProtKB O00305-1). S and P, supernatant and pellet fractions, respectively. Single and double black arrows indicate the amount of corresponding protein that cosedimented with actin. The assays were repeated at least 3 times (Supplementary Fig. 15A). **C** Size exclusion chromatography profiles for $Ca_V\beta_4$ R482X (carrying no Ala substitutions) (black), $Ca_V\beta_4$ R482X 6Ala (orange), and $Ca_V\beta_4$ R482X 8Ala (green). **D** SDS-PAGE of F-actin cosedimentation assays for $Ca_V\beta_4$ R482X (lanes 2–5), $Ca_V\beta_4$ R482X 6Ala (lanes 6–9), and $Ca_V\beta_4$ R482X 8Ala (lanes 10–13). S, supernatant; P, pellet. Asterisks indicate protein bands that pelleted with actin. Each experiment was repeated three times; full images are shown in Supplementary Fig. 15C. **E** Fraction of the indicated $Ca_V\beta_4$ R482X proteins bound to actin. In box plot: mean (dashed line), median (continuous line), interquartile range (25th–75th percentiles, box edges), and whiskers (1.5× interquartile range). Each dot represents an independent experiment; *p*-values, unpaired two-tailed *t*-test. **F** SDS-PAGE of a representative pull-down assay using as bait GST, either alone or fused to AID (GST-AID), and as prey $Ca_V\beta_4$ R482X (–), $Ca_V\beta_4$ R482X 6Ala (6Ala), or $Ca_V\beta_4$ R482X 8Ala (8Ala). Molecular weight standard (lane 1), $Ca_V\beta_4$ R482X-derived proteins used as input (lanes 2–4), elution fractions from the pull down assay using either GST (lanes 5, 7, and 9) as control or GST-AID (lanes 6, 8, and 10) and the indicated proteins. Each experiment was repeated three times; full images are shown in Supplementary Fig. 15D.

Fig. 15B). However, the ability of $Ca_V\beta_4$ R482X hotspot mutants to bind actin was dramatically reduced. Whereas > 80% of $Ca_V\beta_4$ R482X cosedimented with actin, only 40% of $Ca_V\beta_4$ R482X 6Ala and < 10% of $Ca_V\beta_4$ R482X 8Ala protein did so (Fig. 5D, E and Supplementary Fig. 15C). In the absence of actin, almost all of the three $Ca_V\beta_4$ R482X proteins remained in the supernatant. Similar to $Ca_V\beta_4$ R482X, both hotspot mutants retained the ability to associate with the AID (Figs. 5F and Supplementary Fig. 15D).

These results demonstrate the crucial contribution of the hotspot residues to $Ca_V\beta_4$–actin complex formation in vitro. They also highlight the very fine agreement between the computationally predicted $Ca_V\beta$ hotspots for actin association and experimental results and confirm the robustness of our integrative strategy employed to define the interaction surface between $Ca_V\beta$ and actin.

$Ca_V\beta_2$ hotspot mutations reduce the number of functionally available L-type $Ca_V1.2$ channels at the plasma membrane

We next assessed the effect of expressing the actin-association-deficient $Ca_V\beta_2$ mutant in living cells. To this aim, full-length WT $Ca_V\beta_2$ or the mutant containing the eight experimentally validated hotspot mutations were fused to mRFP to generate $Ca_V\beta_2$-mRFP fusion constructs (hereafter referred to as $Ca_V\beta_2$ WT and $Ca_V\beta_2$ 8Ala, respectively). The WT protein is targeted to the plasma membrane[75–77], and

laser scanning confocal microscopy images of cells expressing either protein show that $Ca_V\beta_2$ 8Ala retains this ability (Fig. 6A). The degree of colocalization with the plasma membrane marker CellMask™ was not statistically different for both $Ca_V\beta_2$ WT and $Ca_V\beta_2$ 8Ala (Fig. 6B). Moreover, western blot analysis of crude lysates from cells expressing either $Ca_V\beta_2$ WT or $Ca_V\beta_2$ 8Ala showed comparable levels of protein expression (Fig. 6C). Therefore, the presence of hotspot mutations in $Ca_V\beta_2$ has no effect on either the cellular localization or expression of the protein.

To test the effect of $Ca_V\beta_2$ 8Ala on currents mediated by L-type $Ca_V1.2$ channels, we performed whole-cell recordings from cells coexpressing the $Ca_V1.2$ subunit and $Ca_V\beta_2$ 8Ala (in the absence of $Ca_V\alpha_2\delta$). These cells showed a significant decrease in the ionic current amplitude, with an average peak current reduction of about 53.0% compared with cells coexpressing $Ca_V1.2$ and $Ca_V\beta_2$ WT (Imax, $Ca_V1.2/Ca_V\beta_2$ WT, -1.32 ± 0.12 nA; $Ca_V1.2/Ca_V\beta_2$ 8Ala, -0.70 ± 0.07 nA; $p = 0.0001$) (Fig. 6D).

No appreciable voltage-dependent ionic currents were obtained for cells expressing the $Ca_V1.2$ subunit alone. Comparable curves for the fraction of activated channels versus voltage for the two channel subunit combinations were obtained indicating no major alterations in their open probabilities[32] (Fig. 6D). The minor change in voltage dependence of activation for $Ca_V1.2/Ca_V\beta_2$ 8Ala channels (rightward shift of by 4 mV in the half-maximal activation voltage) does not account for the drastic reduction in $Ca_V1.2$-mediated currents induced by $Ca_V\beta_2$ 8Ala.

The amplitude of the ionic current depends on the number of functionally available channels (n), the unitary conductance (γ), and the probability of the channel being in the open state (Po) (Eq. 5). We first addressed whether downregulation of $Ca_V1.2$-mediated currents is caused by decreased cell surface expression of the channel induced by $Ca_V\beta_2$ 8Ala. For this, we recorded gating currents from cells coexpressing $Ca_V1.2$ with either $Ca_V\beta_2$ WT or $Ca_V\beta_2$ 8Ala, as previously described[78–81]. Gating currents arise from the voltage-driven movement of charged residues within the voltage sensor—their integral over time provides the total gating charge (Qon) moved during the voltage step and is a direct quantification of the number of channels present at the plasma membrane[78–80,82,83]. The Qon value was not statistically different for $Ca_V1.2$ coexpressed with either $Ca_V\beta_2$ WT (363 ± 33 fC) or $Ca_V\beta_2$ 8Ala (304 ± 28 fC; $p = 0.19$), suggesting that impaired $Ca_V\beta_2$/actin association does not compromise the cell surface targeting of $Ca_V1.2$ channels (Fig. 6E). However, gating current measurements compute the contributions of all channel proteins with an intact voltage sensor and do not distinguish between channels that can or cannot mediate ion permeation. Therefore, these results do not preclude the possible coexistence of ion conduction-competent and conduction-incompetent channels, with an increased proportion of the latter in the presence of the actin-association-deficient $Ca_V\beta_2$ mutant.

To address the possibility that ion conduction incompetent channels may contribute to the measured gating currents and to evaluate the unitary properties of the channels, we conducted stationary noise analysis of macroscopic currents. Noise analysis provides information about both the number of channels available for activation and the unitary conductance[84,85]. Conduction silent channels do not contribute to the macroscopic current nor to fluctuations in the macroscopic current around its mean value (variance).

Fluctuations in the whole-cell current in cells coexpressing $Ca_V1.2$ with either $Ca_V\beta_2$ WT or $Ca_V\beta_2$ 8Ala were computed for repeated current recordings at different voltages, as previously described[86]. For each cell, the ratio between current variance and mean current amplitude times driving force ($\frac{\delta^2}{\langle I\rangle(Vm-Vrev)}$) was plotted against whole-cell conductance ($\frac{\langle I\rangle}{Vm-Vrev}$). This yielded a straight line plot from which the unitary conductance γ and the number of functionally available channels n are directly obtained from the y-intercept and slope, respectively (Eq. 6, Fig. 7A).

Data obtained from all analyzed cells are summarized in Fig. 7B, C. Box plots for all values calculated for n, γ, and maximal Po (Po_{max}, calculated from Eq. 7) and bootstrap distributions[87] showed that γ and Po_{max} values for $Ca_V1.2$ channels complexed with $Ca_V\beta_2$ WT and those complexed with $Ca_V\beta_2$ 8Ala are statistically indistinguishable (γ, 3.9 ± 0.1 pS and 4.0 ± 0.1 pS; $p = 0.40$ and Po_{max}, 0.59 ± 0.02 and 0.60 ± 0.02; $p = 0.66$, for $Ca_V1.2/Ca_V\beta_2$ WT and $Ca_V1.2/Ca_V\beta_2$ 8Ala, respectively); however, the mean number of channels differs significantly ($Ca_V1.2/Ca_V\beta_2$ WT, 12233 ± 1219; $Ca_V1.2/Ca_V\beta_2$ 8Ala, 6580 ± 899; $p = 0.0002$) (Fig. 7C). The reduction of about 53.8% in the number of functionally available channels closely matches the 53% percentage reduction in the macroscopic peak current. Given that the unitary properties of the remaining channels were unaltered, these findings indicate that a $Ca_V\beta_2$ 8Ala-induced reduction in the number of conduction-competent channels is responsible and sufficient for the downregulation of Ca_V-mediated ionic currents.

Earlier experiments showed that pharmacological disruption of the actin filaments by cytochalasin D inhibits the interaction between actin and $Ca_V\beta_2$ in living cells[32]. If the effect of the actin-association-deficient $Ca_V\beta_2$ mutant is mediated by its impaired interaction with actin filaments, then it is expected that subsequent disruption of actin filaments has little further effect on Ca_V-mediated currents.

We thus treated cells coexpressing $Ca_V1.2$ with either wild-type $Ca_V\beta_2$ or the 8Ala hotspot mutant with the cytochalasin D actin filament disruptor and recorded ionic and gating currents (Supplementary Fig. 16). Time-lapse confocal fluorescence images of HEK293 cells stained for actin filaments demonstrate effective filament disruption under our experimental conditions. Cytochalasin D reduces ionic currents while preserving gating currents (Qon) from $Ca_V1.2/Ca_V\beta_2$ WT channels, as compared with non-treated cells ($p = 0.02$ and $p = 0.24$, respectively), resembling the effect of the $Ca_V\beta_2$ 8Ala hotspot mutant. Moreover, the average peak current amplitudes from cytochalasin D-treated cells coexpressing $Ca_V1.2$ with either $Ca_V\beta_2$ WT or $Ca_V\beta_2$ 8Ala are statistically indistinguishable from each other (Imax, -0.81 ± 0.18 nA for $Ca_V1.2/Ca_V\beta_2$ WT and -0.58 ± 0.08 nA for $Ca_V1.2/Ca_V\beta_2$ 8 Ala; $p = 0.25$) (Supplementary Fig. 16). These results demonstrate that disruption of the actin filaments blunts the current reduction mediated by the actin-association-deficient $Ca_V\beta_2$ mutant and indicate that the effect of this mutant is a direct consequence of its impaired interaction with actin filaments and not a general effect.

To examine a potential functional impact of $Ca_V\alpha_2\delta$, we expressed this subunit along with the $Ca_V1.2/Ca_V\beta_2$ channel core complex. Currents mediated by the $Ca_V1.2/Ca_V\beta_2/Ca_V\alpha_2\delta_1$ tripartite channel complex marginally differed from the ones obtained with the $Ca_V1.2/Ca_V\beta_2$ (Supplementary Fig. 17). $Ca_V\alpha_2\delta_1$ speeds the kinetics of activation of the channel complex, confirming its expression in the recorded cells. In the background of the tripartite channel complex, the actin-association-deficient $Ca_V\beta_2$ hotspot mutant continued downregulating current amplitude while preserving channel number.

$Ca_V\beta_4$ R482X actin-association-deficient mutant preserves Ca_V-mediated ionic currents

It has been shown that $Ca_V\beta_4$ R482X exhibits normal nuclear localization, as compared with the wild-type $Ca_V\beta_4$[34]. Here, $Ca_V\beta_4$ R482X and the actin-association-deficient $Ca_V\beta_4$ R482X mutant, bearing the eight hotspot mutations (8Ala) displayed comparable nuclear localization and levels of expression (Figs. 8A, B and Supplementary Fig. 18A). The $Ca_V\beta_4$ R482X 8Ala mutant showed dramatically decrease in the in vitro binding to actin, but did not significantly alter the magnitude of whole-cell currents through L-type $Ca_V1.2$ channels or of the gating currents as compared with $Ca_V\beta_4$ R482X ($Imax$, -0.29 ± 40.2 nA and -0.27 ± 32.4 nA; $p = 0.8$ and Qon, 234 ± 24 fC and 259 ± 37 fC; $p = 0.60$

https://doi.org/10.1038/s41467-025-59548-x

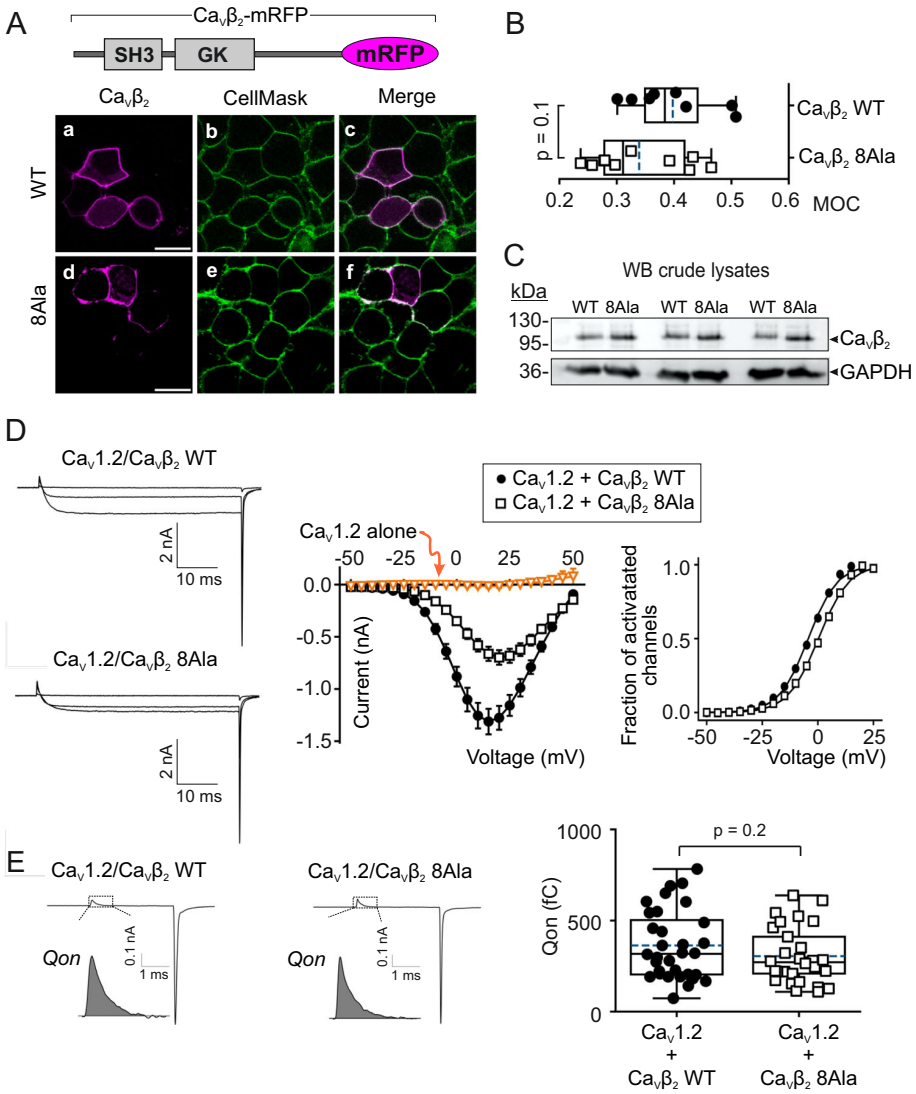

Fig. 6 | An actin-association-deficient $Ca_V\beta_2$ mutant decreases $Ca_V1.2$-mediated ionic current but not gating currents. A Schematic of the membrane-associated $Ca_V\beta_2$ fused to mRFP ($Ca_V\beta_2$-mRFP) and laser scanning confocal images of HEK293 cells expressing either the wild-type full-length $Ca_V\beta_2$ (WT) or the eight hotspot mutant (8Ala). Fluorescence images for the indicated $Ca_V\beta_2$ (a;d, magenta) and the plasma membrane marker CellMask™ (b;e, green); overlapping pixels appear as white (c;f). Scale bar, 15 μm (for all images). **B** Colocalization analysis between the indicated $Ca_V\beta_2$ protein and CellMask™. Box plot shows the mean (dashed line), median (continuous line), interquartile range (25th–75th percentiles, box edges) and whiskers (1.5 × interquartilee range). Each dot represents the Mander's overlap coefficient (MOC) for a field of view containing between 150 and 200 cells; *p*-value, two-tailed *t*-test. **C** Western blot (WB) of crude lysates from cells expressing either $Ca_V\beta_2$ WT or $Ca_V\beta_2$ 8Ala. Lysates from three separate experiments were probed with anti-$Ca_V\beta_2$ and anti-GAPDH antibodies. **D** Representative ionic current traces and plots of ionic current versus voltage (I/V) and fraction of activated channels versus voltage obtained from HEK293 cells cotransfected with $Ca_V1.2$ and either $Ca_V\beta_2$ WT or $Ca_V\beta_2$ 8Ala. Only the traces induced by −40, +15, and +40 mV pulses are shown. Currents were elicited by voltages of −50 to +50 mV in 5 mV increments from a holding potential of −90 mV; Data are presented as mean ± SEM; number of recorded cells = 32, 29 and 5 for $Ca_V1.2/Ca_V\beta_2$ WT, $Ca_V1.2/Ca_V\beta_2$ 8Ala, and $Ca_V1.2$ alone, respectively. **E** Representative gating currents obtained from cells in panel (**D**) and total charge movement (*Qon*) calculated from the integral of the *On* gating current (shaded area) during the voltage step to the reversal potential for the carrier ion, Ba^{2+}. In box plot: mean (dashed line), median (continuous line), interquartile range (25th–75th percentiles, box edges) and whiskers (1.5 × interquartile range). Each dot represents an individual recorded cell; *p*-values, unpaired two-tailed *t*-test. Mean values ± S.E.M: 363 ± 33 fC (n = 32) and 304 ± 28 fC (n = 29) for $Ca_V1.2/Ca_V\beta_2$ WT and $Ca_V1.2/Ca_V\beta_2$ 8Ala, respectively.

for $Ca_V1.2$ complexed with $Ca_V\beta_4$ R482X and $Ca_V\beta4$ R482X 8Ala, respectively, Fig. 8C, D). Correspondingly, noise analysis revealed statistically comparable values of the number of functional channels (N, 2901 ± 509 and 3425 ± 437; p = 0.43), the single-channel conductance (γ, 3.4 ± 0.1 pS and 3.8 ± 0.3 pS; p = 0.15) and the maximal open probability (*Pomax*, 0.61 ± 0.02 and 0.63 ± 0.03; p = 0.43) between $Ca_V1.2/Ca_V\beta_4$ R482X and $Ca_V1.2/Ca_V\beta_4$ R482X 8Ala (Fig. 8E).

We also tested whether $Ca_V\beta_4$ R482X 8Ala affects currents mediated by the presynaptic, $Ca_V2.2$ (N-type) channel that directly mediates the calcium influx for neurotransmitter release. We observed neither changes in the macroscopic current amplitude nor in the voltage-dependence of activation between $Ca_V2.2$ channels assembled wild-type $Ca_V\beta_4$, $Ca_V\beta4$ R482X or $Ca_V\beta_4$ R482X 8Ala (Supplementary Figs. 18B, C).

In conclusion, neither $Ca_V\beta_4$ R482X, which improves actin binding, nor the actin-association deficient $Ca_V\beta_4$ R482X mutant alters current amplitudes when coexpressed with either $Ca_V1.2$ or $Ca_V2.2$ pore-forming subunits. This highlights the functional specificity of $Ca_V\beta_2$ uncovered in this study.

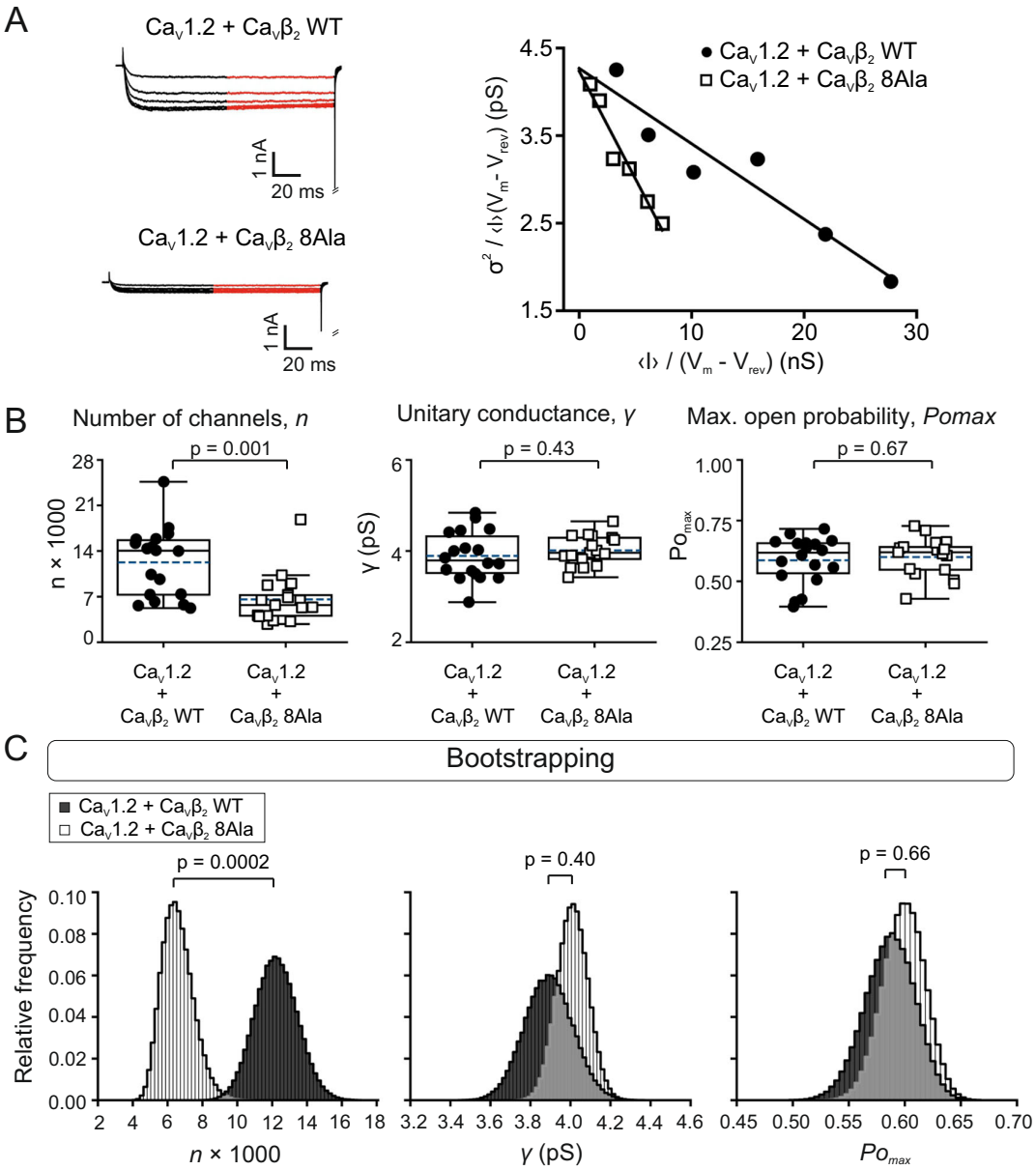

Fig. 7 | The Ca$_V$β$_2$ actin association-deficient mutant reduces the number of functional Ca$_V$1.2 channels and does not alter the channel conductance or maximal open probability. A Representative ionic current traces, with red lines delineating the time window used for noise analysis and plotting the relationship between variance and mean macroscopic current $\left(\frac{\sigma^2}{\langle I\rangle(Vm-Vrev)}\right)$ versus $\left(\frac{\langle I\rangle}{Vm-Vrev}\right)$ obtained at different voltages for two representative cells expressing Ca$_V$1.2 complexed with either Ca$_V$β$_2$ WT or Ca$_V$β$_2$ 8Ala. The number of functional channels *n* and the unitary conductance γ were calculated from the slope and *y*-intercept of the linear fit, respectively (Eq. 6). **B** Box plots for *n*, *γ*, and Po_{max}. The box edges represent interquartile ranges (25th–75th percentiles), the continuous and dashed lines the median and mean values and the ranges of the whiskers denote 1.5× the interquartile range. Each data point represents an individual recorded cell (number of cells = 18 and 17 for Ca$_V$1.2/Ca$_V$β$_2$ WT and Ca$_V$1.2/Ca$_V$β$_2$ 8Ala, respectively). *P*-values were determined by unpaired two-tailed *t*-test. The smaller unitary conductance value for Ca$_V$1.2 reported here is explained by the absence of Ca$_V$ agonists in our whole-cell current recordings[96]. **C** Bootstrap sample distributions for *n*, γ, and Po_{max} (bootstrap sample N = 500,000). The mean values for *n*, *γ*, and Po_{max} obtained from the corresponding bootstrap distributions are; *n*, 12233 ± 1219 for Ca$_V$1.2/Ca$_V$β$_2$ WT and 6580 ± 899 for Ca$_V$1.2/Ca$_V$β$_2$ 8Ala; *γ*, 3.9 ± 0.1 pS for Ca$_V$1.2/Ca$_V$β$_2$ WT and 4.0 ± 0.1 pS for Ca$_V$1.2/Ca$_V$β$_2$ 8Ala; and $Po_{max,}$ 0.59 ± 0.02 for Ca$_V$1.2/Ca$_V$β$_2$ WT and 0.60 ± 0.02 for Ca$_V$1.2/Ca$_V$β$_2$ 8Ala; *p*-values were determined by bootstrap *t*-test.

Discussion

PPIs are involved in almost every biological process and, since their aberrancy has been implicated in several human diseases, they are rapidly emerging as pharmacological targets in drug discovery[88–93]. Therefore, determining the contact surfaces for PPIs advances our understanding of the molecular mechanisms underlying cell function and dysfunction.

In this study, we identified the PPI interface between Ca$_V$β and actin using XL-MS and protein-protein docking experiments. We generated and evaluated the functional impact of Ca$_V$β hotspot mutants with a reduced capacity to bind actin. The Ca$_V$β–actin interface displays electrostatic complementarity that was confirmed by the sensitivity of the binding reaction to the ionic strength of the buffer. Electrostatic interactions between actin-binding proteins

and the negatively charged actin surface have been frequently observed[38,94].

In cells, coexpression of $Ca_V1.2$ and the $Ca_V\beta_2$ hotspot mutant (compared with WT protein) induced a significant decrease in the macroscopic current. A combination of gating current recordings and noise analysis showed no change in the charge movement, the voltage-dependence of activation and unitary properties of the channels, indicating that impaired $Ca_V\beta_2$-actin association still allows the insertion of normal $Ca_V1.2$ channels at the plasma membrane. The fact that the ionic current reduction induced by the actin-association-deficient $Ca_V\beta_2$ mutant occurs at identical channel numbers at the cell surface and single-channel properties necessarily implies the occurrence of an increased fraction of conduction-defective channels, which contribute to gating currents but not to ionic currents. Moreover, the extent of decrease in the number of functionally available $Ca_V1.2$ channels can fully account for the current downregulation.

Based on our data, we cannot unambiguously discount $Ca_V\beta_2$ 8Ala-mediated stabilization of the null gating $Ca_V1.2$ channel mode[95–99]; however, all experimental evidence published to date shows that $Ca_V\beta$ lacks the ability to arrest channels in a silent gating mode. This mechanism has been reported for $Ca_V1.2$ inhibition by the small GTPase Rem[100]. Instead, $Ca_V\beta$ facilitates pore opening by increasing the fraction of time that the channel spends in the open state within the high open gating mode without affecting the proportions of high and low *Po* and null gating modes[98,99,101].

$Ca_V1.2$ channels at the cell surface are subjected to a highly dynamic endocytic turnover with an internalization rate of a few minutes and depending on an intact actin cytoskeleton[81,102]. Internalized $Ca_V1.2$ channels are effectively replaced by newly inserted $Ca_V1.2$ protein originating from the recycling rather than from the exocytic biosynthetic pathway on a relatively short timescale[102]. This mechanism is able to maintain a steady state level of ionic currents, despite of the constant endocytic loss of channels, for at least 20 h after inhibition of biosynthetic delivery[102]. The main finding of the present study is that an intact $Ca_V\beta$–actin interaction is strictly required to prevent the accumulation of conduction-defective channels at the plasma membrane, supporting the maintenance of stable $Ca_V1.2$ current amplitudes. We cannot unambiguously extrapolate this conclusion to the clearance of other conformationally impaired channels, since our electrophysiological measurements only detect alterations in channel permeation.

The potential source of conduction-defective $Ca_V1.2$ channels has been previously discussed[102]. Conformationally impaired plasma membrane proteins are continuously produced by local unfolding as a consequence of internal or external cellular stimuli, environmental stress, cellular insult and aging, and, in order to maintain proteostasis, they are sensed and endocytically removed[103–106]. The plethora of post-translational modifications and ligand interactions of $Ca_V1.2$ may alter the molecular environment of the channel and introduce local unfolding, including alterations in regions affecting ion permeation. Biosynthetic misfolded proteins that escaped cytosolic quality control checkpoints may also contribute to the pool of defective of channels at the plasma membrane.

A proposed quality control during $Ca_V1.2$ channel biogenesis is the interaction of the $Ca_V1.2/Ca_V\beta$ core complex with the endoplasmic reticulum membrane protein complex and $Ca_V\alpha_2\delta_1$ accessory subunit[107]. In our hands, coexpression of $Ca_V\alpha_2\delta$ along with the $Ca_V1.2/Ca_V\beta_2$ channel core complex marginally altered the biophysical properties of the channel complex and did not prevent the effect of the actin-association-deficient $Ca_V\beta_2$ mutant. Therefore, under our experimental conditions, $Ca_V\alpha_2\delta$ is neither mandatory for the channel functional assembly nor for its clearance at the plasma membrane.

We found no effect of $Ca_V\beta_4$ R482X and the actin-association hotspot mutant (as compared with wild-type $Ca_V\beta_4$) on either $Ca_V1.2$- or $Ca_V2.2$-mediated currents and no changes in their subcellular distribution. Previous reports also showed a fairly modest increase in $Ca_V2.1$ currents with $Ca_V\beta_4$ R482X in *X. laevis* oocytes, and nuclear localization comparable to the wild-type subunit[13,34]. Thus, these results did not explain the pathophysiology behind the diseased condition and led to the suggestion that a non-channel-related function of $Ca_V\beta_4$ (i.e, independent of its modulatory role on $Ca_V\alpha_1$ activity) underlies the neurological dysfunction.

Compared with the WT $Ca_V\beta_4$-core, the naturally occurring $Ca_V\beta_4$ R482X mutant associated with epilepsy appears to have a higher in vitro affinity for actin. Unfortunately, a direct comparison of the actin affinities of full-length $Ca_V\beta_4$ and $Ca_V\beta_4$ R482X in vitro was not viable because the high salt concentration required to stabilize the former precludes actin binding. In the future, it will be interesting to investigate whether an aberrant $Ca_V\beta_4$ R482X–actin interaction causes neuronal hyperactivity and hyperexcitability. This hypothesis is now testable thanks to the actin-association deficient $Ca_V\beta_4$ R482X mutant designed in the present work. It is also worth mentioning that the human $Ca_V\beta_4$ Q343E variant, annotated as potentially linked to idiopathic generalized epilepsy, is a substitution on an actin-binding hotspot identified in our work (Supplementary Table 8). Moreover, several others non-synonymous single nucleotide polymorphisms at the actin-binding hotspots in $Ca_V\beta_4$ and $Ca_V\beta_2$ have been reported, though their clinical significance is still unknown. The identification of $Ca_V\beta$-actin PPI may provide insights on factors contributing to the unresolved etiology of $Ca_V\beta$-associated disorders.

As expected from the high degree of sequence homology and similarity of three-dimensional structures among $Ca_V\beta$s, our data show conservation of the PPIs between actin and the two $Ca_V\beta$ proteins, $Ca_V\beta_2$ and $Ca_V\beta_4$. The lack of crystallographic structural data for the variable N- and C-terminal and HOOK regions within $Ca_V\beta$ prevents an assessment of the contribution of these segments to the interaction. It has been proposed that context-specific PPI networks determine the functional outcome across cellular types and that intrinsically disordered regions mediate molecular recognition in PPI networks[108,109]. Therefore, the unstructured variable regions of $Ca_V\beta$ may also regulate protein interactions and, thus, the specific biological outcome. Within this context, the clearance of $Ca_V1.2$ conducting-defective channels mediated by $Ca_V\beta_2$ expands the list of its specific functions that are not common to all members of the family[2,4].

Our results have identified the molecular interaction surface between $Ca_V\beta_2$ and actin responsible for clearing corrupted $Ca_V1.2$ channels from the plasma membrane (Fig. 9). A surveillance mechanism to monitor the conformational state of $Ca_V1.2$ at the cell surface is essential for proper calcium signaling and for maintaining proteostasis and the integrity of the cell membrane. Malfunctioning protein clearance and the consequent accumulation of damaged proteins are hallmarks of aging and neurodegenerative conditions[110,111]. The molecular model for $Ca_V\beta$–actin interaction presented here increases the potential for drug-targetable PPI interfaces in Ca_V-associated channelopathies and age-related diseases[93,112,113].

Methods

cDNA constructs and chemicals

Rat $Ca_V\beta_2$ and human $Ca_V\beta_4$ (corresponding to UniProtKB accession numbers Q8VGC3-2 and O00305-1, respectively) were used in this study. The pRSETB plasmids (Invitrogen, Carlsbad, CA, USA) containing the core regions of $Ca_V\beta_2$ (residues 23–422) and $Ca_V\beta_4$ (residues 50–408) were described previously[21,32,33]. The pRSETB vector containing the $Ca_V\beta_4$ R482X epilepsy-causing mutant (residues 1–431) was generated by overlapping PCR and standard molecular biology methods using the pRSETB $Ca_V\beta_4$ vector as a template. All recombinant proteins were expressed with a 6xHistidine tag fused to the N-terminus. $Ca_V1.2$-mNeonGreen (rabbit $Ca_V1.2$; UniProtKB accession number P15381), $Ca_V2.2$-GFP (human $Ca_V2.2$; UniProtKB Q00975-1) and the $Ca_V\beta_2$-mRFP cDNA constructs used for electrophysiology experiments were

https://doi.org/10.1038/s41467-025-59548-x

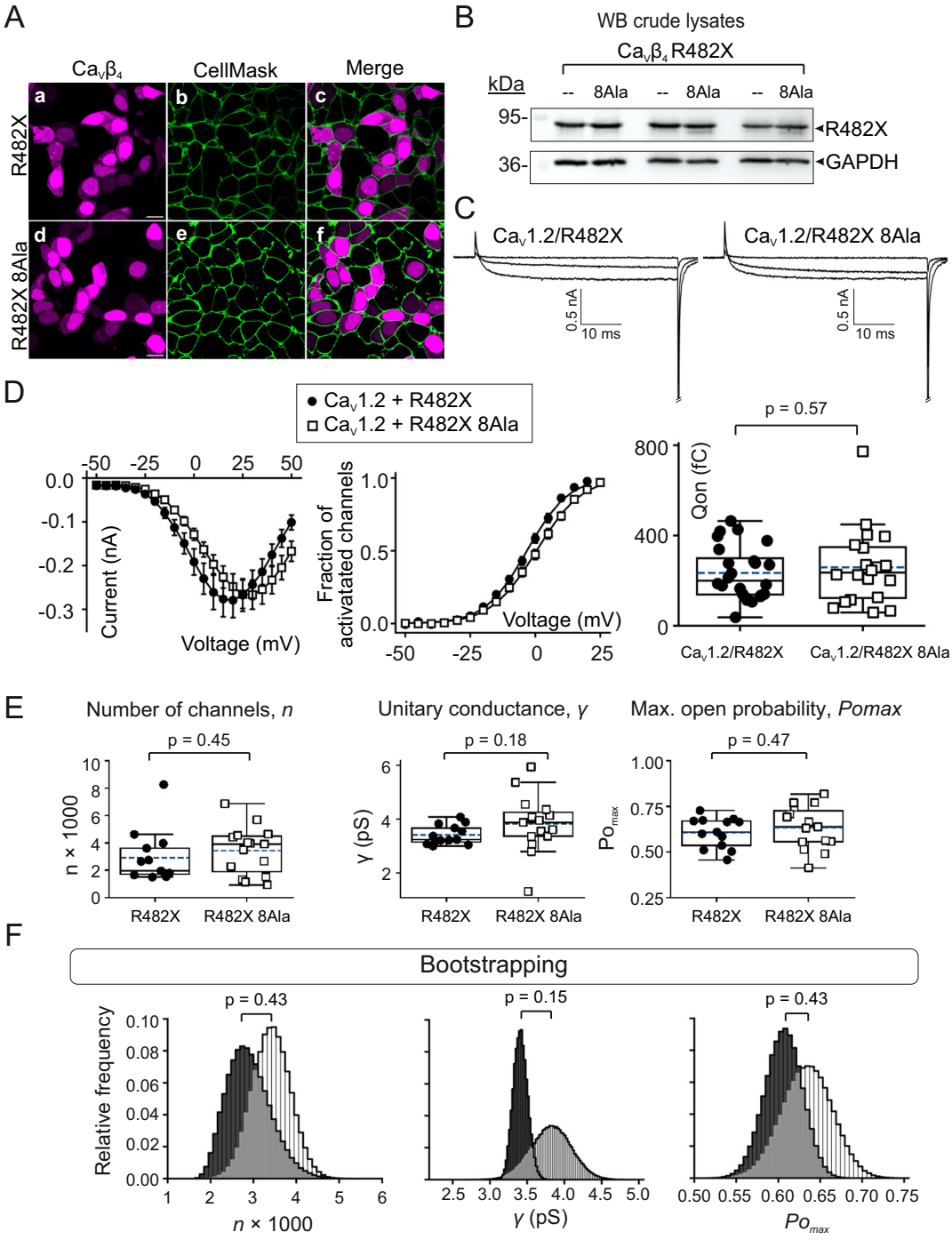

Fig. 8 | $Ca_V\beta_4$ R482X hotspots mutant keeps $Ca_V1.2$-mediated ionic current intact. A Representative laser scanning confocal images of HEK293 cells expressing either $Ca_V\beta_4$ R482X (a;c) or $Ca_V\beta_4$ R482X 8Ala (d;f) fused to mCherry. Plasma membrane was stained with CellMask™ (b;e, green). Merged images (c;f). Scale bar, 15 μm (for all images). **B** Western blot of three separate crude lysates from cells expressing either $Ca_V\beta_4$ R482X (--) or the 8Ala mutant (8Ala) probed with anti-$Ca_V\beta_4$ and anti-GAPDH antibodies. Uncropped images are shown in Supplementary Fig. 18A. **C** Representative ionic current traces (induced by −35, +20, and +45 mV pulses) from cells co-expressing $Ca_V1.2$ with either $Ca_V\beta_4$ R482X or $Ca_V\beta_4$ R482X 8Ala. **D** Plots of ionic current and fraction of activated channels versus voltage, and total charge movement (*Qon*) from the indicated channel subunit combinations. Ionic currents were elicited by voltages of −50 to +50 mV in 5 mV increments from a holding potential of −90 mV; data are presented as mean ± SEM. In the box plot, the edges represent interquartile ranges (25th–75th percentiles), the continuous and dashed lines, the median and mean values and whiskers denote 1.5× the interquartile range. Each data point represents an individual recorded cell. Qon mean values ± SEM: 234 ± 24 fC and 259 ± 37 fC (number of cells = 24 and 20) for $Ca_V1.2/Ca_V\beta_4$ R482X and $Ca_V1.2/Ca_V\beta_4$ R482X 8Ala, respectively. **E** Box plots for *n*, *γ*, and Po_{max} for the indicated channel subunit combinations with interquartile ranges (25th–75th percentiles), median (continuous line), mean (dashed lines) and whiskers (1.5× the interquartile range). Each individual data point represents an individual recorded cell (number of cells = 13 and 15 for $Ca_V1.2/Ca_V\beta_4$ R482X and $Ca_V1.2/Ca_V\beta_4$ R482X 8Ala, respectively); *p*-values, unpaired two-tailed *t*-test. **F** Bootstrap distributions from the data shown in panel (**E**). Bootstrap sample N = 500,000. The mean values for *n*, *γ*, and Po_{max} are: *n*, 2901 ± 509; *γ*, 3.4 ± 0.1 pS and Po_{max}, 0.61 ± 0.02 for $Ca_V1.2/Ca_V\beta_4$ R482X, and *n*, 3425 ± 437; 3.8 ± 0.3 pS and 0.63 ± 0.03 for $Ca_V1.2/Ca_V\beta_4$ R482X 8Ala; *p*-values, bootstrap *t*-test.

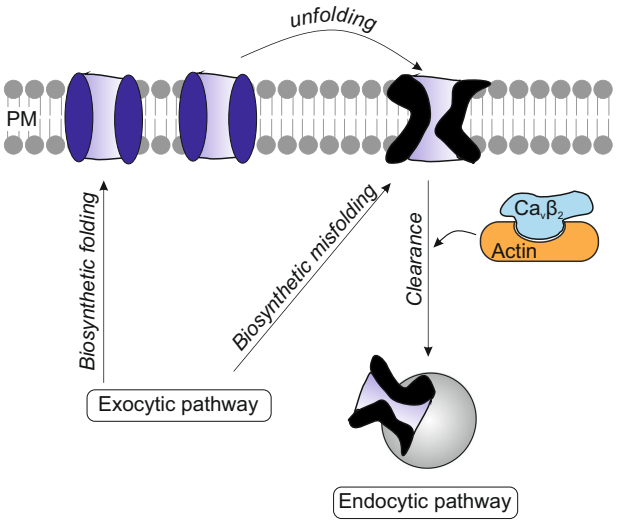

Fig. 9 | Model for the clearance of corrupted Ca$_V$1.2 channels from the plasma membrane. Conformationally impaired Ca$_V$1.2 proteins at the plasma membrane can be generated by diverse cellular stimuli, which change the channel environment leading to local unfolding, or by exocytic insertion of misfolded channels that evade cytosolic quality control (biosynthetic misfolding). Ca$_V$β–actin interaction is mandatory for the endocytic removal of corrupted Ca$_V$1.2 channels, which prevents their build-up and maintains stable Ca$_V$1.2 currents, but not for the insertion of functionally folded channels. PM, plasma membrane.

described previously[32,33,81]. Rabbit skeletal muscle actin protein (UniProtKB accession number P68135) and the actin-binding protein Biochem kit were purchased from Cytoskeleton (Denver, CO, USA). The mass spectrometry cleavable cross-linkers DSBU and DSSO were purchased from Thermo Fischer Scientific (Langerwehe, Germany). Key reagents and antibodies are listed in Supplementary Table 9.

Mutagenesis

The Ca$_V$β$_2$-core 8Ala, Ca$_V$β$_2$-core 6Ala, Ca$_V$β$_4$ R482X 8Ala, and Ca$_V$β$_4$ R482X 6Ala constructs were generated by overlapping PCR and standard molecular biology methods using the pRSETB Ca$_V$β$_2$-core and pRSETB Ca$_V$β$_4$ R482X vectors as templates for the Ca$_V$β$_2$ and Ca$_V$β$_4$ mutants, respectively. Ca$_V$β$_2$ 8Ala-mRFP was inserted into the p156rrl vector in a similar way as for pRSETB Ca$_V$β$_2$-core 8Ala, but using the p156rrl Ca$_V$β$_2$-mRFP plasmid as a template. Likewise, Ca$_V$β$_4$ R482X 8Ala-mCherry was inserted into the Fsy1.1 GW vector using Fsy1.1 GW Ca$_V$β$_4$ R482X mCherry plasmid as a template.

Expression and purification of Ca$_V$βs

Recombinant Ca$_V$β subunits were expressed in *E. coli* and purified from the soluble fraction of crude lysate using Ni^{2+}-affinity chromatography (HisTrap™, Cytiva), followed by size exclusion chromatography using a Superdex-200 16/60 column (Cytiva), as described previously[32,33]. Both chromatographic steps were done using a Fast Performance Liquid Chromatography (FPLC) ÄKTA™ system (ÄKTA™ pure, Cytiva). Fractions eluted from the Superdex-200 column equilibrated with GF-150 buffer (150 mM NaCl, 20 mM phosphate, pH 8) for Ca$_V$β$_2$-core WT and mutants or GF-300 buffer (300 mM NaCl, 20 mM phosphate, pH 8) for Ca$_V$β$_4$-core, Ca$_V$β$_4$ R482X, and the alanine mutants were pooled, concentrated, flash frozen, and stored at −80 °C until use. Rabbit skeletal muscle actin protein was prepared and polymerized according to the manufacturer's instructions (Cytoskeleton).

Chemical cross-linking and protein digestion

Ca$_V$β$_2$-core and polymerized actin were cross-linked. For this, Ca$_V$β protein in GF-150 buffer was centrifuged at 150,000 × *g* for 45 minutes at 4 °C to remove aggregates. The supernatant was transferred to a new tube and stored for cross-linking reactions. Ca$_V$β (5 μg) and actin (5 μg) were mixed and incubated at RT for 30 minutes to enable interaction. A molar excess of 5× for DSBU or 2.5× for DSSO was added and the reaction mix was incubated for 60 minutes at RT. The reaction volume was 50 μl. Control reactions were performed by incubating each protein alone with and without cross-linker and both proteins together without cross-linker. The reactions were then quenched by the addition of Tris-HCl pH 8 to a final concentration of 50 mM. The cross-linked products were then analyzed by SDS-PAGE. After staining the gel with R-250 Coomassie blue, the desired bands were excised, dehydrated, and stored at -20 °C until use. The protein bands were cut into small pieces and reduced in 20 mM dithiothreitol for 30 minutes at 56 °C, cooled to RT, and then alkylated with 10 mM iodoacetamide for 30 minutes in the dark. Samples were then digested overnight at 37 °C with MS-grade approved trypsin (SERVA, Germany) using an enzyme:protein ratio of 1:50. Peptides were desalted using home-made C18 STAGE-Tips[114].

LC-MS/MS analysis

Digested peptides were analyzed using an EASY-nanoLC coupled to a Q Exactive Plus (DSBU samples) or Orbitrap Eclipse mass spectrometer (DSSO samples) (Thermo Fisher Scientific) with a nanospray source. Peptides were separated in a 50 cm long, self-packed column containing 1.9 μm C18-AQ Reprosil-Pur beads (Dr. Maisch) and the column temperature was maintained at 50 °C in a column oven (PRSO-V2). Peptides were eluted with an effective solvent gradient of 2–35% buffer B within 30 or 60 minutes for DSBU and DSSO, respectively.

To identify DSBU/DSSO cross-links, digested proteins were analyzed using a higher-energy collision dissociation and collision-induced dissociation-acquisition method. Full scans were recorded at resolution of 70,000 and a scan range of 375–1750 m/z (AGC 3.6e6, max injection time 20 ms). MS/MS scans were recorded at a resolution of 35,000 and a scan range of 200–2000 m/z (AGC 5e5, max injection time 115 ms for CID isolation width 1.9 m/z). Singly and doubly charged ions were excluded from fragmentation because cross-linked peptides tend to occur at a charge state of 3+ or above. All selected precursors were excluded from fragmentation for 20 seconds.

Cross-link identification

Raw MS data were converted to the *mzML* format with ProteoWizard Toolkit version 3[115]. Cross-linked peptide fragments were subsequently identified using Merox v.2.0, MetaMorpheus v.1.0.2, and MaxLynx v.2.2.0.0[39–41]. Fasta sequence files for Ca$_V$β$_2$-core (residues 23–422) and actin (corresponding to UniProtKB accession numbers Q8VGC3-2 and P68135, respectively) were provided and searches were performed using the following settings: 10 ppm as precursor, 20 ppm as fragment ion precision, CSM-level false discovery rate of 0.01, fixed modification of cysteine carbamidomethylation, and variable modifications of N-terminus acetylation and methionine oxidation, with up to three missed tryptic cleavages allowed. Contaminant protein databases provided by the software packages were included in the searches.

Cross-link filtering

The identified unique intermolecular cross-links identified by LC-MS/MS were examined on the DisVis webserver (version 2.3.0) to check the consistency of the cross-link dataset and quantify the information content of the corresponding distance restraints[42,43]. The identified cross-linked residues mapped to a narrow cluster on Ca$_V$β$_2$ and to two discrete patches on different accessible surfaces of the actin monomer. The latter forms a continuous patch exposed across two adjacent actin subunits on one surface of an actin protofilament. Hence, the input files used for DisVis analysis were two adjacent actin subunits (*n* and *n* + 2 or chains A and C, respectively, from PDB 5OOE) as the

fixed chain and $Ca_V\beta_2$ (PDB 5V2P) as the scanning chain[113,116]. Distance restraints were defined considering that the $Ca_V\beta_2$/actin cross-links can be formed with either monomer of two adjacent actin subunits. The allowed distance range of these restraints was set to 0–30 Å to account not only for the lengths of the Lys side chains and the cross-linker, but also for conformational dynamics[117,118] and potential errors in the side chain crystallographic position[55]. The same upper bound distance was used for all XL-MS-derived distance restraints, as some inter-XLs were identified with both DSSO and DSBU. DisVis filtering was applied iteratively: in each step, restraints with a high probability of being false positives were discarded and the remaining restraints were used as subsequent input for the next DisVis iteration. This multistep filtering procedure resulted in a set of self-consistent distance restraints from the XL-MS data that were used to guide protein-protein docking with the HADDOCK 2.4 webserver[44,45]. Structural analysis and visualization were carried out with Visual Molecular Dynamics, VMD (version 1.9.3)[119].

Bioinformatics predictions

The XL-MS derived distance restraints are long range (~30 Å for the DSSO and DSBU cross-linkers). Therefore, additional information on the putative interfaces was used to guide docking, i.e., from bioinformatics predictions[118,120,121]. First, we used NACCESS (version 2.1.1) to identify residues with solvent accessibility of ≥ 40% in each protein[122]. Then, the list of NACCESS residues was filtered in DisVis using complete scanning of the dimeric actin and $Ca_V\beta_2$ structures and the set of identified self-consistent XL-MS derived distance restraints[42,43]. Residues predicted to have an interaction fraction of > 0.5 in each protein were kept. However, for $Ca_V\beta_2$ such filtering yielded only putative interacting residues in the GK domain because all XL-MS derived distance restraints were located in this domain. Therefore, prediction of additional putative protein-protein interface residues in the $Ca_V\beta_2$ SH3 domain and in actin was carried out using the Consensus Prediction Of interface Residues in Transient complexes (CPORT) webserver (version 0.2.0)[123]. The list of CPORT-predicted actin residues was manually curated to select residues facing the same side of the filament as the cross-linked residues. The manually curated list of CPORT residues for $Ca_V\beta_2$ SH3 and actin, and the DisVis-filtered list of NACCESS residues for $Ca_V\beta_2$ GK and actin were used as active residues for the information-driven docking of both proteins.

Protein-protein docking

The X-ray structure of rat $Ca_V\beta_2$ (PDB 5V2P)[113] or rat $Ca_V\beta_4$ (PDB 1VYV)[26] and a dimeric structure of rabbit skeletal muscle actin (extracted from PDB 5OOE) were used for XL-MS-guided protein-protein docking on the HADDOCK 2.4 webserver[44,45]. The sequence identity between rat (used for docking) and human $Ca_V\beta_4$ (used for experimental assays) is 98.8%. Distance restraints were defined using a hybrid protocol. Unambiguous restraints were defined using the DisVis-filtered distance restraints between $Ca_V\beta_2$ and actin, allowing a Cα-Cα distance between cross-linked residues of 0–30 Å[55,117,118]. The same upper bound distance was used for all XL-MS-derived distance restraints, as some inter-XLs were identified with both DSSO and DSBU. In addition, ambiguous restraints were defined using the bioinformatics-predicted residues as active residues, as explained above[42,43] and a center of mass restraint was included to enforce contact between the two partners. The docking calculation comprises three stages: (i) rigid body docking to generate 1000 initial protein-protein complex structures; (ii) semi-flexible simulated annealing simulation with flexible interface residues to refine the 200 best-scored poses from stage (i); and (iii) a final refinement of those 200 poses with a 2.5 ns molecular dynamics simulation in water in which the two proteins are fully flexible. The final 200 docking structures were clustered based on the (positional) interface ligand RMSD. This i-l-RMSD was calculated by first superimposing the docking structures on the flexible interface backbone atoms of actin and then calculating the RMSD on the flexible interface backbone atoms of $Ca_V\beta$, with the flexible interface defined by default as all residues that make intermolecular contacts within 5 Å, considering all docking models. HADDOCK default clustering parameters were used, specifically an i-l-RMSD cutoff value of 7.5 Å and a number of neighbors of 4. The clusters thus obtained were ranked based on the average HADDOCK score of their top four members. Such HADDOCK score was calculated as $1.0\,E_{vdw} + 0.2\,E_{elec} + 1.0\,E_{desol} + 0.1\,E_{air}$, where the terms E_{vdw} and E_{elec} represent the van der Waals and electrostatic intermolecular energies, E_{desol} the desolvation energy and E_{air} the distance restraints energy. The latter includes violations of both the unambiguous restraints (i.e., the XL-MS-derived distance restraints) and of the ambiguous restraints (here based on bioinformatics predictions).

Besides the i-l-RMSD used for clustering, we further assessed model similarity by calculating additional RMSD-based metrics[46,47,124]. The global RMSD is calculated using the alpha carbon atoms of all residues of both proteins and thus provides information on the overall complex similarity of the docking models with respect to the best scored model (instead of only the $Ca_V\beta$ residues predicted to form the PPI surface for the i-l-RMSD). The interface RMSD (i-RMSD) is the backbone RMSD of all interface residues of both proteins (defined using an interatomic distance of 10 Å), after superimposing these interfacial residues. Complementarily, the ligand RMSD (l-RMSD) is the backbone RMSD calculated on $Ca_V\beta$ after fitting on actin. Whereas the i-RMSD provides information on the similarity of the PPI surfaces of both actin and $Ca_V\beta$, the l-RMSD gives an idea of the position and orientation of $Ca_V\beta$ on the surface of actin. For all RMSD calculations described below, the reference structure is the top model with the best (lowest) HADDOCK score, unless otherwise stated.

The cluster with the best average HADDOCK score was selected for further analysis. In case of several clusters with HADDOCK scores within standard deviation of the top cluster, we compared the clusters with overlapping HADDOCK scores and selected the best one based on additional experimental information. For each cluster, the docking structures were checked for consistency with the XL-MS derived distance restraints by calculating the Cα-Cα distance for each $Ca_V\beta$–actin pair of the set of self-consistent inter-XLs. In addition, for the top cluster of the $Ca_V\beta$–actin docking simulation, we evaluated the residue contact frequency as the number of structures in the top cluster in which residue *i* of one protein partner is within 5 Å of the other protein in the complex, and then normalized by the total number of structures in the top cluster. We assumed that residues with higher contact frequencies have a higher probability of being located at the protein-protein interface, as previously reported[123,125]. The electrostatic potential of each protein partner was calculated using the corresponding crystal structure and the APBS webserver (version 3.4.1)[126].

Control docking simulations

To validate the integration of XL data in our protein-protein docking protocol, we performed several docking simulations without XL-MS-derived distance restraints. To ensure close proximity of the two proteins, these simulations made use of the ab initio docking options of HADDOCK, as summarized in Supplementary Table 6. In addition, to account for the ambiguity of the XL-MS data, which cannot distinguish whether the cross-linked residues on the actin surface come from either one or two actin subunits, we also performed a docking simulation with $Ca_V\beta_2$ and one single actin monomer. DisVis filtering was performed as described in section "Cross-link filtering", but using the structure of only one actin subunit as fixed chain (chain A from PDB 5OOE) and defining XL-MS-derived distance restraints with this single actin monomer. The distance restraints classified by DisVis as self-consistent were employed as unambiguous restraints in HADDOCK, together with ambiguous restraints based on bioinformatics analyzes. For the latter, active residues were defined as explained in section "Bioinformatics predictions",

using NACCESS[122] and CPORT[123] for prediction of putative protein-protein interface residues between monomeric actin and the GK and SH3 domains of $Ca_V\beta_2$, respectively.

Computational alanine scanning

The top four structures of the selected HADDOCK cluster were analyzed using computational alanine scanning to predict putative hotspots (i.e., residues at the $Ca_V\beta$–actin interaction surface that most contribute to the binding energy of the complex). A set of six different webtools was used to calculate ΔΔG; three are based on empirical energy functions (Anchor, BUDE Alanine Scan, and Robetta), and three on machine-learning-trained statistical potentials (BeAtMuSiC, Mutabind2, and SAAMBE-3D)[67–73]. Residues were ranked according to the ΔΔG values averaged over the four docked structures analyzed (to account for protein flexibility) and then over the six webtools used (to obtain a consensus prediction).

The eight $Ca_V\beta$ hotspots selected for experimental validation were further characterized using the PRODIGY webserver (version 2.2.2)[127,128]. Intermolecular contacts between the $Ca_V\beta$ hotspots and actin residues were considered to be present if any of their heavy atoms is within a distance of 5.5 Å. As done for the computational alanine scanning analysis, the top 4 models of the first cluster were analyzed for each actin–$Ca_V\beta$ docking calculation, in order to account for protein dynamics.

In vitro F-actin cosedimentation assay

F-actin cosedimentation assays were performed according to the manufacturer's instructions (except that Tris-HCl was replaced by HEPES in the polymerization buffer), as previously described[32,33]. Actin was polymerized by incubation in actin-polymerizing buffer containing 0.2 mM $CaCl_2$, 50 mM KCl, 2 mM $MgCl_2$, 1 mM ATP, and 5 mM HEPES, pH 8.0. Recombinant $Ca_V\beta$ proteins were incubated with polymerized actin in polymerization buffer (50 µl reaction volume), followed by high-speed centrifugation for 20 minutes at 150,000 × *g* and 4 °C. The supernatant and pellet fractions were resolved by denaturing SDS-PAGE. Control reactions contained $Ca_V\beta$ alone to quantify protein sedimentation in the absence of actin. Phalloidin was used in all experiments at a concentration of 25 µM to stabilize actin filaments. Raw intensities of protein bands were estimated by densitometry using Fiji ImageJ software (version 1.44p)[129]. The association of $Ca_V\beta$ proteins with F-actin was reported as the fraction of bound $Ca_V\beta$, as calculated from the ratio of band intensities of pelleted over total protein (i.e., protein found in supernatant and pellet).

Pull down assays

GST fused to the AID peptide (GST-AID) or GST alone (negative control) was used as bait in a standard GST pull down assay, as previously described[130]. Briefly, GST-AID or GST was immobilized onto glutathione-Sepharose beads and then incubated with the desired $Ca_V\beta$ constructs at RT. After several washing steps, bound proteins were eluted with SDS-loading buffer and resolved by SDS-PAGE.

Intrinsic fluorescence spectroscopy

Intrinsic fluorescence experiments were performed using a FS5 Fluorescence Spectrometer (Edinburgh Instruments, UK) equipped with a 500 µl cuvette coupled to a SC-25 temperature holder and a TC-1S temperature controller (Quantum Northwest, WA, USA). Excitation was done at 280 nm over a temperature range of 20–74 °C and emission spectra were recorded at 300–430 nm in 1 nm steps. For data analysis, the spectral center of mass (CM) was determined as follows, and plotted against the temperature:

$$CM_i = \frac{\sum_i F_i \lambda_i}{\sum_i F_i} \quad (1)$$

where F is the fluorescence intensity and λ the wavelength at a temperature i.

Transition temperatures were then obtained by non-linear regression fitting using a two-state transition model:

$$y = \frac{\alpha_n + \beta_n T}{1 + e^{\frac{4T_m(T-T_m)}{T\Delta T}}} + \frac{\alpha_d + \beta_d T}{1 + e^{\frac{4T_m(T_m-T)}{T\Delta T}}} \quad (2)$$

where y is CM, α and β are the y-intercept and slope of the native (N) or denatured (D) states, respectively, T is the temperature, T_m the is the transition temperature, ΔT is the width of the transition, and e is the exponential function.

Cell culture and transfection

HEK293 cells were cultured in Dulbecco's modified Eagle medium supplemented with 10% fetal bovine serum (Sigma-Aldrich, Darmstadt, Germany) and L-glutamine (2 mM), and incubated in a 5% CO_2 atmosphere. For electrophysiological experiments, cells were seeded onto 50 mm dishes and transfected using Lipofectamine 2000 (Thermo Fisher Scientific) following the manufacturer's instructions using 3 µg of $Ca_V1.2$-mNeonGreen and 1 µg of $Ca_V\beta_2$-mRFP (WT or 8Ala mutant) expression constructs, or 4 µg of $Ca_V2.2$-GFP with 2 µg of $Ca_V\beta_4$-mCherry (WT, R482X or R482X 8Ala). For western blot analysis, the same protocol was followed except that cells were transfected with only the wild-type and mutant $Ca_V\beta$s expression constructs. For laser scanning confocal fluorescence microscopy, HEK293 cells were seeded onto 35 mm glass-bottom dishes (µ-Dish ibidi, Ibidi, Gräfelfing, Germany) and transfected with 2 µg of the corresponding $Ca_V\beta$ expression constructs using also Lipofectamine 2000 (Thermo Fisher Scientific).

Western blot analysis of cell lysates

Cells were lysed using RIPA buffer supplemented with a protease inhibit cocktail (Sigma-Aldrich). Lysates were clarified by centrifugation and soluble proteins were resolved by SDS-PAGE. Proteins were then blotted onto nitrocellulose membrane (GE Healthcare, Life Science, Solingen, Germany) for 1 h. Membranes were blocked in 5% BSA in TBS buffer (10 mM Tris, 150 mM NaCl, pH 7.5) and incubated with the primary antibodies, anti-CACNB2 (Novus Biologicals, Wiesbaden Nordenstadt, Germany), anti-CACNB4 (Novus Biologicals, Wiesbaden Nordenstadt, Germany) and anti-GADPH (Cell Signaling, Leiden, Netherlands). After several washes, membranes were incubated with a goat anti-rabbit IgG HRP-conjugated secondary antibody (Thermo Fisher Scientific). Protein bands were detected using a chemiluminescent detection kit (SuperSignal West Femto Chemiluminescent Substrate, Thermo Fisher Scientific).

Laser scanning confocal fluorescence microscopy

Confocal imaging of live HEK293 cells transiently transfected with $Ca_V\beta_2$-mRFP constructs (wild-type and 8Ala mutant) and $Ca_V\beta_4$-mCherry (R482X and R482X 8Ala mutant) was performed using an inverted Leica confocal microscope equipped with a 63× oil immersion objective lens. Images were acquired 18–24 h post-transfection. Before imaging, cells were stained with the plasma membrane marker CellMask™ Green (Thermo Fisher Scientific) following the manufacturer's instructions. mRFP and mCherry fusion proteins were excited using a 594-nm laser, and emission was detected in the 600–650 nm range. CellMask™ Green was excited at 514 nm, and emission was monitored in the 520–540 nm range. Colocalization analysis was conducted by calculating the Mander´s overlap coefficient using the JACoP plugin integrated into ImageJ 1.44p software, as previously described[130,131]. For each protein, 8–10 different fields of view, derived from two independent transfections and comprising 150–250 transfected cells, were analyzed. Statistical comparison between samples was performed using a two-tailed Student's *t*-test. All values are presented as mean ± SEM. For imaging actin filaments, cells

were seeded on coverslips and stained with Phalloidin-Atto 488 (Sigma-Aldrich) as described[102]. Briefly, control and cytochalasin D-treated cells were fixed with 4% PFA, and simultaneously permeabilized, blocked and incubated with phalloidin using 5% chemiBLOCKER (Merck) supplemented with 0.05% Triton-X100. After several washes, the coverslips were mounted on glass slides using Aqua-Poly-Mount (Polysciences) and imaged the next day.

Electrophysiology

Whole-cell patch clamp recordings of cells transiently coexpressing either $Ca_V1.2$-mNeonGreen or $Ca_V2.2$-GFP with $Ca_V\beta_2$-mRFP or $Ca_V\beta_4$-mCherry derivatives expression constructs were performed 24 h after transfection using the EPC-10 amplifier equipped with PatchMaster software (HEKA Elektronik, Stuttgart, Germany). Fusion of the channel subunits to the fluorescence proteins (mNeonGreen, mRFP and mCherry) enable the recognition of transfected cells. Recording and analysis were done blind with respect to the $Ca_V\beta$ construct used.

Ionic currents were elicited by 60 ms voltage steps from +50 mV to +70 mV in 5 mV increments from a holding potential of -90 mV and using Ba^{2+} as the charge carrier. Gating currents were recorded during voltage steps near to the reversal potential for Ba^{2+}, as determined empirically by stepping to different potentials in 2 mV increments[79,81]. The total charge movement was obtained by integrating the *On* gating current elicited at the reversal potential for Ba^{2+} over time. Borosilicate glass patch pipettes (Harvard Apparatus, Holliston, MA, USA) were pulled using a Sutter P-1000 puller (Harvard Apparatus) and fire-polished using a Narishige MF-830 microforge (Tokyo, Japan). Patch pipettes with an electrical resistance of 1.0–2.0 MΩ were used. Series resistance compensation was applied, resulting in a voltage error of > 5 mV. The pipette solution contained 135 mM cesium methanesulfonate, 10 mM EGTA, 5 mM CsCl, 1 mM $MgCl_2$, and 10 mM HEPES, adjusted to pH 7.3 with CsOH. The extracellular recording solution contained 140 mM tetraethylammonium-$MeSO_3$, 10 mM $BaCl_2$, and 10 mM HEPES buffer, adjusted to pH 7.3 with tetraethylammonium hydroxide. Data were analyzed with Python version 3.8 using common libraries including NumPy, Pandas, Pyplot, SciPy, and Seaborn and presented as the mean ± SEM. Differences between data sets were analyzed using the *t*-test. For the pharmacological treatment with cytochalasin D (Sigma-Aldrich), cells expressing the corresponding $Ca_V1.2/Ca_V\beta_2$ complexes were incubated for 40 min with 10 μM of cytochalasin D, as described[32].

The voltage dependence of the relative open probabilities ($P_{open}(V)$) was calculated by normalizing steady-state current amplitudes to the maximal value (I/Imax) and fitted with a Boltzmann function to obtain the half-activation voltage ($V_{1/2}$) (Eq. 3).

$$P_{open}(V) = \frac{1}{1 + e^{\frac{-(V_m - V_{1/2})}{k}}} \tag{3}$$

where V_m is the membrane potential, V_{rev} is the reversal potential, and k is the slope.

Stationary noise variance analysis

Analysis of the variance (σ^2) of the mean macroscopic current ($\langle I \rangle$) of repeated current recordings obtained at different voltages was performed as previously described[86]. Currents were elicited by 150 ms voltage steps from +50 mV to +70 mV in 5 mV increments from a holding potential of −90 mV and using Ba^{2+} as the charge carrier. The number of functional channels and unitary conductance were computed for each cell. Since the unitary (single-channel) conductance of Ca_Vs does not change with voltage[95,132,133] and, therefore, the single-channel current (i) varies linearly with the driving force, i is given by Eq. 4 and the ionic current recorded through a defined population of ion channels by Eq. 5,

$$i = \gamma(V_m - V_{rev}) \tag{4}$$

$$I = n \times \gamma(V_m - V_{rev}) \times Po \tag{5}$$

where n is the number of functionally available channels unitary channel conductance, γ is the unitary conductance, $(V_m - V_{rev})$ is the driving force (where V_m is the applied membrane potential and V_{rev} the reversal potential), and Po is the probability of the channel being in the open state.

In this case, the relationship between the variance and mean macroscopic current ($\langle I \rangle$) is given by Eq. 6 [86], and the number of functionally available channels n and the unitary conductance γ are obtained by fitting the data.

$$\frac{\sigma^2}{\langle I \rangle (V_m - V_{rev})} = -\frac{1}{n}\left(\frac{\langle I \rangle}{V_m - V_{rev}}\right) + \gamma \tag{6}$$

Having determined *n and γ*, the maximum open probability of the channel (Po_{max}) is obtained from Eq. 7.

$$Po_{\max} = \frac{I_{\max}}{n \times i} \tag{7}$$

Values for the three parameters, n, γ, and Po_{max}, obtained from the original set of data were subjected to bootstrap iterations[87], in which random samples with replacements were taken from the original set of measurements to generate a synthetic distribution for each parameter. This procedure was repeated 500,000 times and the reported values are given by the mean value and SD. Differences between data sets were analyzed using a bootstrap *t*-test.

Electrophysiological data were analyzed using Python 3.8. Parameters estimated from the noise analysis were compared using a bootstrap *t*-test. All data are presented as mean ± SEM. Box-and-whisker plots show the interquartile range (IQR), median, and the 25th (Q1) and 75th (Q3) percentiles. Whiskers extend to 1.5 times the IQR below Q1 and above Q3. Normality was assessed using the Shapiro-Wilk test. Statistical significance between groups was assessed using a two-tailed *t*-test.

Reporting summary

Further information on research design is available in the Nature Portfolio Reporting Summary linked to this article.

Data availability

The following protein sequences were used in this study: rat $Ca_V\beta_2$, UniProtKB Q8VGC3-2 [https://www.uniprot.org/uniprotkb/Q8VGC3] human $Ca_V\beta_4$ UniProtKB O00305-1 [https://www.uniprot.org/uniprotkb/O00305] rabbit $Ca_V1.2$, UniProtKB human $Ca_V2.2$, UniProtKB Q00975-1 [https://www.uniprot.org/uniprotkb/Q00975] human $Ca_V\alpha_2\delta_1$, UniProt P54289-1 [https://www.uniprot.org/uniprotkb/P54289] rabbit skeletal muscle actin, UniProtKB P68135. Raw mass spectrometry and search data have been deposited to the ProteomeXchange Consortium via the PRIDE partner repository[134] with the dataset identifiers PXD053456 (DSBU) and PXD053481 (DSSO) respectively. Data required to reproduce the docking results and resulting $Ca_V\beta$-F/actin complex models, along with the source data underlying Supplementary Figs 4, 6, 9, 13 and 14 and Supplementary Tables 4 and 6, are available at Zenodo [https://doi.org/10.5281/zenodo.8276447]. The following experimental protein structures were used for the docking calculations: rabbit skeletal muscle actin, PDB 5OOE; rat $Ca_V\beta_2$, PDB 5V2P; rat $Ca_V\beta_4$, PDB 1VYV.

The source data underlying Figs. 3E, 4D, 5E, 6B, D, E, 7A, B and 8D, E and Supplementary Figs. 2B, 11B, 15B, 16B, C, 17 and 18C are

provided as a source data file. Source data are provided with this paper.

References

1. Catterall, W. A. Voltage-gated calcium channels. *Cold Spring Harb. Perspect. Biol.* **3**, a003947 (2011).
2. Hidalgo, P. & Neely, A. Multiplicity of protein interactions and functions of the voltage-gated calcium channel β-subunit. *Cell calcium* **42**, 389–396 (2007).
3. Neely, A. & Hidalgo, P. Structure-function of proteins interacting with the α_1 pore-forming subunit of high-voltage-activated calcium channels. *Front. Physiol.* **5**, 209 (2014).
4. Rima, M. et al. Protein partners of the calcium channel β-subunit highlight new cellular functions. *Biochemical J.* **473**, 1831–1844 (2016).
5. Buraei, Z. & Yang, J. Structure and function of the beta subunit of voltage-gated Ca(2)(+) channels. *Biochimica et. biophysica acta* **1828**, 1530–1540 (2013).
6. Muller, C. S. et al. Quantitative proteomics of the Ca_V2 channel nano-environments in the mammalian brain. *Proc. Natl Acad. Sci. USA* **107**, 14950–14957 (2010).
7. Zamponi, G. W., Striessnig, J., Koschak, A. & Dolphin, A. C. The physiology, pathology, and pharmacology of voltage-gated calcium channels and their future therapeutic potential. *Pharm. Rev.* **67**, 821–870 (2015).
8. Bidaud, I. & Lory, P. Hallmarks of the channelopathies associated with L-type calcium channels: a focus on the Timothy mutations in Ca(v)1.2 channels. *Biochimie* **93**, 2080–2086 (2011).
9. Wemhoner, K. et al. Gain-of-function mutations in the calcium channel CACNA1C (Cav1.2) cause non-syndromic long-QT but not Timothy syndrome. *J. Mol. Cell. Cardiol.* **80**, 186–195 (2015).
10. Andrade, A. et al. Genetic associations between voltage-gated calcium channels and psychiatric disorders. *Int. J. Mol. Sci.* **20**, 3537 (2019).
11. Lorenzon, N. M. & Beam, K. G. Disease causing mutations of calcium channels. *Channels (Austin, Tex.)* **2**, 163–179 (2008).
12. Lorenzon, N. M. & Beam, K. G. Calcium channelopathies. *Kidney Int* **57**, 794–802 (2000).
13. Escayg, A. et al. Coding and noncoding variation of the human calcium-channel beta4- subunit gene CACNB4 in patients with idiopathic generalized epilepsy and episodic ataxia. *Am. J. Hum. Genet.* **66**, 1531–1539 (2000).
14. Coste de Bagneaux, P. et al. A homozygous missense variant in CACNB4 encoding the auxiliary calcium channel beta4 subunit causes a severe neurodevelopmental disorder and impairs channel and non-channel functions. *PLoS Genet* **16**, e1008625 (2020).
15. Trus, M., Servili, E., Taieb-Cohen, T. & Atlas, D. Autism associated mutations in β(2) subunit of voltage-gated calcium channels constitutively activate gene expression. *Cell calcium* **108**, 102672 (2022).
16. Cordeiro, J. M. et al. Accelerated inactivation of the L-type calcium current due to a mutation in CACNB2b underlies Brugada syndrome. *J. Mol. Cell. Cardiol.* **46**, 695–703 (2009).
17. Buraei, Z. & Yang, J. The β-subunit of voltage-gated Ca^{2+} channels. *Physiol. Rev.* **90**, 1461–1506 (2010).
18. Cruz-Garcia, Y. et al. Nanoenviroments of the β-subunit of L-type voltage-gated calcium channels in adult cardiomyocytes. *Front. Cell Developmental Biol.* **9**, 724778 (2021).
19. Skinnider, M. A. et al. An atlas of protein-protein interactions across mouse tissues. *Cell* **184**, 4073–4089 (2021).
20. Takahashi, S. X., Miriyala, J., Tay, L. H., Yue, D. T. & Colecraft, H. M. A $Ca_V\beta$ SH3/guanylate kinase domain interaction regulates multiple properties of voltage-gated Ca^{2+} channels. *J. Gen. Physiol.* **126**, 365–377 (2005).
21. Gonzalez-Gutierrez, G. et al. The guanylate kinase domain of the β-subunit of voltage-gated calcium channels suffices to modulate gating. *Proc. Natl Acad. Sci. USA* **105**, 14198–14203 (2008).
22. Opatowsky, Y., Chomsky-Hecht, O., Kang, M. G., Campbell, K. P. & Hirsch, J. A. The voltage-dependent calcium channel beta subunit contains two stable interacting domains. *J. Biol. Chem.* **278**, 52323–52332 (2003).
23. Pragnell, M. et al. Calcium channel β-subunit binds to a conserved motif in the I-II cytoplasmic linker of the α_1-subunit. *Nature* **368**, 67–70 (1994).
24. Van Petegem, F., Clark, K. A., Chatelain, F. C. & Minor, D. L. Jr. Structure of a complex between a voltage-gated calcium channel β-subunit and an α-subunit domain. *Nature* **429**, 671–675 (2004).
25. Opatowsky, Y., Chen, C. C., Campbell, K. P. & Hirsch, J. A. Structural analysis of the voltage-dependent calcium channel β-subunit functional core and its complex with the α_1-interaction domain. *Neuron* **42**, 387–399 (2004).
26. Chen, Y. H. et al. Structural basis of the α_1-β subunit interaction of voltage-gated Ca^{2+} channels. *Nature* **429**, 675–680 (2004).
27. Hofmann, F., Belkacemi, A. & Flockerzi, V. Emerging alternative functions for the auxiliary subunits of the voltage-gated calcium channels. *Curr. Mol. Pharmacol.* **8**, 162–168 (2015).
28. Pickel, S. et al. The β(2)-subunit of voltage-gated calcium channels regulates cardiomyocyte hypertrophy. *Front. cardiovascular Med.* **8**, 704657 (2021).
29. Belkacemi, A. et al. IP(3) Receptor-dependent cytoplasmic Ca(2+) signals are tightly controlled by Cavβ3. *Cell Rep.* **22**, 1339–1349 (2018).
30. Erdogmus, S. et al. Cavβ1 regulates T cell expansion and apoptosis independently of voltage-gated Ca(2+) channel function. *Nat. Commun.* **13**, 2033 (2022).
31. Vergnol, A., Traoré, M., Pietri-Rouxel, F. & Falcone, S. New insights in CaVβ subunits: role in the regulation of gene expression and cellular homeostasis. *Front. cell developmental Biol.* **10**, 880441 (2022).
32. Stölting, G. et al. Direct interaction of $Ca_V\beta$ with actin up-regulates L-type calcium currents in HL-1 cardiomyocytes. *J. Biol. Chem.* **290**, 4561–4572 (2015).
33. Guzman, G. A., Guzman, R. E., Jordan, N. & Hidalgo, P. A tripartite interaction among the calcium channel α1- and β-subunits and F-actin increases the readily releasable pool of vesicles and its recovery after depletion. *Front. Cell. Neurosci.* **13**, 125 (2019).
34. Etemad, S., Campiglio, M., Obermair, G. J. & Flucher, B. E. The juvenile myoclonic epilepsy mutant of the calcium channel β_4 subunit displays normal nuclear targeting in nerve and muscle cells. *Channels (Austin, Tex.)* **8**, 334–343 (2014).
35. Kao, A. et al. Development of a novel cross-linking strategy for fast and accurate identification of cross-linked peptides of protein complexes. *Mol. Cell. Proteom.: MCP* **10**, M110.002212 (2011).
36. Müller, M. Q., Dreiocker, F., Ihling, C. H., Schäfer, M. & Sinz, A. Cleavable cross-linker for protein structure analysis: reliable identification of cross-linking products by tandem MS. *Anal. Chem.* **82**, 6958–6968 (2010).
37. Heier, J. A., Dickinson, D. J. & Kwiatkowski, A. V. Measuring protein binding to F-actin by Co-sedimentation. *J. VIS. EXP.* **123**, 55613(2017).
38. Kumari, A., Kesarwani, S., Javoor, M. G., Vinothkumar, K. R. & Sirajuddin, M. Structural insights into actin filament recognition by commonly used cellular actin markers. *EMBO J.* **39**, e104006 (2020).
39. Yılmaz, Ş., Busch, F., Nagaraj, N. & Cox, J. Accurate and automated high-coverage identification of chemically cross-linked peptides with MaxLynx. *Anal. Chem.* **94**, 1608–1617 (2022).
40. Iacobucci, C. et al. A cross-linking/mass spectrometry workflow based on MS-cleavable cross-linkers and the MeroX software for

studying protein structures and protein-protein interactions. *Nat. Protoc.* **13**, 2864–2889 (2018).
41. Lu, L. et al. Identification of MS-cleavable and noncleavable chemically cross-linked peptides with metaMorpheus. *J. Proteome Res.* **17**, 2370–2376 (2018).
42. van Zundert, G. C. & Bonvin, A. M. DisVis: quantifying and visualizing accessible interaction space of distance-restrained biomolecular complexes. *Bioinformatics* **31**, 3222–3224 (2015).
43. van Zundert, G. C. et al. The DisVis and PowerFit web servers: explorative and integrative modeling of biomolecular complexes. *J. Mol. Biol.* **429**, 399–407 (2017).
44. van Zundert, G. C. P. et al. The HADDOCK2.2 web server: user-friendly integrative modeling of biomolecular complexes. *J. Mol. Biol.* **428**, 720–725 (2016).
45. Dominguez, C., Boelens, R. & Bonvin, A. M. HADDOCK: a protein-protein docking approach based on biochemical or biophysical information. *J. Am. Chem. Soc.* **125**, 1731–1737 (2003).
46. Lensink, M. F., Méndez, R. & Wodak, S. J. Docking and scoring protein complexes: CAPRI 3rd Edition. *Proteins* **69**, 704–718 (2007).
47. Collins, K. W. et al. CAPRI-Q: The CAPRI resource evaluating the quality of predicted structures of protein complexes. *J. Mol. Biol.* **436**, 168540 (2024).
48. Iacobucci, C. et al. First community-wide, comparative cross-linking mass spectrometry study. *Anal. Chem.* **91**, 6953–6961 (2019).
49. Schiffrin, B., Radford, S. E., Brockwell, D. J. & Calabrese, A. N. PyXlinkViewer: a flexible tool for visualization of protein chemical crosslinking data within the PyMOL molecular graphics system. *Protein Sci.: a Publ. Protein Soc.* **29**, 1851–1857 (2020).
50. Piersimoni, L., Kastritis, P. L., Arlt, C. & Sinz, A. Cross-linking mass spectrometry for investigating protein conformations and protein-protein interactions—a method for all seasons. *Chem. Rev.* **122**, 7500–7531 (2022).
51. Cohen, S. & Schneidman-Duhovny, D. A deep learning model for predicting optimal distance range in crosslinking mass spectrometry data. *Proteomics* **23**, e2200341 (2023).
52. Mintseris, J. & Gygi, S. P. High-density chemical cross-linking for modeling protein interactions. *Proc. Natl Acad. Sci. USA* **117**, 93–102 (2020).
53. Wang, X. et al. Molecular details underlying dynamic structures and regulation of the human 26S proteasome. *Mol. Cell. Proteom.: MCP* **16**, 840–854 (2017).
54. Bullock, J. M. A., Sen, N., Thalassinos, K. & Topf, M. Modeling protein complexes using restraints from crosslinking mass spectrometry. *Struct. (Lond., Engl.: 1993)* **26**, 1015–1024.e1012 (2018).
55. Rappsilber, J. The beginning of a beautiful friendship: cross-linking/mass spectrometry and modelling of proteins and multi-protein complexes. *J. Struct. Biol.* **173**, 530–540 (2011).
56. Matthew Allen Bullock, J., Schwab, J., Thalassinos, K. & Topf, M. The Importance of non-accessible crosslinks and solvent accessible surface distance in modeling proteins with restraints from crosslinking mass spectrometry. *Mol. Cell. Proteom.: MCP* **15**, 2491–2500 (2016).
57. Kahraman, A. et al. Cross-link guided molecular modeling with ROSETTA. *PloS one* **8**, e73411 (2013).
58. Vreven, T. et al. Integrating cross-linking experiments with Ab initio protein-protein docking. *J. Mol. Biol.* **430**, 1814–1828 (2018).
59. Saponaro, A., Maione, V., Bonvin, A. & Cantini, F. Understanding docking complexes of macromolecules using HADDOCK: the synergy between experimental data and computations. *Bio Protoc.* **10**, e3793 (2020).
60. Trellet, M., van Zundert, G. & Bonvin, A. Protein-protein modeling using cryo-EM restraints. *Methods Mol. Biol. (Clifton, N. J.)* **2112**, 145–162 (2020).
61. Stahl, K. et al. Modelling protein complexes with crosslinking mass spectrometry and deep learning. *Nat. Commun.* **15**, 7866 (2024).
62. Feng, S. et al. Integrated structure prediction of protein–protein docking with experimental restraints using ColabDock. *Nat Mach Intell* **6**, 924–935 (2024)
63. Dominguez, R. & Holmes, K. C. Actin structure and function. *Annu Rev. Biophys.* **40**, 169–186 (2011).
64. Pollard, T. D. Actin and actin-binding proteins. *Cold Spring Harb. Perspect. Biol.* **8**, a018226 (2016).
65. Dominguez, R. A common binding site for actin-binding proteins on the actin surface. In: Actin-Monomer-Binding Proteins. Molecular Biology Intelligence Unit. Springer, New York, NY. (2007)
66. Merino, F., Pospich, S. & Raunser, S. Towards a structural understanding of the remodeling of the actin cytoskeleton. *Semin. cell developmental Biol.* **102**, 51–64 (2020).
67. Meireles, L. M., Dömling, A. S. & Camacho, C. J. ANCHOR: a web server and database for analysis of protein-protein interaction binding pockets for drug discovery. *Nucleic Acids Res* **38**, W407–411 (2010).
68. Kortemme, T., Kim, D. E. & Baker, D. Computational alanine scanning of protein-protein interfaces. *Sci. STKE* **2004**, pl2 (2004).
69. Ibarra, A. A. et al. Predicting and experimentally validating hot-spot residues at protein-protein interfaces. *ACS Chem. Biol.* **14**, 2252–2263 (2019).
70. Wood, C. W. et al. BAlaS: fast, interactive and accessible computational alanine-scanning using BudeAlaScan. *Bioinformatics* **36**, 2917–2919 (2020).
71. Pahari, S. et al. SAAMBE-3D: predicting effect of mutations on protein-protein interactions. *Int. J. Mol. Sci.* **7**, 2563 (2020).
72. Dehouck, Y., Kwasigroch, J. M., Rooman, M. & Gilis, D. BeAtMuSiC: prediction of changes in protein-protein binding affinity on mutations. *Nucleic Acids Res* **41**, W333–339 (2013).
73. Zhang, N. et al. MutaBind2: predicting the impacts of single and multiple mutations on protein-protein interactions. *iScience* **23**, 100939 (2020).
74. Van Petegem, F., Duderstadt, K. E., Clark, K. A., Wang, M. & Minor, D. L. Jr. Alanine-scanning mutagenesis defines a conserved energetic hotspot in the CaValpha1 AID-CaVbeta interaction site that is critical for channel modulation. *Structure* **16**, 280–294 (2008).
75. Qin, N. et al. Unique regulatory properties of the type 2a Ca2+ channel beta subunit caused by palmitoylation. *Proc. Natl Acad. Sci. USA* **95**, 4690–4695 (1998).
76. Chien, A. J., Carr, K. M., Shirokov, R. E., Rios, E. & Hosey, M. M. Identification of palmitoylation sites within the L-type calcium channel beta2a subunit and effects on channel function. *J. Biol. Chem.* **271**, 26465–26468 (1996).
77. Miranda-Laferte, E., Schmidt, S., Jara, A. C., Neely, A. & Hidalgo, P. A short polybasic segment between the two conserved domains of the beta2a-subunit modulates the rate of inactivation of R-type calcium channel. *J. Biol. Chem.* **287**, 32588–32597 (2012).
78. Hidalgo, P., Gonzalez-Gutierrez, G., Garcia-Olivares, J. & Neely, A. The α_1-β-subunit interaction that modulates calcium channel activity is reversible and requires a competent α-interaction domain. *J. Biol. Chem.* **281**, 24104–24110 (2006).
79. Gonzalez-Gutierrez, G., Miranda-Laferte, E., Neely, A. & Hidalgo, P. The Src homology 3 domain of the β-subunit of voltage-gated calcium channels promotes endocytosis via dynamin interaction. *J. Biol. Chem.* **282**, 2156–2162 (2007).
80. Miranda-Laferte, E. et al. Homodimerization of the Src homology 3 domain of the calcium channel β-subunit drives dynamin-dependent endocytosis. *J. Biol. Chem.* **286**, 22203–22210 (2011).
81. Conrad, R., Kortzak, D., Guzman, G. A., Miranda-Laferte, E. & Hidalgo, P. Ca(V) β controls the endocytic turnover of Ca(V) 1.2 L-type calcium channel. *Traffic (Cph., Den.)* **22**, 180–193 (2021).

82. Neely, A., Wei, X., Olcese, R., Birnbaumer, L. & Stefani, E. Potentiation by the β subunit of the ratio of the ionic current to the charge movement in the cardiac calcium channel. *Science* **262**, 575–578 (1993).
83. Bezanilla, F. & Stefani, E. Gating currents. *Methods Enzymol.* **293**, 331–352 (1998).
84. Alvarez, O., Gonzalez, C. & Latorre, R. Counting channels: a tutorial guide on ion channel fluctuation analysis. *Adv. Physiol. Educ.* **26**, 327–341 (2002).
85. Tsien, R. W., Bean, B. P., Lansman, J. B., Nilius, B. & Nowycky, M. C. Mechanisms of calcium channel modulation by β-afrenergic agents and dihydropyridine Ca agonist. *J. Mol. Cell. Cardiol.* **18**, 691–710 (1986).
86. Sesti, F. & Goldstein, S. A. Single-channel characteristics of wild-type IKs channels and channels formed with two minK mutants that cause long QT syndrome. *J. Gen. Physiol.* **112**, 651–663 (1998).
87. Efron, B. & Tibshirani, J. R. *An Introduction to the Bootstrap. Monographs on Statistics and Applied Probability*. (Chapman & Hall/CRC, Boca Raton, Florida, USA, 1993).
88. Lu, H. et al. Recent advances in the development of protein-protein interactions modulators: mechanisms and clinical trials. *Signal Transduct. Target. Ther.* **5**, 213 (2020).
89. Murakami, Y., Tripathi, L. P., Prathipati, P. & Mizuguchi, K. Network analysis and in silico prediction of protein-protein interactions with applications in drug discovery. *Curr. Opin. Struct. Biol.* **44**, 134–142 (2017).
90. Jubb, H. C. et al. Mutations at protein-protein interfaces: Small changes over big surfaces have large impacts on human health. *Prog. biophysics Mol. Biol.* **128**, 3–13 (2017).
91. Wang, X., Ni, D., Liu, Y. & Lu, S. Rational design of peptide-based inhibitors disrupting protein-protein interactions. *Front. Chem.* **9**, 682675 (2021).
92. Petta, I., Lievens, S., Libert, C., Tavernier, J. & De Bosscher, K. Modulation of protein-protein interactions for the development of novel therapeutics. *Mol. Ther.: J. Am. Soc. Gene Ther.* **24**, 707–718 (2016).
93. Rusconi, F. et al. Peptidomimetic targeting of $Ca_v\beta2$ overcomes dysregulation of the L-type calcium channel density and recovers cardiac function. *Circulation* **134**, 534–546 (2016).
94. Kostan, J. et al. Molecular basis of F-actin regulation and sarcomere assembly via myotilin. *PLoS Biol.* **19**, e3001148 (2021).
95. Reuter, H., Stevens, C. F., Tsien, R. W. & Yellen, G. Properties of single calcium channels in cardiac cell culture. *Nature* **297**, 502–503 (1982).
96. Hess, P., Lansman, J. B. & Tsien, R. W. Different modes of Ca channel gating behaviour favored by dihydropyridine Ca agonist and antagonists. *Nature* **311**, 538–544 (1984).
97. Yue, D. T., Herzig, S. & Marban, E. Beta-adrenergic stimulation of calcium channels occurs by potentiation of high-activity gating modes. *Proc. Natl Acad. Sci. USA* **87**, 753–757 (1990).
98. Neely, A. et al. Dual activation of the cardiac Ca^{2+} channel α_{1C} subunit and the modulation by the β subunit. *Am. J. Physiol.* **268**, C732–C740 (1995).
99. Dzhura, I. & Neely, A. Differential modulation of cardiac Ca2+ channel gating by beta-subunits. *Biophys. J.* **85**, 274–289 (2003).
100. Xu, X., Marx, S. O. & Colecraft, H. M. Molecular mechanisms, and selective pharmacological rescue, of Rem-inhibited CaV1.2 channels in heart. *Circulation Res.* **107**, 620–630 (2010).
101. Costantin, J. et al. Facilitation by the beta2a subunit of pore openings in cardiac Ca2+ channels. *J. Physiol. (Lond.)* **507**, 93–103 (1998).
102. Conrad, R. et al. Rapid turnover of the cardiac L-Type $Ca_V1.2$ channel by endocytic recycling regulates its cell surface availability. *iScience* **7**, 1–15 (2018).
103. Sardana, R. & Emr, S. D. Membrane protein quality control mechanisms in the endo-lysosome system. *Trends cell Biol.* **31**, 269–283 (2021).
104. Babst, M. Quality control: quality control at the plasma membrane: one mechanism does not fit all. *J. cell Biol.* **205**, 11–20 (2014).
105. Apaja, P. M. & Lukacs, G. L. Protein homeostasis at the plasma membrane. *Physiol. (Bethesda, Md.)* **29**, 265–277 (2014).
106. Apaja, P. M., Xu, H. & Lukacs, G. L. Quality control for unfolded proteins at the plasma membrane. *J. cell Biol.* **191**, 553–570 (2010).
107. Chen, Z. et al. EMC chaperone-Ca(V) structure reveals an ion channel assembly intermediate. *Nature* **619**, 410–419 (2023).
108. Cumberworth, A., Lamour, G., Babu, M. M. & Gsponer, J. Promiscuity as a functional trait: intrinsically disordered regions as central players of interactomes. *Biochemical J.* **454**, 361–369 (2013).
109. Pancsa, R. & Fuxreiter, M. Interactions via intrinsically disordered regions: what kind of motifs? *IUBMB life* **64**, 513–520 (2012).
110. Vilchez, D., Saez, I. & Dillin, A. The role of protein clearance mechanisms in organismal ageing and age-related diseases. *Nat. Commun.* **5**, 5659 (2014).
111. Hommen, F., Bilican, S. & Vilchez, D. Protein clearance strategies for disease intervention. *J. Neural Transm. (Vienna)* **129**, 141–172 (2022).
112. Lanzetti, S. & Di Biase, V. Small molecules as modulators of voltage-gated calcium channels in neurological disorders: state of the art and perspectives. *Molecules* **27**, 1312 (2022).
113. Findeisen, F. et al. Stapled voltage-gated calcium channel (Ca_V) α-Interaction Domain (AID) peptides act as selective protein-protein interaction inhibitors of Ca_V Function. *ACS Chem. Neurosci.* **8**, 1313–1326 (2017).
114. Rappsilber, J., Mann, M. & Ishihama, Y. Protocol for micro-purification, enrichment, pre-fractionation and storage of peptides for proteomics using StageTips. *Nat. Protoc.* **2**, 1896–1906 (2007).
115. Chambers, M. C. et al. A cross-platform toolkit for mass spectrometry and proteomics. *Nat. Biotechnol.* **30**, 918–920 (2012).
116. Merino, F. et al. Structural transitions of F-actin upon ATP hydrolysis at near-atomic resolution revealed by cryo-EM. *Nat. Struct. Mol. Biol.* **25**, 528–537 (2018).
117. Merkley, E. D. et al. Distance restraints from crosslinking mass spectrometry: mining a molecular dynamics simulation database to evaluate lysine-lysine distances. *Protein Sci.: a Publ. Protein Soc.* **23**, 747–759 (2014).
118. Orban-Nemeth, Z. et al. Structural prediction of protein models using distance restraints derived from cross-linking mass spectrometry data. *Nat. Protoc.* **13**, 478–494 (2018).
119. Humphrey, W., Dalke, A. & Schulten, K. VMD: visual molecular dynamics. *J. Mol. Graph* **14**, 27–38 (1996).
120. Orbán-Németh, Z. et al. Reply to 'Defining distance restraints in HADDOCK'. *Nat. Protoc.* **13**, 1503–1505 (2018).
121. Bonvin, A., Karaca, E., Kastritis, P. L. & Rodrigues, J. Defining distance restraints in HADDOCK. *Nat. Protoc.* **13**, 1503 (2018).
122. Hubbard, S. & Thornton, J. *NACCESS, Computer Program* (Department of Biochemistry Molecular Biology, University College London, 1993).
123. de Vries, S. J. & Bonvin, A. M. CPORT: a consensus interface predictor and its performance in prediction-driven docking with HADDOCK. *PloS one* **6**, e17695 (2011).
124. Honorato, R. V. et al. The HADDOCK2.4 web server for integrative modeling of biomolecular complexes. *Nat. Protoc.* **19**, 3219–3241 (2024).
125. Paudyal, S. et al. Combined computational and experimental analysis of a complex of ribonuclease III and the regulatory macrodomain protein, YmdB. *Proteins* **83**, 459–472 (2015).
126. Jurrus, E. et al. Improvements to the APBS biomolecular solvation software suite. *Protein Sci.: a Publ. Protein Soc.* **27**, 112–128 (2018).

127. Xue, L. C., Rodrigues, J. P., Kastritis, P. L., Bonvin, A. M. & Vangone, A. PRODIGY: a web server for predicting the binding affinity of protein-protein complexes. *Bioinformatics* **32**, 3676–3678 (2016).
128. Vangone, A. & Bonvin, A. M. Contacts-based prediction of binding affinity in protein-protein complexes. *eLife* **4**, e07454 (2015).
129. Schindelin, J. et al. Fiji: an open-source platform for biological-image analysis. *Nat. Methods* **9**, 676–682 (2012).
130. Miranda-Laferte, E. et al. The N-terminal domain tethers the voltage-gated calcium channel β_{2e}-subunit to the plasma membrane via electrostatic and hydrophobic interactions. *J. Biol. Chem.* **289**, 10387–10398 (2014).
131. Schneider, C. A., Rasband, W. S. & Eliceiri, K. W. NIH Image to ImageJ: 25 years of image analysis. *Nat. Methods* **9**, 671–675 (2012).
132. Handrock, R. et al. Single-channel properties of L-type calcium channels from failing human ventricle. *Cardiovascular Res.* **37**, 445–455 (1998).
133. Fox, A. P., Nowycky, M. C. & Tsien, R. W. Single-channel recordings of three types of calcium channels in chick sensory neurones. *J. Physiol. (Lond.)* **394**, 173–200 (1987).
134. Perez-Riverol, Y. et al. The PRIDE database resources in 2022: a hub for mass spectrometry-based proteomics evidences. *Nucleic Acids Res* **50**, D543–D552 (2022).

Acknowledgements

We thank Prof. Marcus Krüger and Dr. Andreas Schmidt (Cluster of Excellence Cellular Stress Responses in Aging-Associated Diseases, University of Cologne, Germany) for Orbitrap mass spectrometry measurements. We are very grateful to Prof. Christoph Fahlke, Prof. Alan Neely and Dr. Bassam Haddad for helpful discussions. FC was funded by the Networking doctoral candidate (Vernetzungsdoktoranden) program, Forschungszentrum Jülich awarded to BSS, MAP and PH. The FP7 WeNMR (project# 261572), H2020 West-Life (project# 675858), the EOSC-hub (project# 777536) and the EGI-ACE (project# 101017567) European e-Infrastructure projects are acknowledged for the use of their web portals, which make use of the EGI infrastructure with the dedicated support of CESNET-MCC, INFN-LNL-2, NCG-INGRID-PT, TW-NCHC, CESGA, IFCA-LCG2, UA-BITP, TR-FC1-ULAKBIM, CSTCLOUD-EGI, IN2P3-CPPM, CIRMMP, SURFsara and NIKHEF, and the additional support of the national GRID Initiatives of Belgium, France, Italy, Germany, the Netherlands, Poland, Portugal, Spain, UK, Taiwan and the US Open Science Grid.

Author contributions

F.C. performed, designed, acquired, and analyzed all data collected for mass spectrometry, protein-protein docking, in vitro cross-linking, binding assays, western blots, and protein expression and purification experiments, and prepared the figures for the manuscript; V.L. designed, performed, recorded, and analyzed all electrophysiological experiments and prepared all the corresponding figures; E.M.L. designed the mutagenesis and captured, analyzed, and discussed the laser scanning confocal microscopy images; N.J. generated the cDNA constructs, expressed and purified recombinant proteins, and cultured cells; P.F.H. contributed to mass spectrometry discussions; B.S.S. designed, analyzed, and discussed all mass spectrometry data; M.A.P. designed, analyzed, and discussed all computational biology experiments; and P.H. conceived the project, designed the experiments, and wrote the manuscript.

Funding

Open Access funding enabled and organized by Projekt DEAL.

Competing interests

The authors declare no competing interests.

Additional information

Supplementary information The online version contains supplementary material available at https://doi.org/10.1038/s41467-025-59548-x.

Correspondence and requests for materials should be addressed to Beatrix Santiago-Schübel, Mercedes Alfonso-Prieto or Patricia Hidalgo.

Peer review information *Nature Communications* thanks the anonymous reviewers for their contribution to the peer review of this work. A peer review file is available.

Supplementary Figure 1A

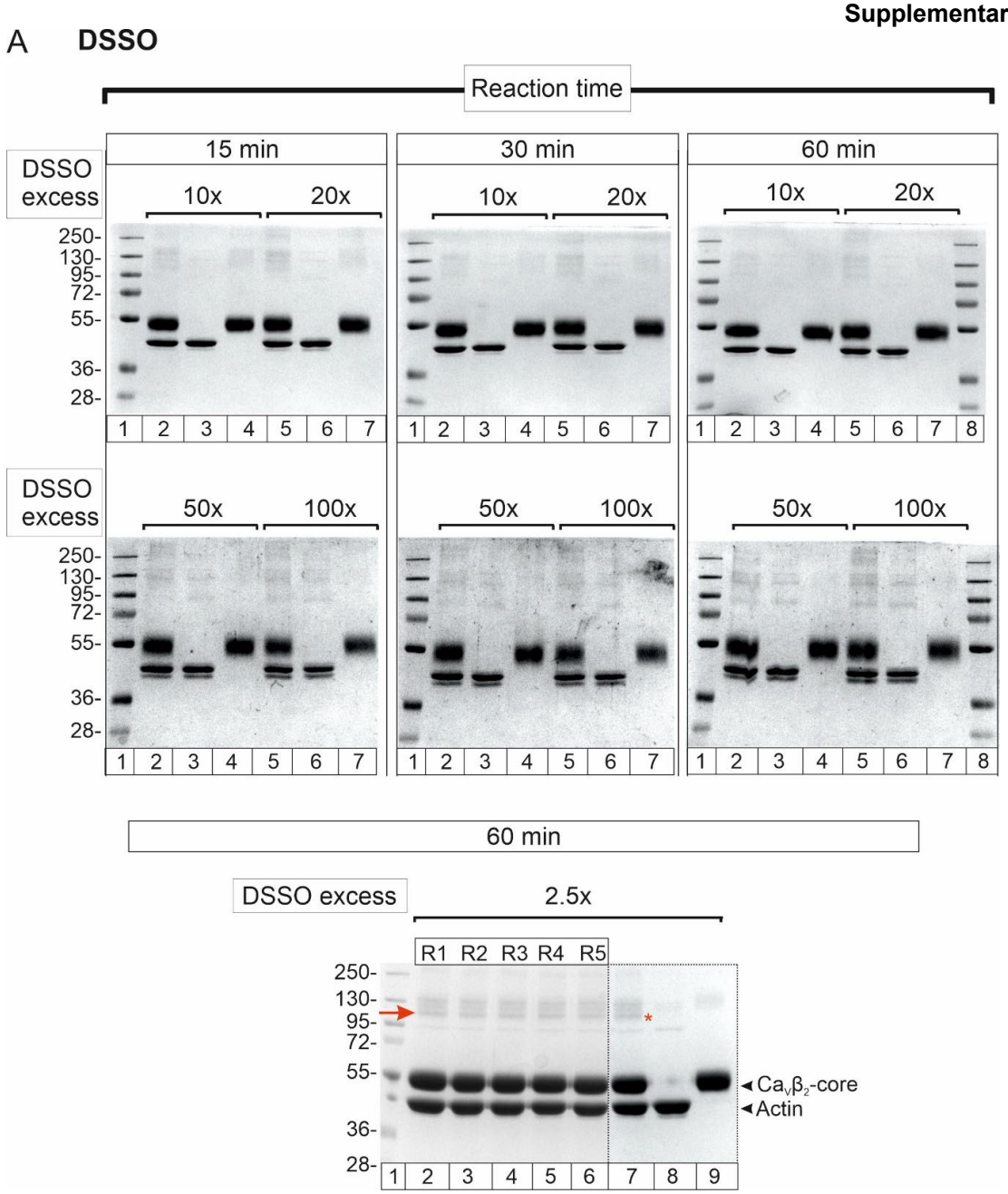

Supplementary Figure 1. Summary of the optimization for the cross-linking reaction conditions of Ca$_V$β and actin with DSSO and DSBU cross-linkers. A, Top panel, images of the SDS-PAGE gels for cross-linking reactions between Ca$_V$β$_2$-core and actin with DSSO at molar excess of ≥ 10 (10x, 20x, 50x, 100x) and different reaction times (15, 30 and 60 min) at RT. For each gel (1.0 mm thickness); lane 1, molecular weight standards with numbers denoting the molecular masses in kDa; lanes 2 and 5, Ca$_V$β–actin cross-linking reaction; lanes 3 and 6, actin alone with cross-linker and lane 4 and 7, Ca$_V$β alone with cross-linker. Bottom panel, SDS-PAGE gel (1.5 mm thickness) of the optimal DSSO cross-linking reaction for Ca$_V$β$_2$-core–actin. A 60-minute reaction time at lower molar excess (2.5x) was found to be the optimal condition for DSSO. The red arrow and asterisk denote the gel band excised and subjected to LC-MS/MS analysis. This band is not visible in control reactions where either each protein was incubated alone with the cross-linker or no cross-linker was added. The replicates analyzed R1 to R5 (lanes 2-6) are documented in Supplementary Table 2. The dotted line box (lanes 7-9) encloses the gel image shown in Figure 2C, main text.

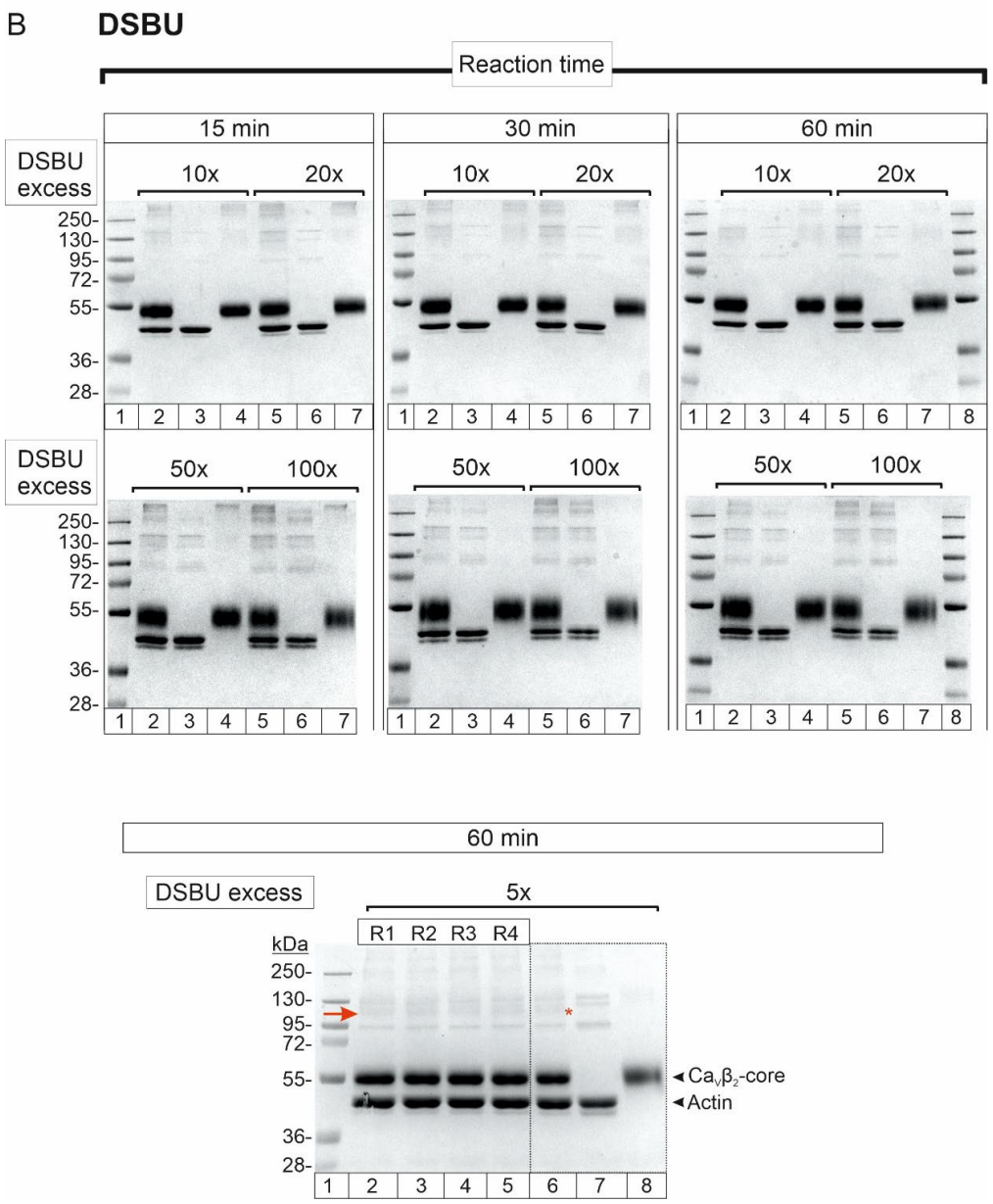

Supplementary Figure 1. Summary of the optimization for the cross-linking reaction conditions of Ca$_V$β and actin with DSSO and DSBU cross-linkers. B, Top panel, same as *A*, but for DSBU. Bottom panel, SDS-PAGE gel (1.5 mm thickness) of the optimal DSBU cross-linking reaction for Ca$_V$β$_2$-core–actin that occurred at a molar excess of 5.0x during a 60-minute reaction time. The replicates analyzed R1 to R4 (lanes 2-5) are documented in Supplementary Table 2. The dotted line box (lanes 6-8) encloses the gel image shown in Figure 2C, main text.

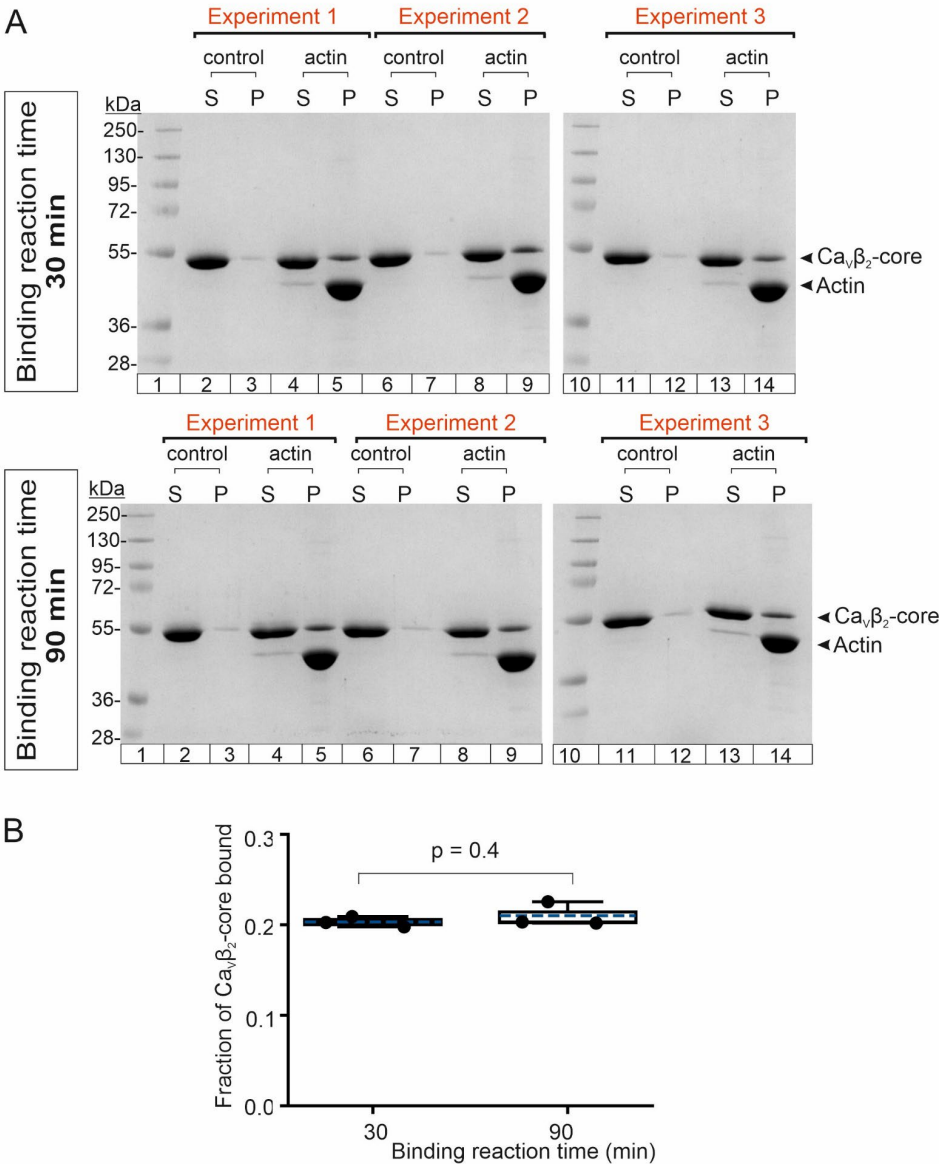

Supplementary Figure 2. Stability of $Ca_V\beta_2$–actin complex formation over time assessed by F-actin cosedimentation assay. **A**, Images of the SDS-PAGE for F-actin cosedimentation assays with $Ca_V\beta_2$-core for binding reaction times of 30 minutes (upper panel) and 90 minutes (lower panel). For each gel, lane 1, molecular weight standards in kDa; S, supernatant; P, pellet. Control and actin denote that the assay was performed in the absence and presence of actin, respectively. Each assay was repeated three times (experiments 1 to 3). **B**, Box plot of the fraction of the $Ca_V\beta_2$-core bound to actin after 30 and 90 minute reaction showing the mean (dashed line), median (continuous line), interquartile range (25th–75th percentiles, box edges) and whiskers (1.5× interquartile range). Each dot represents a separate experiment (n = 3). p-value was determined by two-sided t-test.

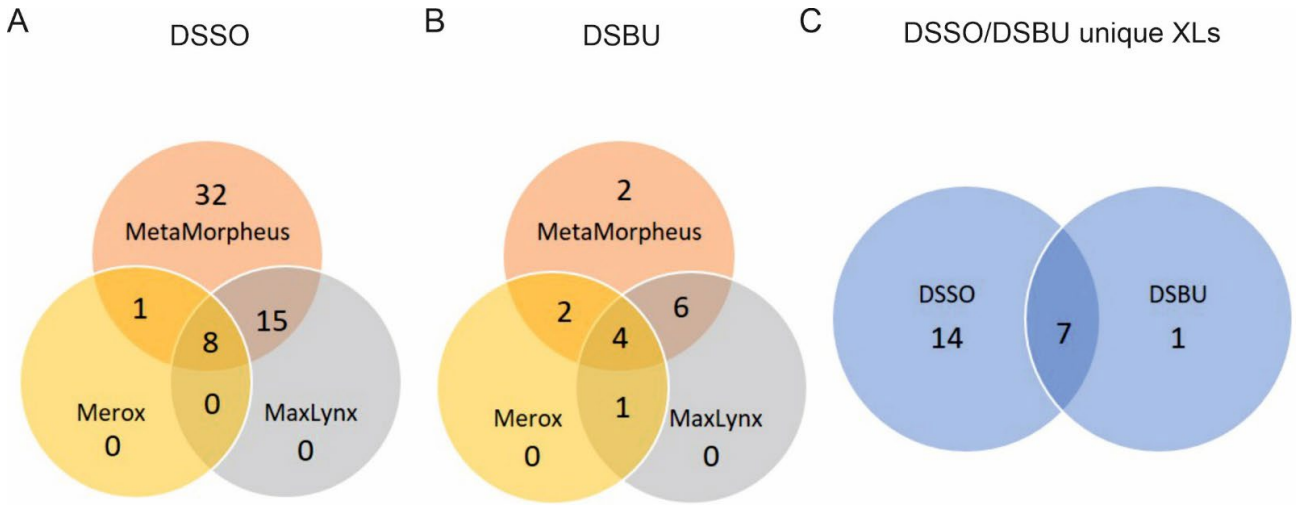

Supplementary Figure 3. Venn diagrams of the number of intermolecular crosslinks (inter-XLs) between $Ca_V\beta_2$ and actin. **A**, Venn diagram of the total intermolecular XLs identified by the three software packages used (MetaMorpheus, MaxLynx and Merox) in five replicates with DSSO as crosslinker. **B**, same as *A*, but for the four replicates with DSBU. **C**, Venn diagram indicating the overlap between unique intermolecular XLs obtained with DSSO and DSBU. Data taken from Supplementary Table 2.

Supplementary Figure 4

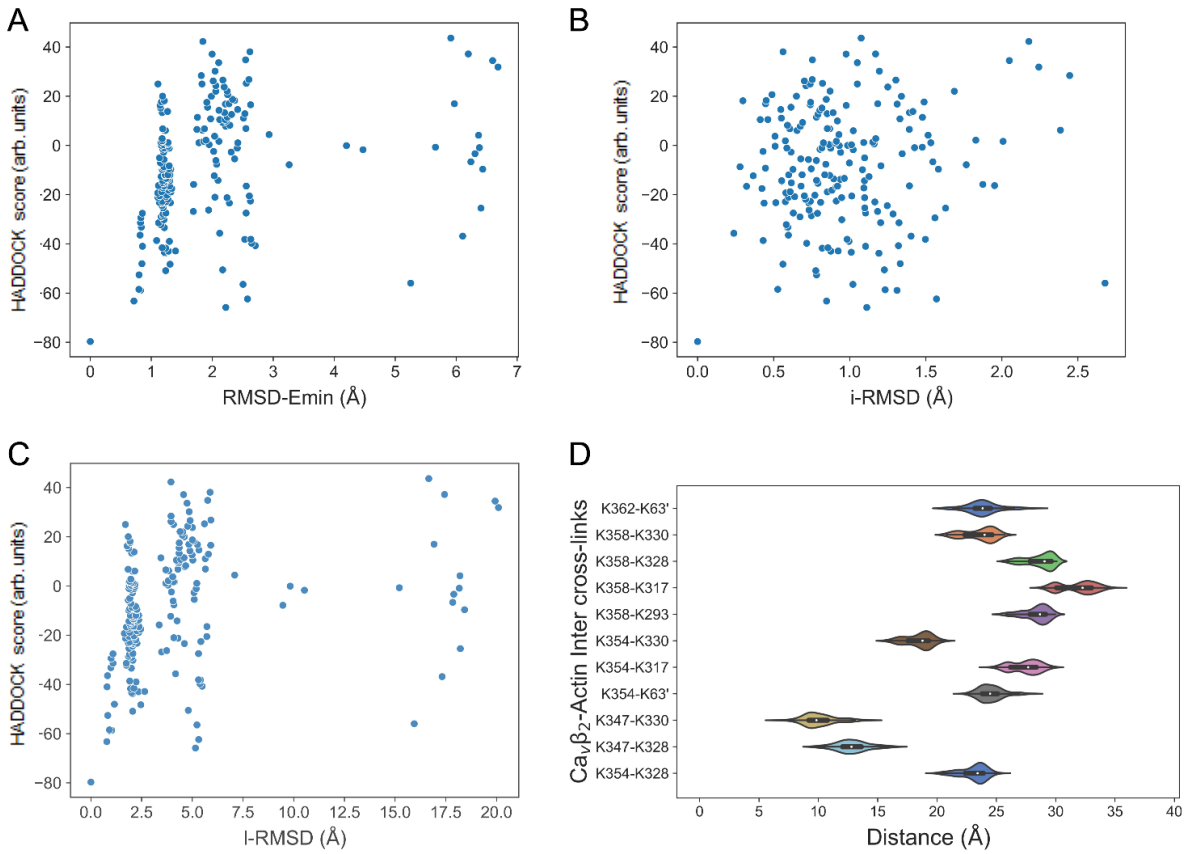

Supplementary Figure 4. Model docking data for $Ca_V\beta_2$ and actin. **A**, HADDOCK score versus global RMSD (RMSD-Emin) plot for the sole cluster obtained for the $Ca_V\beta_2$–actin docking containing 198 out of 200 generated models. The global RMSD is calculated including the alpha carbon atoms of all residues of both proteins, using as reference the structure with the lowest HADDOCK score. **B**, HADDOCK score versus interface RMSD (i-RMSD) plot for $Ca_V\beta_2$–actin docking structures. The interface RMSD is calculated including the backbone atoms of all interface residues of both proteins, after superimposing these interfacial residues, which are defined using an interatomic distance of 10 Å. The reference structure is the one with the lowest HADDOCK score. **C**, HADDOCK score versus ligand RMSD (l-RMSD) plot for $Ca_V\beta_2$–actin docking structures. The ligand RMSD is calculated including the backbone atoms of $Ca_V\beta_2$ (as ligand) after fitting on the actin dimer and using as reference the structure with the lowest HADDOCK score. **D**, Mapped Euclidean Cα-Cα cross-linked pair distance distribution for the 198 docking structures belonging to the best cluster generated by HADDOCK 2.4 for $Ca_V\beta_2$–actin.

Supplementary Figure 5

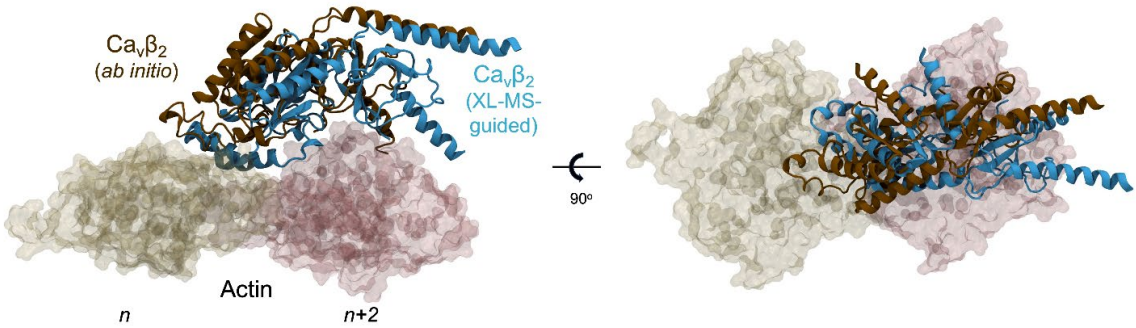

Supplementary Figure 5. *Ab initio* docking model with the lowest l-RMSD compared to the best scored XL-MS-guided model of the $Ca_V\beta_2$-actin complex. Superimposition of backbone heavy atoms of actin-bound $Ca_V\beta_2$ structures generated with the two different docking approaches (brown and cyan for the *ab initio* and XL-MS-guided models, respectively). The two actin subunits used as reference for the alignment are shown in space-filling mode (yellow and pink, respectively). Based on the HADDOCK score, the *ab initio* docking model was ranked as number 208 out of 400 models in the respective control simulation (see Supplementary Table 6). The l-RMSD between the two actin-bound $Ca_V\beta_2$ structures is 14.0 Å, whereas the i-RMSD is 7.9 Å, considering actin and $Ca_V\beta$ residues found to be at the interface (i.e. within 10 Å of the other protein partner) for both models, which comprise 73% of the PPI surface.

Supplementary Figure 6

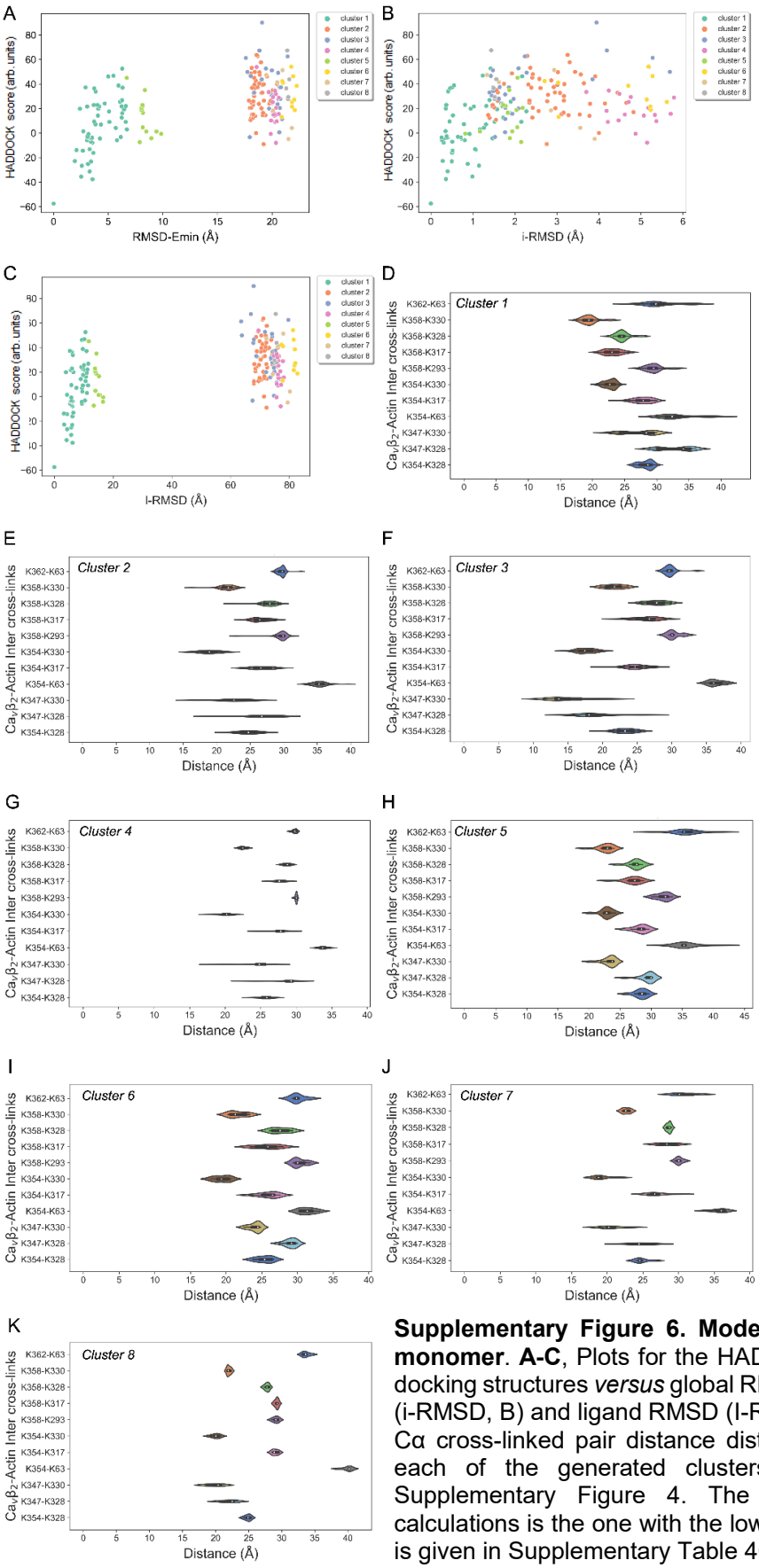

Supplementary Figure 6. Model docking data for $Ca_V\beta_2$-and actin monomer. **A-C**, Plots for the HADDOCK score of $Ca_V\beta_2$-actin monomer docking structures *versus* global RMSD (RMSD-Emin, A), interface RMSD (i-RMSD, B) and ligand RMSD (l-RMSD, C). **D-K**, Mapped Euclidean Cα-Cα cross-linked pair distance distribution for the docking structures for each of the generated clusters. A-C, calculated as explained in Supplementary Figure 4. The reference structure for all RMSD calculations is the one with the lowest HADDOCK score. The cluster size is given in Supplementary Table 4C.

Supplementary Figure 7

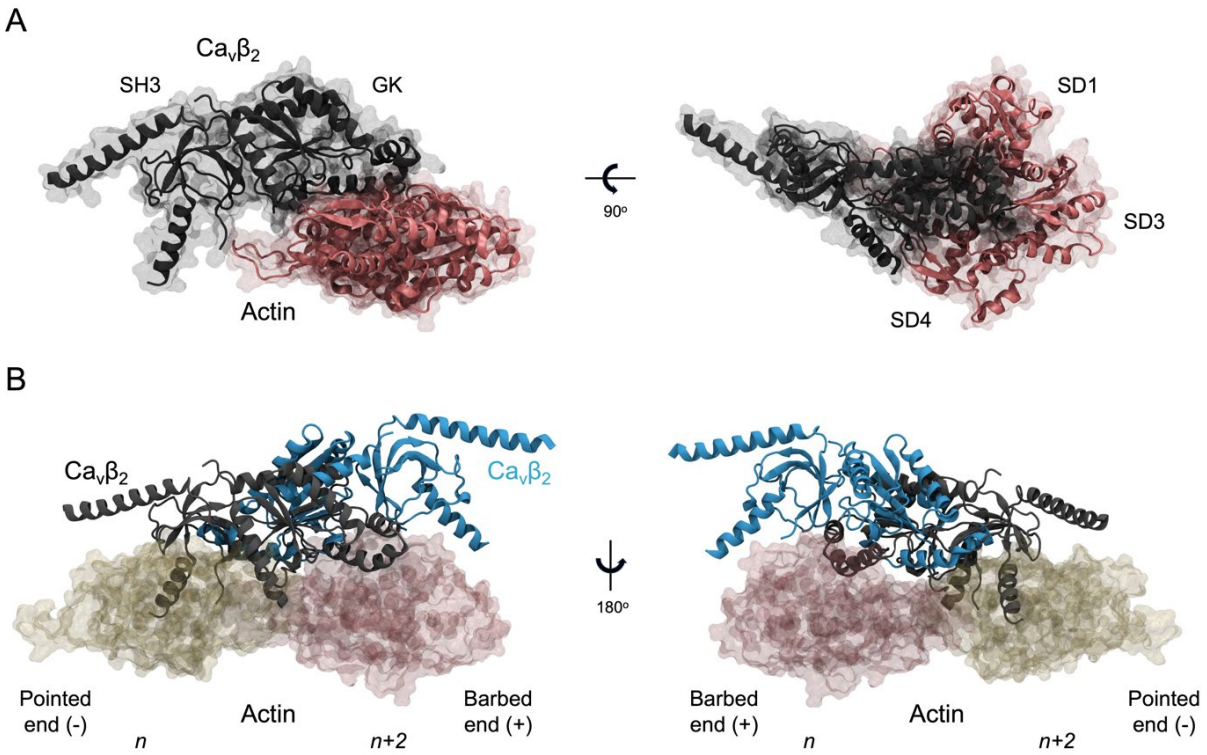

Supplementary Figure 7. Structural docking model of $Ca_V\beta_2$ bound to an actin monomer. A, Space-filling and ribbon diagram showing two views related by a 90° rotation of the best-scoring docking model of $Ca_V\beta_2$ (gray) complexed with an actin monomer (pink). **B**, Superimposition of backbone heavy atoms of actin-bound structures of $Ca_V\beta_2$. Each $Ca_V\beta$ structure represents the average of the top four models of the best-scored cluster generated by docking to actin, either monomeric or dimeric (gray and blue ribbons, respectively). The two actin subunits are shown in space-filling model (yellow and pink); the *n+2* actin subunit was used as reference for the alignment.

Supplementary Figure 8

Full-size images of SDS-PAGE gels for all F-actin cosedimentation assays with $Ca_V\beta_2$-core at different NaCl concentrations (n=3)

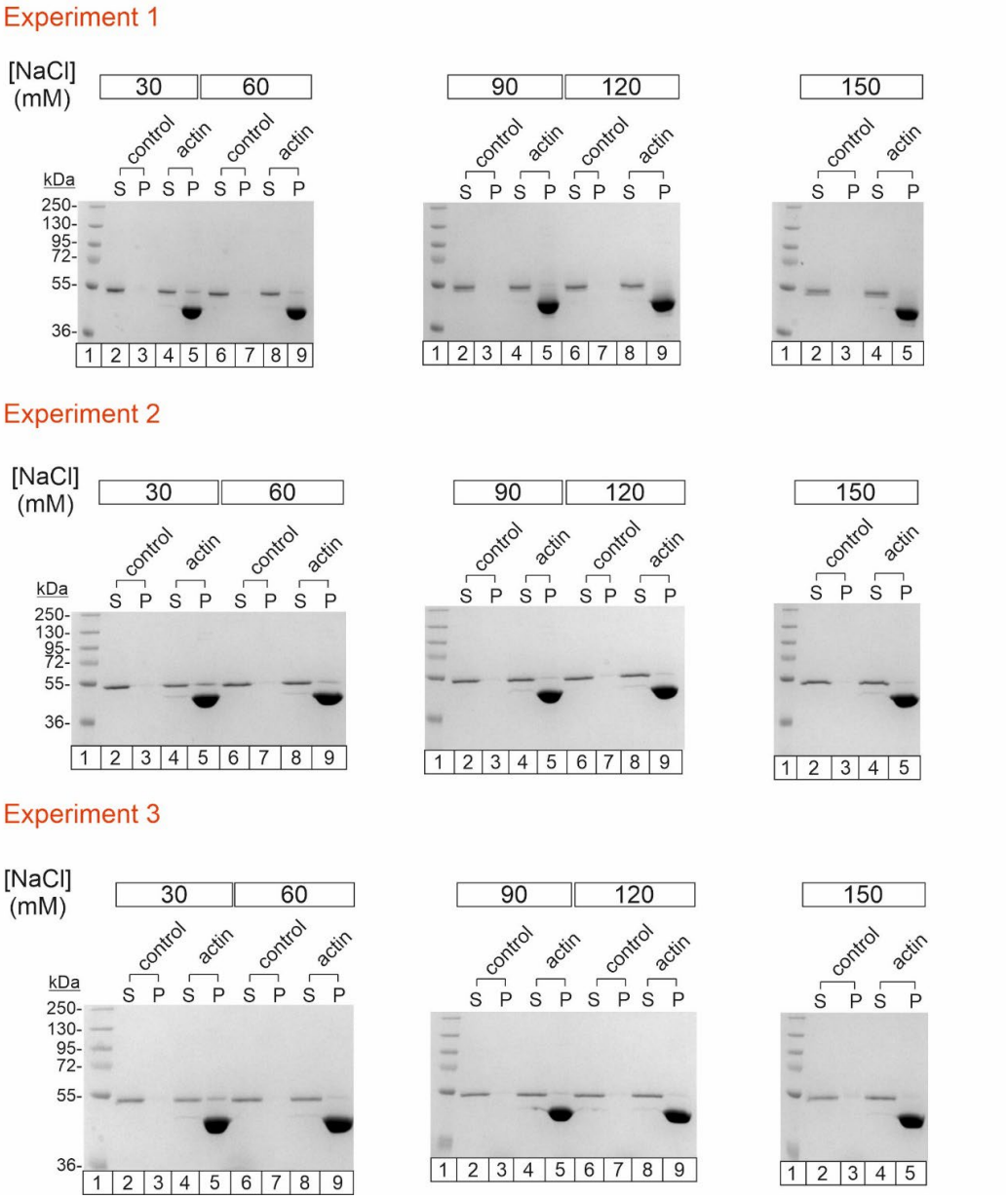

Supplementary Figure 8. Binding of $Ca_V\beta_2$-core to actin at different NaCl concentrations. Full-size images of the SDS-PAGE gels for all F-actin cosedimentation assays with $Ca_V\beta_2$-core at the indicated NaCl concentration (n=3 for each NaCl concentration). For each gel, the NaCl concentration used in the assay is shown in a box; S and P denote supernatant and pellet, respectively; and control and actin denote that the assay was performed in the absence ($Ca_V\beta_2$-core alone) and presence of actin, respectively. The same molecular weight standards were used in each experiment, with the molecular masses in kDa shown adjacent to the left-most gel.

Supplementary Figure 9

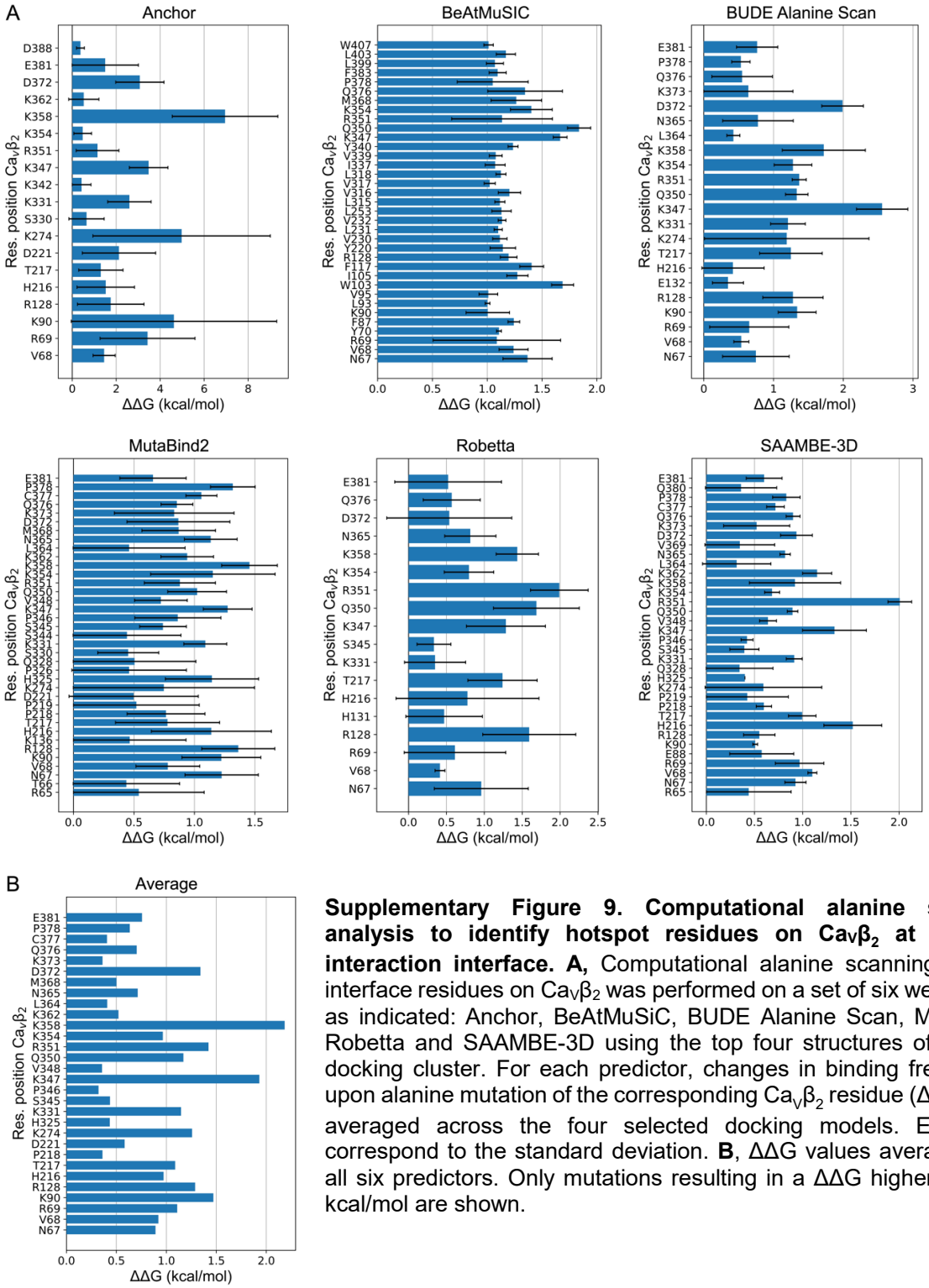

Supplementary Figure 9. Computational alanine scanning analysis to identify hotspot residues on $Ca_V\beta_2$ at its actin interaction interface. A, Computational alanine scanning of actin interface residues on $Ca_V\beta_2$ was performed on a set of six webservers, as indicated: Anchor, BeAtMuSiC, BUDE Alanine Scan, Mutabind2, Robetta and SAAMBE-3D using the top four structures of the best docking cluster. For each predictor, changes in binding free energy upon alanine mutation of the corresponding $Ca_V\beta_2$ residue (ΔΔG) were averaged across the four selected docking models. Error bars correspond to the standard deviation. **B**, ΔΔG values averaged over all six predictors. Only mutations resulting in a ΔΔG higher than 0.3 kcal/mol are shown.

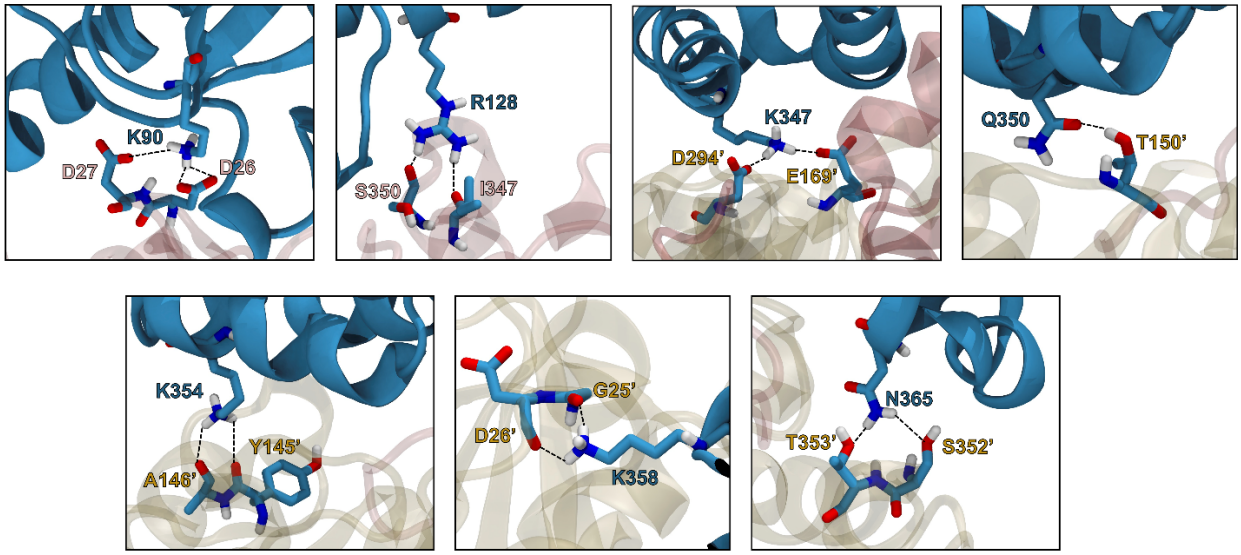

Supplementary Figure 10. Short-range interactions formed by $Ca_V\beta_2$ hotspot residues at the protein-protein interface with actin. The best scored model of the $Ca_V\beta_2$-actin complex was used for the visual inspection of the protein-protein interactions. The two proteins are shown as ribbons, with $Ca_V\beta_2$ and hotspot residues in blue, and the two actin subunits and interacting residues in light pink and grey (*n+2* and *n* monomers, respectively). Residues are displayed as sticks and interactions are indicated with dashed lines.

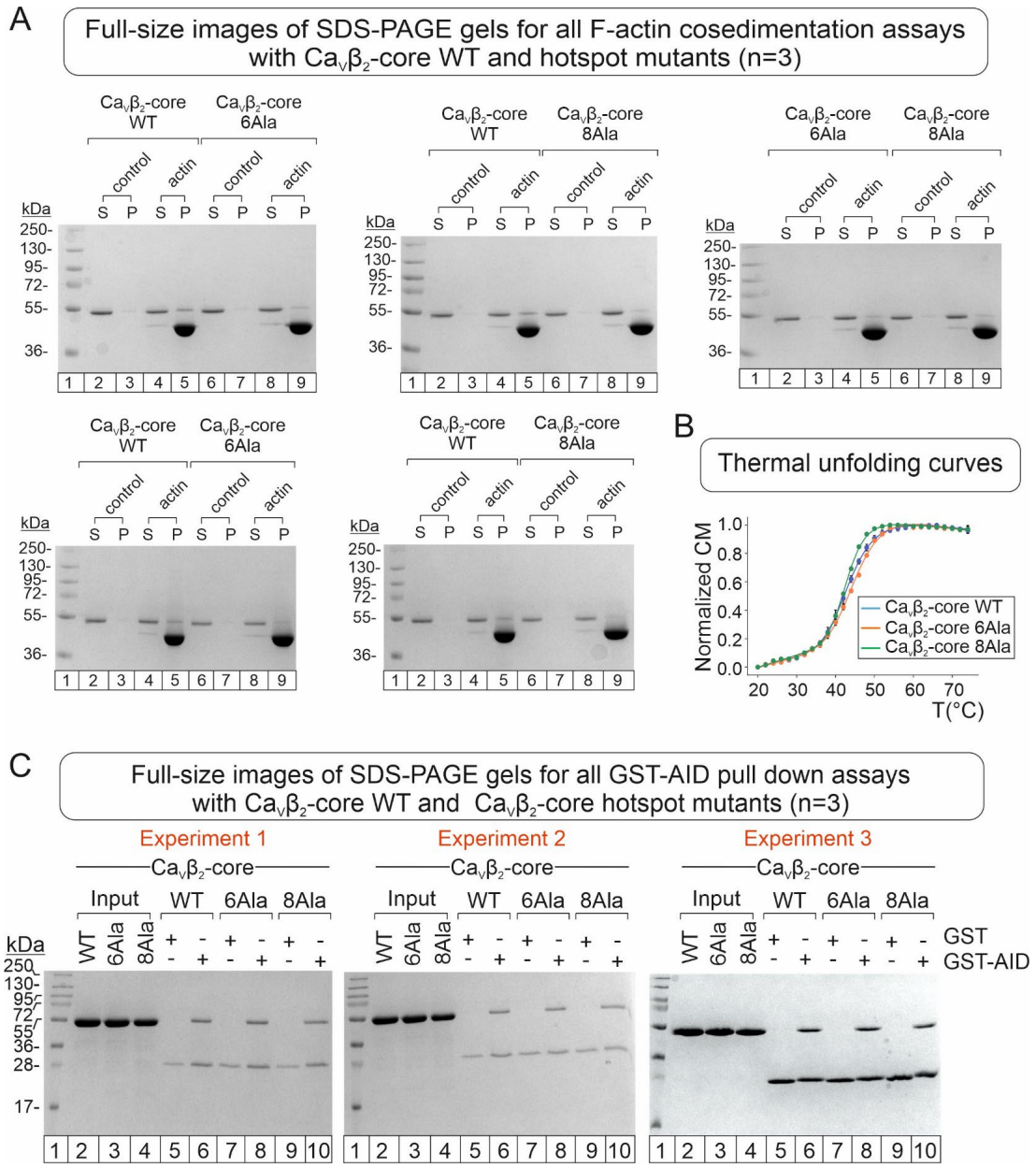

Supplementary Figure 11. F-actin co-sedimentation assays, thermal stability, and GST-AID pull downs of $Ca_V\beta_2$-core, and the hotspot mutants, $Ca_V\beta_2$-core 6Ala and $Ca_V\beta_2$-core 8Ala. A, Full-size images of the SDS-PAGE for all F-actin cosedimentation assays with $Ca_V\beta_2$-core wild-type (WT), $Ca_V\beta_2$-core 6Ala (6Ala) and $Ca_V\beta_2$-core 8Ala (8Ala). For each gel, lane 1 contains the molecular weight standards, S and P denote supernatant and pellet, respectively, and control and actin denote that the assay was performed in the absence (WT and hotspot mutants alone) and presence of actin, respectively. **B**, Thermal unfolding curves for $Ca_V\beta_2$-core WT, 6Ala, and 8Ala with Tm values (± SE, °C) of 43.9± 0.1, 45.6±0.3 and 43.1±0.1, respectively. CM, center of mass, determined as in Eq. 1. **C**, Full-size images of all SDS-PAGE gels for GST-AID pull down assays with $Ca_V\beta_2$-core WT and the hotspot mutants 6Ala and 8Ala. Each pull down assay was repeated three times. For each gel: lanes 2–4, input proteins; and lanes 5–10, eluted fractions for the indicated protein in either control pull downs using GST alone as bait (lanes 5, 7, and 9) or test assays using GST-AID (lanes 6, 8, and 10). The same molecular weight standards were used in each experiment, with the molecular masses in kDa shown adjacent to the left-most gel.

Supplementary Figure 12

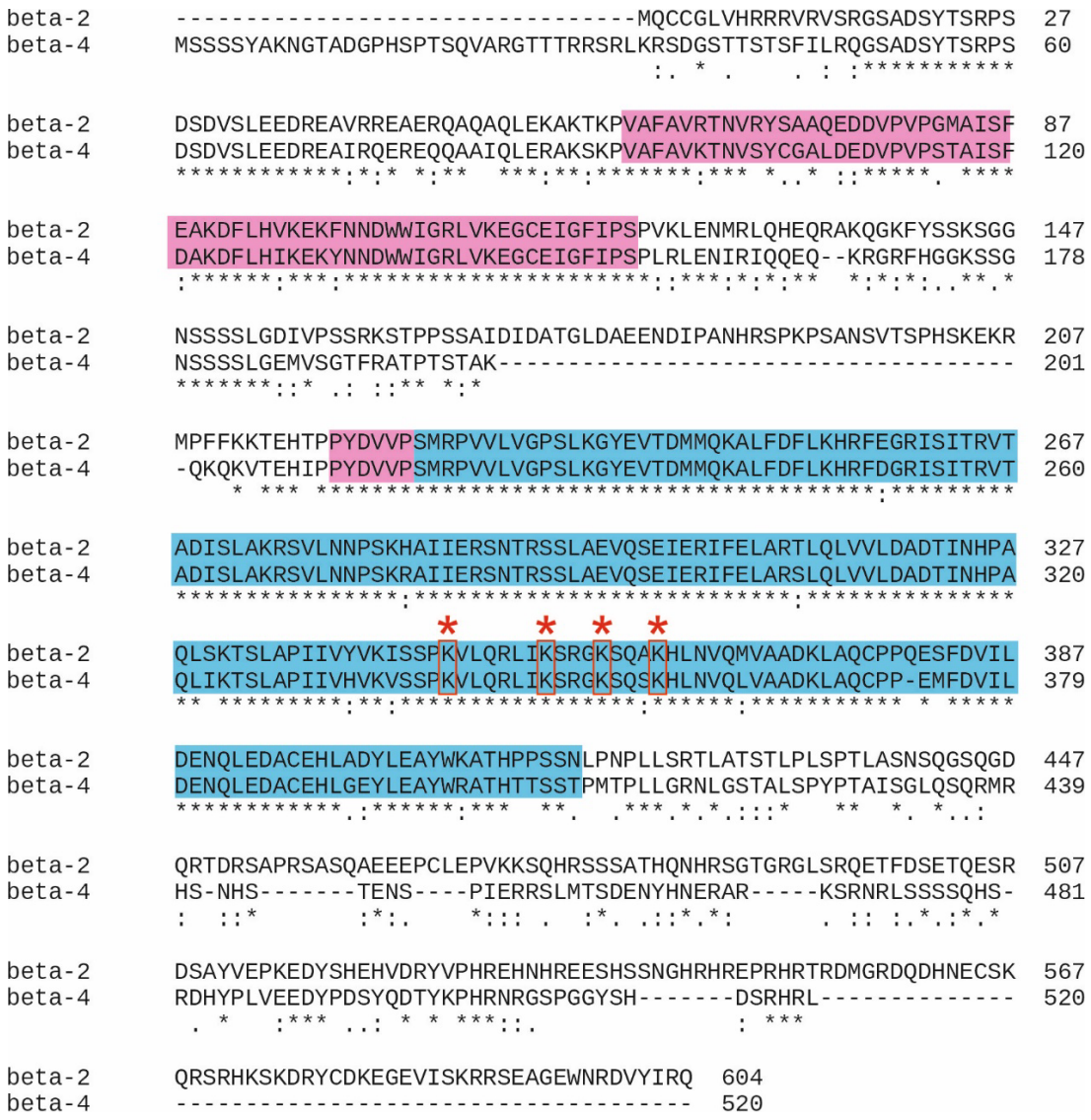

Supplementary Figure 12. Sequence alignment of $Ca_V\beta_2$ and $Ca_V\beta_4$. The amino acid sequences of $Ca_V\beta_2$ (UniProtKB Q8VGC3-2) and $Ca_V\beta_4$ (UniProtKB O00305-1) used in this study were aligned using Clustal Omega. The SH3 and GK domains are enclosed in pink and blue, respectively. All four lysine residues involved in the set of self-consistent inter-molecular cross-links identified in $Ca_V\beta_2$ are fully conserved in $Ca_V\beta_4$ (shown enclosed in a red frame and labeled with a red asterisk).

Supplementary Figure 13

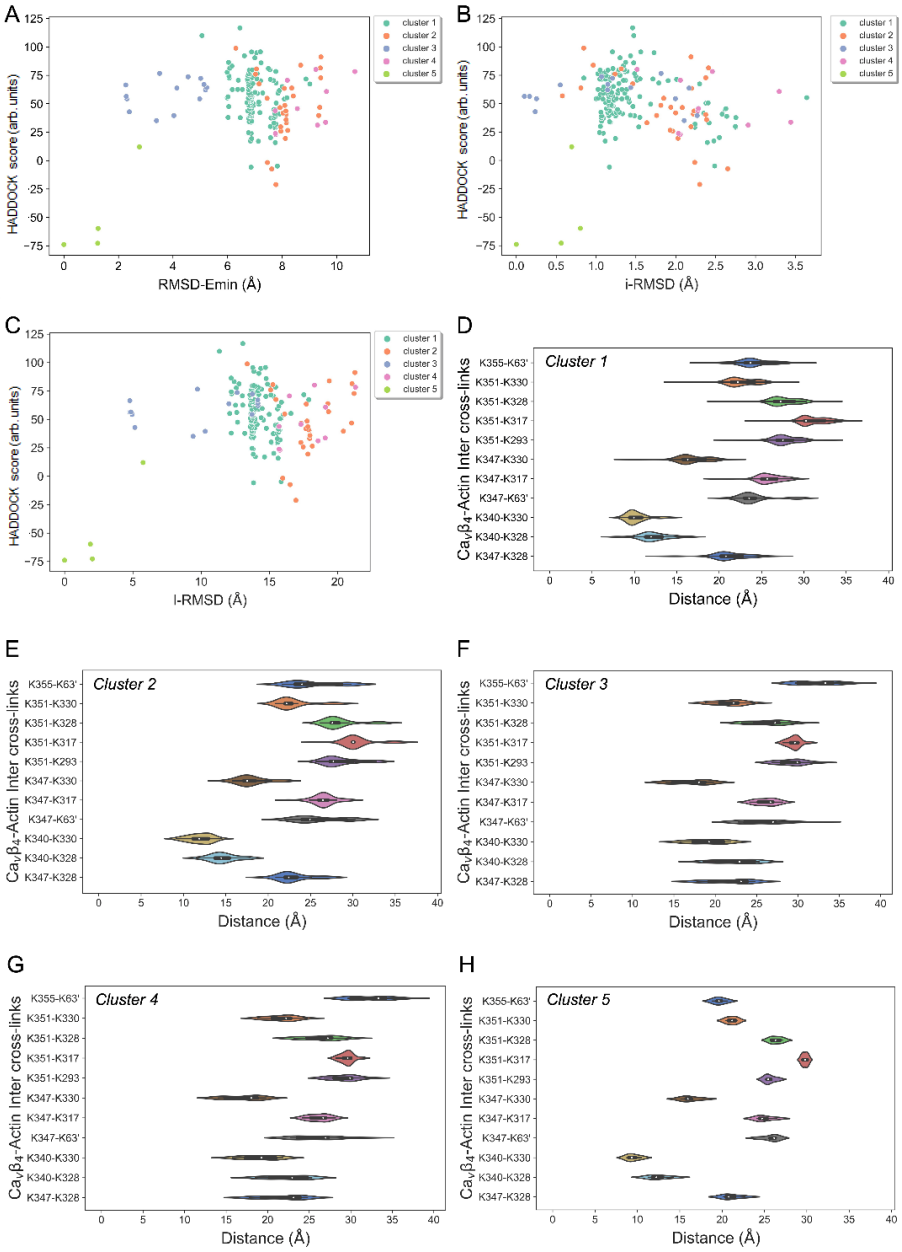

Supplementary Figure 13. Model docking data for $Ca_V\beta_4$ and actin. A, HADDOCK score versus global RMSD (RMSD-Emin) plot for $Ca_V\beta_4$–actin docking structures. **B**, HADDOCK score versus interface RMSD (i-RMSD) plot for $Ca_V\beta_4$–actin docking structures. **C**, HADDOCK score versus ligand RMSD (l-RMSD) plot for $Ca_V\beta_4$–actin docking structures. **D-H**, Mapped Euclidean Cα-Cα cross-linked pair distance distribution for all the docking structures belonging to the clusters 1-5, respectively, generated by HADDOCK 2.4 for $Ca_V\beta_4$–actin. The three RMSD metrics in panels A-C are calculated as explained in Supplementary Figure 4; the reference structure for all RMSD calculations is the one with the lowest HADDOCK score, which in the $Ca_V\beta_4$–actin docking belongs to cluster 5. The cluster size is given in Supplementary Table 4B.

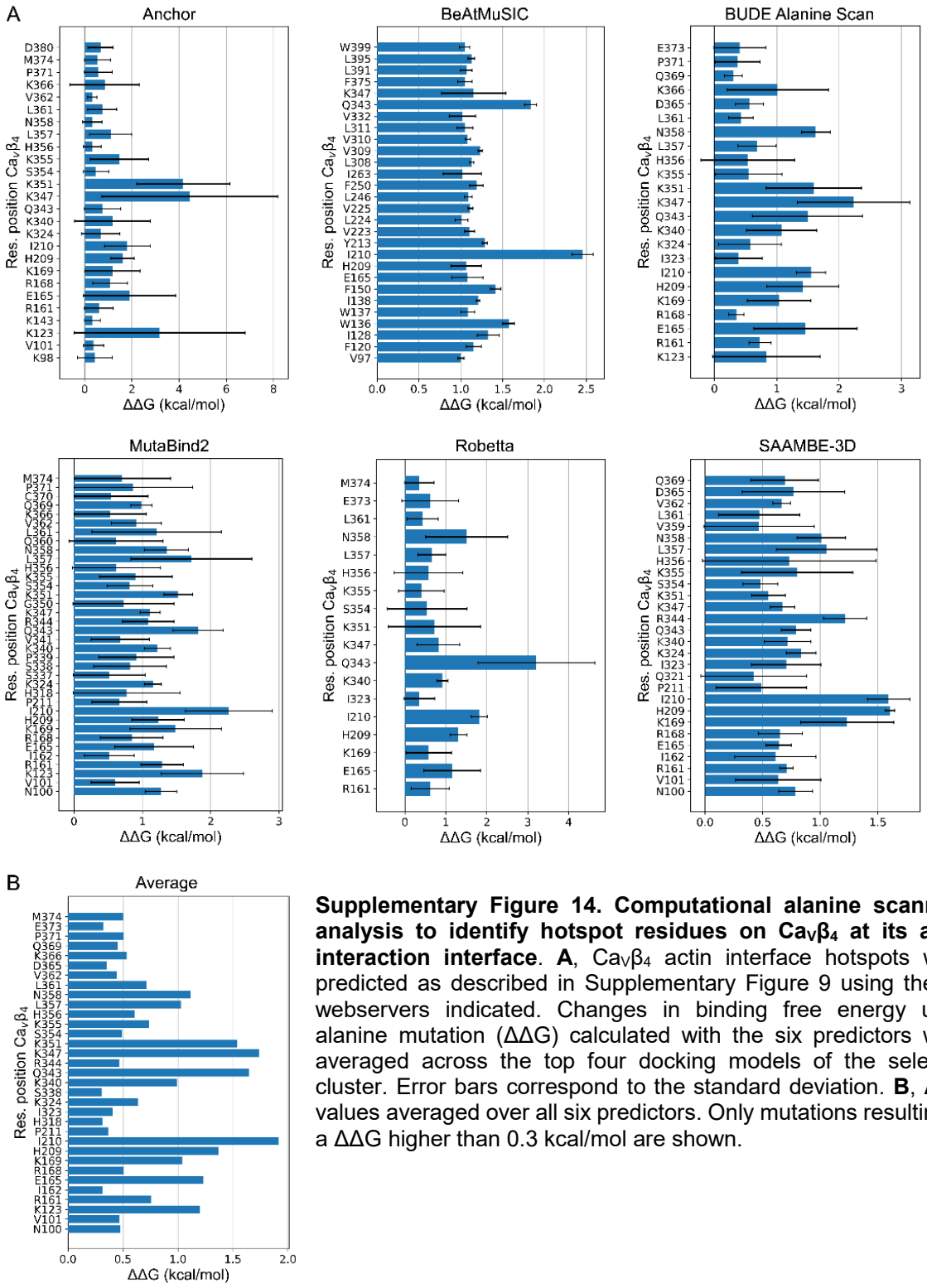

Supplementary Figure 14. Computational alanine scanning analysis to identify hotspot residues on $Ca_V\beta_4$ at its actin interaction interface. **A**, $Ca_V\beta_4$ actin interface hotspots were predicted as described in Supplementary Figure 9 using the six webservers indicated. Changes in binding free energy upon alanine mutation (ΔΔG) calculated with the six predictors were averaged across the top four docking models of the selected cluster. Error bars correspond to the standard deviation. **B**, ΔΔG values averaged over all six predictors. Only mutations resulting in a ΔΔG higher than 0.3 kcal/mol are shown.

Supplementary Figure 15A-C

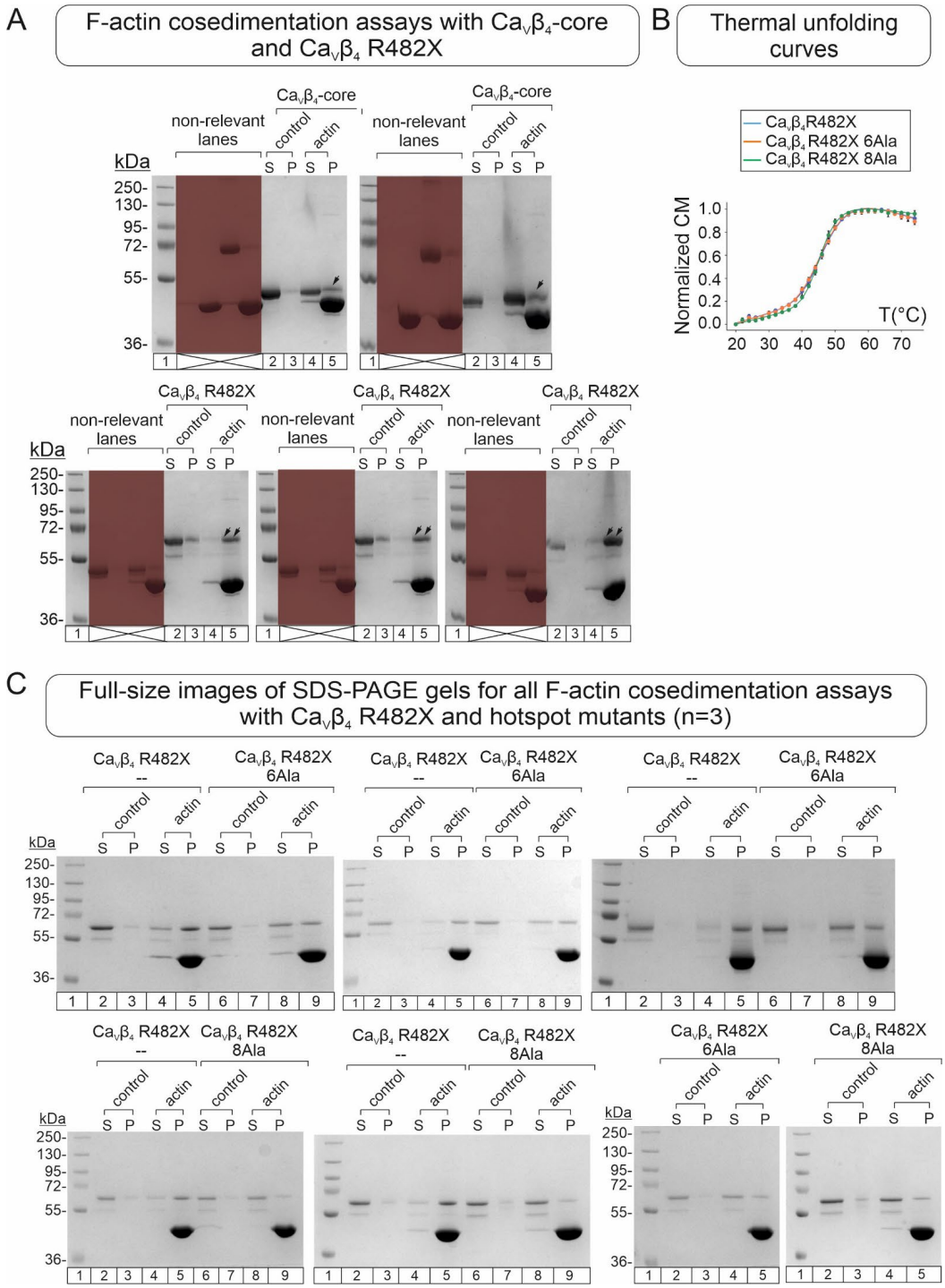

Supplementary Figure 15. Comparison of thermal stability and binding to F-actin and GST-AID of $Ca_V\beta_4$ R482X and the hotspot mutants. A, Full-size images of the SDS-PAGE of separate F-actin cosedimentation assays with $Ca_V\beta_4$-core and $Ca_V\beta_4$ R482X. For each gel: lane 1, molecular weight standards and lanes 2, 3, 4 and 5 correspond to supernatant (S) and pellet (P) denote and pellet fractions

for the indicated assay. Control and actin denote the assay performed in the absence and presence of actin, respectively. Lanes relevant for this study are enclosed in a black square while irrelevant lanes outside the scope of this work are not numbered and marked with a blue cross in the gel. **B**, Thermal unfolding curves for $Ca_V\beta_4$ R482X bearing no alanine substitution, $Ca_V\beta_4$ R482X 6Ala, and $Ca_V\beta_4$ R482X 8Ala with Tm values (± SE, °C) of 47.7±0.2, 47.7±0.3 and 45.9±0.2, respectively. CM, center of mass, as determined as in Eq. 1. **C**, Full-size images of the SDS-PAGE of all F-actin cosedimentation assays with $Ca_V\beta_4$ R482X bearing no Ala substitutions (--), $Ca_V\beta_4$ R482X 6Ala, and $Ca_V\beta_4$ R482X 8Ala. For each gel: lane 1, molecular weight standards; S and P denote supernatant and pellet, respectively; and control and actin denote the assay performed in the absence ($Ca_V\beta_4$ R482X and hotspot mutants alone) and presence of actin, respectively. The same molecular weight standards were used in each experiment, with the molecular masses in kDa shown adjacent to the left-most gel.

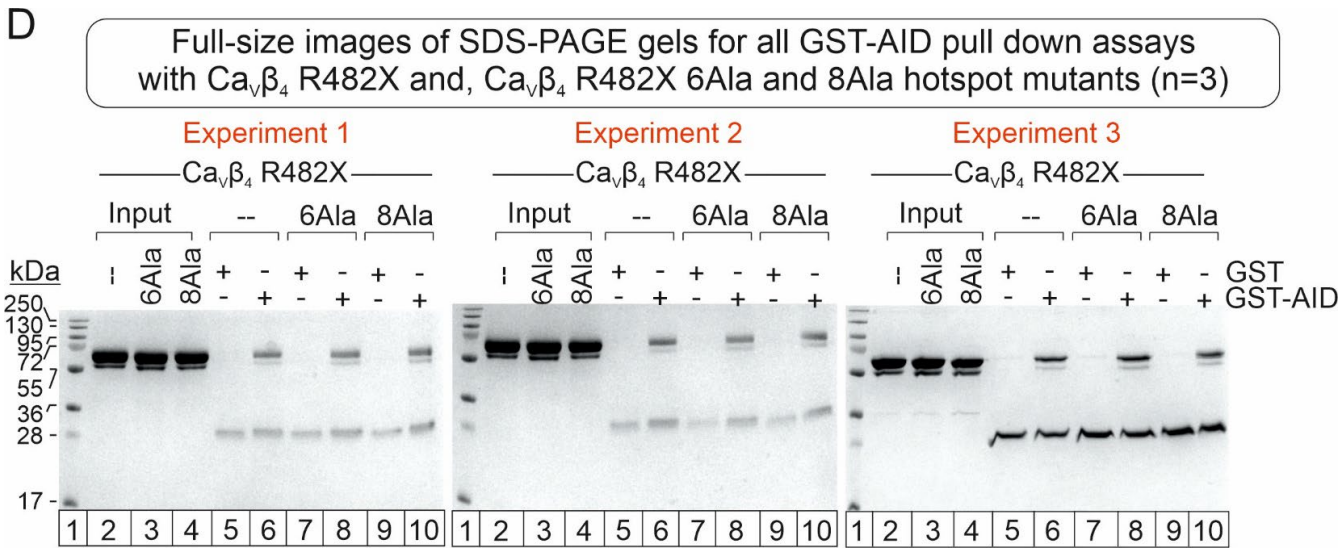

Supplementary Figure 15. Comparison of thermal stability and binding to F-actin and GST-AID of $Ca_V\beta_4$ R482X and the hotspot mutants. D, Full-size images of all SDS-PAGE gels for GST-AID pull down assays with $Ca_V\beta_4$ R482X with no Ala substitutions (--), $Ca_V\beta_4$ R482X 6Ala (6Ala), and $Ca_V\beta_4$ R482X 8Ala (8Ala). Each pull down assay was repeated three times. For each gel: lane 1, molecular weight standards, lanes 2–4, input proteins; and lanes 5–10, eluted fractions for the indicated protein in either control pull downs using GST alone as bait (lanes 5, 7, and 9) or test assays using GST-AID (lanes 6, 8, and 10). The same molecular weight standards were used in each experiment, with the molecular masses in kDa shown adjacent to the left-most gel.

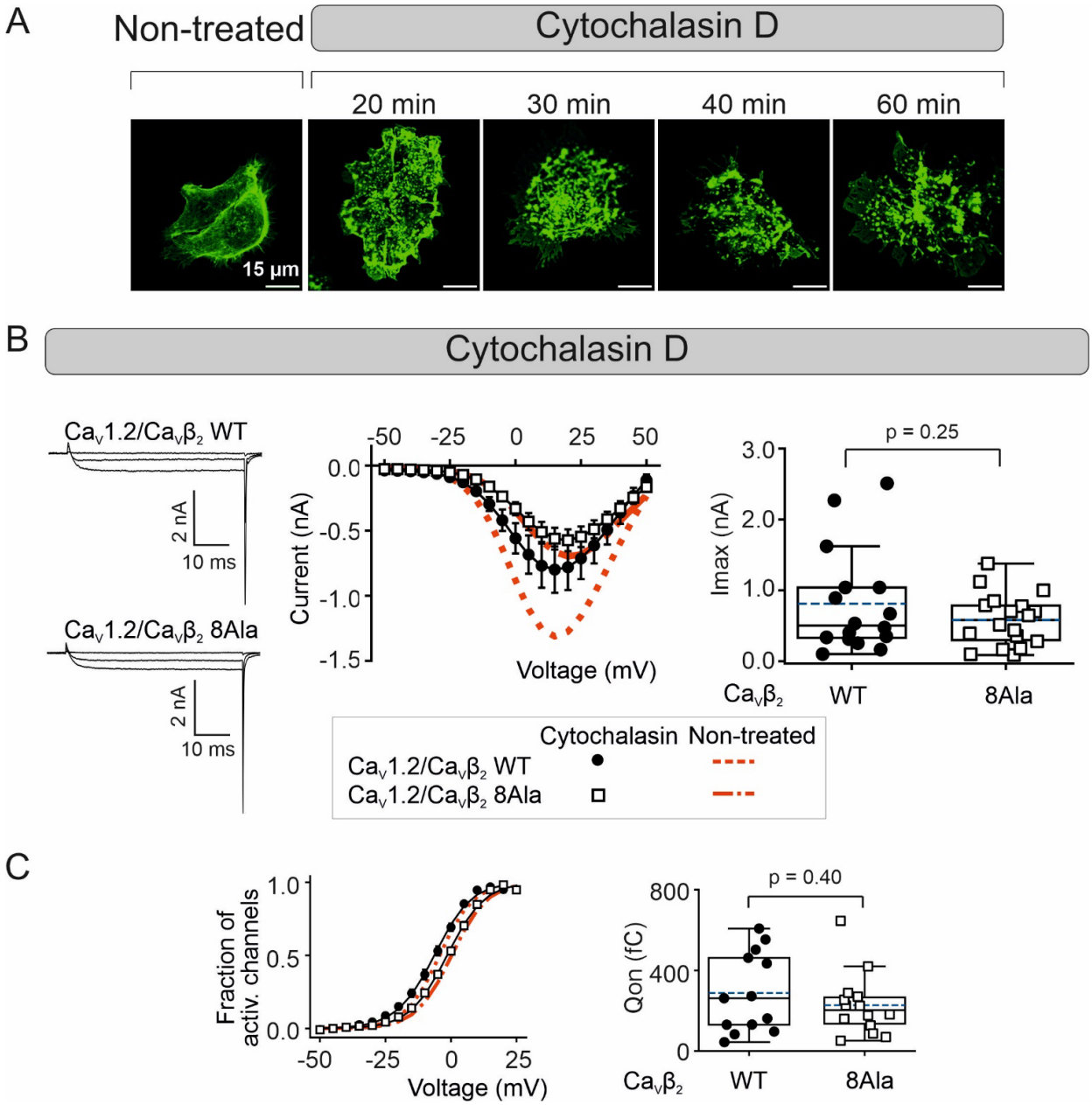

Supplementary Figure 16. Pharmacological disruption of actin filaments inhibits current reduction mediated by the actin-association-deficient $Ca_V\beta_2$ mutant. **A**, Representative laser scanning confocal images of HEK293 cells stained for actin using phalloidin-488 after incubation with 10 µM of the actin filament disrupter cytochalasin D for the indicated time periods. The experiment was repeated twice with cells from different number of passages. **B**, Representative ionic current traces from cells transiently cotransfected with $Ca_V1.2$ (fused to mNeonGreen) and either $Ca_V\beta_2$ WT or $Ca_V\beta_2$ 8Ala (fused to mRFP) (left panel) and plot of the mean current amplitude at voltages between -50 to +50 mV in 5 mV increments from a holding potential of -90 mV (middle panel). Recordings were done after incubation for 40 minutes with 10 µM of cytochalasin D. Only the current traces induced by -40, +15, and +40 mV pulses are shown. Data are presented as mean ± SEM. Imax: -0.81 ± 0.18 nA for $Ca_V1.2/Ca_V\beta_2$ WT (number of individual recorded cells, n = 16) and -0.58 ± 0.08 nA for $Ca_V1.2/Ca_V\beta_2$ 8Ala (n = 18). For comparison the I/V curves obtained from non-cytochalasin D

treated cells expressing the same subunit combinations (from Figure 6, main text) are shown in red lines. The box plot (right panel) shows the average peak current (Imax) for the indicated channel subunit combination taken from the I/V plot. Each dot represents an individual recorded cell. Dashed lines represent the mean and the continuous line the median, the box edges denote the interquartile range (25th–75th percentiles) and whiskers, the 1.5× interquartile range. **C**, Plot of the fraction of activated channels versus voltage and box plot of the total charge movement (Qon) obtained from the cells in panel B. Red lines correspond to the curves obtained for non-cytochalasin D treated cells expressing the same subunit combinations (from Figure 6, main text). Data are presented as mean ± SEM. In the box plot: mean (dashed line), median (continuous line), interquartile range (25th–75th percentiles, box edges) and whiskers (1.5× interquartile range). Each dot represents an individual recorded cell (n). Qon was calculated from the integral of the On gating current during the voltage step to the reversal potential for the carrier ion. Qon (mean ± S.E.M: 288 ± 53 fC (n, = 13) and 227 ± 40 fC (n = 14) for $Ca_V1.2/Ca_V\beta_2$ WT and $Ca_V1.2/Ca_V\beta_2$ 8Ala, respectively. p-values were determined by two-sided t-test.

Supplementary Figure 17

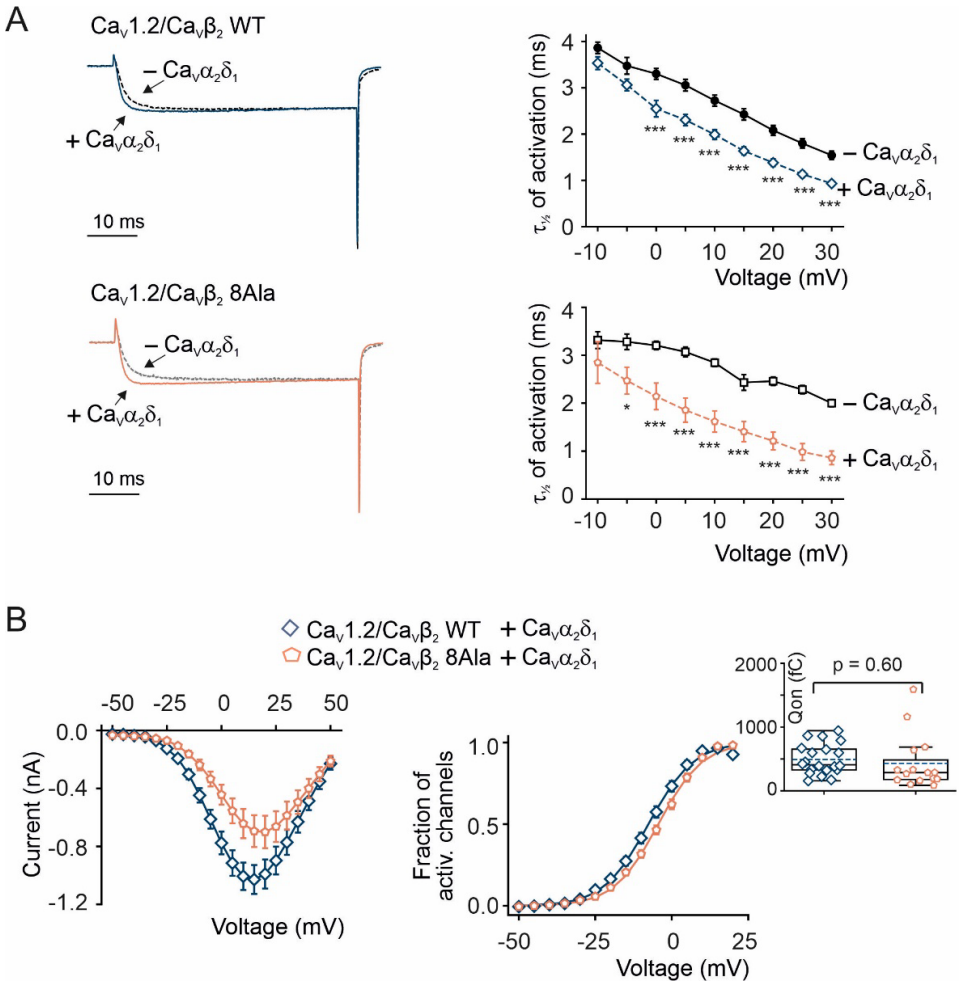

Supplementary Figure 17. Expression of $Ca_V\alpha_2\delta_1$ subunit marginally affects the functional competence of the $Ca_V1.2/Ca_V\beta_2$ core complex in HEK293 cells. **A**, Representative normalized ionic current traces at +20 mV and plot of the mean $\tau_{½}$ values (± S.E.M) for the current activation at different voltages from cells expressing $Ca_V1.2/Ca_V\beta_2$ (either $Ca_V\beta_2$ WT or $Ca_V\beta_2$ 8Ala hotspot mutant) with and without $Ca_V\alpha_2\delta_1$. * $p < 0.05$; ***$p < 0.001$; t-test. $Ca_V\alpha_2\delta_1$ speeds up the activation kinetics. **B**, Current-to-voltage (I/V) plot and fraction of activated channels versus voltage plot obtained from cells expressing $Ca_V1.2/\beta_2/\alpha_2\delta_1$ channels encompassing either $Ca_V\beta_2$ WT (number of recorded cells, n =20) or $Ca_V\beta_2$ 8Ala hotspot mutant (n =15). Ionic currents were elicited by steps to voltages between -50 to +50 mV in 5 mV increments from a holding potential of -90 mV. Data are presented as mean ± SEM. Inset shows the box of the total charge movement (Qon) with mean (dashed line), median (continuous line), interquartile range (25th–75th percentiles, box edges) and whiskers (1.5× interquartile range). Each dot represents an individual recorded cell. Qon was calculated from the integral of the On gating current during the voltage step to the reversal potential for the carrier ion determined empirically by stepping to several potentials in 2 mV increments. Mean values ± S.E.M: Imax, -1.1 ± 0.1 nA and -0.7 ± 0.1 nA (p = 0.03), Qon, 491 ± 52 fC and 432 ± 107 fC for $Ca_V1.2/\beta_2/\alpha_2\delta_1$ encompassing $Ca_V\beta_2$ WT and 8Ala mutant, respectively. P-values were determined by two-sided t-test. ($Ca_V\alpha_2\delta_1$ from Scholl et al., *Nature Genetics* **45**, 1050-4 (2013)).

Supplementary Figure 18

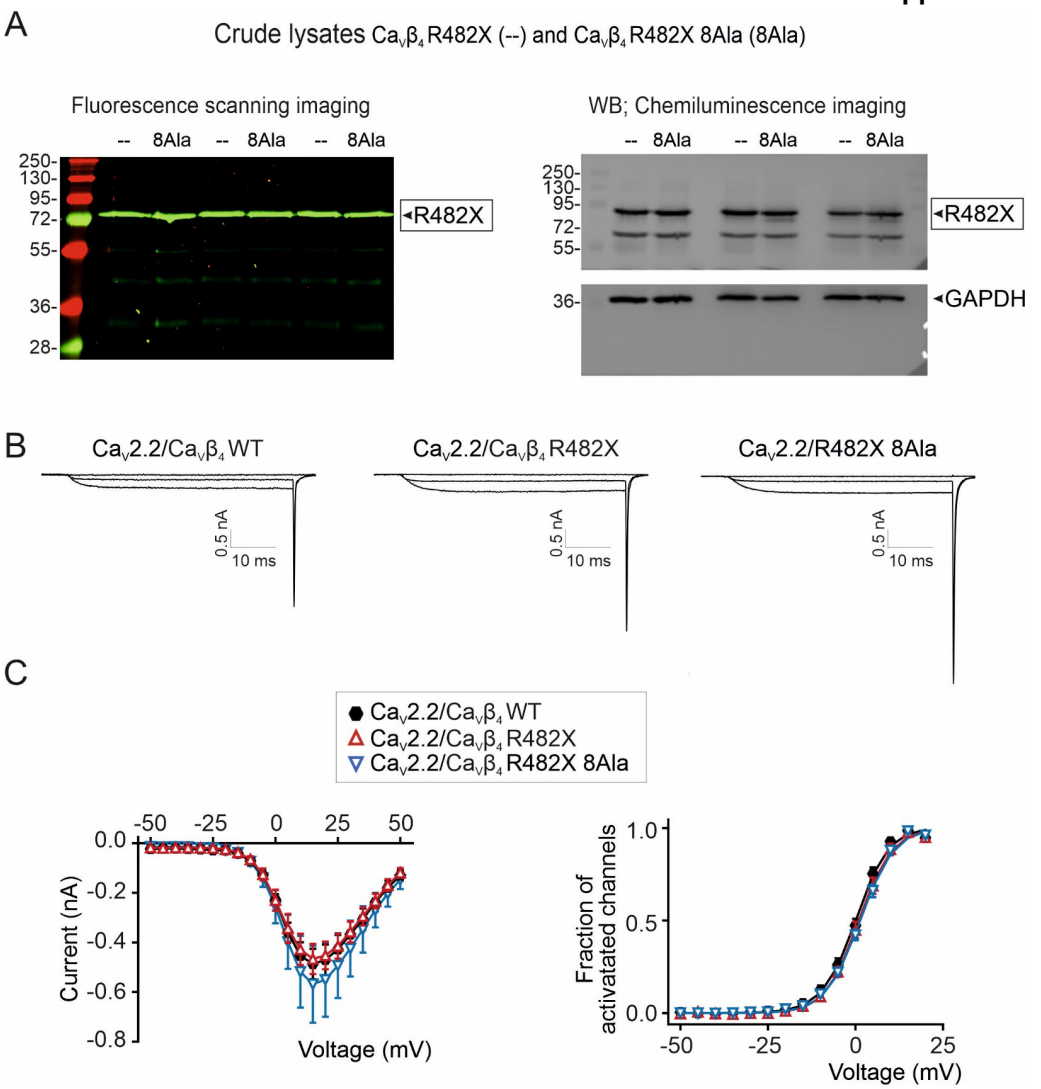

Supplementary Figure 18. Effect of $Ca_V\beta_4$ R482X and the actin-association-deficient $Ca_V\beta_4$ R482X mutant on $Ca_V2.2$ mediated currents in HEK 293 cells. **A**, Full images of SDS-PAGE from crude lysates of HEK293 cells expressing $Ca_V\beta_4$ R482X (--) and $Ca_V\beta_4$ R482X 8Ala (8Ala), both fused to mCherry. Lysates from three separate experiments were loaded in two separate gels for fluorescence scanning (left panel) and for Western blot analysis (WB) with anti-$Ca_V\beta_4$ and anti-GAPDH antibodies. **B**, Representative current traces mediated by heterologous $Ca_V2.2$ coexpressed in HEK293 cells with either wild-type $Ca_V\beta_4$ ($Ca_V\beta_4$ WT) or the $Ca_V\beta_4$ R482X variant bearing ($Ca_V\beta_4$ R482X 8Ala) or not ($Ca_V\beta_4$ R482X) the hotspot mutations leading to impaired association with actin. For visualization of transfected cells, $Ca_V2.2$ was fused to GFP while $Ca_V\beta_4$ constructs to mCherry. Currents were elicited by voltage steps from -50 to +50 in 5 mV increments from a holding potential of -90 mV and using Ba^{2+} as charge carrier. For clarity, only the current traces induced by -35, +20, and +45 mV pulses are shown. The pipette solution contained 135 mM cesium methanesulfonate, 10 mM EGTA, 5 mM CsCl, 1 mM $MgCl_2$, and 10 mM HEPES, adjusted to pH 7.3 with CsOH. The extracellular recording solution contained 140 mM tetraethylammonium-$MeSO_3$, 10 mM $BaCl_2$, and 10 mM HEPES buffer, adjusted to pH 7.3 with tetraethylammonium hydroxide. **C**, Plots of ionic current versus voltage (I/V) and fraction of activated channels versus voltage obtained from HEK293 cells transiently expressing the indicated constructs shown in A. Data are presented as mean ± SEM. Number of recorded cells (n) = 13 for $Ca_V2.2/Ca_V\beta_4$ WT, 12 for $Ca_V2.2/Ca_V\beta_4$ R482X, and 12 for $Ca_V2.2/Ca_V\beta_4$ R482X 8Ala. Mean current amplitudes (± SEM) are shown.

Supplementary Table 1. Summary of the cross-linked spectrum matches (CSMs). The table summarizes the number of CSMs per class (total, inter, intra, looplinked and dead-end) identified by the different software.

Cross-linker	Number of replicates	Software	Total CSMs	Inter CSMs	Intra CSMs	Looplinked CSMs	Dead-end CSMs
DSSO	5	MaxLynx	249	52	24	11	162
		MetaMorpheus	893	179	120	68	526
		Merox	67	14	12	1	40
DSBU	4	MaxLynx	331	14	31	68	218
		MetaMorpheus	370	19	53	80	218
		Merox	103	7	12	14	70

Supplementary Table 2. Intermolecular cross-links between actin and $Ca_V\beta2$ identified with DSSO and DSBU cross-linkers. Only unique intermolecular cross-links (inter-XLs) are reported; for each inter-XL, the replicate (Rep) number and the number of cross-linked spectra matches (CSMs) detected with each software are listed, with 'x' indicating 'not detected'. All CSMs fulfill the false discovery rate cutoff of 0.01.

Unique inter-XLs (ID)	DSSO[a]	DSBU[a]	Sequence Actin	Position	Sequence $Ca_V\beta_2$	Position recombinant protein ß2-core	Corresponding position Uniprot Q8VGC3-2	DSSO Rep_1 (CSMs) ML_MM_Me	DSSO Rep_2 (CSMs) ML_MM_Me	DSSO Rep_3 (CSMs) ML_MM_Me	DSSO Rep4 (CSMs) ML_MM_Me	DSSO Rep5 (CSMs) ML_MM_Me	DSBU Rep1 (CSMs) ML_MM_Me	DSBU Rep2 (CSMs) ML_MM_Me	DSBU Rep3 (CSMs) ML_MM_Me	DSBU Rep4 (CSMs) ML_MM_Me	Selected unique inter-XLs[b]	Self consistent inter-XLs[c]
1	*	*	HQGVMVGMGQKDSYVGDEAQSK	52	LIKSR	364	354	2_3_1	0_19_0	0_1_0	0_1_0	0_1_0	1_1_0	x	x	x	*	
2	*		HQGVMVGMGQKDSYVGDEAQSK	52	GKSQAK	368	358	0_1_0	x	x	0_1_0	x	x	x	x	x		
3	*		DSYVGDEAQSKR	63	AKQGK	146	136	0_1_0	x	x	0_3_0	x	x	x	x	x		
4	*		DSYVGDEAQSKR	63	ISSPKVLQR	357	347	0_6_0	x	x	0_2_0	x	x	x	x	x		
5	*	*	DSYVGDEAQSKR	63	LIKSR	364	354	6_7_2	1_1_0	x	1_2_1	0_1_0	2_1_1	x	1_1_0	x	*	*
6	*		DSYVGDEAQSKR	63	GKSQAK	368	358	0_2_0	x	x	0_1_0	x	x	x	x	x		
7	*		DSYVGDEAQSKR	63	SQAKHLNVQMVAADK	372	362	2_5_0	x	x	x	x	x	x	x	x	*	*
8	*		KDLYANNVMSGGTTMYPGIADR	293	GKSQAK	368	358	2_1_0	x	x	0_1_0	x	x	x	x	x	*	*
9	*		MQKEITALAPSTMK	317	AKQGK	146	136	1_1_0	x	x	x	x	x	x	x	x	*	
10	*		MQKEITALAPSTMK	317	ISSPKVLQR	357	347	0_2_0	0_2_0	x	0_1_0	x	x	x	x	x		
11	*		MQKEITALAPSTMK	317	LIKSR	364	354	2_3_1	5_5_0	x	3_1_2	x	x	x	x	x	*	*
12	*		MQKEITALAPSTMK	317	GKSQAK	368	358	6_12_0	0_1_0	x	3_5_0	x	x	x	x	x	*	*
13	*		EITALAPSTMKIK	328	AKQGK	146	136	2_1_0	x	x	0_1_0	x	x	x	x	x	*	
14		*	EITALAPSTMKIK	328	ISSPKVLQR	357	347	x	x	x	x	x	0_1_1	x	0_1_0	x	*	*
15	*	*	EITALAPSTMKIK	328	LIKSR	364	354	1_3_1	1_2_0	x	x	x	1_1_0	x	x	x	*	*
16	*		EITALAPSTMKIK	328	GKSQAK	368	358	3_4_1	x	x	1_3_0	x	x	x	x	x	*	*
17	*		IKIIAPPER	330	AKQGK	146	136	3_7_0	1_12_0	x	1_4_0	x	x	x	x	x	*	
18	*	*	IKIIAPPER	330	VTADISLAKR	284	274	x	x	x	x	0_1_0	x	1_0_1	1_1_0	x	*	
19	*	*	IKIIAPPER	330	ISSPKVLQR	357	347	0_12_0	1_12_1	0_2_0	0_3_0	0_1_0	2_2_1	1_1_0	2_2_1	1_1_0	*	*
20	*	*	IKIIAPPER	330	LIKSR	364	354	0_4_0	3_10_0	0_5_0	1_9_0	0_1_0	0_3_1	x	1_2_1	x	*	*
21	*		IKIIAPPER	330	GKSQAK	368	358	0_5_2	0_11_0	0_3_0	0_5_0	0_1_0	x	x	x	x	*	*
22	*	*	IKIIAPPER	330	SQAKHLNVQMVAADK	372	362	x	0_4_0	x	x	x	x	x	0_1_0	x		

[a] Unique inter-XLs detected with the indicated cross-linker.
[b] Inter-XLs were selected when detected with more than one software (MaxLynx (ML), Metamorpheus (MM) and Merox (Me)).
[c] Inter-XLs were identified as self-consistent by DisVis.

Supplementary Table 3. Data consistency and violation analysis of XL-MS data obtained for $Ca_V\beta_2$-actin interaction performed with DisVis webserver. Only self-consistent restraints are listed. Note that the restraints are defined as fixed chain/scanning chain (actin-$Ca_V\beta_2$), i.e swapped order compared to the main text.

(A) $Ca_V\beta_2$–actin dimer			
#	**Restraint**	**Average violated fraction**	**Standard deviation**
1	K328-K354	0.16	0.20
2	K328-K358	0.17	0.19
3	K330-K354	0.17	0.21
4	K330-K358	0.18	0.19
5	K293-K358	0.20	0.18
6	K317-K354	0.23	0.17
7	K317-K358	0.24	0.16
8	K328-K347	0.27	0.19
9	K330-K347	0.29	0.19
10	K63'-K354	0.42	0.18
11	K63'-K362	0.43	0.18

(B) $Ca_V\beta_2$–actin monomer			
#	**Restraint**	**Average violated fraction**	**Standard deviation**
1	K330-K354	0.15	0.23
2	K328-K354	0.16	0.23
3	K328-K358	0.18	0.23
4	K330-K358	0.18	0.23
5	K317-K354	0.20	0.22
6	K317-K358	0.22	0.22
7	K293-K358	0.23	0.21
8	K330-K347	0.25	0.22
9	K328-K347	0.25	0.21
10	K63-K362	0.74	0.34
11	K63-K354	0.78	0.30

Supplementary Table 4. Statistics from the HADDOCK information-driven docking calculations for the $Ca_V\beta_2$–actin and $Ca_V\beta_4$–actin complex models.

A, HADDOCK statistics for **$Ca_V\beta_2$–actin dimer** docking structures								
Cluster	**HADDOCK score (arb. units)**	**Cluster size**	**Global RMSD (Å)**	**van der Waals energy (E_{vdw}, kcal^{-1} mol)**	**Electrostatic energy (E_{elec}, kcal^{-1} mol)**	**Desolvation energy (E_{desol}, kcal^{-1} mol)**	**Restraints violation energy (E_{air}, kcal^{-1} mol)**	**Buried surface area (BSA, Å^2)**
#1	-67.8 ± 7.0	198	1.4 ± 1.1	-87.7 ± 9.1	-525.3 ± 104.4	43.3 ± 6.0	815.8 ± 55.5	3208.0 ± 203.6

B, HADDOCK statistics for **$Ca_V\beta_4$–actin dimer** docking structures								
Cluster	**HADDOCK score (arb. units)**	**Cluster size**	**Global RMSD (Å)**	**van der Waals energy (E_{vdw}, kcal^{-1} mol)**	**Electrostatic energy (E_{elec}, kcal^{-1} mol)**	**Desolvation energy (E_{desol}, kcal^{-1} mol)**	**Restraints violation energy (E_{air}, kcal^{-1} mol)**	**Buried surface area (BSA, Å^2)**
#1	5.5 ± 10.9	135	7.4 ± 0.4	-68.8 ± 1.2	-328.3 ± 59.0	18.4 ± 8.1	1216.8 ± 196.3	2795.9 ± 230.3
#2	-2.7 ± 14.6	29	7.7 ± 0.2	-108.0 ± 12.4	-301.1 ± 20.5	22.7 ± 6.2	1428.7 ± 50.0	3540.4 ± 338.7
#3	43.0 ± 7.1	15	3.0 ± 0.7	-47.9 ± 5.1	-402.8 ± 59.8	30.5 ± 4.9	1409.0 ± 104.7	2128.5 ± 91.3
#4	27.9 ± 4.6	10	8.6 ± 0.8	-65.2 ± 11.1	-254.7 ± 61.2	10.8 ± 0.8	1332.1 ± 161.0	2294.1 ± 410.6
#5	-48.6 ± 35.4	4	1.3 ± 1.0	-94.2 ± 17.7	-512.6 ± 103.4	34.3 ± 2.9	1138.5 ± 114.0	3424.7 ± 481.7

C, HADDOCK statistics for **$Ca_V\beta_2$–actin monomer** docking structures								
Cluster	**HADDOCK score (arb. units)**	**Cluster size**	**Global RMSD (Å)**	**van der Waals energy (E_{vdw}, kcal^{-1} mol)**	**Electrostatic energy (E_{elec}, kcal^{-1} mol)**	**Desolvation energy (E_{desol}, kcal^{-1} mol)**	**Restraints violation energy (E_{air}, kcal^{-1} mol)**	**Buried surface area (BSA, Å^2)**
#1	-40.5 ± 10.1	57	2.3 ± 1.4	-91.1 ± 6.3	-357.1 ± 58.3	16.1 ± 2.4	1059.7 ± 97.6	2982.6 ± 221.4
#2	3.5 ± 8.6	54	18.5 ± 0.5	-49.0 ± 9.7	-264.7 ± 89.4	7.9 ± 5.6	975.5 ± 104.2	1629.6 ± 200.1
#3	6.1 ± 7.7	25	19.9 ± 1.2	-62.1 ± 5.4	-261.5 ± 41.9	8.6 ± 2.0	1118.6 ± 93.0	1825.1 ± 78.1
#4	2.5 ± 7.3	18	20.2 ± 0.2	-46.4 ± 8.7	-244.3 ± 16.6	11.5 ± 3.6	862.8 ± 51.7	1524.7 ± 36.5
#5	-2.7 ± 3.3	13	9.0 ± 0.7	-63.1 ± 6.7	-469.8 ± 70.3	26.4 ± 6.1	1278.8 ± 57.4	2453.9 ± 184.4
#6	19.7 ± 4.5	10	21.7 ± 0.5	-39.0 ± 5.2	-297.9 ± 56.7	13.3 ± 3.8	1049.5 ± 64.8	1427.1 ± 83.1
#7	14.8 ± 17.5	6	21.0 ± 0.7	-46.2 ± 10.4	-316.8 ± 65.1	14.4 ± 4.1	1099.4 ± 90.2	1621.7 ± 163.9
#8	34.3 ± 6.4	5	21.5 ± 0.1	-36.5 ± 4.8	-210.8 ± 22.8	2.1 ± 1.3	1109.4 ± 157.7	1256.2 ± 107.2

Computational docking was performed on the HADDOCK 2.4 webserver. The resulting docking structures (199, 198 and 188 for the $Ca_V\beta_2$–actin dimer, $Ca_V\beta_4$–actin dimer and $Ca_V\beta_2$–actin monomer complexes, respectively) were clustered based on the interface ligand RMSD (i-l-RMSD) from the lowest HADDOCK score structure using a 7.5 Å cutoff (see Supplementary Table 5). Clusters are ranked by the average HADDOCK score of the top four structures. Global RMSD, intermolecular van der Waals, electrostatic, desolvation and restraints violation energy terms, as well as buried surface area, are also averaged over the top four structures of each cluster.

Supplementary Table 5. Dependence of the cluster metrics on the i-l-RMSD cutoff used for clustering. For each cutoff value, the average and standard deviation of three different RMSD metrics (i-l-RMSD, i-RMSD and l-RMSD, see Methods) are given to assess the similarity among the structures belonging to the first cluster. For all RMSD calculations described below, the reference structure is the model with the lowest HADDOCK score, which belongs to the first cluster for the $Ca_V\beta_2$-actin dimer docking or to the fifth cluster for the $Ca_V\beta_4$-actin dimer docking.

(A) $Ca_V\beta_2$–actin dimer models, cluster #1				
i-l-RMSD cutoff (Å)	**cluster size**	**i-l-RMSD (Å)**	**i-RMSD (Å)**	**l-RMSD (Å)**
5.0	181	3.0±1.3	0.9±0.4	3.1±1.6
5.5	184	3.0±1.3	0.9±0.4	3.2±1.6
6.0	184	3.0±1.3	0.9±0.4	3.2±1.6
6.5	185	3.1±1.4	0.9±0.4	3.2±1.7
7.0	186	3.1±1.5	0.9±0.4	3.3±1.8
7.5*	198	3.7±2.6	1.0±0.4	4.3±4.1
8.0	200	3.7±2.6	1.0±0.4	4.3±4.1
8.5	200	3.7±2.6	1.0±0.4	4.3±4.1
9.0	200	3.7±2.6	1.0±0.4	4.3±4.1
9.5	200	3.7±2.6	1.0±0.4	4.3±4.1
10.0	200	3.7±2.6	1.0±0.4	4.3±4.1

* For the top 4 models of the first cluster identified with a 7.5 Å i-l-RMSD cutoff, the i-l-RMSD, i-RMSD and l-RMSD values are 3.1±2.7 Å, 0.9±0.6 Å and 2.8±2.4 Å, respectively.

(B) $Ca_V\beta_4$–actin dimer models, cluster #1				
i-l-RMSD cutoff (Å)	**cluster size**	**i-l-RMSD (Å)**	**i-RMSD (Å)**	**l-RMSD (Å)**
5.0	102	15.8±0.9	1.2±0.2	14.0±0.7
5.5	108	15.6±1.1	1.3±0.2	14.1±0.8
6.0	114	15.5±1.4	1.3±0.2	14.0±0.9
6.5	117	15.5±1.5	1.3±0.2	14.1±1.0
7.0	120	15.5±1.6	1.3±0.3	14.1±1.1
7.5*	135	15.6±1.5	1.4±0.5	14.2±1.1
8.0	141	15.6±1.5	1.5±0.5	14.3±1.2
8.5	152	15.2±1.6	1.5±0.5	14.7±1.8
9.0	167	15.3±1.6	1.5±0.5	14.8±1.8
9.5	170	15.3±1.6	1.5±0.5	14.9±1.8
10.0	171	15.3±1.6	1.5±0.5	14.9±1.9

* For the top 4 models of the first cluster identified with a 7.5 Å i-l-RMSD cutoff, the i-l-RMSD, i-RMSD and l-RMSD values are 16.3±0.6 Å, 1.8±0.7 Å and 15.0±0.8 Å, respectively.

(C) $Ca_V\beta_4$–actin dimer models, cluster #2				
i-l-RMSD cutoff (Å)	**cluster size**	**i-l-RMSD (Å)**	**i-RMSD (Å)**	**l-RMSD (Å)**
5.0	24	13.7±0.7	2.0±0.4	17.1±1.8
5.5	33	13.1±1.0	1.9±0.5	16.0±2.4
6.0	22	14.0±0.9	2.0±0.5	18.1±1.6
6.5	22	14.0±0.9	2.0±0.5	18.3±1.5
7.0	22	14.0±0.9	2.0±0.5	18.3±1.5
7.5*	29	13.9±1.2	1.9±0.5	17.9±1.9
8.0	30	13.9±1.2	1.9±0.5	17.8±1.9

* For the top 4 models of the second cluster identified with a 7.5 Å i-l-RMSD cutoff, the i-l-RMSD, i-RMSD and l-RMSD values are 13.4±0.3 Å, 2.3±0.2 Å and 16.8±0.7 Å, respectively.

N.B. The cluster analyzed for each of the i-l-RMSD cutoff values listed above is the one containing the top 4 structures of the second cluster identified with a 7.5 Å i-l-RMSD cutoff. For cutoff values 5.0, 7.5 and 8.0 Å, the corresponding cluster is #2 (as shown in the Supplementary Table 5C header), whereas for the cutoff range 5.5-7.0 Å, it is numbered as #3. For cutoff values above 8.5 Å, the aforementioned top 4 structures are classified within cluster #1; thus, the statistics are no longer reported here but in Supplementary Table 5C.

Supplementary Table 5 (*cont.*).

(D) $Ca_V\beta_4$–actin dimer models, cluster #5				
i-l-RMSD cutoff (Å)	**cluster size**	**i-l-RMSD (Å)**	**i-RMSD (Å)**	**l-RMSD (Å)**
5.0	8	4.4±1.4	0.4±0.2	4.3±1.4
5.5	10	4.4±2.4	0.5±0.5	4.4±2.5
6.0	11	4.9±2.7	0.7±0.7	4.9±2.8
6.5	11	4.9±2.7	0.7±0.7	4.9±2.8
7.0	11	4.9±2.7	0.7±0.7	4.9±2.8
7.5*	4	2.2±1.8	0.5±0.3	2.4±2.1
8.0	4	2.2±1.8	0.5±0.3	2.4±2.1
8.5	16	9.0±3.6	1.1±0.7	9.4±4.2
9.0	6	21.5±1.5	2.9±0.7	19.7±2.1
9.5	19	7.9±4.2	1.0±0.7	8.3±4.7
10.0	19	7.9±4.2	1.0±0.7	8.3±4.7

* For the top 4 models of the fifth cluster identified with a 7.5 Å i-l-RMSD cutoff, the i-l-RMSD, i-RMSD and l-RMSD values are the same as listed in the table above, as the cluster size contains only these four structures.

N.B. The cluster analyzed for each of the i-l-RMSD cutoff values listed above is the one containing the top 4 structures of the fifth cluster identified with a 7.5 Å i-l-RMSD cutoff (as shown in the Supplementary Table 5D header). For the cutoff range 5.0-7.0 Å and 8.0 Å, the corresponding cluster is #4, whereas for cutoff values 8.5-9.0 Å and 9.5-10.0 Å, it is numbered as #3 and #2, respectively.

Supplementary Table 6. Control protein-protein docking simulations without XL-MS-based distance restraints. The same protein structures as in the XL-MS guided docking presented in Supplementary Table 4A were used, but sampling of docking solutions was increased to 10,000 (rigid body docking) and 400 (simulated annealing and water refinement steps). The *ab initio* docking options listed below were employed in place of the XL-MS-based distance restraints to ensure the contact between the two proteins; several control simulations were run, with different combinations of such *ab initio* docking options. Regardless of the *ab initio* docking settings used, the resulting models were largely inconsistent with the experimentally identified interXLs; depending on the control simulation, only between 0 and 6 models (out of 400 generated in each docking) were consistent with the XL-MS data. The best scored *ab initio* docking models (top 1 and top 10, ranking based on the HADDOCK score) were also significantly different from the XL-MS guided (and experimentally validated) actin–$Ca_v\beta_2$ complex model, as shown by their I-RMSD values.

Control simulation #	*Ab initio* docking settings[(a)]			Docking comparison[(b)]			InterXL consistency[(c)]	
	Center of mass restraints	Random AIRs	Surface contact restraints	Top 1 scored model I-RMSD (Å)	Top 10 scored models I-RMSD (Å)	Closest model I-RMSD (Å) & ranking position	# Models consistent with interXLs	XL consistent models I-RMSD (Å)
1	yes	yes	yes	78.9	69.8±9.5	14.0, #208[(d)]	4	91.7, 14.0 81.2, 87.1
2	yes	no	yes	66.6	72.6±6.5	19.9, #248	6	91.4, 83.7 83.7, 83.8 83.7, 45.6
3	yes	yes	no	64.4	77.0±19.6	26.0, #150	3	91.8, 83.9 81.2
4	no	yes	yes	79.8	70.5±10.8	31.7, #35	3	82.5, 79.9 83.1
5	no	no	yes	73.9	70.6±12.8	33.4, #344	2	95.2, 62.3
6	no	yes	no	55.3	67.0±26.5	18.5, #10	0	–

[a] The following *ab initio* docking options available in the HADDOCK webserver were used. (i) Center of mass restraints are defined between each molecule as an ambiguous distance restraint with centers averaging between all Cα atoms of each molecule. The upper distance limit is automatically defined as the sum of the "effective radius" of each molecule, which is in turn defined as half the average length of the three principal components. (ii) Random ambiguous interaction restraints (AIRs) are based on solvent accessible residues (>20% relative accessibility). During the rigid body docking step, such AIRs are defined from a 5 Å radius patch randomly selected from one protein to a 7.5 Å radius patch randomly selected on the other molecule and vice versa, whereas in the simulated annealing step the AIRs are automatically defined between all residues within 5 Å across the interface.(iii) Surface contact restraints are defined between each molecule as an ambiguous distance restraint with sum averaging between all Cα atoms of one protein and all Cα atoms of the other protein; the upper distance limit is set to 7 Å.

[b] The *ab initio* docking models turned out to be very heterogeneous, with clustering (using the default i-l-RMSD cutoff of 7.5 Å) resulting in either a single cluster containing only 1% of the 400 structures generated or a large number of clusters (between 17 and 28, depending on the control simulation) covering only a subset of docking models (between 9 and 54%). Thus, for the analyses presented here we chose to consider all 400 *ab initio* models without clustering. As the docking between the actin dimer and $Ca_v\beta_2$ is a multibody docking simulation of a ternary complex, some of the generated models showed a disrupted actin dimer interface. Hence, we first filtered the generated 400 actin–$Ca_v\beta_2$ complex models based on the actin backbone RMSD with respect to the initial structure of the actin dimer alone; only those models with RMSD below 3.5 Å were retained for further analysis. We then compared the two docking protocols (XL-MS-guided and *ab initio*) using two different approaches. The first comparison was performed by selecting the best scored *ab initio* docking models, either the first (top 1) or the first ten (top 10) structures ranked by HADDOCK score, and calculating their l-RMSD (see Methods), using as reference the best scored XL-MS-guided docking model. The second comparison consisted in identifying the *ab initio* docking model with the lowest l-RMSD with respect to the best scored XL-MS-guided docking model and reporting its l-RMSD value together with the HADDOCK score-based ranking position among the 400 models generated in the corresponding control simulation.

[c] Models were considered to be consistent with XL data if the Euclidean distances of all 11 identified inter-crosslinks (see Supplementary Table 3A) were lower or equal to 35.0 Å. The l-RMSD was calculated as explained in the Methods, using as reference the best scored actin–$Ca_v\beta_2$ complex model obtained in the XL-MS-guided docking simulation.

[d] It is worth mentioning that one of the models of control simulation #1 was consistent with the XL-MS data and, with respect to the best XL-MS-guided docking model, displayed the lowest l-RMSD value (14.0 Å) across all six control simulations. However, this *ab initio* model was ranked 208 (out of 400 models in control simulation #1) and thus would not have been selected based on the HADDOCK score alone. Moreover, the superposition of this *ab initio* model with the XL-MS guided actin–$Ca_v\beta_2$ complex model (see Supplementary Figure 5) showed that the protein-protein interface of the two complexes is different, as evidenced by the i-RMSD value of 7.9 Å.

Supplementary Table 7. Intermolecular contacts involving the eight $Ca_V\beta$ hotspot residues at the protein-protein interface with actin. The top 4 models of the first cluster of the $Ca_V\beta$-actin dimer docking simulations were analyzed with the PRODIGY webserver. Actin residues in monomer *n+2* are indicated with a prime (') symbol. Contacts observed/absent in the corresponding model are indicated with a tick/cross, respectively.

(A) $Ca_V\beta_2$ hotspot–actin contacts					
$Ca_V\beta2$ hotspot	**Actin interacting residue**	**Top1 structure**	**Top 2 structure**	**Top 3 structure**	**Top 4 structure**
K90	T7	×	×	×	✓
	D26	✓	✓	✓	✓
	D27	✓	×	✓	×
	A28	✓	×	✓	×
	R30	×	✓	✓	✓
R128	Y145	✓	×	✓	×
	I347	✓	×	✓	×
	L348	✓	×	✓	×
	A349	×	✓	×	✓
	S350	✓	✓	✓	✓
	L351	✓	✓	✓	✓
	S352	×	✓	✓	✓
	Q355	×	✓	×	✓
K347	G148’	✓	✓	✓	×
	R149’	✓	✓	✓	×
	T150’	✓	✓	✓	×
	T151’	✓	✓	✓	×
	Y168’	✓	✓	✓	×
	E169’	✓	✓	✓	×
	K293’	×	×	✓	×
	D294’	✓	✓	✓	×
	N298’	✓	×	✓	×
Q350	L144’	×	✓	×	✓
	Y145’	×	✓	×	×
	S147’	×	✓	×	×
	G148’	✓	✓	✓	✓
	R149’	✓	✓	✓	✓
	T150’	✓	✓	✓	✓
	T151’	×	×	✓	×
K354	L144’	×	✓	×	×
	Y145’	✓	✓	✓	✓
	A146’	✓	✓	✓	✓
	S147’	✓	✓	✓	✓
	G148’	✓	✓	✓	✓
	R149’	×	✓	×	×
	I343’	×	✓	×	×
	I347’	✓	✓	✓	✓

– Continued in the next page –

(A) $Ca_V\beta_2$ hotspot–actin contacts (*cont.*)					
$Ca_V\beta2$ hotspot	**Actin interacting residue**	**Top1 structure**	**Top 2 structure**	**Top 3 structure**	**Top 4 structure**
K358	G25’	✓	✓	✓	✓
	D26’	✓	✓	✓	✓
	D27’	✓	✓	✓	✓
	A28’	×	×	×	✓
	S346’	✓	×	×	×
	I347’	✓	✓	✓	×
	S350’		✓	×	×
L364	Y145’	✓	×	×	×
	L351’	✓	×	×	×
	S352’	✓	×	×	×
N365	V45	✓	×	✓	×
	G48	✓	×	✓	×
	M49	✓	×	×	×
	Y145’	×	×	✓	×
	L351’	✓	✓	✓	✓
	S352’	✓	✓	×	×
	T353’	✓	✓	✓	✓

Supplementary Table 7 (*cont.*).

(B) $Ca_V\beta_4$ hotspot–actin contacts					
$Ca_V\beta_4$ hotspot	**Actin interacting residue**	**Top1 structure**	**Top 2 structure**	**Top 3 structure**	**Top 4 structure**
K122	G25	×	×	×	✓
	D26	✓	×	×	✓
	D27	✓	×	×	✓
	A28	✓	×	×	✓
	R30	×	×	✓	×
R160	T8	×	✓	✓	×
	A24	×	✓	✓	×
	G25	×	✓	✓	×
	D26	×	✓	✓	×
	S350	✓	×	×	✓
	L351	✓	×	×	✓
	S352	✓	×	×	✓
K339	P245	×	×	×	✓
	R149’	✓	✓	✓	
	K293’	✓	×	×	✓
	D294’	✓	×	×	✓
	L295’	✓	×	×	
	Y296’	×	×	×	✓
	A297’	✓	×	×	✓
	N298’	✓	×	×	
	M327’	×	×	×	✓
	K328’	×	×	×	✓
	K330’	×	✓	×	×
	I331’	×	✓	✓	×
	I332’	×	✓	✓	×
	A333’	×	✓	✓	×
Q342	A146’	×	✓	✓	×
	S147’	✓	✓	✓	×
	G148’	✓	✓	✓	×
	R149’	✓	✓	✓	×
	T150’	✓	×	×	×
	D294’	×	×	×	✓
	A297’	×	×	×	✓
	N298’	×	×	×	✓
	I332’	×	✓	✓	×
	P334’	×	✓	✓	×

– Continued in the next page –

(B) $Ca_V\beta_4$ hotspot–actin contacts (*cont.*)					
$Ca_V\beta_4$ hotspot	**Actin interacting residue**	**Top1 structure**	**Top 2 structure**	**Top 3 structure**	**Top 4 structure**
K346	D27’	×	✓	✓	×
	A146’	✓	×	×	×
	S147’	✓	×	×	×
	G148’	✓	×	×	×
	R149’	×	×	×	✓
	A297’	×	×	×	✓
	N298’	×	×	×	✓
	I332’	×	×	×	✓
	P335’	×	✓	✓	×
	E336’	×	✓	✓	×
	I342’	×	×	✓	×
K350	G25’	×	✓	✓	×
	D26’	×	✓	✓	×
	D27’	×	✓	✓	×
	A28’	×	✓	✓	×
	R30’	×	✓	✓	×
	A146’	×	×	×	✓
	S147’	×	×	×	✓
	I343’	×	×	×	✓
	I347’	×	×	×	✓
L356	Y145’	×	✓	✓	×
	A146’	×	✓	✓	×
	S147’	×	✓	✓	×
	G148’	✓	✓	✓	✓
	R149'	✓	×	✓	✓
	I347’	×	✓	×	×
N357	V45	✓	✓	✓	×
	G48	✓	×	×	×
	M49	✓	×	×	×
	L144’	×	✓	×	×
	Y145’	×	✓	✓	×
	A146’	×	✓	×	×
	S147’	×	✓	×	×
	G148’	×	✓	✓	✓
	R149’	×	✓	✓	✓
	T150’	✓	✓	✓	✓
	T151’	×	×	×	✓
	E169’	×	×	×	✓
	I347’	×	✓	×	×

Supplementary Table 8. Non-synonymous SNPs of human $Ca_V\beta_2$ and $Ca_V\beta_4$ at amino acid positions analogous to the eight $Ca_V\beta$ hotspot residues at the protein-protein interface with actin.
(**A**) Human $Ca_V\beta_2$ (www.uniprot.org/uniprotkb/Q08289/variant-viewer). (**B**) Human $Ca_V\beta_4$ (www.uniprot.org/uniprotkb/O00305/variant-viewer). Data retrieved on November 2024 from the UniProt database.

(A) Non-synonymous SNPs for $Ca_V\beta_2$ actin hotspots					
rat $Ca_V\beta_2$ (Q8VGC3-2)	**human $Ca_V\beta_2$ (Q082289-1)**	**Variant ID**	**Change**	**Description & Clinical Significance**	**Provenance**
K90	K145	rs1554831385	K>*		Ensembl
R128	R183	TCGA novel	R>S	Variant assessed as somatic; MODERATE impact (NCI-TCGA)	NCI-TCGA
		rs2050158937	R>G		TOPmed
K347	K402	rs1554840899	K>*		Ensembl
Q350	Q405	rs1554841459	Q>*		Ensembl
		rs1206230612	Q>H		TOPmed gnomAD
		rs1281052136	Q>R		TOPmed
K354	K409	rs1554841468	K>*		Ensembl
		TCGA novel	K>Q	Variant assessed as somatic; MODERATE impact (NCI-TCGA)	NCI-TCGA
		rs2053546700	K>R		TOPmed
K358	K413	rs1554841479	K>*		Ensembl
L364	L419	rs1202561047	L>P		gnomAD
N365	N420	COSV56627386	N>S	Variant assessed as somatic; MODERATE impact (NCI-TCGA)	NCI-TCGA Cosmic cosmic curated

Supplementary Table 8 (*cont.*).

(B) Non-synonymous SNPs for $Ca_V\beta_4$ actin hotspots					
rat CaVβ4 (D4A055-2)	**human CaVβ4 (O00305-1)**	**Variant ID**	**Change**	**Effect**	**Provenance**
K122	K123	rs761287173	K>E		ExAC gnomAD
		rs753508642	K>T		ExAC gnomAD
R160	R161	rs1199094751	R>Q		gnomAD
		COSV52393347 rs1257214495	R>W	Variant assessed as somatic; MODERATE impact (NCI-TCGA)	NCI-TCGA Cosmic cosmic curated TOPmed dbSNP gnomAD
K339	K340	rs1553746911	K>*		Ensembl
Q342	Q343	rs1328517680	Q>*		TOPmed gnomAD
		CA348789818 RCV000634979 rs1328517680	Q>E	Idiopathic generalized epilepsy (ClinVar) Variant of uncertain significance (Ensembl, ClinVar)	ClinGen ClinVar TOPMed dbSNP gnomAD
K346	K347	rs1169198515	K>*		gnomAD
		rs1169198515	K>E		gnomAD
K350	K351	rs1553746086	K>*		Ensembl
L356	L357	rs1553746054	L>*		Ensembl
N357	N358	rs746420663	N>S		ExAC gnomAD

Supplementary Table 9

REAGENT or RESOURCE	SOURCE	IDENTIFIER
Antibodies		
anti-CACNB2	Novus Biologicals	NBP186680
anti-GADPH	Sigma-Aldrich	G9545
anti-CACNB4	Novus Biologicals	NBP212908
goat anti-rabbit IgG HRP-conjugated	Thermo Fisher Scientific	31463
Bacterial and cell lines		
BL21 (DE3) competent *E.coli* cells (recombinant protein production)	Thermo Scientific	Cat #EC0114
TOP10F competent *E.coli* cells (molecular biology)	Invitrogen	Cat#C303006
HEK293	Sigma-Aldrich	Cat #12022001
Chemicals		
Cesium methanesulfonate	Sigma	Cat#C1426
EGTA	Sigma	Cat#E3889
Cesium chloride	Sigma	Cat#289329
Magnesium chloride·6H2O	Serva	Cat#39771.01
HEPES	PanReac	Cat#A1069
Cesium hydroxide solution	Sigma	Cat#232041
Barium chloride dihydrate	Sigma	Cat#B0750
Tetraethylammonium hydroxide solution	Sigma	Cat#86633
CellMask™ Plasma Membrane Stain Green	Thermo Fisher Scientific	Cat#C37608
Opti-MEM™	Thermo Fisher Scientific	Cat#11058021
DMEM, high glucose, GlutaMAX™ Supplement	Thermo Fisher Scientific	Cat#61965026
Penicillin-Streptomycin (5,000 U/mL)	Thermo Fisher Scientific	Cat#15070063
Fetal Bovine Serum	Thermo Fisher Scientific	Cat#10270106
Dimethylsulfoxide (DMSO) anhydrous	Invitrogen	Cat#D12345
DSBU (Disuccinimidyl Dibutyric Urea)	Thermo Fisher Scientific	Cat#A35459
DSSO (Disuccinimidyl Sulfoxide)	Thermo Fisher Scientific	Cat#A33545
cOmplete™ EDTA-free Protease Inhibitor Cocktail	Roche	Cat#05056489001
Rabbit skeletal muscle actin	Cytoskeleton	Cat#AKL99

Trypsin	SERVA	Cat#37286.01

Acknowledgements

El agradecimiento a otros, en opinión del autor, se demuestra a través de las interacciones del día a día, ya sea en persona o a distancia. Por tanto, no existen palabras que, en este diminuto pasaje de esta contribución científica, puedan expresar propiamente lo profundamente agradecido que me encuentro con todas las personas con las que me he relacionado durante el doctorado. De hecho, el autor de esta tesis insistió profusivamente en no redactar los agradecimientos y únicamente lo hizo bajo coerción física y psicológica ejercida en su contra por parte de quienes requieren constante atención.

Agradezco entonces, en nombre y apellido, a quienes afirman ser mis padres, Víctor Lugo y Berlyz García. Me dieron la vida y el sustento para vivirla con gusto y responsabilidad. A mi hermano, el mejor tanque de todos, Manuel Lugo. A mi hermana, Angie Lugo, quien trajo felicidad a nuestras vidas a través de mis sobrinas Rebeca y Miranda. A mi tía Haydée Lugo, a quien voy alcanzando. A mi abuela Edith Mondragón, la persona más fuerte de este planeta. Al abuelo con quien comparto nombre, Víctor Lugo. Y a mis abuelos José de los Santos García Parra, alias Santos, y María Antonia Arocha Armas, alias Antonieta, que en paz descansen. Los padres crían; los abuelos consienten.

Agradezco a mi supervisor, el Prof. Christoph Fahlke, quien es la viva imagen de la creatividad, la originalidad y la ética científica de un investigador exitoso. Muchísimas gracias por permitirme realizar investigación científica en el área en la que quería trabajar. A la Prof. Hidalgo, cuya nobleza y transparencia son únicamente equiparables a su calidad científica. Al resto del personal del IBI-1, en especial a Arne Franzen, Meike Berndt y Nadine Jordan, cuyas vidas, sin duda, se llenaron de felicidad desde que tuvieron el placer de conocer al autor. Por supuesto, a lo mejor que me sucedió en el instituto: Jan-Gerrit Folkerts. Que descanses en paz.

Agradezco a la familia que tengo en Alemania. A Bassam G. Haddad, cuya G significa «gánster»; al gran Markus Eicheldinger y al joven Yannick Güthoff. Se han comportado como verdaderos amigos durante lo que ya son bastantes años. Inclusive Piersilvio Longo, cuyo calificativo es reservado por el autor por motivos de discreción y decoro. A Lea, con quien comparto puntos de vista. Al nuevo compañero de viajes, Julius Körber. A la señora de los ojos bonitos, aunque no del todo operativos, Supriya Ulaganathan, víctima de una estrategia fríamente calculada y científicamente planificada que la dejó sin opción alguna de escapatoria. Le toca ahora tratar de conquistar el mundo.

A los miembros del instituto que me precedieron y a los que me sucederán, ambos grupos curiosamente más añejados en rasgos que el autor. A Bettina Kolen, Daniel Kortzak, Nataliia Dmitrieva y un tal Bart Borghans, quienes tenían mucho que enseñar, menos sentido del humor. A Nruthyathi, Assalla, Kateryna, Juan, Francisco, Ignacio, Claudia, Daniel, Inge, Alex, Cansu y el señor J. Porto. Al cuartel de las feas, Marlon y Albert.

Evidentemente, el autor se agradece a sí mismo por el esfuerzo realizado y a todos aquellos que, de alguna manera u otra, han apoyado este emprendimiento de investigación científica, con el cual se esperan dividendos en divisas en el futuro, una vez que saque la cura de todos los males que tiene escondida debajo de la cama.

Bibliography

1 **Südhof, T.C.** 2021. The cell biology of synapse formation. *J. Cell Biol.* **220(7):** 1–18. *doi:10.1083/jcb.202103052.*

2 **Jabeen, S. and Thirumalai, V.** 2018. The interplay between electrical and chemical synaptogenesis. *J. Neurophysiol.* **120(4):** 1914–1922. *doi:10.1152/jn.00398.2018.*

3 **Goodman, S.R. ed.** 2008. *Medical cell biology.* 3rd ed. Amsterdam, the Netherlands: Elsevier/Academic Press. *ISBN:9780123704580.*

4 **Pal, M.M.** 2021. Glutamate: The master neurotransmitter and its implications in chronic stress and mood disorders. *Front. Hum. Neurosci.* **15, 722323:** 1–4. *doi:10.3389/fnhum.2021.722323.*

5 **Mutluay, S.U. and Karataş, H.** 2022. A review of glutamate and its receptors: Their roles in brain physiology and pathology. *Acta Med.* **53(2):** 99–109. *doi:10.32552/2022.ActaMedica.650.*

6 **Scannevin, R.H. and Huganir, R.L.** 2000. Postsynaptic organization and regulation of excitatory synapses. *Nat. Rev. Neurosci.* **1(2):** 133–141. *doi:10.1038/35039075.*

7 **Magi, S., Piccirillo, S., Amoroso, S. and Lariccia, V.** 2019. Excitatory amino acid transporters (EAATs): glutamate transport and beyond. *Int. J. Mol. Sci.* **20(22), 5674:** 1–11. *doi:10.3390/ijms20225674.*

8 **Kovermann, P., Engels, M., Müller, F. and Fahlke, C.** 2022. Cellular physiology and pathophysiology of EAAT anion channels. *Front. Cell. Neurosci.* **15, 815279:** 1–14. *doi:10.3389/fncel.2021.815279.*

9 **Bak, L.K., Schousboe, A. and Waagepetersen, H.S.** 2006. The glutamate/GABA–glutamine cycle: aspects of transport, neurotransmitter homeostasis and ammonia transfer. *J. Neurochem.* **98(3):** 641–653. *doi:10.1111/j.1471-4159.2006.03913.x.*

10 **McKenna, M.C.** 2007. The glutamate–glutamine cycle is not stoichiometric: fates of glutamate in brain. *J. Neurosci. Res.* **85(15):** 3347–3358. *doi:10.1002/jnr.21444.*

11 **Pietrancosta, N., Djibo, M., Daumas, S. and Czaplicki, G.** 2020. Molecular, structural, functional, and pharmacological sites for vesicular glutamate transporter regulation. *Mol. Neurobiol.* **57(6):** 3118–3142. *doi:10.1007/s12035-020-01912-7.*

12 **Li, F., Eriksen, J., Finer-Moore, J., Chang, R., Nguyen, P., Bowen, A., Myasnikov, A., Yu, Z., Bulkley, D., Cheng, Y., Edwards, R.H. and Stroud, R.M.** 2020. Ion transport and regulation in a synaptic vesicle glutamate transporter. *Science* **368(6493):** 893–897. *doi:10.1126/science.aba9202.*

13 **Maycox, P.R., Deckwerth, T., Hell, J.W. and Jahn, R.** 1988. Glutamate uptake by brain synaptic vesicles: energy dependence of transport and functional reconstitution in proteoliposomes. *J. Biol. Chem.* **263(30):** 15423–15428. *doi:10.1016/S0021-9258(19)37605-7*.

14 **Juge, N., Gray, J.A., Omote, H., Miyaji, T., Inoue, T., Hara, C., Uneyama, H., Edwards, R.H., Nicoll, R.A. and Moriyama, Y.** 2010. Metabolic control of vesicular glutamate transport and release. *Neuron* **68(1):** 99–112. *doi:10.1016/j.neuron.2010.09.002*.

15 **Carlson, M.D., Kish, P.E. and Ueda, T.** 1989. Characterization of the solubilized and reconstituted ATP-dependent vesicular glutamate uptake system. *J. Biol. Chem.* **264(13):** 7369–7376. *doi:10.1016/S0021-9258(18)83243-4*.

16 **Hartinger, J. and Jahn, R.** 1993. An anion binding site that regulates the glutamate transporter of synaptic vesicles. *J. Biol. Chem.* **268(31):** 23122–23127. *doi:10.1016/S0021-9258(19)49435-0*.

17 **Preobraschenski, J., Zander, J.-F., Suzuki, T., Ahnert-Hilger, G. and Jahn, R.** 2014. Vesicular glutamate transporters use flexible anion and cation binding sites for efficient accumulation of neurotransmitter. *Neuron.* **84(6):** 1287–1301. *doi:10.1016/j.neuron.2014.11.008*.

18 **Schenck, S., Wojcik, S.M., Brose, N. and Takamori, S.** 2009. A chloride conductance in VGLUT1 underlies maximal glutamate loading into synaptic vesicles. *Nat. Neurosci.* **12(2):** 156–162. *doi:10.1038/nn.2248*.

19 **Eriksen, J., Bjørn-Yoshimoto, W.E., Juge, N. and Edwards, R.H.** 2016. Protons regulate vesicular glutamate transporters through an allosteric mechanism. *Neuron* **90(4):** 768–780. *doi:10.1016/j.neuron.2016.03.026*.

20 **Martineau, M., Guzman, R. E., Fahlke, C. and Klingauf, J.** 2017. VGLUT1 functions as a glutamate/proton exchanger with chloride channel activity in hippocampal glutamatergic synapses. *Nat. Commun.* **8, 2279:** 1–13. *doi:10.1038/s41467-017-02367-6*.

21 **Niswender, C. M. and Conn, P. J.** 2010. Metabotropic glutamate receptors: physiology, pharmacology and disease. *Annu. Rev. Pharmacol. Toxicol.* **50:** 295–322. *doi:10.1146/annurev.pharmtox.011008.145533*.

22 **Chang, R., Eriksen, J. and Edwards, R. H.** 2018. The dual role of chloride in synaptic vesicle glutamate transport. *eLife* **7:** e34896. *doi:10.7554/eLife.34896*.

23 **Kolen, B., Borghans, B., Kortzak, D., Lugo, V., Hannack, C., Guzman, R. E., Ullah, G. and Fahlke, C.** 2023. Vesicular glutamate transporters are H^+-anion exchangers that operate at variable stoichiometry. *Nat. Commun.* **14, 2723:** 1–14. *doi:10.1038/s41467-023-38340-9*.

24 **El Mestikawy, S., Wallén-Mackenzie, Å., Fortin, G.M., Descarries, L. and Trudeau, L.-É.** 2011. From glutamate co-release to vesicular synergy: vesicular glutamate transporters. *Nat. Rev. Neurosci.* **12(4):** 204–216. *doi:10.1038/nrn2969.*

25 **Moechars, D., Weston, M.C., Leo, S., Callaerts-Vegh, Z., Goris, I., Daneels, G., Buist, A., Cik, M., van der Spek, P., Kass, S., Meert, T., D'Hooge, R., Rosenmund, C. and Hampson, R.M.** 2006. Vesicular glutamate transporter VGLUT2 expression levels control quantal size and neuropathic pain. *J. Neurosci.* **26(46):** 12055–12066. *doi:10.1523/JNEUROSCI.2556-06.2006.*

26 **Fazekas, C. L., Szabó, A., Török, B., Bánrévi, K., Correia, P., Chaves, T., Daumas, S. and Zelena, D.** 2022. A new player in the hippocampus: a review on VGLUT3+ neurons and their role in the regulation of hippocampal activity and behaviour. *Int. J. Mol. Sci.* **23(2), 790:** 1–22. *doi:10.3390/ijms23020790.*

27 **Favier, M., Pietrancosta, N., El Mestikawy, S. and Gangarossa, G.** 2021. Leveraging VGLUT3 functions to untangle brain dysfunctions. *Trends Pharmacol. Sci.* **42(6):** 475–487. *doi:10.1016/j.tips.2021.03.003.*

28 **Ni, B., Rosteck, P.R. Jr., Nadi, N.S. and Paul, S.M.** 1994. Cloning and expression of a cDNA encoding a brain-specific Na^+-dependent inorganic phosphate cotransporter. *Proc. Natl. Acad. Sci. U.S.A.* **91(12):** 5607–5611. *doi:10.1073/pnas.91.12.5607.*

29 **Aihara, Y., Mashima, H., Onda, H., Hisano, S., Kasuya, H., Hori, T., Yamada, S., Tomura, H., Yamada, Y., Inoue, I., Kojima, I. and Takeda, J.** 2000. Molecular cloning of a novel brain-type Na^+-dependent inorganic phosphate cotransporter. *J. Neurochem.* **74(6):** 2622–2625. *doi:10.1046/j.1471-4159.2000.0742622.x.*

30 **Takamori, S., Rhee, J.S., Rosenmund, C. and Jahn, R.** 2000. Identification of a vesicular glutamate transporter that defines a glutamatergic phenotype in neurons. *Nature.* **407(6801):** 189–194. *doi:10.1038/35025070.*

31 **Bellocchio, E.E., Reimer, R.J., Fremeau, R.T. Jr. and Edwards, R.H.** 2000. Uptake of glutamate into synaptic vesicles by an inorganic phosphate transporter. *Science.* **289(5481):** 957–960. *doi:10.1126/science.289.5481.957.*

32 **Takamori, S., Rhee, J.S., Rosenmund, C. and Jahn, R.** 2001. Identification of differentiation-associated brain-specific phosphate transporter as a second vesicular glutamate transporter (VGLUT2). *J. Neurosci.* **21(22), RC182:** 1–6. *doi:10.1523/JNEUROSCI.21-22-j0002.2001.*

33 **Gras, C., Herzog, E., Bellenchi, G.C., Bernard, V., Ravassard, P., Pohl, M., Gasnier, B., Giros, B. and El Mestikawy, S.** 2002. A third vesicular glutamate transporter expressed by cholinergic and serotoninergic neurons. *J. Neurosci.* **22(13):** 5442–5451. *doi:10.1523/JNEUROSCI.22-13-05442.2002.*

34 **Juge N., Yoshida Y., Yatsushiro S., Omote H. and Moriyama Y.** 2006. Vesicular glutamate transporter contains two independent transport machineries. *J. Biol. Chem.* **281(51):** 39499–39506. *doi:10.1074/jbc.M607670200.*

35 **Wallén-Mackenzie, Å., Gezelius, H., Thoby-Brisson, M., Nygård, A., Enjin, A., Fujiyama, F., Fortin, G. and Kullander, K.** 2006. Vesicular glutamate transporter 2 is required for central respiratory rhythm generation but not for locomotor central pattern generation. *J. Neurosci.* **26(47):** 12294–12307. *doi:10.1523/JNEUROSCI.3855-06.2006.*

36 **Kashani, A., Betancur, C., Giros, B., Hirsch, E. and El Mestikawy, S.** 2007. Altered expression of vesicular glutamate transporters VGLUT1 and VGLUT2 in Parkinson disease. *Neurobiol. Aging.* **28(4):** 568–578. *doi:10.1016/j.neurobiolaging.2006.02.010.*

37 **van der Hel, W.S., Verlinde, S.A.M.W., Meijer, D.H.M., de Wit, M., Rensen, M.G., van Gassen, K.L.I., van Rijen, P.C., van Veelen, C.W.M. and de Graan, P.N.E.** 2009. Hippocampal distribution of vesicular glutamate transporter 1 in patients with temporal lobe epilepsy. *Epilepsia.* **50(7):** 1717–1728. *doi:10.1111/j.1528-1167.2009.02054.x.*

38 **Oni-Orisan, A., Kristiansen, L.V., Haroutunian, V. and Meador-Woodruff, J.H.** 2008. Altered vesicular glutamate transporter expression in the anterior cingulate cortex in schizophrenia. *Biol. Psychiatry.* **63(8):** 766–775. *doi:10.1016/j.biopsych.2007.10.020.*

39 **Wood, O.W.G., Walby, J., Yeung, J.H., Ke, S., Palpagama, T.H., Turner, C., Waldvogel, H.J., Faull, R.L.M. and Kwakowsky, A.** 2024. Alzheimer's disease-associated region-specific decrease of vesicular glutamate transporter immunoreactivity in the medial temporal lobe and superior temporal gyrus. *Neuroscience.* **546:** 75–87. *doi:10.1016/j.neuroscience.2024.03.027.*

40 **Vigneault, É., Poirel, O., Riad, M., Prud'homme, J., Dumas, S., Turecki, G., Fasano, C., Mechawar, N. and El Mestikawy, S.** 2015. Distribution of vesicular glutamate transporters in the human brain. *Front. Neuroanat.* **9, 23:** 1–14. *doi:10.3389/fnana.2015.00023.*

41 **Inta, D., Vogt, M.A., Perreau-Lenz, S., Schneider, M., Pfeiffer, N., Wojcik, S.M., Spanagel, R. and Gass, P.** 2012. Sensorimotor gating, working and social memory deficits in mice with reduced expression of the vesicular glutamate transporter VGLUT1. *Behav. Brain Res.* **228(2):** 328–332. *doi:10.1016/j.bbr.2011.12.012.*

42 **Scherrer, G., Low, S.A., Wang, X., Zhang, J., Yamanaka, H., Urban, R., Solorzano, C., Harper, B., Hnasko, T.S., Edwards, R.H. and Basbaum, A.I.** 2010. VGLUT2 expression in primary afferent neurons is essential for normal acute pain and injury-induced heat hypersensitivity. *Proc. Natl. Acad. Sci. U.S.A.* **107(51):** 22296–22301. *doi:10.1073/pnas.1013413108.*

43 **Tordera, R.M., Totterdell, S., Wojcik, S.M., Brose, N., Elizalde, N., Lasheras, B. and Del Rio, J.** 2007. Enhanced anxiety, depressive-like behaviour and impaired recognition memory in mice with reduced expression of the vesicular glutamate transporter 1 (VGLUT1). *Eur. J. Neurosci.* **25(1):** 281–290. *doi:10.1111/j.1460-9568.2006.05259.x.*

44 **Xu, Y., Wu, Z., Sun, H., Zhu, Y., Kim, E.R., Lowell, B.B., Arenkiel, B.R., Xu, Y. and Tong, Q.** 2013. Glutamate mediates the function of melanocortin receptor 4 on Sim1 neurons in body weight regulation. *Cell Metab.* **18(6):** 860–870. *doi:10.1016/j.cmet.2013.11.003.*

45 **Xu, Y., Jiang, Z., Li, H., Cai, J., Jiang, Y., Ortiz-Guzman, J., Xu, Y., Arenkiel, B.R. and Tong, Q.** 2023. Lateral septum as a melanocortin downstream site in obesity development. *Cell Rep.* **42(5):** 112502. *doi:10.1016/j.celrep.2023.112502.*

46 **Hayashi, M., Otsuka, M., Morimoto, R., Muroyama, A., Uehara, S., Yamamoto, A., Moriyama, Y. and Yamamoto, A.** 2003. Expression and localization of vesicular glutamate transporters in pancreatic islets, upper gastrointestinal tract, and testis. *J. Histochem. Cytochem.* **51(10):** 1375–1390. *doi:10.1177/002215540305101014.*

47 **Gheni, G., Ogura, M., Iwasaki, M., Yokoi, N., Minami, K., Nakayama, Y., Harada, K., Hastoy, B., Wu, X., Takahashi, H., Kimura, K., Matsubara, T., Hoshikawa, R., Hatano, N., Sugawara, K., Shibasaki, T., Inagaki, N., Bamba, T., Mizoguchi, A., Fukusaki, E., Rorsman, P. and Seino, S.** 2014. Glutamate acts as a key signal linking glucose metabolism to incretin/cAMP action to amplify insulin secretion. *Cell Rep.* **9(2):** 661–673. *doi:10.1016/j.celrep.2014.09.030.*

48 **Hnasko, T.S., Chuhma, N., Zhang, H., Goh, G.Y., Sulzer, D., Palmiter, R.D., Rayport, S. and Edwards, R.H.** 2010. Vesicular glutamate transport promotes dopamine storage and glutamate corelease in vivo. *Neuron.* **65(5):** 643–656. *doi:10.1016/j.neuron.2010.02.012.*

49 **Amilhon, B., Lepicard, E., Renoir, T., Mongeau, R., Popa, D., Poirel, O., Miot, S., Gras, C., Gardier, A.M., Gallego, J., Hamon, M., Lanfumey, L., Gasnier, B., Giros, B. and El Mestikawy, S.** 2010. VGLUT3 (vesicular glutamate transporter type 3) contribution to the regulation of serotonergic transmission and anxiety. *J. Neurosci.* **30(6):** 2198–2210. *doi:10.1523/JNEUROSCI.5196-09.2010.*

50 **Seal, R.P., Akil, O., Yi, E., Weber, C.M., Grant, L., Yoo, J., Clause, A., Kandler, K., Noebels, J.L., Glowatzki, E., Lustig, L.R. and Edwards, R.H.** 2008. Sensorineural deafness and seizures in mice lacking vesicular glutamate transporter 3. *Neuron.* **57(2):** 263–275. *doi:10.1016/j.neuron.2007.11.032.*

51 **Ruel, J., Emery, S., Nouvian, R., Bersot, T., Amilhon, B., Van Rybroek, J.M., Rebillard, G., Lenoir, M., Eybalin, M., Delprat, B., Sivakumaran, T.A., Giros, B., El Mestikawy, S., Moser, T., Smith, R.J.H., Lesperance, M.M. and Puel, J.-L.** 2008. Impairment of SLC17A8 encoding vesicular glutamate transporter-3, VGLUT3, underlies nonsyndromic deafness DFNA25 and inner hair cell dysfunction in null mice. *Am. J. Hum. Genet.* **83(2):** 278–292. *doi:10.1016/j.ajhg.2008.07.008.*

52 **Wojcik, S.M., Rhee, J.S., Herzog, E., Sigler, A., Jahn, R., Takamori, S., Brose, N. and Rosenmund, C.** 2004. An essential role for vesicular glutamate transporter 1 (VGLUT1) in postnatal development and control of quantal size. *Proc. Natl. Acad. Sci. U.S.A.* **101(18):** 7158–7163. *doi:10.1073/pnas.0401764101.*

53 **Gras, C., Amilhon, B., Lepicard, E.M., Poirel, O., Vinatier, J., Herbin, M., Dumas, S., Tzavara, E.T., Wade, M.R., Nomikos, G.G., Hanoun, N., Saurini, F., Kemel, M.-L., Gasnier, B., Giros, B. and El Mestikawy, S.** 2008. The vesicular glutamate transporter VGLUT3 synergizes striatal acetylcholine tone. *Nat. Neurosci.* **11(3):** 292–300. *doi:10.1038/nn2052.*

54 **Sakae, D.Y., Marti, F., Lecca, S., Vorspan, F., Martín-García, E., Morel, L.J., Henrion, A., Gutiérrez-Cuesta, J., Besnard, A., Heck, N., Herzog, E., Bolte, S., Prado, V.F., Prado, M.A.M., Bellivier, F., Eap, C.B., Crettol, S., Vanhoutte, P., Caboche, J., Gratton, A., Moquin, L., Giros, B., Maldonado, R., Daumas, S., Mameli, M., Jamain, S. and El Mestikawy, S.** 2015. The absence of VGLUT3 predisposes to cocaine abuse by increasing dopamine and glutamate signaling in the nucleus accumbens. *Mol. Psychiatry.* **20(11):** 1448–1459. *doi:10.1038/mp.2015.104.*

55 **Ramet, L., Zimmermann, J., Bersot, T., Poirel, O., De Gois, S., Silm, K., Sakae, D.Y., Mansouri-Guilani, N., Bourque, M.-J., Trudeau, L.-E., Pietrancosta, N., Daumas, S., Bernard, V., Rosenmund, C. and El Mestikawy, S.** 2017. Characterization of a human point mutation of VGLUT3 (p.A211V) in the rodent brain suggests a nonuniform distribution of the transporter in synaptic vesicles. *J. Neurosci.* **37(15):** 4181–4199. *doi:10.1523/JNEUROSCI.0282-16.2017.*

56 **Rostamipour, K., Talandashti, R. and Mehrnejad, F.** 2022. Atomistic insight into the luminal allosteric regulation of vesicular glutamate transporter 2 by chloride and protons: An all-atom molecular dynamics simulation study. *Proteins Struct. Funct. Bioinform.* **90(12):** 2045–2056. *doi:10.1002/prot.26396.*

57 **Gray, P.T.A.** 1994. Chapter 8: Analysis of whole-cell currents to estimate the kinetics and amplitude of underlying unitary events: relaxation and 'noise' analysis. pp. 189–207. In: Ogden, D. ed. *Microelectrode techniques: The Plymouth workshop handbook.* Cambridge, UK: The Company of Biologists Ltd. *ISBN:9780948601491.*

58 **Alvarez, O., Gonzalez, C. and Latorre, R.** 2002. Counting channels: a tutorial guide on ion channel fluctuation analysis. *Adv. Physiol. Educ.* **26(4):** 327–341. *doi:10.1152/advan.00006.2002.*

59 **Ho, S.N., Hunt, H.D., Horton, R.M., Pullen, J.K. and Pease, L.R.** 1989. Site-directed mutagenesis by overlap extension using the polymerase chain reaction. *Gene.* **77(1):** 51–59. *doi:10.1016/0378-1119(89)90358-2.*

60 **DeFelice, L.J.** 1981. *Introduction to membrane noise.* New York, NY, USA: Plenum Press. *ISBN:9780306405136.*

61 **Zerangue, N. and Kavanaugh, M.P.** 1996. Flux coupling in a neuronal glutamate transporter. *Nature.* **383(6601):** 634–637. *doi:10.1038/383634a0.*

62 **Rudnick, G.** 1998. Chapter 16: Ion-coupled neurotransmitter transport: thermodynamic vs. kinetic determinations of stoichiometry. pp. 233–247. In: Amara, S.G. ed. *Methods in enzymology, Vol. 296: neurotransmitter transporters.* San Diego, CA, USA: Academic Press. *ISBN:9780121821975.*

63 **Owe, S.G., Marcaggi, P. and Attwell, D.** 2006. The ionic stoichiometry of the GLAST glutamate transporter in salamander retinal glia. *J. Physiol.* **577(2):** 591–599. *doi:10.1113/jphysiol.2006.116830.*

64 **Tabb, J.S., Kish, P.E., Van Dyke, R. and Ueda, T.** 1992. Glutamate transport into synaptic vesicles. Roles of membrane potential, pH gradient and intravesicular pH. *J. Biol. Chem.* **267(22):** 15412–12418. *doi:10.1016/S0021-9258(19)49549-5.*

65 **Molleman, A.** 2003. *Patch clamping: an introductory guide to patch clamp electrophysiology.* Chichester, West Sussex, England: Wiley. *ISBN:9780471486855.*

66 **Lok Lei, C., Clerx, M., Whittaker, D.G., Gavaghan, D.J., de Boer, T.P. and Mirams, G.R.** 2020. Accounting for variability in ion current recordings using a mathematical model of artefacts in voltage-clamp experiments. *Philos. Trans. A Math. Phys. Eng. Sci.* **378(2173):** 1–21. *doi:10.1098/rsta.2019.0348.*

67 **Wonderlin, W.F., French, R.J., Arispe, N.J.** 1990. Recording and analysis of currents from single ion channels. pp. 35–142. In: Boulton, A.A., Baker, G.B. and Vanderwolf, C.H. eds. *Neurophysiological techniques: basic methods and concepts. Neuromethods, Vol. 14.* Totowa, NJ, USA: Humana Press. *ISBN:9780896031609.*

68 **Dixon, P.M.** 2006. Bootstrap resampling. pp. 1–9. *doi:10.1002/9780470057339.vab028.* In: El-Shaarawi A.H. and Piegorsch, W.W. eds. *Encyclopedia of environmetrics.* Chichester, West Sussex, England: Wiley.

69 **Iwi, G., Millard, R.K., Palmer, A.M., Preece, A.W. and Saunders, M.** 1999. Bootstrap resampling: a powerful method of assessing confidence intervals for doses from experimental data. *Phys. Med. Biol.* **44(4):** 55–62. *doi:10.1088/0031-9155/44/4/021.*

70 **Colquhoun, D. and Hawkes, A.G.** 1994. Chapter 7: The interpretation of single channel recordings. pp. 141–188. In: Ogden, D. ed. *Microelectrode techniques: The Plymouth workshop handbook.* Cambridge, UK: The Company of Biologists Ltd. *ISBN:9780948601491.*

71 **Weiss, J.N.** 1997. The Hill equation revisited: uses and misuses. *FASEB J.* **11(11):** 835–841. *doi:10.1096/fasebj.11.11.9285481.*

72 **Borghans, B., Kortzak, D., Longo, P., Kolen, B., Machtens, J.P. and Fahlke, C.** 2025. Allosteric modulation of proton binding confers Cl^- activation and glutamate selectivity to vesicular glutamate transporters. *PLoS Comput. Biol.* **21(6):** 1–32. *doi:10.1371/journal.pcbi.1013214.*

73 **Li, F., Eriksen, J., Oses-Prieto, J.A., Gomez, Y.K., Xu, H., Hareendranath, S., Das, P., Finer-Moore, J., Nguyen, P., Bowen, A., Nelson, A., Burlingame, A., Grabe M., Stroud, R.M. and Edwards, R.H.** 2025. Substrate recognition and allosteric regulation of synaptic vesicle glutamate transporter VGLUT2. *Nat. Struct. Mol. Biol. doi:10.1038/s41594-025-01568-8.*

74 **Hebeisen, S., Heidtmann, H., Cosmelli, D., Gonzalez, C., Poser, B., Latorre, R., Alvarez, O. and Fahlke C.** 2003. Anion permeation in human ClC-4 channels. *Biophys. J.* **84(4):** 2306–2318. *doi: 10.1016/S0006-3495(03)75036-X.*

75 **Hebeisen, S., Biela, A., Giese, B., Müller-Newen, G., Hidalgo, P. and Fahlke, C.** 2004. The role of the carboxyl terminus in ClC chloride channel function. *J. Biol. Chem.* **279(13):** 13140–13147. *doi: 10.1074/jbc.M312649200.*

76 **Kovermann, P., Machtens, J.P., Ewers, D. and Fahlke, C.** 2010. A conserved aspartate determines pore properties of anion channels associated with excitatory amino acid transporter 4 (EAAT4). *J. Biol. Chem.* **285(31):** 23676–23686. *doi:10.1074/jbc.M110.126557.*

77 **Machtens, J.P., Fahlke, C. and Kovermann, P.** 2011. Noise analysis to study unitary properties of transporter-associated ion channels. *Channels.* **5(6):** 468–474. *doi:10.4161/chan.5.6.17453.*

78 **Grewer, C. and Rauen, T.** 2005. Electrogenic glutamate transporters in the CNS: molecular mechanism, pre-steady-state kinetics and their impact on synaptic signaling. *J. Membr. Biol.* **203(1):** 1–20. *doi:10.1007/s00232-004-0731-6.*

79 **Grewer, C., Gameiro, A., Zhang, Z., Tao, Z., Braams, S. and Rauen, T.** 2008. Glutamate forward and reverse transport: from molecular mechanism to transporter-mediated release after ischemia. *IUBMB Life.* **60(9):** 609–619. *doi:10.1002/iub.98.*

80 **Fahlke, C.** 2001. Ion permeation and selectivity in ClC-type chloride channels. *Am. J. Physiol.Renal Physiol.* **280:** 748–757. *doi: 10.1152/ajprenal.2001.280.5.F748.*

81 **Daniels, R.W., Collins, C.A., Gelfand, M.V., Dant, J., Brooks, E.S., Krantz, D.E. and DiAntonio, A.** 2004. Increased expression of the *Drosophila* vesicular glutamate transporter leads to excess glutamate release and a compensatory decrease in quantal content. *J. Neurosci.* **24(46):** 10466–10474. *doi:10.1523/JNEUROSCI.3001-04.2004.*

82 **Ronstedt, K., Sternberg, D., Detro-Dassen, S., Gramkow, T., Begemann B., Becher, T., Kilian, P., Grieschat, M., Machtens J.P., Schmalzing, G., Fischer M. and Fahlke, C.** 2015. Impaired surface membrane insertion of homo- and heterodimeric human muscle chloride channels carrying amino-terminal myotonia-causing mutations. *Sci. Rep.* **5:15382** 1–16. *doi: 10.1038/srep15382.*

83 **Egashira, Y., Takase M., Watanabe, S., Ishida, J., Fukamizu, A., Kaneko, R., Yanagawa, Y. and Takamori, S.** 2016. Unique pH dynamics in GABAergic synaptic vesicles illuminates the mechanism and kinetics of GABA loading. *Proc. Natl. Acad. Sci. USA.* **113(38):** 10702–10707. *doi:10.1073/pnas.1604527113.*

84 **Miesenböck, G., De Angelis, D.A. and Rothman, J.E.** 1998. Visualizing secretion and synaptic transmission with pH-sensitive green fluorescent proteins. *Nature.* **394(6689):** 192–195. *doi:10.1038/28190.*

85 **Atluri, P.P. and Ryan T.A.** 2006. The kinetics of synaptic vesicle reacidification at hippocampal nerve terminals. *J. Neurosci.* **26(8):** 2313–2320. *doi:10.1523/JNEUROSCI.4425-05.2006.*

86 **Schellinger, J.N., Sun Q., Pleinis, J.M., An, S.W., Hu, J., Mercenne, G., Titos, I., Huang, C.L., Rothenfluh, A. and Rodan, A.R.** 2022. Chloride oscillation in pacemaker neurons regulates circadian rhythms through a chloride-sensing WNK kinase signaling cascade. *Curr. Biol.* **32(6):** 1429–1438. *doi:10.1016/j.cub.2022.03.017.*

87 **Hori, T. and Takahashi, T.** 2012. Kinetics of synaptic vesicle refilling with neurotransmitter glutamate. *Neuron.* **76(3):** 511–517. *doi:10.1016/j.neuron.2012.08.013.*

88 **Joshi, Y., Petit, C.P., Miot, S., Guillet, M., Sendin, G., Bourien, J., Wang, J., Pujol, R., El Mestikawy, S., Puel, J.L. and Nouvian, R.** 2021. VGLUT3-p.A211V variant fuses stereocilia bundles and elongates synaptic ribbons. *J. Physiol.* **599(24):** 5397–5416. *doi:10.1113/JP282181.*

89 **Brini, M., Calì, T., Ottoloni, D. and Carafoli, E.** 2013. Chapter 5: Intracellular calcium homeostasis and signaling. pp. 119–168. In: Banci, L. ed. *Metal ions in life sciences, Vol. 12: metallomics and the cell.* Dordrecht, Netherlands: Springer *ISBN:9789400755611.*

90 **Carafoli, E. and Krebs, J.** 2016. Why calcium? How calcium became the best communicator. *J. Biol. Chem.* **291(40):** 20849–20857. *doi:10.1074/jbc.R116.735894.*

91 **Berridge, M.J., Lipp, P. and Bootman, M.D.** 2000. The versatility and universality of calcium signalling. *Nat. Rev. Mol. Cell Biol.* **1:** 11–21 *doi:10.1038/35036035.*

92 **Corry, B. and Hool, L.** 2006. Chapter 7: Calcium channels. pp. 241–300. In: Chung, S.H., Andersen, O.S. and Krishnamurthy, V. eds. *Biological membrane ion channels: dynamics, structure and applications.* New York, USA: Springer. *ISBN:9780387333236.*

93 **Yao, X., Gao, S. and Yan, N.** 2023. Structural biology of voltage-gated calcium channels. *Channels.* **18(1):** 1–19. *doi:10.1080/19336950.2023.2290807.*

94 **Catterall, W.A.** 2011. Voltage-gated calcium channels. *Cold Spring Harb. Perspect. Biol.* **3(8):** 1–23. *doi:10.1101/cshperspect.a003947.*

95 **Neely, A. and Hidalgo, P.** 2014. Structure–function of proteins interacting with the α_1 pore-forming subunit of high-voltage-activated calcium channels. *Front. Physiol.* **5(209):** 1–19. *doi:10.3389/fphys.2014.00209.*

96 **Buraei, Z. and Yang, J.** 2010. The β subunit of voltage-gated Ca^{2+} channels. *Physiol. Rev.* **90(4):** 1461–1506. *doi:10.1152/physrev.00057.2009.*

97 **Anderson, J.M.** 1996. Cell signalling: MAGUK magic. *Curr. Biol.* **6(4):** 382–384. *doi:10.1016/s0960-9822(02)00501-8.*

98 **Wu, J., Yan, Z., Li, Z., Qian, X., Lu, S., Dong, M., Zhou, Q. and Yan, N.** 2016. Structure of the voltage-gated calcium channel $Ca_V1.1$ at 3.6 Å resolution. *Nature.* **537(7619):** 191–196. *doi:10.1038/nature19321.*

99 **Chen, Y.H., Li, M.H., Zhang, Y., He, L.L., Yamada, Y., Fitzmaurice, A., Shen, Y., Zhang, H., Tong, L. and Yang, J.** 2004. Structural basis of the α_1–β subunit interaction of voltage-gated Ca^{2+} channels. *Nature.* **429(6992):** 675–680. *doi:10.1038/nature02641.*

100 **Rima, M., Daghsni, M., Fajloun, Z., M'rad, R., Brusés, J.L., Ronjat, M. and De Waard, M.** 2016. Protein partners of the calcium channel β subunit highlight new cellular functions. *Biochem. J.* **473(13):** 1831–1844. *doi:10.1042/BCJ20160125.*

101 **Stölting, G., de Oliveira, R.G., Guzman, R.E., Miranda-Laferte, E., Conrad, R., Jordan, N., Schmidt, S., Hendriks, J., Gensch, T. and Hidalgo, P.** 2015. Direct interaction of $Ca_V\beta_2$ with actin up-regulates L-type calcium currents in HL-1 cardiomyocytes. *J. Biol. Chem.* **290(8):** 4561–4572. *doi:10.1074/jbc.M114.573956.*

102 **Conrad, R., Stölting, G., Hendriks, J., Ruello, G., Kortzak, D., Jordan, N., Gensch, T. and Hidalgo, P.** 2018. Rapid turnover of the cardiac L-type $Ca_V\beta_2$ channel by endocytic recycling regulates its cell surface availability. *iScience.* **7:** 1–15. *doi:10.1016/j.isci.2018.08.012.*

103 **Guzman, G.A., Guzman, R.E., Jordan, N., Hidalgo, P.** 2019. A tripartite interaction among the calcium channel α_1- and β-subunits and F-actin increases the readily releasable pool of vesicles and its recovery after depletion. *Front. Cell Neurosci.* **13(125):** 1–16. *doi:10.3389/fncel.2019.00125.*

104 **Conrad, R., Kortzak, D., Guzman, G.A., Miranda-Laferte, E. and Hidalgo, P.** 2021. $Ca_V\beta$ controls the endocytic turnover of $Ca_V1.2$ L-type calcium channel. *Traffic.* **22(6):** 180–193. *doi:10.1111/tra.12788.*

105 **Ullrich, F., Blin, S., Lazarow, K., Daubitz, T., von Kries, J.P. and Jentsch, T.J.** 2019. Identification of TMEM206 proteins as pore of PAORAC/ASOR acid-sensitive chloride channels. *Elife.* **18(8):** e49187. *doi:10.7554/eLife.49187.*

106 **Yang, J., Chen, J., Vitery, M.D.C., Osei-Owusu, J., Chu, J., Yu, H., Sun S. and Qiu, Z.** 2019. PAC, an evolutionarily conserved membrane protein, is a proton-activated chloride channel. *Science.* **64(6438):**395–399. *doi:10.1126/science.aav9739.*

107 **Ran, F.A., Hsu, P.D., Wright, J., Agarwala, V., Scott, D.A. and Zhang, F.** 2013. Genome engineering using the CRISPR-Cas9 system. *Nat. Protoc.* **8(11):** 2281–2308. *doi:10.1038/nprot.2013.143.*

108 **Müller, C.S., Haupt, A., Bildl, W., Schindler, J., Knaus, H-G., Meissner, M., Rammner, B., Striessnig, J., Flockerzi, V., Fakler, B. and Schulte, U.** 2010. Quantitative proteomics of the Cav2 channel nano-environments in the mammalian brain. *Proc. Natl. Acad. Sci. U.S.A.* **107(34):** 14950–-14957. *doi:10.1073/pnas.1005940107.*

109 **Catterall, W.A., Perez-Reyes, E., Snutch, T.P. and Striessnig, J.** 2005. International Union of Pharmacology. XLVIII. Nomenclature and structure-function relationships of voltage-gated calcium channels. *Pharmacol. Rev.* **57(4):** 411–-425. *doi:10.1124/pr.57.4.5.*

110 **Escayg, A., De Waard, M., Lee, D.D., Bichet, D., Wolf, P., Mayer, T., Johnston, J., Baloh, R., Sander, T. and Meisler, M.H.** 2000. Coding and noncoding variation of the human calcium-channel beta4-subunit gene CACNB4 in patients with idiopathic

generalized epilepsy and episodic ataxia. *Am. J. Hum. Genet.* **66(5):** 1531–1539. *doi:10.1086/302909.*

111 **Etemad, S., Campiglio, M., Obermair, G.J. and Flucher, B.E.** 2014. The juvenile myoclonic epilepsy mutant of the calcium channel β_4 subunit displays normal nuclear targeting in nerve and muscle cells. *Channels* **8(4):** 334–343. *doi:10.4161/chan.29322.*

112 **Bezanilla, F.** 2018. Gating currents. *J. Gen. Physiol.* **150(7):** 911–-932. *doi:10.1085/jgp.201812090.*

113 **Catacuzzeno, L., Conti, F. and Franciolini, F.** 2023. Fifty years of gating currents and channel gating. *J. Gen. Physiol.* **155(8)e202313380:** 1–-33. *doi:10.1085/jgp.202313380.*

114 **Chatterjee, S. and Simonoff, J.S.** 2013. *Handbook of regression analysis.* Hoboken, NJ: Wiley. *ISBN:9780470887165.*

115 **Tombola, F., Pathak, M.M. and Isacoff, E.Y.** 2006. How does voltage open an ion channel? *Annu. Rev. Cell. Dev. Biol.* **22:** 23–52. *doi:10.1146/annurev.cellbio.21.020404.145837.*

116 **Chanda, B. and Chowdhury, S.** 2023. Chapter 2: Voltage-dependent gating of ion channels. pp. 21–43. *doi:10.1201/9781003096214-3.* In: Zheng, J. and Trudeau, M.C., eds. *Textbook of Ion Channels: Basics and Methods.* Boca Raton, USA: CRC Press, Taylor & Francis Group. *ISBN:9781003096214.*

Annex

During the course of this doctoral research, the author contributed to the following peer-reviewed publication:

Kolen. B.[†], Borghans, B.[†], Kortzak, D., **Lugo, V.,** Hannack, C., Guzman, R.E., Ullah, G., Fahlke, C. 2023. **Vesicular glutamate transporters are H^+-anion exchangers that operate at variable stoichiometry.** *Nat. Commun.* 14, 2723: 1–14.

—Contribution: Performed patch-clamp recordings to estimate glutamate/proton exchange stoichiometry and characterize Rose Bengal inhibition of rVGLUT1-mediated channel and transport currents.

Eidesstattliche Erklärung

Ich versichere an Eides Statt, dass die Dissertation von mir selbstständig und ohne unzulässige fremde Hilfe unter Beachtung der “Grundsätze zur Sicherung guter wissenschaftlicher Praxis an der Heinrich-Heine-Universität Düsseldorf” erstellt worden ist.

Ort, Datum

Victor Lugo